Mathematical Modelling of Oncolytic Virotherapy

Alexander Shabala

New College

University of Oxford

A thesis submitted for the degree of

Doctor of Philosophy

Trinity 2013

Acknowledgements

This study was funded by the Rhodes Trust, and I would like to thank them for helping me fulfil my dream. I would also like to acknowledge New College, University of Oxford for taking me on as a Junior Dean towards the end of my studies.

I am deeply indebted to my supervisors; Jon Chapman, Sarah Waters and Chris Breward. I have learned a tremendous amount from you these past few years, and this work would not have been possible without your guidance, support and patience. In addition, I would like to thank Eamonn Gaffney from the Centre for Mathematical Biology and Steve Webb from University of Liverpool for agreeing to be my examiners, as well as for their constructive comments and advice that have improved this work.

I am grateful to all my friend and colleagues within the Oxford Centre for Industrial and Applied Mathematics over the past four years, but in particular, Chris Lustri, Mohit Dalwadi, Cara Morgan, Jonny Black and Natalie Pearson. Monday mornings will never be the same.

On a more personal level, I would like to thank my friends in Oxford, who have made this one of the most memorable experience of my life. This margin is too narrow to contain a comprehensive list of all those who have kept me sane, but a special mention must be made of Mark Curtis, Chris Hinchcliffe, Ashley Nord, Gavin Sourgen and Matt Alkaitis. I am very fortunate that our paths have crossed, and I look forward to the many adventures that the future has in store for us.

Huge thanks go to my family, particularly my parents Sergey and Svetlana, and brother Stas, for their interest in my work and for their continued support. From reading (and in some cases, not reading) sections, to dispensing invaluable advice and encouragement, each of you has been a pillar of strength for me. Finally, I would like to thank my fiancée, Nicolina, for her patience, understanding and companionship throughout. This work is for you.

Abstract

This thesis is concerned with mathematical modelling of oncolytic virotherapy: the use of genetically modified viruses to selectively spread, replicate and destroy cancerous cells in solid tumours. Traditional spatially-dependent modelling approaches have previously assumed that virus spread is due to viral diffusion in solid tumours, and also neglect the time delay introduced by the lytic cycle for viral replication within host cells.

A deterministic, age-structured reaction-diffusion model is developed for the spatially-dependent interactions of uninfected cells, infected cells and virus particles, with the spread of virus particles facilitated by infected cell motility and delay. Evidence of travelling wave behaviour is shown, and an asymptotic approximation for the wave speed is derived as a function of key parameters.

Next, the same physical assumptions as in the continuum model are used to develop an equivalent discrete, probabilistic model for that is valid in the limit of low particle concentrations. This mesoscopic, compartment-based model is then validated against known test cases, and it is shown that the localised nature of infected cell bursts leads to inconsistencies between the discrete and continuum models.

The qualitative behaviour of this stochastic model is then analysed for a range of key experimentally-controllable parameters. Two-dimensional simulations of *in vivo* and *in vitro* therapies are then analysed to determine the effects of virus burst size, length of lytic cycle, infected cell motility, and initial viral distribution on the wave speed, consistency of results and overall success of therapy.

Finally, the experimental difficulty of measuring the effective motility of cells is addressed by considering effective medium approximations of diffusion through heterogeneous tumours. Considering an idealised tumour consisting of periodic obstacles in free space, a two-scale homogenisation technique is used to show the effects of obstacle shape on the effective diffusivity. A novel method for calculating the effective continuum behaviour of random walks on lattices is then developed for the limiting case where microscopic interactions are discrete.

Statement of Originality

I confirm that this thesis is wholly my own original work, and that no part of this thesis has been accepted or is currently being submitted for any degree, diploma, certificate, or other qualification at the University of Oxford or elsewhere. All methods and techniques used in this thesis that have been developed by other authors have been acknowledged by citation of the relevant publications.

Contents

List of Figures

Chapter 1

Introduction

1.1 Biological overview

The field of cancer gene research has grown considerably over the past few decades. This broad area of research involves the use of genetic material to modify cells for the purpose of destroying the tumour mass. Generally speaking, the methods used can be split into one of three fields: immunotherapy, gene transfer and the use of oncolytic agents (Figure 1.1).

Immunotherapy is based around the concept of stimulating the body's immune system to better recognise and destroy cancer cells. While traditional immunotherapy has previously had limited success, the current methods of using gene therapy to create recombinant cancer vaccines (created artificially by combining two or more sequences) have shown promising results, with a number of studies reaching Phase III trials (Cross and Burmester, 2006). Harvested cancer cells are grown in vitro, and engineered to be more recognisable to the immune system by altering genes that produce pro-inflammatory immune-stimulating molecules. These altered cells are then incorporated into a vaccine administered to patients, in the hope of boosting the immune response.

Gene transfer treatments refer to the insertion of a foreign gene into the cancer cell or surrounding tissue to express specific genes such as angiogenesis or suicide genes. Unlike immunotherapy techniques, this treatment does not rely on an immune response, and due the variety of gene expressions possible, this approach is considered extremely broad. Typically, replication-incompetent viruses, such as modified strains of adenovirus, have been used to deliver these genes, although such methods have met difficulties. Problems arising from gene silencing (the gene not being expressed for a long enough time period) as well as the accurate insertion of the agent without contaminating surrounding tissue have been challenging for the current level of technology, although trials of a modified adenovirus to deliver the p53 gene to cancer cells have currently reached Phase III trials. No large-scale efficacy studies have been published, but there is growing optimism for

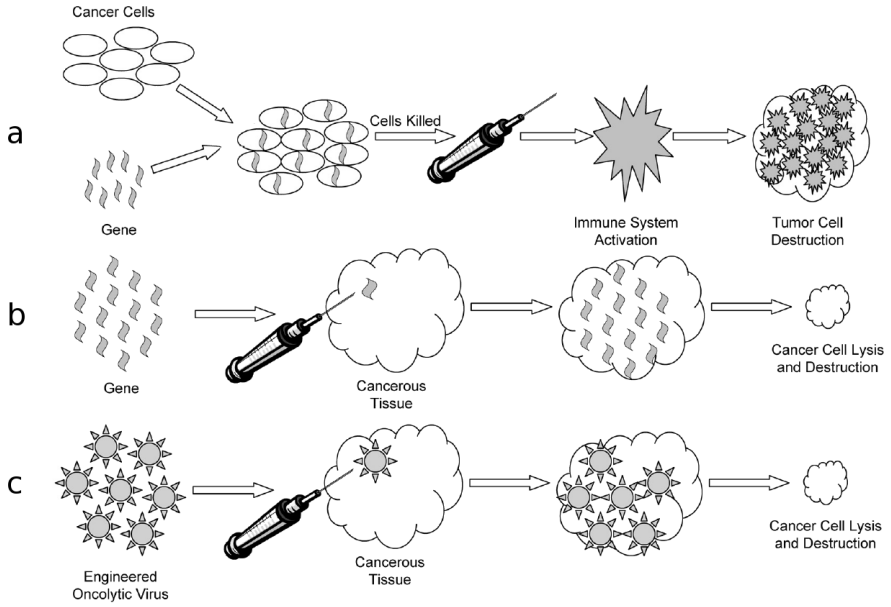

Figure 1.1: Conceptual schematic of gene therapy mechanisms. Pathway A represents immunotherapy, Pathway B gene transfer and Pathway C represents oncolytic virotherapy (adapted from Cross and Burmester, 2006).

improved techniques to deal with the problem of delivery and immune response (Cross and Burmester, 2006).

In this work, we will be focusing on the applications of the third form of gene therapy treatments, known as oncolytic virotherapy. This treatment involves the use of oncolytic agents, namely genetically modified viruses to selectively infect cancer cells and induce cell death through lysis and further propagation of the virus. A number of viruses such as the adenovirus, herpes simplex virus and Newcastle diseases have previously been used for such purposes (Aghi and Martuza, 2005), each having particular advantages in terms of preferential targeting of cancer cells and ease of genetic manipulation. In contrast to gene transfer treatments which utilise replication-incompetent viruses to alter the characteristics of cancer cells, oncolytic agents have the ability to selectively replicate within the target cancer cell, resulting in an amplification effect in areas of tumour growth, allowing for safer doses of viral agent to be used in treatment (Liu and Kirn, 2008).

1.1.1 Virus properties and the lytic cycle

While trials treating solid tumours in immunodeficient mice have been extremely promising (Mcauliffe et al., 2000; Liu et al., 2006), human trials have been less successful due to the nature of the viruses used.

Due to the metastatic nature of aggressive tumours, the bloodstream has previously been used as a delivery mechanism for therapeutic agents to multiple tumours (Jain, 1999, 2001). However, viruses outside of a host cell are essentially inert particles, and as virus particles are an order of magnitude larger than traditional chemotherapeutic agents (Mok

et al., 2009), they rely on passive targeting to reach a tumour systemically (Guo et al., 2008). This approach has had limited success due to the common virus strains used in virotherapy. Virus particles injected into the bloodstream are vulnerable to inactivation by complement proteins, and an immune response is often mounted before the virus has sufficient time to spread to the tumour mass (Power et al., 2007). More success has been achieved with intratumoural injections of virus particles, where lower doses can be used (Parato et al., 2005; Liu et al., 2007; Wang et al., 2003).

Once inside the tumour, virus particles can infect host cells to begin the replication process. The exact mechanism of replication and eventual release depends on the specific virus family. Most naked viruses and some enveloped viruses required cell lysis in order to release new virions from the host cell. In addition to increasing virus population, cell lysis results in host cell death, and is therefore the primary mechanism for tumour destruction in oncolytic virotherapy (Heise et al., 1999). The lytic cycle consists of five stages (Shors, 2011, pp.69–85)

1. Attachment: The virus binds to specific receptors on the host cell.

2. Entry: Naked viruses typically inject nucleic acid into the host cell, whereas for enveloped viruses, the host cell can phagocytose the entire virus particle into a vacuole and when the virus breaks out of the vacuole, it releases nucleic acid into the cell.

3. Replication: The virus's nucleic acid instructs the host cell to replicate the virus DNA or RNA.

4. Assembly: New virus particles are assembled.

5. Lysis and Release: The virus directs the production of an enzyme which damages the host cell wall, causing the host cell to swell and burst. The burst of the host cell membrane causes cell death, and the newly formed virus particles are released, free to enter new cells, spreading the infection.

The location and method of replication also varies between RNA and DNA viruses (Table 1.1). The genome replication of most DNA viruses takes place in the cell's nucleus. The majority of these enter the cell by receptor-mediated endocytosis, although certain viruses (such as herpesvirus) can enter the cell by direct fusion with the cell membrane. The replication of RNA viruses, on the other hand, usually takes place in the cytoplasm. Whether a virus has an RNA or a DNA genome is significant when it comes to developing antiviral agents to control viruses (Shors, 2011, pp. 48–50). In the case of RNA viruses, all of the enzymes used in genome replication and transcription are viral encoded enzymes different from those of the host cell so these enzymes can potentially be targeted. On the other hand, DNA viruses use the host cell's RNA transcription machinery and DNA replication

machinery, so these enzymes, shared by the virus and the host cell, cannot be targeted by the immune system without killing the host cell.

The total duration of the lytic cycle (known as the burst time), as well as the number of virions produced in the replication stage, varies with virus properties, and depends on the type of nucleic acid and strandedness, as well as genome size and site of replication. Viruses are commonly grouped into families on the basis of these properties in what is known as the Baltimore classification (Shors, 2011, pp. 56). The properties of commonly used oncolytic viruses are summarised in Table 1.1.

Virus (Type)	Group (Baltimore Classification)	Enveloped (E) or Naked (N)	Approximate Size (nm)	Genome Size (kb)	Site of Replication	Burst Time (hrs)
Reovirus (Reoviradae)	III (segmented double-stranded RNA)	N	$60-90$	$18.2-30.5$	Cytoplasm + Nucleus	18
Adenovirus (Adenoviridae)	I (linear double-stranded DNA)	N	$70-90$	$35-36$	Nucleus	24
HSV-1 (Herpesviridae)	I (linear double-stranded DNA)	E	$150-200$	$120-240$	Nucleus	12
Newcastle Disease (Paramyxoviridae)	V (negative single-stranded RNA)	E	$150-300$	15	Cytoplasm	18
Vaccinia (Poxviridae)	I* (linear double-stranded DNA)	Complex coats	200×300	$130-375$	Cytoplasm	8

Table 1.1: Properties and characteristics of common oncolytic viruses (Aghi and Martuza, 2005; Parato et al., 2005; Chaston and Lidbury, 2001).

1.1.2 Tumours and interstitial space

Solid tumours, also known as neoplasms, account for over 85% of human cancers (Jang et al., 2003). They are organ-like structures that are heterogeneous and structurally complex, comprising of cancer cells and stromal cells (fibroblasts and inflammatory cells) that are embedded in a network of proteins (Trédan et al., 2007).

Tumours that originate spontaneously often grow slowly, or exist for long periods of time in a near-steady-state size, even when tumour cells express activated oncogenes or enhanced growth factor signalling mechanisms (Matzavinos, 2004). During this period,

which can last from several months to many years, tumour cells persist in a host under growth restraint, and are described as being in a dormant or latent state (Wheelock et al., 1981). In contrast, malignant tumours, colloquially known as cancers, are tumours that invade surrounding tissues, traversing at least one basement membrane zone, growing in the mesenchyme at the primary site and have the ability to grow in a distant mesenchyme to form secondary cancers or metastases (Matzavinos, 2004).

As in normal tissues, the interstitial space of tumours is composed predominantly of a collagen and elastic fibre network, giving structural integrity to the tissue. This cross-linked structure, known as the extracellular matrix (ECM), is filled with the interstitial fluid and macromolecules which form a hydrophilic gel, and acts as a compression buffer against the stress placed on the ECM (Netti et al., 2000). The fibre-forming macromolecular components of the ECM include collagen, fibrin, fibronectin, connective tissue cells such as fibroblasts and inflammatory cells. Fibrillar collagen I is the major fibrous protein of the tumour ECM, and is produced by host stromal cells in most tumours. Fibrils, which range from $50 - 200$ nm in diameter and lengths of up to several micrometers, assemble to form compartments, and it is the fusion of these narrow compartments can lead to the formation of fibres (Birk and Trelstad, 1986). Other macromolecular components of the ECM are comprised of polysaccharides such as glycosaminoglycans and proteoglycans, which allows cells to bind to collagen via cell surface integrins, as well as provide structural integrity to the matrix and resistance to compressive forces.

Collagen I content and structure have previously been correlated with limited diffusion (Netti et al., 2000; Pluen et al., 2001; Ramanujan et al., 2002; Brown et al., 2003; Davies et al., 2002), and Levick (1987) observed that fibrillar components such as collagen may significantly influence transport in tissue, because of hydrodynamic drag and the tortuous nature of the flow path, as well as by affecting the distribution and effective concentration of glycosaminoglycans. The ECM can vary greatly among tumours, both in amount and in composition (Trédan et al., 2007), and in several tumours studied to date, collagen content of tumours is higher than that of the host normal tissue, limiting the proliferation of therapeutic agents throughout tumours (Liotta, 1986).

Due to the accumulation of fluid in the tumour interstitium, there are almost no pressure gradients between the vasculature and surrounding tissue, and convection is negligible in solid tumours (except at the tumour periphery), due to the uniform interstitial fluid pressure (Boucher et al., 1990). Interstitial transport of molecular therapeutics is therefore governed mainly by diffusion. However, large therapeutics, such as oncolytic viruses, are orders of magnitude larger than conventional chemotherapeutics (< 1 nm compared with $50 - 300$ nm, Mok et al., 2009), and encounter severe transport limitations in the tumour interstitium due to the structure of the ECM (Wu et al., 2001; Parato et al., 2005; Liu et al., 2007; Sauthoff et al., 2003). This is shown in Figure 1.2, where negligible mass

transport of large, heavy macromolecules is seen in extravascular space for both normal and neoplastic tissue.

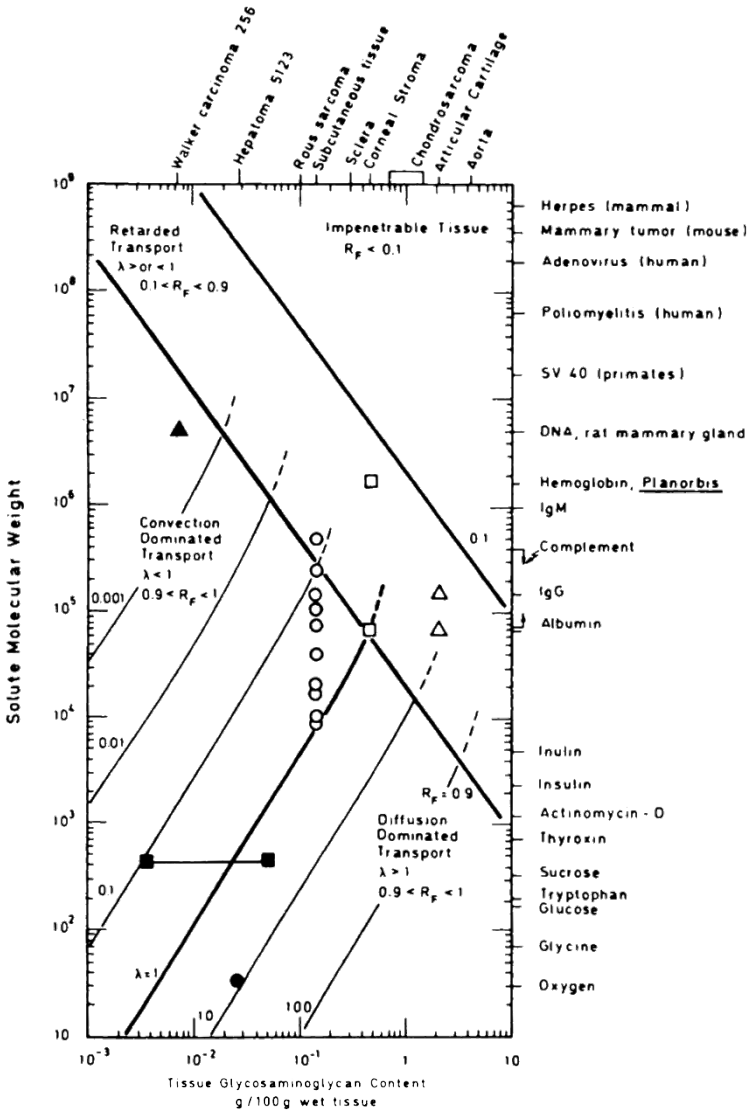

Figure 1.2: Diffusive and convective mass transport in extravascular space of normal and neoplastic tissue at $37 - 38°$. The retardation factor R_F, is the solute convective flow velocity/solvent convective flow velocity for flow through a polysaccharide network, and λ is the ratio of diffusive to convective flux (reproduced from Swabb et al., 1974).

Solid tumours are dense tissues with relatively little interstitial space, with the average distance between tumour cells shown to be approximately 20 nm, which is smaller than the narrowest dimension of even the smallest of oncolytic viruses (Nagano et al., 2008). The diffusion of solutes is considerably slower through connective tissue than water (Burstein et al., 1993), and measurements of diffusivity in a variety of tissues has established a negative monotonic relationship with total collagen content (Swabb et al., 1974; Netti et al., 2000), and concluding that tumour collagen composition and organization significantly affect the penetration of macromolecules. The role of tumour fibrillar collagen as the primary causes of diffusive hindrance in tumours was confirmed by Ramanujan et al. (2002),

whose *in vitro* study of diffusion coefficients in collagen gels matched tumour diffusion coefficients once tortuosity of the tumour interstitial space was taken into account.

Hindered diffusion in tissue (Syková and Nicholson, 2008) has been shown to be dependent on both the molecular weight and radius of therapeutic agents (Swabb et al., 1974; Jain, 1990; Netti et al., 2000). Netti et al. (2000) have also observed that diffusivity of macromolecules in tumours follows power law expression with macromolecule radius, with a power dependence ranging from -1.5 to -3. It is generally well accepted that macromolecules, such as oncolytic viruses, do not reach uniform concentration in a large tumour for a long time because of large diffusion distances and large size of molecules (Jain, 1990; Smith et al., 2011). From Figure 1.2, cancer viruses fall in the retarded transport or impenetrable tissue regions, depending on tissue glycosaminoglycan content and virus size. These particles would, therefore, be essentially immobile in the interstitial space of neoplastic tissue under normal circumstances (Swabb et al., 1974). Instead, the proliferation of the virus is dependent on cell interaction mechanisms, such as via motility of infected cells, as the density of tissue will render viral diffusion negligible (Mok, 2007; Guo et al., 2008).

1.1.3 Cell motility and trafficking

Another important function of the ECM is to modulate the adhesion of cells to the underlying substratum, which is required in order to exert the tractional forces required for cell motility (Lester and McCarthy, 1992). The interstitial stroma of most tissues does not normally contain pre-existing passageways for cells, and the basement membrane is an insoluble, continuous, flexible structure which is impermeable to large proteins (Liotta, 1986). This acts as an exoskeleton, and the fibre network morphology modulates cell shape, which has a direct impact on how much resistance a moving cell encounters (Lester and McCarthy, 1992).

Tumour cells can migrate either collectively, retaining their intracellular junctions, or individually. Individual cell migration strategies are broadly classified as either mesenchymal or amoeboid. The mesenchymal type of cell migration resembles fibroblast-like motility, which is initiated by the formation of actin-rich filopodia and lamellipodia at the leading edge, and results in an elongated spindle-like shape. If the cross-section of the migrating, elongated cell matches or is slightly below the mesh size, then the cell encounters no resistance, or steric hindrance (Brábek et al., 2010).

Amoeboid migration is similar to the motility of amoeba, which is characterised by cycles of expansion and contraction of the cell body and bleb-like protrusions mediated by cortically localized actin-myosin interactions. This type of motility is seen in large mesh sizes, and tumour cells that exhibit an amoeboid mode of migration usually show a rounded shape in 3D substrates. If the mesh size is too large, the migration speed decreases due

to a loss of cell-fibre attachment sites that are needed to either push or pull the cell body forward (Harley et al., 2008).

Due to the dense environment of solid tumours, this cell motility can be utilised as a carrier mechanism for propagation of viruses. The use of cells as carriers for virus particles is known as virus trafficking, and has also been used in the blood-stream for targeting multiple metastatic tumours. This approach has previously been used to deliver herpes simplex, adenovirus, vaccinia and measles throughout solid tumours, and has the additional benefit of bypassing the pre-existing antiviral immunity (Guo et al., 2008). After infection with viral agent, the infected host cell morphology is usually drastically affected, along with changes in the actin and microtubule cytoskeleton (Ploubidou and Way, 2001). These are referred to as cytopathic effects, and their extent varies with different virus and cell types. This hijacking of the host cell motor mechanism can result in deficiencies of fine control of actin cytoskeleton regulation, which can impair or enhance cell migration (Vicente-Manzanares et al., 2005). For example, adenovirus disrupts the actin cytoskeleton shortly after infection. Vaccinia virus induces the polymerization of action into tail-like structures directly behind the virion, which can propel virions inter-cellularly. Herpes simplex virus induces projections at the cell surface early in infection. The role of these projections has not been fully understood, as they disappear from the cell before extracellular virions are first detected (Cudmore et al., 1997).

While the exact extent of hijacking of the host cell's motor mechanism varies for different viral agents, Fisher and Seymour (2009) have stated that this usually results in reduced cell motility, possibly due to the energy demand of viral replication. The "trojan horse" approach to virus trafficking has been demonstrated successfully in vitro, with yields of $100-200$ pfu (Plaque Forming Units, a measure of non-defective, viable virions per sample unit volume) of virus particles released per cell burst in the process of cell migration.

In spite of these obstacles, the potential lack of cross resistance (the reduced effectiveness of therapy due to other treatments) with standard therapies and low initial doses means that virotherapy holds great promise as a means of treating tumours. In order to better understand the shortcomings of the human trial of oncolytic agents, as well optimise the characteristics and delivery of these agents as treatment, it is useful to develop mathematical models describing the interaction of cancer cells and the viral agents used to treat them. To date, there have been several approaches undertaken to aid in the understanding of specific aspects of treatment.

1.2 Modelling approaches

There has been considerable work in the development of mathematical models of tumour growth, delivery of therapeutics as well as the dynamics of virus-host cells. A good starting point for these are reviews by Byrne et al. (2006), Eftimie et al. (2011) and Zeyaullah et al.

(2012), as well as the more general work of Wodarz (2007) for illustrating approaches for modelling virus-tumour-immune system interactions.

In this section, we present an overview of existing approaches to modelling virus-tumour interactions in solid tumours. Broadly speaking, these can be split into two approaches: spatially-independent, population-interaction models describing the homogeneous mixtures of virus particles and tumour cells, and spatially-dependent models describing the heterogeneous spread of virus particles through solid tumours. Traditionally, these have taken the form of deterministic differential equations, appealing to the law of mass action. More recently, a probabilistic approach has also been applied to spatially-dependent models in the form of lattice-based mesoscopic models for cell interaction.

Each of these approaches has its benefits and limitations, and we provide a brief summary of the key assumptions, results and limitations.

1.2.1 Population interaction models

Despite best efforts in engineering viruses to specifically target cancer cells, the question of administering safe doses remains an important issue in oncolytic virotherapy. In addition to this, the presence of the immune response and failure of sufficient viral spread can result in the overall failure of therapy, dictating a minimal required dose.

To address this issue of optimising dosage, as well as determining the sensitivity of treatment outcomes to certain key parameters, several models focusing on species interaction have been developed. Rather than attempting to describe the spatio-temporal dynamics of tumour growth and treatment, these models consider the simpler case of spatially homogeneous mixture of species, and formulate systems of ordinary differential equations describing the rate of change of populations in time.

The first such model was proposed by Wodarz (2001, 2003), and was later generalised by Dingli et al. (2006). These models considered a system consisting of three species: uninfected cancer cells, a free virus population, and cancer cells infected by virus particles. The untreated tumour, represented by the population of uninfected cancer cells was assumed to undergo logistic growth, as described by a Bertalanffy-Richards model with some prescribed tumour carrying capacity. Uninfected cells were assumed to combine with virus particles, which proliferated rapidly within the cell to form infected cells. Infected cells were removed from the system due to natural or virus-inflicted death, the latter resulting in the addition of multiple virus particles to the free virus population.

The behaviour of the ordinary differential equations governing these population interactions was analysed from a dynamical systems point of view by considering the stability of equilibria in the system. Three equilibria corresponding to the complete success, partial success and complete failure of therapy were identified, and although analytic criteria for these outcomes were not tractable, numeric solutions illustrating these cases based on

experimentally fitted sets of parameters were obtained. Although the parameters required for complete success of therapy were beyond the physical properties of the viruses used experimentally, an interesting conclusion reached was that virus species that killed infected cells at a slower rate were often better suited to treatments, as they allowed for greater virus proliferation. Further extensions to this set of models considered the effects of pairing oncolytic virotherapy with more traditional chemotherapy treatments through the addition of radioactive species, both within the tumour and outside it, as well as cancer cells affected by the radiation, which did not proliferate, but still occupied space in the system, affecting the population dynamics (Dingli et al., 2006).

Motivated by experimental evidence, Bajzer et al. (2008) suggested that the fusing of uninfected and infected cancer cells to form syncytia rather than the free virus population was the physical mechanism driving intratumour spread. As these fused cell aggregates no longer contributed to the growth of the tumour, the addition of this effect amounted to an additional term describing the loss of uninfected cells, and the incorporation of the fused cells to the infected cell population. This population was now considered to consist of both solitary infected cells, as well as syncytia, which are single cells containing multiple nuclei formed through cell fusion. This generalisation of the population model was once again analysed from a dynamical systems perspective, resulting in revised conditions for stability, and hence the success or failure of therapy. The authors presented numerical simulations illustrating Hopf bifurcations, leading to oscillations of uninfected cell populations which was concluded to correspond to the physical case of periodic tumour remission (reduction of tumour mass). However, it was noted that in the time between pulsations the tumour may reach a very small size, and erroneously considered as being eradicated when, in fact, another large tumour spike is imminent.

By estimating physical parameter values through fitting untreated tumour growth curves to experimental data from tumour growth in immunodeficient mice, these models were able to suggest the minimal dose of viral agent required to have a maximum effect based on the experimentally determined carrying capacity of the tumour. Although these models were in reasonable agreement with the experimental trials presented, certain parameter values could not be determined experimentally, and were assumed. This, coupled with the lack of an adequate immune response in the model suggests that further development is required before using these models to determine individual patient dosage in clinical situations.

Recently published work by Wang et al. (2013) developed a population model incorporating a more realistic description of the lytic cycle. Extending the approach by Wodarz (2001) as well as that of Wang et al. (2011), they incorporated a constant time delay term for the burst of infected cells. This delay, corresponding to the burst time from initial infection to virion release, as well as the burst size, were considered as the key parameters in the resultant system of non-linear delay differential equations.

Analytic results revealed two threshold values of burst size, with a functional relationship between the bifurcation value of the delay parameter for values of burst size above the second threshold. When the period of the lytic cycle was longer than the bifurcation value, the system exhibited Hopf bifurcations, and had orbitally stable periodic solutions. It was shown that the critical value of the period of the viral lytic cycle was determined by the viral burst size, which resulted in the coexistence of virus and tumour cells in the system.

1.2.2 Spatially-dependent models

In order to describe the spread of virus particles throughout a tumour, it becomes necessary to consider the spatial variations of uninfected cancer cell and virus particle concentrations.

Wu et al. (2001) proposed a system of partial differential equations (PDEs) describing the spatio-temporal dynamics of a three-dimensional, radially-symmetric tumour infected with a replication-competent virus with the aim of determining the optimal injection site of the initial dose of virus particles. The model considered four physical variables: uninfected tumour cells, free virus particles, tumour cells infected by virus and necrotic cells left over as debris after tumour cell death. The tumour volume was treated as an incompressible fluid occupied by constant density of cells, and the incorporation of tumour growth throughout treatment resulted in the formulation of a moving boundary or Stefan condition at the edge of the tumour. A constant pressure gradient was assumed throughout the volume, with the exception of the periphery, implying no convection of virus particles was possible within the bulk of the tumour. Crucially, cells at the tumour edge were assumed to move due to the convection at a velocity proportional to the proliferation of uninfected cells and removal of necrotic cells.

The resulting system of PDEs governing the time evolution of the particle species considered the proliferation, infection and convection of uninfected cells, the birth, death and convective transport of infected cells, the creation, removal and convection of necrotic cells, as well as the clearance and creation of new virus particles.

The model was then used to compare the overall efficacy of several initial injection locations. The cases of uniform injection of virus throughout the tumour mass, injection of virus into the tumour core, as well injection at the edge of the tumour mass were considered. After incorporating the effects of nutrient-limited necrosis, it was concluded that injecting virus particles in the rim was more effective than a core injection in sustained reduction of the tumour, and it was hypothesised that this was due to the natural necrosis of the tumour core due to a lack of nutrients.

Although this model was a promising starting point for describing spatially-dependent virus-tumour interactions, it failed to incorporate several key mechanisms of realistic systems required when making comparisons between this model and clinical data. Most not-

ably, an additional mechanism for removing uninfected cells provided by the stimulation of the immune system to the presence of cells infected by virus particles was not taken into account, which was addressed in a later extension by Wein et al. (2003). This modification introduced additional death terms to the equation governing the rate of change of infected cell, and modified the speed of tumour growth accordingly to account for this.

Similar analysis relating to optimal location of initial viral injection was undertaken, with the conclusion that a broad spatial distribution was far more important than the initial viral dose in the success or failure of therapy. After estimating key parameters from experimental data, it was shown that this model was consistent with preclinical and clinical trials to date. However, due to the nature of these parameter estimates, the authors cautiously noted that this was not necessarily validation of the model, but rather useful comparison of key mechanisms.

Further analysis by Friedman and Tao (2003) showed that the Wein-Wu-Kirn model was ill-posed, because without a viral diffusion term, the system does not have a mathematical solution in general. On the basis of this analysis, Tao and Guo (2005) extended the model to incorporate a diffusion term for free virus density, and established the global existence of a unique solution to the model. While this approach was mathematically valid, the physical basis for incorporating a viral diffusion term was not well justified, and was treated in the same manner as traditional chemotherapeutic agents. As a result, the diffusion coefficient chosen was several orders of magnitude larger than what is observed in dense tissue (Section 1.1.2).

A spatially-dependent model describing the growth of a solid tumour in the presence of an immune response was proposed by Matzavinos (2004). Focusing their attention on tumour-infiltrating cytotoxic lymphocytes (TICLs), they considered a system of tumour cells, TICLs, infected cells, TICL-tumour complexes, inactivated TICLs and chemokines using the law of mass action. While this model was not explicitly derived with oncolytic virotherapy in mind, the physical assumptions on the properties of the tumour cell-fighting TICLs draw similar parallels with oncolytic virotherapy, and this model is therefore of considerable interest. Numerical solutions of this system showed a supercritical Hopf bifurcations and is able to depict a wide range of spatio-temporal behaviours, including, under specific conditions, spatio-temporal chaos. For a simplified system of radially symmetric solid tumour growth, numerical solutions showed a train of solitary-like waves invading the tissue and subsequently creating a spatially heterogeneous distribution of tumour cell density throughout. Chaplain (2008) extended this further, and showed the existence of travelling waves in the system.

1.2.3 Stochastic and agent-based models

Another spatially-dependent modelling approach that has recently been utilised is stochastic and agent-based modelling of cell interactions. In contrast to the deterministic modelling approaches from Section 1.2.2, virus-cell interactions occur with fixed probability, and numerical simulations are typically implement using a rule-based approach. This method has better physical justification than the empirical law of mass action typically used in continuum models, and is also valid at low concentrations of species where continuum models may not be valid. However, it is usually computationally intensive, and due to the inherent probabilistic nature of the system, simulations must be repeated many times in order to establish a representative sample of behaviour.

This probabilistic approach was first applied to the study of oncolytic virotherapy by Paiva et al. (2009). Discretising a two-dimensional domain into a lattice of square compartments, the spatial interactions between normal cells, uninfected and infected tumour cells, necrotic cells, and free viruses were considered in a discretised reaction-diffusion framework. At each point in time, each cancer cell, randomly selected with equal probability, could carry out one of three actions: replication, death, or becoming infected if yet uninfected. Contact inhibition was incorporated by imposing a maximum compartment occupancy for normal and necrotic (but not tumour) cells, and spread of virus through cell lysis was simulated by assigning random fractions of burst virions to the infected cell's current compartment, and distributing the remainder equally to neighbouring cells. Finally, an immune response was implemented by means of a clearance rate. Numerical simulations showed regions of parameters space corresponding to tumour eradication, monotonic growth and oscillatory growth for a range of viral diffusion coefficients and cell lysis times, and concluded that there is an optimal range for viral cytotoxicity for the elimination of tumour cells.

Reis et al. (2010) developed a simpler rule-based mesoscopic model, consisting of three cell types: cancer cells and virus-infected cancer cells, and remaining lattice points not occupied by either of the former are assumed to be occupied by normal tissue cells. In contrast to the model by Paiva et al. (2009), free virus particles were not explicitly considered due to the limited diffusion of macromolecules in solid tumours. Instead, virus infection of cancer cells was modelled through cell-to-cell fusion. This spread of infection occurred with fixed probability, and infected cells could also die with a probability greater than that of cancer cells. Cell motility was represented by the reproduction of tumour cells, chosen at random, which resulted in a replica of itself filling neighbouring empty sites, or pushing existing cells away, hence generating pressure within the tumour. Numerical simulations were performed in a 3D domain, for initial viral seeding in the centre of the tumour and on the surface. The death probability of infected cells was considered as a key experimentally-controlled parameter, and the authors concluded that in the absence of an immune response, slower cancer cell killing may give superior results by enabling higher

virus amplification. The site of initial infection was found to play an important role on the outcome of therapy, and for cancers that have a significant supportive stroma, infection of the core of the tumour may be more likely to lead to cancer control or eradication. No significant differences between initial core and surface injections were seen for compact tumours with minimal stroma.

More recently, Wodarz et al. (2012); Wodarz (2013) developed a spatially dependant, probabilistic formulation of their population interaction model outlines in Section 1.2.1. They considered a two-dimensional, compartment-based model of oncolytic virotherapy consisting of uninfected and infected cells. Each compartment had a maximum occupancy, and could either contain an uninfected cell, an infected cell or be empty. Uninfected cell motility was modelled with inter-compartment jumps to vacant neighbours, and infected cells could infect adjacent uninfected cells with fixed probability. Both uninfected and infected cells could also die with different fixed probability. Numerical simulations showed qualitative agreement with experimental data, and for an initial central injection of virus particles, four distinct spatial patterns were observed. These were identified as a hollow ring (radial wave front) expansion, a mixed expansion of virus and uninfected cells in coexistence, concentric circle expansion, and expansion with sparse mixing of a small number of virus particles.

While each of these models was a step in the right direction for an *in silico* description of spatially explicitly solid tumour dynamics, each failed to adequately incorporate key physical processes, such as delayed bursts and static free virus populations affected by immune clearance.

1.3 Dissertation plan

In this work, we will apply concepts from both well mixed population interaction and spatially dependent modelling techniques in describing several key areas of oncolytic virotherapy.

We look at the spread of free virus particles throughout a dense environment of solid tumour cells in the early avascular stages, as transported by motile infected cells in the absence of diffusion or convection of virus particles. This approach has parallels with population models of Wodarz (2001, 2003); Bajzer et al. (2008), but critically, is spatially dependent, and incorporates the effects of the viral lytic cycle by incorporating a delay term.

In the continuum formulation presented in Chapter 2, we derive an age-structured system of PDEs from the law of mass action describing the spatio-temporal evolution of the system, before looking at the conditions necessary for the indefinite, sustained spread of virus particles. Crucially, we assume cell motility in the form of a diffusion-like random walk by both uninfected and infected tumour cells rather than the convection of uninfected

cells assumed in previous spatially-varying models. The time delay between the infection of cells and the death (and subsequent release of virions) is considered the key mechanism for driving virus spread, underlining the key difference between our formulation and existing models. We demonstrate the presence of travelling wave solutions, and present an analytic form for the travelling wave speed as a function of the key parameters, and compare this to numerical solutions of the system of PDEs.

In an attempt to address the issue of infinitesimal (and physically impossible) threshold concentrations of tumour cells mentioned in Section 1.2.1, we develop an alternative, rule-based stochastic formulation describing this evolution of this system in Chapter 3, and use these Monte Carlo simulations to validate the behaviour seen in the continuum case.

In Chapter 4, we look at the sensitivity of the discrete formulation of the virus-tumour model for typical parameter ranges. After developing metrics to analyse the multiple realisations of the stochastic algorithm, we present the qualitative effects of experimentally-controlled parameters on the wave speed of infection propagation, overall success as well as the consistency of therapy for typical *in vivo* and *in vitro* scenarios.

We discuss extensions to the physical model by extending the physical domain to incorporate periodic obstacles that impeded the motility of cells, such as macrophages, fibroblasts and cellular debris. In Chapter 5, we review the general theory of multi-scale homogenization, and compare theoretical results to numerical simulations of cell motility in the presence of obstacles in two dimensions. We present a proof-of-concept numerical solution scheme for the PDE model in 2D, and discuss the applicability of homogenization theory in the limit of large obstacles size. Further considering this limiting case in Chapter 6, we develop a novel analytic method of determining the effective diffusion and drift properties of discrete random walks on lattices. After determining the conditions under which drift or diffusion dominate on the macroscopic scale, we present closed-form results applicable to physically-motivated cases in biology as well as solid-state physics, and compare these to numerical simulations.

Finally, we discuss the plausibility of these models and the difficulties encountered thus far, as well as suggest future modifications and extensions.

Chapter 2

Continuum model of virus spreading

In this chapter we develop a simple mathematical model describing the spatial and temporal interactions between a delayed-release oncolytic agent and cancer cells. The aim is to optimise the spread of the oncolytic agent throughout the spatial domain, so we look at the case where a heterogeneous initial distribution of virus particles results in a sustained reaction on an unbounded domain. Motivated by apparent travelling wave behaviour obtained from numerical solutions of this general model, we look at a time-invariant travelling wave formulation of the governing equations to find the parameter range under which such waves are possible. We derive an analytic expression for the constant wave speed as a function of the incubation period and diffusion ratio, and compare this with numerical results from the full time-dependent problem.

Finally, we discuss the validity of the continuum modelling approach and physical interpretations of virus extinction, suggesting that a discrete modelling approach may be more suitable in this limiting case.

2.1 Introduction

The extracellular matrix (ECM) is a network of proteins secreted by cells in the body that acts as scaffolding for tissue. In addition to structural support, it acts as a reservoir for signalling factors, as well as a source of information for cells. The anchoring of healthy cells to the ECM, as well as inter-cellular adhesion, is controlled by cell adhesion molecules (CAM), which are expressed on the surface of cells. Tumour cell migration occurs via either mesenchymal or amoeba-type migration, which makes use of protrusion and retraction of actin filaments to exert a tractional force on the ECM.

As discussed in Section 1.1.2, the interstitial fluid in the inner regions of avascular solid tumours is at constant pressure. This lack of pressure gradients implies that convection of large macromolecules such as oncolytic viruses ($50-300$ nm) is negligible in solid tumours. As virus particles lack a biological motor, the only viable mechanism of motility in solid

tumours other than convection is diffusion. The diffusivity can be estimated using kinetic theory arguments from the Einstein-Stokes relation

$$D = \frac{k_B T}{6\pi\eta r}, \tag{2.1}$$

where k_B is Boltzmann's constant, η is the viscosity of the medium, T is the temperature and r is the particle radius (Berg, 1993, pp. 49). It has previously been shown that tumours have large values for extracellular fluid viscosity (due to the presence large molecules such as collagen and proteins) (Jang et al., 2003), suggesting a small effective diffusion coefficient for large particles, such as oncolytic viruses.. This theoretical prediction has been confirmed by Swabb et al. (1974); Jain (1990); Netti et al. (2000); Mok et al. (2009), concluding that the dense tissue is impenetrable to the virus by either convection or diffusion. In contrast, cells contain biological motors, allowing them to undertake random walks along the ECM. Cells infected with virus particles are also capable of moving along the ECM, although at a considerably slower rate than uninfected cells due to the virus replication in the cytoplasm slowing down their motor functions (Fisher and Seymour, 2009). As such, in the context of modelling the spread of injected viral agents into a solid tumour, we should consider the virus particles as being stationary, and view the motility of infected cancer cells during the incubation period as a mechanism for transport of the oncolytic agent throughout the tumour. More specifically, we consider the case of a dormant solid tumour (Section 1.1.2), corresponding to a steady state of cell growth and expansion.

In contrast to the spatially-independent models for virus-cell interactions such as those proposed by Wodarz (2001); Dingli et al. (2006), we seek to develop a model that describes the spatial distribution of virus particles in time, with the aim of maximising the viral yield through the optimal choice of initial conditions and experimentally controlled parameters. In this chapter, we will consider a one-dimensional representation of a dense tumour of uniform density, with no diffusion of virus particles throughout the domain.

2.2 Age structured model

We consider a model consisting of three species: uninfected tumour cells, tumour cells which have been infected with virus particles, and virus particles. Our key assumption is that at some given age τ, infected cells die, releasing multiple virus particles in the process. Since infected cells remain mobile, the location where they burst and release virus particles is not the same as where they were infected. Thus we track the age, a, of infected cells as well as their positions in order to determine where they burst. We neglect the effect of virus particles linking with already infected cells, as it has previously been shown that this does not affect infected cell behaviour, and does not alter the burst time or burst size at the end of the lytic cycle. While this assumption may not be valid when the number of

virus particles in the system is small, its effects on virus population can be incorporated into a simple viral death rate. We suppose that virus particles have a "natural" death rate accounting for lack of nutrients, defects in the virus and a limited immune response. For simplicity, the role of oxygen gradients are neglected in the model, therefore limiting its applicability to the core, necrotic regions of solid tumours.

The infection, virus decay and infected cell burst interactions in terms of particles are described by the reactions

$$\begin{aligned} \text{Uninfected Cell}+\text{Virus Particle} &\rightarrow \text{Infected Cell}, && (2.2)\\ \text{Virus Particle} &\rightarrow (\text{Dead Virus}), && (2.3)\\ \text{Infected Cell} &\rightarrow \alpha\times\text{Virus Particles (when they reach age } \tau) && (2.4) \end{aligned}$$

and are also illustrated in Figure 2.1.

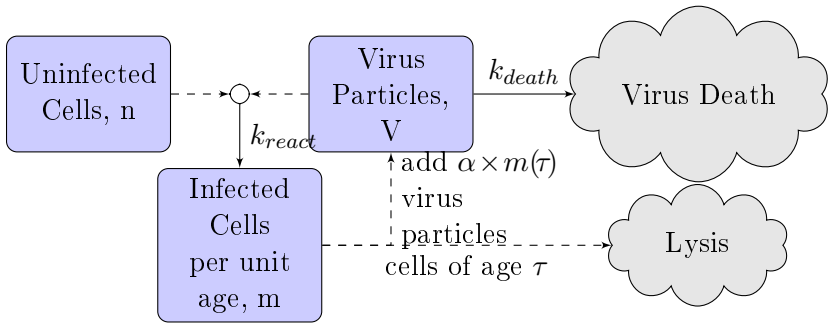

Figure 2.1: Interactions between uninfected cells, infected cells and virus particles.

We let n be the concentration of uninfected cells, V be the concentration of virus particles, and m be the concentration per unit age of infected cells. We assume that uninfected and infected cells undergo random walks with motility coefficients D_n and D_m, respectively. Then, appealing to the law of mass action, our model reads

$$\begin{aligned} \frac{\partial n(x,t)}{\partial t} &= D_n \frac{\partial^2 n(x,t)}{\partial x^2} - k_{react} V(x,t)\, n(x,t), && (2.5)\\ \frac{\partial m(x,t,a)}{\partial t} + \frac{\partial m(x,t,a)}{\partial a} &= D_m \frac{\partial^2 m(x,t,a)}{\partial x^2}, && (2.6)\\ \frac{\partial V(x,t)}{\partial t} &= -k_{react} V(x,t)\, n(x,t) - k_{death} V(x,t) \\ &\quad + \alpha m(x,t,\tau), && (2.7) \end{aligned}$$

where a is the age of each infected cell, k_{react} is the infection rate, k_{death} is the virus death rate, and age $a = \tau$ is the time when infected cells burst, releasing α virus particles into the system at their current position. Equations (2.5)–(2.7) form an age-structured model

(Murray, 2002), with the left-hand side of (2.6) taking into account the ageing of infected cells. Since infected cells do not contribute to the dynamics of the system after bursting, we do not track infected cell populations of age $a > \tau$, and in the numerical implementation presented in Section 2.4, burst cells are simply discarded. For simplicity, we ignore the uptake of virus particles by infected cells due to multiplicity of infection in Equations (2.6)–(2.7). While these effects may become important at low virus concentration, their inclusion would limit the tractability of the travelling wave analysis in Section 2.6. Finally, we consider these physical processes in one spatial dimension, x, although this description can be generalised to higher spatial dimensions, as illustrated in Chapter 5.

It remains to specify initial and boundary conditions for the model. Initially, we consider a one-dimensional system with a uniform density of uninfected cells, n_0, no infected cells, and a prescribed initial spatial distribution of virus particles, $V_0(x)$, clustered around $x = 0$. The infection process in (2.2) corresponds to an initial condition at age $a = 0$. Our initial conditions in time and age are thus

$$n(x,0) = n_0, \tag{2.8}$$

$$m(x,0,a) = 0, \tag{2.9}$$

$$V(x,0) = V_0(x), \tag{2.10}$$

$$m(x,t,0) = k_{react} V(x,t)\, n(x,t). \tag{2.11}$$

Far away from the place where virus particles are introduced, we suppose there is no flux of infected or uninfected cells and thus write

$$\frac{\partial n}{\partial x} = 0 \text{ as } x \to \pm\infty, \tag{2.12}$$

$$\frac{\partial m}{\partial x} = 0 \text{ as } x \to \pm\infty. \tag{2.13}$$

2.3 Non-dimensionalisation

We now non-dimensionalise the governing equations (2.5)–(2.7) by introducing the rescalings

$$\begin{aligned} x &= \sqrt{\frac{D_n}{k_{react}V_{max}}}\hat{x}, && (2.14)\\ t &= \frac{1}{k_{react}V_{max}}\hat{t}, && (2.15)\\ a &= \frac{1}{k_{react}V_{max}}\hat{a}, && (2.16)\\ n &= n_0\hat{n}, && (2.17)\\ m &= k_{react}V_{max}n_0\hat{m}, && (2.18)\\ V &= V_{max}\hat{V}, && (2.19) \end{aligned}$$

where $V_{max} = \max\{V(x,0)\}$.

Substituting into (2.5)–(2.7) and dropping the hat notation, the dimensionless governing equations become

$$\begin{aligned} \frac{\partial n(x,t)}{\partial t} &= \frac{\partial^2 n(x,t)}{\partial x^2} - V(x,t)\,n(x,t), && (2.20)\\ \frac{\partial m(x,t,a)}{\partial t} + \frac{\partial m(x,t,a)}{\partial a} &= D\frac{\partial^2 m(x,t,a)}{\partial x^2}, && (2.21)\\ \frac{\partial V(x,t)}{\partial t} &= -k_D V(x,t) - k_C V(x,t)\,n(x,t) \\ &\quad + k_B m(x,t,\tau_B), && (2.22) \end{aligned}$$

with dimensionless parameters

$$\begin{aligned} D &= \tfrac{D_m}{D_n}, && \text{ratio of diffusion coefficients}\\ k_D &= \tfrac{k_{death}}{k_{react}V_{max}}, && \text{ratio of death rate to maximum initial infection rate}\\ k_C &= \tfrac{n_0}{V_{max}}, && \text{ratio of initial uninfected cell to virus particle concentrations}\\ k_B &= \tfrac{\alpha n_0}{V_{max}}, && \text{initial virus "yield" ratio}\\ \tau_B &= k_{react}V_{max}\tau, && \text{burst time scaled with initial infection rate} \end{aligned} \quad (2.23)$$

The initial conditions become

$$\begin{aligned} n(x,0) &= 1, && (2.24)\\ m(x,0,a) &= 0, && (2.25)\\ V(x,0) &= V_0(x), && (2.26)\\ m(x,t,0) &= V(x,t)\,n(x,t), && (2.27) \end{aligned}$$

where $V_0(x) = V_{max}\hat{V}(x)$, and boundary conditions

$$\frac{\partial n}{\partial x} = 0 \text{ as } x \to \pm\infty, \tag{2.28}$$

$$\frac{\partial m}{\partial x} = 0 \text{ as } x \to \pm\infty. \tag{2.29}$$

The system of coupled, non-linear partial differential equations (2.20)–(2.22) subject to initial and boundary conditions (2.24)–(2.29) does not admit any trivial analytic solutions, and must be solved numerically. This is done by discretising the spatial, temporal and age domains, and approximating the derivative terms using finite-differences, shown in Section 2.4.

2.3.1 Size of non-dimensional parameters

The dimensionless length- and time-scales in (2.20)–(2.29) are chosen relative to the typical uninfected cell diffusion lengths and virus reaction times, respectively.

The motility coefficient of cells is difficult to measure *in situ* (Stylianopoulos et al., 2010). For a typical dense tumour environment, a lower bound on the uninfected cell diffusion coefficient is $D_n = 2.08 \times 10^{-5}$ mm^{2}hr^{-1} (Matzavinos, 2004). Estimates for infected cell motility are not readily available, but we assume that the virus replication process is energy intensive, resulting in a reduced infected motility relative to that of uninfected cells (Fisher and Seymour, 2009). In solid tumours, the effective virus reaction rate has previously been estimated to be $k_{react} = 10^{-8}$mm^{3}hr^{-1}vir^{-1} (Friedman et al., 2006). The reaction time-scale, $\hat{t}$, is related to the maximum amplitude of initial virus particle distribution, V_{max}. Total viral dosages in clinical trials range from $10^7 - 10^{12}$ plaque forming units ml^{-1} (Kirn et al., 2001), and while the peak initial concentration depends on the spatial distribution, it is reasonable to assume a typical value $V_{max} \approx 10^9$ vir mm^{-3}. A typical infected cell burst time is in the range $\tau \in [5, 25]$ hours (Section 1.1.1), with a typical infected burst size of 100 virus particles (Friedman et al., 2006) and clinical trial durations are often $4 - 8$ weeks (Kirn, 2001; Heise et al., 1999).

These typical parameter values imply that $\hat{x} \approx 10^3 x$ and $\hat{t} \approx 10^{-2} t$. For physical parameters relevant to *in vivo* and *in vitro* treatments (seen later in Section 3.3), these scales imply dimensionless parameters in the range $D \approx 10^{-2} - 10^{-1}$, $k_D \approx 10^{-4} - 10^{-1}$, $k_C \approx 10^{-4} - 10^{-1}$, $k_B \approx 10^{-2} - 10^{1}$ and $\tau_B \approx 10^2$.

Since the reaction time-scale is fast in comparison to the overall infected cell burst times, this implies the need for a very fine time step discretisation, Δt, in a numeric method for solving the PDE over the time-scales of therapy. Therefore, we seek to reduce the computational requirements of solving the system of equations (2.20)–(2.29) by reformulating the problem.

2.4 Numerical solution of PDE

The governing PDEs derived in Section 2.2 are functions of one spatial variable, x, and two time-like variables, t and a. Equation (2.20) is second-order parabolic PDE, which can be solved numerically with a Crank-Nicolson Finite Difference scheme (Smith, 1985), while the first-order PDE (2.22) can be solved with a simple Euler iteration. The governing equation for the time evolution of infected cells, (2.21), is a function of age, as well as space and time. While this equation can be solved numerically using finite-differences for each discretised age, this approach is computationally inefficient. We note that (2.21) is coupled to the system through the burst at (2.22) and the initial infection condition (2.27), and seek an analytic solution to the linear PDE (2.21) at age $a = \tau_B$ by using a Fourier Transform in the spatial variable.

2.4.1 Analytic expression for infected cell burst

In order to solve (2.21), we begin by taking the Fourier Transform, $\overline{m} \equiv \mathcal{F}\{m\}$, in spatial variable, x. Using the definition

$$\overline{m} = \int_{-\infty}^{\infty} m(x,t,a) \exp(-i\omega x)\, dx,$$

equation (2.21) reduces to the first-order differential equation

$$\frac{\partial \overline{m}}{\partial t} + \frac{\partial \overline{m}}{\partial a} + D\omega^2 \overline{m} = 0. \tag{2.30}$$

Solving this by the method of characteristics (Figure 2.2), we obtain the solution

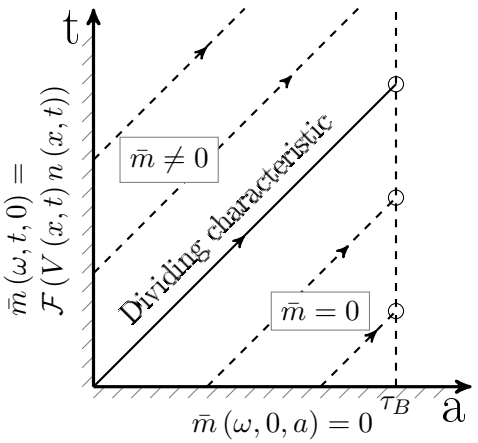

Figure 2.2: Characteristics of infected cell Fourier transform. Burst term is zero for $t < a$.

$$\overline{m}(\omega, t, a) = \overline{m}_0(\omega, t-a) \exp\left(-D\omega^2 a\right), \tag{2.31}$$

where the Fourier transformed initial condition from (2.25) is given by

$$\overline{m}_0(\omega, t-a) = \begin{cases} \int_{-\infty}^{\infty} V(x, t-a)\, n(x, t-a) \exp(-i\omega x)\, dx, & t > a \\ 0 & t < a \end{cases} \tag{2.32}$$

The system (2.20)–(2.22) that we want to solve can now be written as

$$\frac{\partial n(x,t)}{\partial t} = \frac{\partial^2 n(x,t)}{\partial x^2} - V(x,t)\, n(x,t), \tag{2.33}$$

$$\frac{\partial V(x,t)}{\partial t} = -k_D V(x,t) - k_C V(x,t)\, n(x,t) + k_B \mathcal{F}^{-1}\left\{\bar{m}_0(\omega, t-\tau_B) \exp\left(-D\omega^2 \tau_B\right)\right\}, \tag{2.34}$$

where $\mathcal{F}^{-1}$ denotes the inverse Fourier transform operator at burst age $a = \tau_B$, defined as

$$\mathcal{F}^{-1}\{\bar{m}(\omega, t, a = \tau_B)\} = \frac{1}{2\pi} \int_{-\infty}^{\infty} \overline{m}(\omega, t, \tau_B) \exp(i\omega x)\, d\omega. \tag{2.35}$$

This system (2.34)–(2.33), subject to appropriate boundary conditions, can now be solved numerically using a mixture of Finite Difference and Fast Fourier Transform methods. It is important to note that the presence of the $(t - \tau_B)$ term in the integral in (2.34) means that the system has memory of previous states.

2.4.2 Finite-difference/fast Fourier transform implementation

Equation (2.33) is a parabolic equation, and can be approximated with a central difference operator for the second-order spatial derivative, and a forward difference operator for the first-order time derivative. This Crank-Nicolson discretisation reduces the truncation error to $O\left(\Delta x^2\right)$ (Smith, 1985, pp. 19). For a general test function $f(x, t, a)$, this second-order spatial derivative discretisation is given by

$$\frac{\partial^2 f}{\partial x^2} \approx \frac{f_{j+1,k}^{i+1} - 2f_{j,k}^{i+1} + f_{j-1,k}^{i+1}}{2\Delta x^2} + \frac{f_{j+1,k}^{i} - 2f_{j,k}^{i} + f_{j-1,k}^{i}}{2\Delta x^2}, \tag{2.36}$$

and the first-order time derivative is given by

$$\frac{\partial f}{\partial t} \approx \frac{f_{j,k}^{i+1} - f_{j,k}^{i}}{\Delta t} \tag{2.37}$$

where i, j and k are indexes for discretised time, space and age (for the case of infected cell concentration) respectively, Δx is the distance between adjacent spatial points, and Δt is the difference between adjacent discrete time steps.

Applying the standard central difference, forward time Crank-Nicolson operator to (2.33), and evaluating the non-linear reaction term on the right-hand side at the old time step i, the discretised formulation of the equation is

$$\frac{n_j^{i+1} - n_j^i}{\Delta t} = \frac{n_{j+1}^{i+1} - 2n_j^{i+1} + n_{j-1}^{i+1}}{2\Delta x^2} + \frac{n_{j+1}^i - 2n_j^i + n_{j-1}^i}{2\Delta x^2} - V_j^i n_j^i, \tag{2.38}$$

with no-flux boundary condition (2.28) is implemented by introducing ghost points such that

$$\frac{n_1^{i+1} - n_2^{i+1}}{\Delta x} = 0, \tag{2.39}$$

$$\frac{n_{M-1}^{i+1} - n_M^{i+1}}{\Delta x} = 0, \tag{2.40}$$

on the left- and right-hand boundaries at $j = 1$ and $j = M$, respectively.

Equation (2.34) does not contain any spatial derivatives, so a simple forward time difference approximation can be used for the time derivative term, and the remaining terms can be evaluated explicitly at the old time step i as

$$\frac{V_j^{i+1} - V_j^i}{\Delta t} = -k_D V_j^i - k_C V_j^i n_j^i + k_B \mathcal{F}^{-1}\left\{ \bar{m}_0^{\,i-\frac{\tau_B}{\Delta t}}(\omega) \exp\left(-D\omega^2 \tau_B\right) \right\}. \tag{2.41}$$

As previously noted, the integral term, $\bar{m}_0$, has memory of previous states on interval $(t - \tau_B, t]$, and is evaluated at discrete time $i - \frac{\tau_B}{\Delta t}$. This term can be evaluated numerically by multiplying the Fast Fourier Transforms (FFT) of $n^{i-\tau_B/\Delta t} V^{i-\tau_B/\Delta t}$ by the heat kernel $\exp\left(-D\omega^2\tau_B\right)$, and taking the inverse Fast Fourier Transform (IFFT).

As discussed in Section 2.3.1, the dimensionless time interval for simulation is large, due to the fast reaction time-scale. However, the memory effects of (2.34) require solutions on a fine temporal scale. For practical reasons, we implement our numerical scheme to solve the system on two time-scales: a refined discretisation for time interval $(t - \tau_B, t]$, and a coarser time-scale for storing the final solution in memory. Our general implementation for the Finite Difference-Fast Fourier Transform method is outlined in Algorithm 1, and implemented in MATLAB.

Algorithm 1 MATLAB pseudo-code for Finite Difference-Fast Fourier Transform method.

1. Define parameters, Length and Time, resolution $\Delta x = {}^{2L}/_{M-1}$, $\Delta t = {}^{t_{max}}/_{N-1}$, time output resolution (coarse)

$$\begin{aligned} \mathbf{x} &\equiv \left[-L \quad (-L+\Delta x) \quad \ldots \quad (L+\Delta x) \quad L\right], \\ \mathbf{t} &\equiv \left[0 \quad \Delta t \quad \ldots \quad (N-2)\,\Delta t \quad t_{max}\right]. \end{aligned}$$

2. Create Finite-Difference Operator Matrices (implicit/explicit scheme) of size $({}^{2L}/_{\Delta x}) \times ({}^{2L}/_{\Delta x}) = M \times M$

$$\mathcal{A}_{M\times M} = \frac{1}{2\Delta x^2}\begin{bmatrix} -2 & 2 & 0 & & 0 \\ -1 & \frac{2\Delta x^2}{\Delta t}+2 & -1 & & \\ & \ddots & \ddots & \ddots & \\ & & -1 & \frac{2\Delta x^2}{\Delta t}+2 & -1 \\ 0 & & 0 & 2 & -2 \end{bmatrix},$$

$$\mathcal{B}_{M\times M} = \frac{1}{2\Delta x^2}\begin{bmatrix} 0 & 0 & 0 & & 0 \\ 1 & \frac{2\Delta x^2}{\Delta t}-2 & 1 & & \\ & \ddots & \ddots & \ddots & \\ & & 1 & \frac{2\Delta x^2}{\Delta t}-2 & 1 \\ 0 & & 0 & 0 & 0 \end{bmatrix}.$$

3. Create vectors n, m, V and set initial/boundary conditions

4. Create $M\frac{\tau}{\Delta t} \times M\frac{\tau}{\Delta t}$ Block Fourier Kernel matrix

$$\mathcal{M} = \frac{2L}{2\pi M}\text{fft}\left(\sqrt{\frac{\pi}{D\tau}}\exp\left(-\frac{\mathbf{x}^2}{4D\tau}\right)\right)\mathbf{1}_{M\times\tau/\Delta t}$$

5. Start time loop at $i_{current} = 2$

   (a) Let $i_{circular} = \begin{cases} \text{mod}\ (i_{current}-1,\tau)+1 & \text{for } t\,(i) \geq \tau \\ i_{current} & \text{for } t\,(i) < \tau \end{cases}$

      i. If $i_{circular} = 1$ and $t\,(i_{current}) \geq \tau$ then calculate burst cells

$$\mathbf{m}_\tau = \text{ifft}\left(\text{fft}\left(\mathbf{V}\mathbf{I}_{M\times M}\mathbf{n}\right)\mathcal{M}\right)$$

   (b) Solve $\mathbf{n}$ at next time step using Crank-Nicolson Finite-Difference matrices $\mathcal{A}$ and $\mathcal{B}$, and $\mathbf{V}$ using explicit Euler scheme

$$\begin{aligned} \mathbf{n}^{(i_{current})} &= \mathcal{A}^{-1}_{M\times M}\left(\mathcal{B}_{M\times M}\mathbf{n}^{(i_{current}-1)} - \mathbf{V}^{(i_{current}-1)} \circ \mathbf{n}^{(i_{current}-1)}\right), \\ \mathbf{V}^{(i_{current})} &= \mathbf{V}^{(i_{current}-1)} + \Delta t\left(-k_C\mathbf{V}^{(i_{current}-1)} \circ \mathbf{n}^{(i_{current}-1)}\right. \\ &\quad \left. -k_D\mathbf{V}^{(i_{current}-1)} + k_B\mathbf{m}_\tau^{(i_{circular})}\right), \end{aligned}$$

   where $\circ$ denotes element-wise matrix multiplication.

   (c) If mod $(t(i_{current}), \text{Desired Output Frequency}) < \Delta t$

      i. Output $\mathbf{n}$ and $\mathbf{V}$ vectors on coarse time-scale

$$\begin{aligned} \mathbf{n}_{out} &= \mathbf{n}^{(i_{current})}, \\ \mathbf{V}_{out} &= \mathbf{V}^{(i_{current})} \end{aligned}$$

   (d) Next $i_{current}$

2.5 Numerical results

Using the numerical scheme developed in the previous section, we now look at some typical solutions of the system of PDEs for an inhomogeneous initial condition of virus particles.

2.5.1 Virus extinction

A common experimental outcome of oncolytic virotherapy is the extinction of the initial viral load. Even in the relatively simple model presented here, there are many parameters that play a role in such failure. Low infected cell motility, characterised by a large diffusivity ratio D, long virus incubation period, τ_B, or an insufficient viral burst yield, described by the parameter $k_B = \alpha k_C$, can all contribute to such an outcome.

A typical case of viral extinction is given by the parameters in Table 2.1. This set of dimensionless parameters corresponds to a physical system with a small burst coefficient, and a strong viral death term. The resultant simulation over time interval $t \in [0, 500]$ shown in Figure 2.3 shows the phenomena of complete failure of therapy.

Dimensionless Parameter	Value
Spatial Domain	$x \in [-219,\ 219]$, $\Delta x = 5.35 \times 10^{-2}$
Diffusion Coefficient	$D = 0.1$
Virus Burst Coefficient	$k_B = 0.1$
Virus Infection Rate	$k_C = 10^{-2}$
Virus Death Rate	$k_D = 1$
Burst Age	$\tau_B = 5$, $\Delta a = \Delta t$
Initial Conditions	$n(x,0) = 1 \quad \forall x$ $m(x,0) = 0 \quad \forall x$ $V(x,0) = \exp\left(-\frac{x^2}{0.1L}\right)$
Time Span	$t \in [0, 500]$, $\Delta t = 5 \times 10^{-2}$

Table 2.1: Parameters used in PDE model illustrating the failure of virus spread in the system.

After an initial injection of virus particles, the relatively small virus burst coefficient, k_B, results in an insufficient release of new virus particles, which combines with natural clearance of virus particles to prevent the reaction continuing indefinitely. The clearance of virus is faster than the rate of new virus creation, resulting in complete removal of virus particles from the system. As the local concentration of virus particles reduces, so does the rate of infection of tumour cells. The migration of uninfected cells from areas of higher concentration gradually increases the local concentration of uninfected cells around the site of virus injection, replacing some of the uninfected cells around the site of injection killed

during the infection phase. In the long-time limit, $t \to \infty$, we expect the uninfected cell concentration to homogenise to an equilibrium state $\lim_{t\to\infty} n(t) < 1$.

The initial failure of therapy in such simulations is not always the final outcome. In certain cases, the delay associated with infected cell bursting can trigger a "re-ignition" phenomenon in the system over long time-scales, as seen in Section 2.5.3, so care must be taken to choose sufficiently long simulation times to ensure that the whole progression is captured.

2.5.2 Virus spread

Ultimately, the goal of oncolytic virotherapy is to minimise the concentration of uninfected tumour cells. To this effect, we are interested in cases resulting in the spreading of oncolytic agent in sufficiently large quantities throughout the spatial domain. This outcome is related to the extinction phenomenon described previously in Section 2.5.1, except the natural virus clearance is balanced by the rate of virus production and spread. This outcome can be seen for a broad range of parameters in the model developed here.

In Section 2.5.1, we saw that the combination of low burst size and high virus death rate can lead to failure of therapy. We now consider a system with the dimensionless parameters shown in Table 2.2. These parameters correspond to a system with a higher burst size, and significantly lower viral death rate than in Section 2.5.1.

Physical Parameter	Value
Spatial Domain	$x \in [-219,\ 219]$, $\Delta x = 5.35 \times 10^{-2}$
Diffusion Coefficient	$D = 0.1$
Virus Burst Coefficient	$k_B = 1$
Virus Infection Rate	$k_C = 10^{-2}$
Virus Death Rate	$k_D = 2.5 \times 10^{-2}$
Burst Age	$\tau_B = 5$, $\Delta a = \Delta t$
Initial Conditions	$n(x,0) = 1 \quad \forall x$ $m(x,0) = 0 \quad \forall x$ $V(x,0) = \exp\left(-\frac{x^2}{0.1L}\right)$
Time Span	$t \in [0, 750]$, $\Delta t = 10^{-3}$

Table 2.2: Parameters used in PDE model illustrating a wave of virus spread from the site of initial infection.

As seen in Figure 2.4, this change has a significant qualitative effect on the dynamics in the system: after initial transient behaviour, the virus particle concentration settles into a pulse of constant amplitude expanding in both directions from the initial viral injection site at $x = 0$. In parallel with this, the uninfected cell concentration near the initial injection

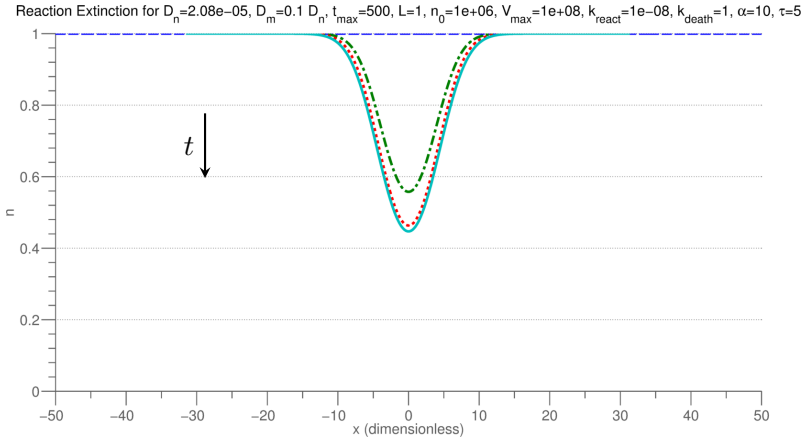

(a) Localised decrease of uninfected cell concentration in the vicinity of virus initial condition, plotted on $x \in [-40, 40]$ for times $t \in [0, 0.9, 1.8, 2.7]$ (blue dashed, green dash-dotted, red dotted and cyan solid, respectively).

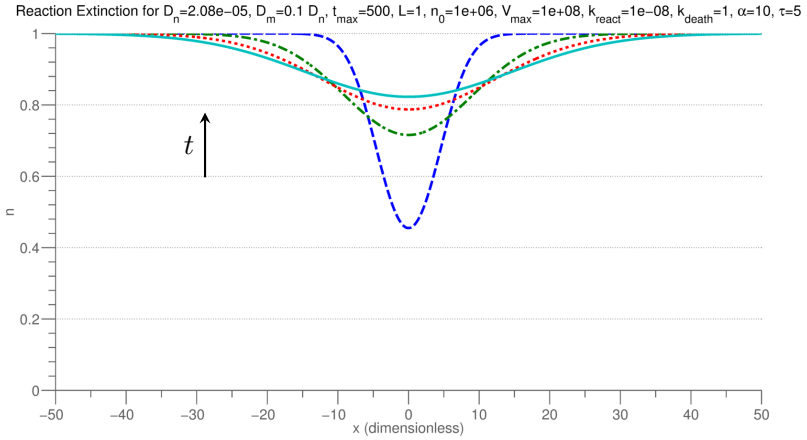

(b) Uninfected cell concentration returning to equilibrium due to uninfected cell migration and extinction of virus particles, plotted on $x \in [-40, 40]$ for times $t \in [3.6, 36.0, 68.5, 101.0]$ (blue dashed, green dash-dotted, red dotted and cyan solid, respectively).

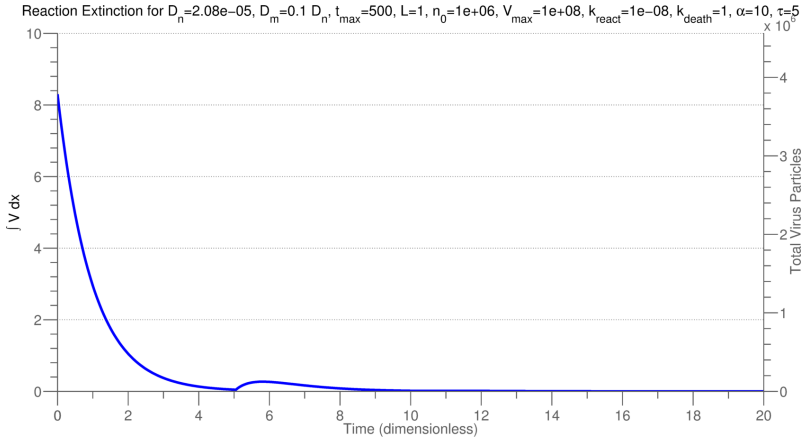

(c) Total number of infected cells, $\int V dx$, for time $t \in [0, 20]$. Virus particles decay rapidly before the first burst at $t = \tau_B = 5$, but continue to decay exponentially, leading to eventual extinction.

Figure 2.3: Extinction of virus particles for parameters specified in Table 2.1.

decays to zero, and a wave front of uninfected cells moves outwards at the same rate as the virus pulse. In this case, reactions take place in a narrow boundary layer, with the upstream uninfected cell concentration remaining at the initial concentration, and apparent elimination of uninfected cells downstream, behind the virus wave pulse.

Qualitatively, simulations such as this show the apparent success of therapy over the time period simulated. However, from an experimental point of view, tumour cell motility allows the tumour to re-establish across the domain into voids created by virus infection and lysis. Therefore, the complete elimination of the tumour requires the propagation of tumour-killing virus particles to be sustained throughout the system, and the conditions required for such behaviour in the model are discussed in Section 2.6.

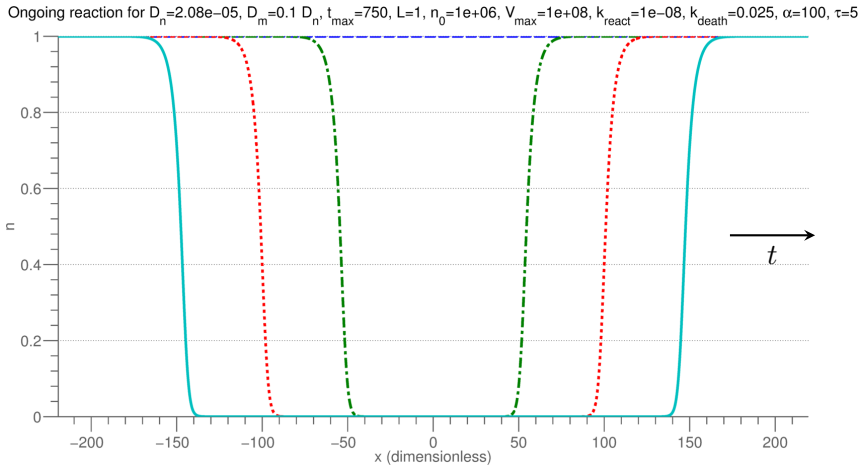

(a) Uninfected cell concentration decreasing in the region of virus initial condition, before settling into a sustained left- and right-moving wave front.

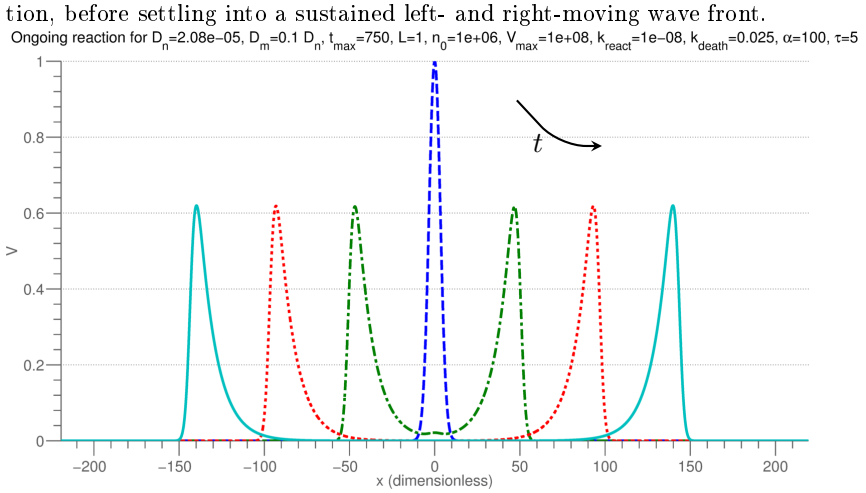

(b) Virus concentration showing decay of initial data, before settling into a constant-amplitude left- and right-moving pulse.

Figure 2.4: Ongoing reaction on spatial interval $x \in [-219, 219]$ for times $t \in [0, 187.5, 375.1, 562.6]$ (blue dashed, green dash-dotted, red dotted and cyan solid, respectively) for parameters specified in Table 2.2.

2.5.3 Virus reignition

Finally, we highlight the case of oscillations of virus particle concentration in time due to alternating periods of bursts and deaths of virus particles. From extensive numerical investigation, we have found that these states are unstable, transient phenomena, and tend to either the extinction or spreading cases shown previously in the long-time limit.

While these cases are physically plausible, they highlight a limitation of the continuum modelling approach in the case of low particle number. Fundamentally, the number of uninfected cells and virus particles in the system is discretised, and in certain cases, the continuum model may predict the continuation of reactions from an infinitesimal concentration that would physically correspond to extinction. To illustrate this, we need to consider the physical interpretation of the dimensionless results, for a special set of dimensional parameters.

In the case of slow infection rate, k_{react}, high virus death rate, k_{death}, and large burst number, α, virus particles are rapidly removed from the system when not in an infected cell, with the virus death and infected cell burst processes competing. To illustrate this, we consider a somewhat artificial scenario of a system with a very low initial viral concentration, such that $\int V_{max} V(x,0)\,dx \approx 1$ virus particle mm^{-2}, with $V_{max} = 10^2$ vir mm^{-3}, $k_{react} = 10^{-10}$ mm^{3}hr^{-1}vir^{-1}, $\alpha = 5.5 \times 10^4$ and $k_{death} = 5.5$ hr for a localised reaction with $D = 10^{-2}$ and a typical burst age of $\tau = 5$ hrs. This choice of constants results in dimensionless parameters which are shown in Table 2.3.

Dimensionless Parameter	Value
Spatial Domain	$x \in [-0.22, 0.22]$, $\Delta x = 1.1 \times 10^{-4}$
Diffusion Coefficient	$D = 0.01$
Virus Burst Coefficient	$k_B = 6 \times 10^8$
Virus Infection Rate	$k_C = 10^4$
Virus Death Rate	$k_D = 5.5 \times 10^8$
Burst Age	$\tau_B = 5 \times 10^{-8}$, $\Delta a = \Delta t$
Initial Conditions	$n(x,0) = 1 \quad \forall x$ $m(x,0) = 0 \quad \forall x$ $V(x,0) = \exp\left(-\frac{x^2}{0.01L}\right)$
Time Span	$t \in [0, 5 \times 10^{-6}]$, $\Delta t = 6.25 \times 10^{-10}$

Table 2.3: Parameters used in PDE model illustrating apparent "re-ignition" over a long time-scale.

The numerical solution for this set of parameters is shown in Figure 2.5, and shows a rapid decrease in the concentration of virus particles before the first burst on time interval $t \in [0, \tau_B)$, similar to the case of virus extinction seen previously. As infected cells burst, the concentration of virus particles increases rapidly, before once again decaying to a minimum

peak value of 1.6×10^{-9} for $t \in (3\tau_B, 4\tau_B)$. These oscillations continue in a similar manner, with the maximum overall concentration of virus particles gradually increasing on a longer time-scale, before eventually reaching a net increase of virus particles compared to the initial condition after $t > 27\tau_B$.

Figure 2.6 shows the total number of virus particles in the system, given by $\int_{-L}^{L} V dx$, with the rescaled dimensional number of particles per mm^{-2} shown on the secondary vertical axis. From these results, we see that the total number of particles decreases to less than one per mm^{-2}, and it is the combination of this small (but non-zero) concentration and the large burst size that result in the steady overall increase in virus particles in the system over time.

For a typical tumour cross-section, these residual concentrations of virus particles are physically meaningless as they refer to fractions of particles, and such behaviour is indicative of the break down of the validity of the continuum assumption. To better understand the true physical behaviour of the system at low particle concentrations, it is necessary to develop a discrete model such as that developed in the following chapter.

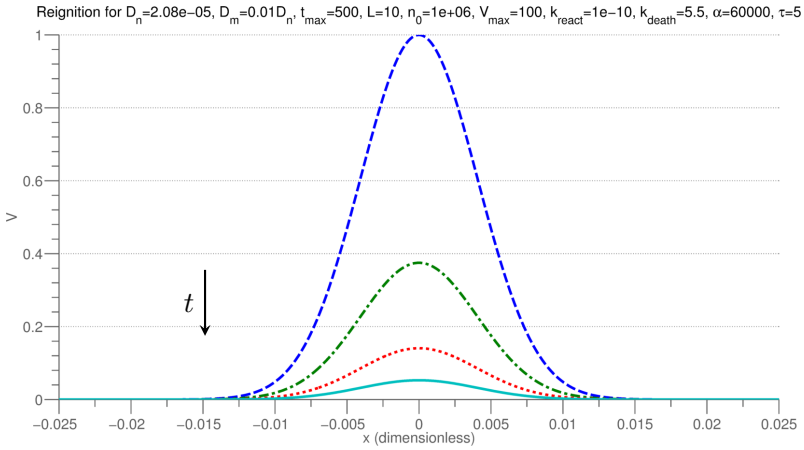

(a) Virus concentration during initial decay for $t \in [0,\ 5.13,\ 10.3,\ 15.4] \times 10^{-8}$ (blue dashed, green dash-dotted, red dotted and cyan solid, respectively).

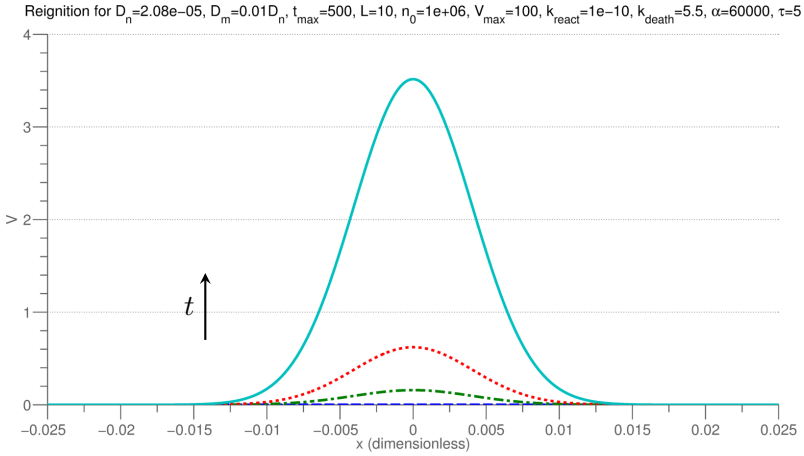

(b) Virus concentration during re-ignition for $t \in [4.61,\ 12.2,\ 19.8,\ 27.4] \times 10^{-7}$ (blue dashed, green dash-dotted, red dotted and cyan solid, respectively).

Figure 2.5: Rapid decrease in virus particle concentration, $V(x)$, followed by reignition of infection, for parameters specified in Table 2.3, shown on spatial interval $x \in [-0.025, 0.025]$.

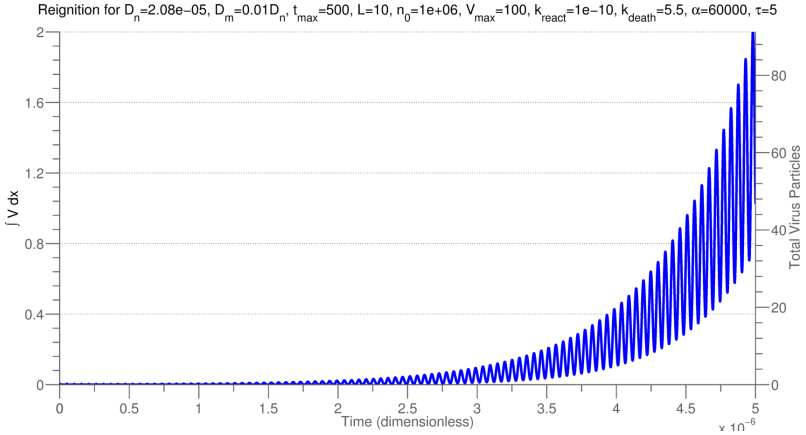

(a) Oscillation in total number of virus particles in system, $\int_{-L}^{L} V(x)\,dx$, due to successive bursts and decay, with an overall increase in the number of particles on the long-time limit.

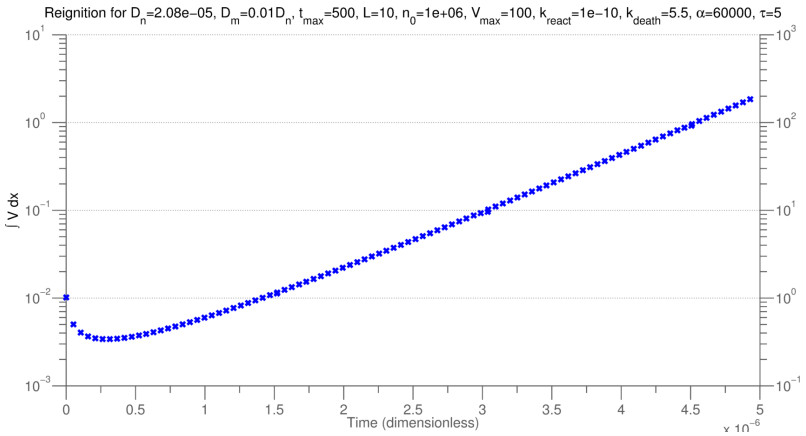

(b) Semi-log plot of maximum total virus particles in system per burst interval, showing number of virus particles < 1 for $t < 5 \times 10^{-7}$.

Figure 2.6: Total virus particles in system, given by $\int V_0 V dx$, for $t \in \left[0, 5 \times 10^{-5}\right]$. The number of particles drops to less than one, before increasing in the long time-scale, illustrating apparent "re-ignition".

2.6 Travelling waves

It is important to understand the conditions under which a sustained propagation wave of infected cells is possible, as well as the speed of such waves. As seen in Figure 2.4, numerical solutions of the system of PDEs are evidence of travelling-wave behaviour in our model. To properly investigate the range of parameters for which this spreading behaviour can be sustained at constant amplitude over an indefinite time interval, we need to determine the conditions under which an initial dose of virus particles can eliminate tumours of arbitrary size. To this effect, we seek a time-independent travelling wave solution to the system of age-structured governing equations (2.20)–(2.22), subject to boundary and initial conditions (2.24)–(2.29).

We consider a travelling frame moving with dimensionless wave speed c, and introduce the new coordinate

$$z = x - ct, \tag{2.42}$$

$$t' = t. \tag{2.43}$$

Due to the spatial symmetry of the problem, we expect both left- and right-moving travelling waves to be present in the system. Restricting our focus to the case of a right-moving travelling wave, we consider the problem over the spatial interval $x \in [0, \infty)$, and define wave speed $c > 0$.

Looking at the long-time limit where $t' \to \infty$, the governing equations (2.20)–(2.22) become functions of travelling wave coordinate, z, and age, a, giving

$$-c\frac{dn}{dz} = \frac{d^2n}{dz^2} - Vn \tag{2.44}$$

$$-c\frac{\partial m}{\partial z} + \frac{\partial m}{\partial a} = D\frac{\partial^2 m}{\partial z^2} \tag{2.45}$$

$$-c\frac{dV}{dz} = -k_D V - k_C V n + k_B m\left(z, \tau_B\right). \tag{2.46}$$

For an infinite spatial domain, the no-flux boundary conditions in (2.28)–(2.29) become

$$\frac{dn}{dz} \to 0 \quad \text{as } z \to \pm\infty, \tag{2.47}$$

$$\frac{\partial m}{\partial z} \to 0 \quad \text{as } z \to \pm\infty. \tag{2.48}$$

The initial condition at $a = 0$ for the birth of infected cells from (2.27) is now given by

$$m\left(z, 0\right) = V\left(z\right) n\left(z\right). \tag{2.49}$$

In the travelling wave coordinate frame, as $z \to \pm\infty$, the solution corresponds to a steady state of the system. At these steady states, (2.44) and (2.47) imply that $\lim_{z\to\pm\infty} Vn = 0$, and (2.48) implies that $\lim_{z\to\pm\infty} m =$ constant. From these conditions, we infer that V must be constant as $z \to \pm\infty$ to satisfy (2.46), and from the additional knowledge of the initial condition (2.26), for a finite wave speed c we must have $V = 0$ as $z \to -\infty$ at the left hand boundary for a right-moving travelling wave.

2.6.1 Reduction of system

Since the infected cell term in (2.46) is only ever evaluated at the burst age τ_B, and (2.45) is only coupled to (2.44) and (2.46) through the initial age condition, (2.49), we reduce the system of governing equations to a set of integro-differential equations by expressing the contribution to virus density from bursting of infected cell in terms of the infection birth conditions at $a = 0$.

We solve (2.45) subject to (2.48) and (2.49) by introducing a Green's function $g(z, a)$, which satisfies the adjoint problem

$$-\frac{\partial g}{\partial a} + c\frac{\partial g}{\partial z} - D\frac{\partial^2 g}{\partial z^2} = \delta(z - \xi)\,\delta(a - \eta), \tag{2.50}$$

where $0 < |\xi| < |z|$ and $0 < \eta < a$, subject to boundary conditions

$$g(z, a) \to 0 \quad \text{as } z \to \pm\infty, \tag{2.51}$$

$$g(z, a) = 0 \quad \text{for } a \geq \eta, \tag{2.52}$$

chosen to simplify the problem.

Multiplying (2.45) by $g(z, a)$ and (2.50) by $m(z, a)$, we subtract the resulting equations, and integrate over $-\infty < z < \infty$ and $0 < a < \infty$ to obtain the expression

$$\begin{aligned} m(\xi, \eta) = &\int_{-\infty}^{\infty}\int_{0}^{\eta}\left(-\frac{\partial(mg)}{\partial a}\right)dadz + \int_{0}^{\eta}\int_{-\infty}^{\infty} c\frac{\partial(mg)}{\partial z}dzda \\ &+ \int_{-\infty}^{\infty}\int_{0}^{\eta} D\left(g\frac{\partial^2 m}{\partial z^2} - m\frac{\partial^2 g}{\partial z^2}\right)dadz. \end{aligned} \tag{2.53}$$

On integrating and applying (2.48), (2.49), (2.51) and (2.52), this expression reduces to the convolution integral

$$m(\xi, \eta) = \int_{-\infty}^{\infty} V(z)\, n(z)\, g(z, 0; \xi; \eta)\, dz. \tag{2.54}$$

We now seek a suitable form of the Green's function $g(z, a)$ that satisfies (2.50) subject

to (2.51) and (2.52). Defining the Fourier transform of the Green's function to be

$$\hat{g}(\omega, a) = \int_{-\infty}^{\infty} g(z, a; \xi; \eta) \exp(-i\omega z)\, dz, \tag{2.55}$$

we take the Fourier transform of the adjoint problem (2.50) to obtain the expression

$$-\frac{\partial \hat{g}}{\partial a} + ci\omega\hat{g} + D\omega^2\hat{g} = \delta(a-\eta)\exp(-i\omega\xi). \tag{2.56}$$

The general solution to (2.56) subject to boundary condition at $a = \eta$ is

$$\hat{g}(\omega, a) = \exp\left(-\left(D\omega^2 + ic\omega\right)(\eta - a) - i\omega\xi\right). \tag{2.57}$$

Taking the inverse Fourier transform of $\hat{g}(\omega, a)$, defined as

$$g(z, a) = \frac{1}{2\pi}\int_{-\infty}^{\infty} \hat{g}(\omega, a)\exp(i\omega z)\, d\omega, \tag{2.58}$$

the Green's function can be written as

$$\begin{aligned} g(z, a) &= \frac{\exp\left(-\frac{(\xi - z + c(\eta - a))^2}{4D(\eta - a)}\right)}{2\pi} \\ &\quad \times \int_{-\infty}^{\infty} \exp\left(-D(\eta - a)\left(\omega + \frac{i(\xi - z + c(\eta - a))}{2D(\eta - a)}\right)^2\right) d\omega. \end{aligned} \tag{2.59}$$

Performing a change of variables $s = \sqrt{D(\eta - a)}\left(\omega + \frac{i(\xi - z + c(\eta - a))}{2D(\eta - a)}\right)$, this is reduced to

$$g(z, a) = \frac{\exp\left(-\frac{(z - \xi - c(\eta - a))^2}{4D(\eta - a)}\right)}{2\sqrt{\pi D(\eta - a)}}, \tag{2.60}$$

and the convolution integral expression (2.56) becomes

$$m(z, a) = \frac{1}{2\sqrt{\pi D a}}\int_{-\infty}^{\infty} V(\xi)\, n(\xi) \exp\left(-\frac{((z - \xi) + ca)^2}{4Da}\right) d\xi. \tag{2.61}$$

2.6.1.1 Small diffusion coefficient limit

The expression (2.61) is valid for arbitrary sets of parameters. However, for certain ranges of parameters, the system can be further simplified. For the case where uninfected cell motility is the dominant motility process in the system, corresponding to $D_n \gg D_m$, this leads to the limiting case of the diffusion ratio $D \to 0$. The integral term in (2.61) can be

rewritten in the form

$$I = \int_{-\infty}^{\infty} V(\xi)\, n(\xi) \exp\left(\frac{1}{D}\phi(\xi; z, a)\right) d\xi, \tag{2.62}$$

where $\phi(\xi; z, a) = -\frac{((z-\xi)+ca)^2}{4a}$. In the limit $D \to 0$, this integral can be approximated using Laplace's method, where the main contribution to the integral comes from the point $\xi_c = z + ca$ at which point the function $\phi(\xi_c)$ has a maximum value. Expanding $\phi(\xi; z, a)$ as a Taylor series about $\xi = \xi_c$, the function becomes

$$\phi(\xi; z, a) = 0 - \frac{(\xi - z - ca)^2}{2}\left(\frac{1}{2a}\right) + O\left(\xi^3\right), \tag{2.63}$$

with the first derivative equal to zero by definition, and the higher-order derivatives also equal to zero.

In the limiting case $D \ll 1$, the integral (2.62) can now be approximated with

$$\begin{aligned} I &\approx \int_{-\infty}^{\infty} \exp\left(-\frac{1}{D}\frac{(\xi - z - ca)^2}{4a}\right) V(\xi_c)\, n(\xi_c)\, d\xi \\ &= V(\xi_c)\, n(\xi_c) \int_{-\infty}^{\infty} \exp\left(\frac{-(\xi - z - ca)^2}{4Da}\right) d\xi \\ &= V(\xi_c)\, n(\xi_c) \int_{-\infty}^{\infty} \exp\left(\frac{-(\xi - z - ca)^2}{4Da}\right) d\xi \\ &= 2\sqrt{\pi Da} V(z + ca)\, n(z + ca), \end{aligned} \tag{2.64}$$

and (2.61) becomes

$$m(z, a) = V(z + ca)\, n(z + ca). \tag{2.65}$$

The governing system of equations for the right-moving travelling wave in the small diffusion coefficient limit becomes

$$-c\frac{dn}{dz} = \frac{d^2 n}{dz^2} - Vn, \tag{2.66}$$

$$-c\frac{dV}{dz} = -k_D V - k_C V n + k_B V(z + c\tau_B)\, n(z + c\tau_B). \tag{2.67}$$

subject to

$$\left.\frac{dn}{dz}\right|_{z \to \pm\infty} = 0, \tag{2.68}$$

$$\lim_{z \to -\infty} V(z) = 0. \tag{2.69}$$

In this asymptotic limit, the order of the system has been reduced to a system of differential equations with a *negative* delay term, known as a Delay Differential Equation of advanced type. While it may be surprising to find this type of equation in a physical system that incorporates time lag, it has previously been noted that systems of delay equations formulated in retarded or neutral form can in fact be of advanced type in the presence of singularities (Campbell, 1980; Zhu and Petzold, 1997). Such problems are known to be ill-posed Fowler (2005), as the reliance on advanced information leads to an infinite number of unsteady states. In this case, any discontinuities in advanced systems become less smooth in each successive interval, and are difficult to deal with numerically (Ascher and Petzold, 1995).

2.6.2 Travelling wave speed dependence on total virus particles

The unknowns in the system are n, m, V and the wave speed, c. This wave speed can be determined by integrating the governing equations (2.44) and (2.46) with respect to the moving frame coordinate z, to give

$$-c\left[n\right]_{-\infty}^{\infty} = \left[\frac{dn}{dz}\right]_{-\infty}^{\infty} - \int_{-\infty}^{\infty} Vndz, \tag{2.70}$$

$$-c\left[V\right]_{-\infty}^{\infty} = -k_D\int_{-\infty}^{\infty} Vdz - k_C\int_{-\infty}^{\infty} Vndz + k_B\int_{-\infty}^{\infty} m\left(z,\tau_B\right)dz. \tag{2.71}$$

According to (2.45), infected cells are only added to the system at age zero, so that the integral of infected cells with respect to space at any age is translationally invariant with age. Using this property, the last term in (2.71) can be replaced with

$$\begin{aligned}\int_{-\infty}^{\infty} m\left(z,\tau_B\right)dz &= \int_{-\infty}^{\infty} m\left(z,0\right)dz \\ &= \int_{-\infty}^{\infty} Vndz,\end{aligned} \tag{2.72}$$

from (2.27). Eliminating $\int_{-\infty}^{\infty} Vndz$ from (2.70) and (2.71) , the wave speed can be expressed as

$$\left[\frac{dn}{dz}\right]_{-\infty}^{\infty} + c\left[n\right]_{-\infty}^{\infty} = \frac{1}{k_B - k_C}\left(-c\left[V\right]_{-\infty}^{\infty} + k_D\int_{-\infty}^{\infty} Vdz\right), \tag{2.73}$$

which can be rearrange to give

$$c\left(\left[n\right]_{-\infty}^{\infty} + \frac{\left[V\right]_{-\infty}^{\infty}}{k_B - k_C}\right) = \frac{k_D\int_{-\infty}^{\infty} Vdz}{k_B - k_C} - \left[\frac{dn}{dz}\right]_{-\infty}^{\infty}, \tag{2.74}$$

and on applying the no-flux boundary condition (2.47), this gives the value of dimensionless wave speed

$$c = \frac{k_D \int_{-\infty}^{\infty} V dz}{(k_B - k_C)[n]_{-\infty}^{\infty} + [V]_{-\infty}^{\infty}}. \tag{2.75}$$

This expression relates the wave speed to the total number of virus particles. Although this integral is not known in advance, this relation can be a useful check for determining whether numerical solutions of the full PDE system have reached equilibrium conditions.

2.6.3 Asymptotic travelling wave speed

In order to evaluate (2.75), we need values for V and n in the travelling wave frame $z = x - ct$, so we now attempt to obtain a more direct formula. A travelling wave solution can be thought of as a homo- or heteroclinic orbit joining an unsteady and steady state in the phase plane, corresponding to a pulse or wave front solutions, respectively. Since the wave speed is finite, the destination steady state is determined by the initial conditions of the PDE given in (2.24)–(2.27). For a finite time t, the upstream conditions as $x \to \infty$ imply that

$$n(z) = 1, \tag{2.76}$$
$$m(z, a) = 0, \tag{2.77}$$
$$V(z) = \lim_{x \to \infty} V_0(x) \tag{2.78}$$

as $z \to \infty$. The initial condition $V_0(x)$ is chosen such that $\lim_{x\to\infty} V_0(x) = 0$, and we therefore expect the upstream steady-state

$$n_{eq} = 1, \tag{2.79}$$
$$m_{eq} = 0, \tag{2.80}$$
$$V_{eq} = 0. \tag{2.81}$$

Defining $N(z) = 1 - n(z)$, equations (2.44)–(2.46) can be rewritten as

$$c\frac{dN}{dz} = -\frac{d^2N}{dz^2} - V + VN, \tag{2.82}$$
$$-c\frac{\partial m}{\partial z} + \frac{\partial m}{\partial a} = D\frac{d^2m}{dz^2}, \tag{2.83}$$
$$-c\frac{dV}{dz} = -(k_D + k_C)V + k_C VN + k_B m(z, \tau_B). \tag{2.84}$$

The character of the solutions N, m and V depends on wave speed c, thus we have an

eigenvalue problem for which we want to determine values of c for which solutions exists, and satisfy

$$\lim_{z\to\infty} N = 0, \tag{2.85}$$
$$\lim_{z\to\infty} m = 0, \tag{2.86}$$
$$\lim_{z\to\infty} V = 0. \tag{2.87}$$

To investigate the behaviour of the wave profile (and its response to small perturbations) near the steady state, we introduce asymptotic expansions for N, m and V of the form

$$N \sim N_1 \exp(-\lambda z), \tag{2.88}$$
$$m \sim m_1(a) \exp(-\lambda z), \tag{2.89}$$
$$V \sim V_1 \exp(-\lambda z), \tag{2.90}$$

where λ is the eigenvalue of the system, N_1 and V_1 are constants, and $m_1(a)$ is independent of z. On substituting these expansions into (2.82)–(2.84), to leading order, the governing equations become

$$-\lambda N_1 \exp(-\lambda z)\, c = -\lambda^2 N_1 \exp(-\lambda z) - V_1 \exp(-\lambda z), \tag{2.91}$$
$$c\lambda m_1(a) \exp(-\lambda z) + \exp(-\lambda z) \frac{dm_1}{da} = D\lambda^2 m_1(a) \exp(-\lambda z), \tag{2.92}$$
$$c\lambda V_1 \exp(-\lambda z) = -(k_D + k_C) V_1 \exp(-\lambda z) + k_B m_1(\tau_B) \exp(-\lambda z), \tag{2.93}$$

in the vicinity of the right-hand boundary, as $z \to \infty$.

Equation (2.92) has solution

$$m_1(a) = \tilde{m}_1 \exp((D\lambda - c)\lambda a), \tag{2.94}$$

where $\tilde{m}_1$ is a constant of integration. Applying the initial birth condition at $a = 0$ from (2.49), gives $\tilde{m}_1 = V_1$, and (2.92) decouples from (2.91) and (2.93), resulting in the dispersion equations

$$-\lambda c = -\lambda^2 - \frac{V_1}{N_1}, \tag{2.95}$$
$$c\lambda = -(k_D + k_C) + k_B \exp((D\lambda - c)\lambda \tau_B). \tag{2.96}$$

Equation (2.95) determines $\frac{V_1}{N_1}$ in terms of λ, while (2.96) gives λ in terms of the other parameters. There are three solutions for eigenvalues λ, and following the repeated-root mechanism discussed in King (2013), the minimum wave speed can be identified by

determining the condition for a degenerate node in the travelling wave phase plane. At this transition, the eigenvalues associated with the leading edge of the wave front switch from being complex- to real-valued, corresponding to the steady state changing from a spiral to a node in the phase-plane. For monotonically decaying, non-oscillating wave fronts, such as those observed in the numerical solutions shown in Section 2.5.2, this heuristic condition governs the minimum wave speed for which a non-negative heteroclinic connection exists between the two equilibria. Writing

$$f(\lambda) = c\lambda + (k_D + k_C) - k_B \exp\left((D\lambda - c)\,\lambda\tau_B\right), \tag{2.97}$$

the degenerate case occurs when $\frac{df}{d\lambda} = 0$, which implies that

$$\lambda = \frac{c}{2k_B\tau_B D}\left(1 + \exp\left((D\lambda - c)\,\lambda\tau_B\right)\right). \tag{2.98}$$

However, (2.95) also has a homogeneous solution, so setting $\frac{V_1}{N_1} = 0$, this results on the condition that

$$\lambda = c. \tag{2.99}$$

The condition on the minimum wave speed is therefore given by solving the simultaneous equations

$$c\lambda \;=\; -(k_D + k_C) + k_B \exp\left((D\lambda - c)\,\lambda\tau_B\right), \tag{2.100}$$

and one of

$$\lambda = \begin{cases} \frac{c}{2k_B\tau_B D}\left(1 + \exp\left((D\lambda - c)\,\lambda\tau_B\right)\right) & \text{or} \\ c \end{cases}, \tag{2.101}$$

choosing the solution that results in the smallest value of c. It has previously been shown that even for reaction-diffusion systems with delays, as long as the PDE initial conditions have compact support, this minimum wave speed is the selected speed of the travelling wave (Al-Omari and Gourley, 2002; Cuesta and King, 2010, and references within). The transcendental equations (2.100)–(2.101) can be solved for λ and c using a numerical root-finding method, and it now remains to compare these analytically-derived predictions with numerical simulations from the full PDE model.

2.6.4 Comparison with numerical solution

It remains to compare the analytic result of Section 2.6.3 to the apparent travelling waves in the numerical solutions of the PDE system in Section 2.5.2.

Physical Parameter	Value
Spatial Domain	$x \in [-438,\ 438]$, $\Delta x = 3.65 \times 10^{-2}$
Diffusion Coefficient	$D = 0.5$
Virus Burst Coefficient	$k_B = 10$
Virus Infection Rate	$k_C = 1$
Virus Death Rate	$k_D = 1$
Burst Age	$\tau_B = 0.25$, $\Delta a = \Delta t$
Initial Conditions	$n(x,0) = 1 \quad \forall x$ $m(x,0) = 0 \quad \forall x$ $V(x,0) = \exp\left(-\frac{x^2}{0.0225L}\right)$
Time Span	$t \in [0,\ 100]$, $\Delta t = 2.5 \times 10^{-3}$

Table 2.4: Dimensionless parameters used for travelling wave comparison in Figure 2.7.

For an initial comparison, we consider the case where the dimensionless parameters are of order unity, as in Table 2.4. This could correspond to a system with a high reaction rate between virus particles and uninfected cells, a low initial peak virus concentration, a strong virus clearance rate, as well as a small burst size and a very short burst time.

Figure 2.7 shows the displacement from $x = 0$ of the peak virus concentration in the half-plane $x \in [0, L]$. The displacement of virus peak from the numerical solution of the PDE, as determined by the line of best fit of displacement, shows perfect agreement with the asymptotic prediction $c_{asymptotic} = 1.85$.

The numerical solution can also be used in conjunction with the travelling wave speed estimate from Section 2.6.2. For a right-moving wave front, the solution at $x = 0$ corresponds to the left-hand boundary in the travelling wave coordinate system as $t \to \infty$. The integral term in (2.75) can therefore be approximated with the numerical approximation in a finite domain as $\int_{-\infty}^{\infty} V(z)\,dz \approx \int_0^L V(x,t)\,dx$ for $t \gg 1$.

Making use of the numerical solution of the PDE, Figure 2.8 shows that the wave speed estimate (2.75) rapidly tends to the asymptotic solution, $c_{asymptotic} = 1.85$, given by (2.100)–(2.101).

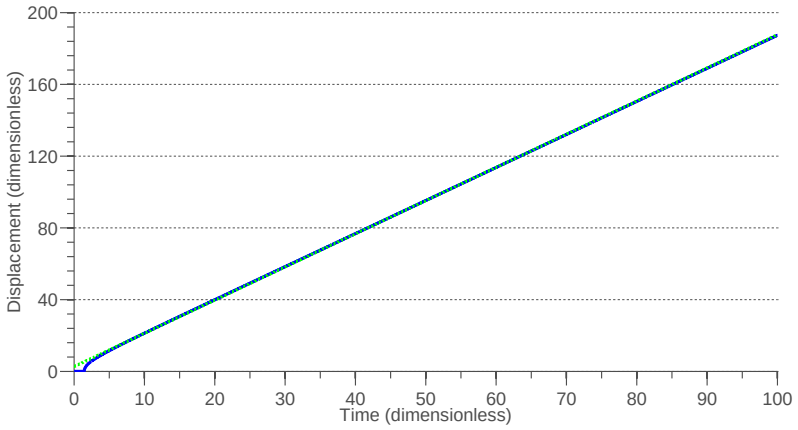

Figure 2.7: Position of peak virus concentration (blue, solid) for parameters in Table 2.4 and asymptotic results, $c = 1.85$ (green, dotted).

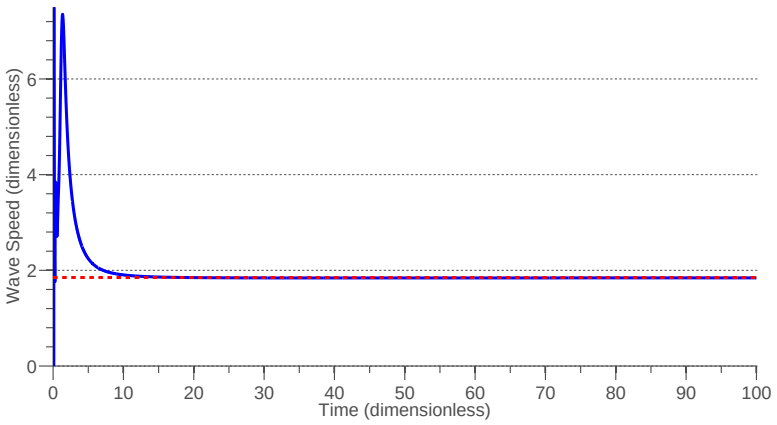

Figure 2.8: Comparison of wave speed estimate from (2.75) (blue, solid) and asymptotic result $c = 1.85$ (red, dashed) for parameters in Table 2.4.

We now consider the physically-motivated case of baseline physical parameters, corresponding to the dimensionless quantities in Table 2.5.

Physical Parameter	Value
Spatial Domain	$x \in [-1938,\ 1938]$, $\Delta x = 0.479$
Diffusion Coefficient	$D = 0.1$
Virus Burst Coefficient	$k_B = 1.25 \times 10^{-2}$
Virus Infection Rate	$k_C = 1.25 \times 10^{-4}$
Virus Death Rate	$k_D = 3.125 \times 10^{-4}$
Burst Age	$\tau_B = 400$, $\Delta a = \Delta t$
Initial Conditions	$n(x,0) = 1 \quad \forall x$ $m(x,0) = 0 \quad \forall x$ $V(x,0) = \exp\left(-\frac{x^2}{0.1L}\right)$
Time Span	$t \in \left[0,\ 6.4 \times 10^4\right]$, $\Delta t = 4$

Table 2.5: Dimensionless parameters used for travelling wave comparison in Figure 2.9.

Once again, the peak virus displacement in Figure 2.9 shows excellent agreement between the asymptotic wave speed, $c_{asymptotic} = 2.88 \times 10^{-2}$, and the numerical-determined line-of-best fit, $c_{numerical} = 2.81 \times 10^{-2}$. The non-zero x-intercept of the numerical solution comes about due to the maximum virus concentration being centred at $x = 0$ for $t < 1.5 \times 10^4$. This corresponds to a transient state of the PDE, before the system reaches a steady-state travelling wave, but does not affect the fitted wave speed.

Figure 2.10 shows the wave speed due to integral expression (2.75). The spike in the wave speed estimate coincides with the non-zero x-intercept from Figure 2.9, and illustrates that the integral estimate is only accurate in the steady state. In the long-time limit, Figure 2.10 shows that this expression tends to the asymptotic solution, $c_{asymptotic} = 2.88 \times 10^{-2}$.

Overall, this general agreement between the numerical solution of the PDE system and asymptotic prediction for wave speed is an encouraging result. Solving transcendental equations (2.100)–(2.101) is considerably less computationally-intensive, and is therefore a more practical method of determining the effects of key parameters on the model. In addition to this, an estimate of the wave speed allows us to make use of the relation derived in Section 2.6.2 to determine the total number of virus particles in the system at steady state, which may also be of practical use.

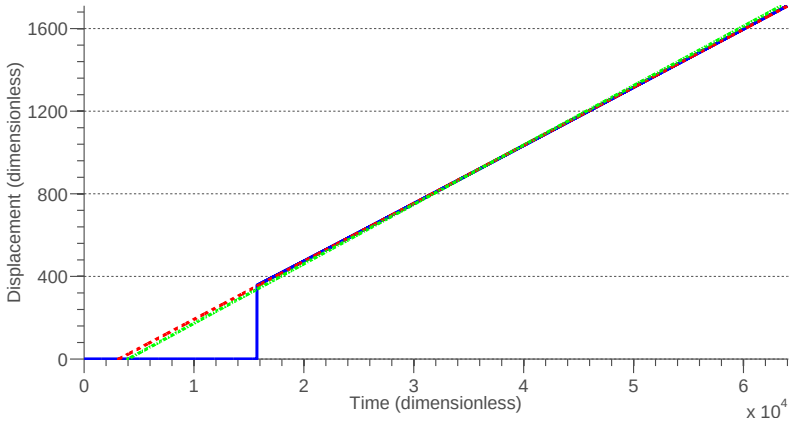

Figure 2.9: Position of peak virus concentration (blue, solid) for parameters in Table 2.5, line of best fit, $x = 2.81 \times 10^{-2} t - 88$ (red, dashed), and asymptotic results, $c = 2.88 \times 10^{-2}$ (green, dash-dotted).

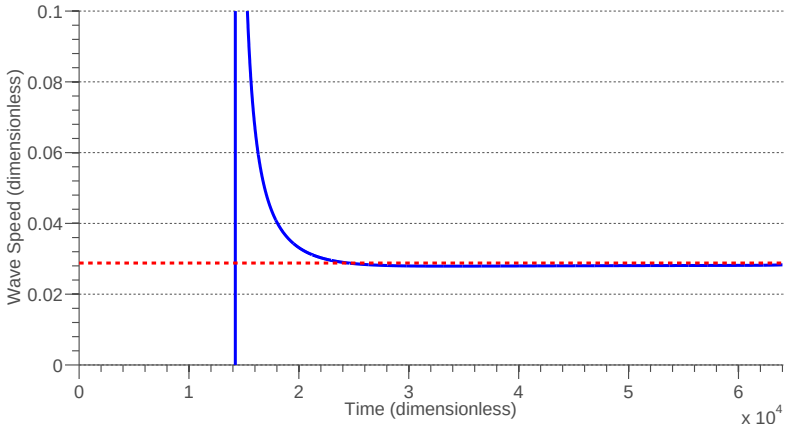

Figure 2.10: Comparison of wave speed estimate from (2.75) (blue, solid) and asymptotic result $c = 2.88 \times 10^{-2}$ (red, dashed) for parameters in Table 2.5.

2.7 Summary

In this chapter, we have developed a basic mathematical model describing the interaction between non-motile anti-tumour viral particles and motile uninfected and infected tumour cells. The resultant system of coupled, non-linear, age-structured partial differential equations were solved numerically using an efficient combination of Fast Fourier Transforms and Finite Difference methods. For spatially heterogeneous initial conditions of virus particles, we showed three distinct qualitative behaviours typical of the system: virus extinction, corresponding to failure of therapy, virus oscillation between decay and growth, and the spread of virus particles through the system in the form of a fixed-amplitude pulse. Motivated by travelling wave-like behaviour in the latter case, we proceeded to explore the conditions under which such behaviour could occur.

In the travelling wave case necessary for sustained viral spread, the system of governing equations was reduced to a mixed system of ordinary-partial differential equations, with new boundary conditions. Making use of asymptotic methods, we linearised the system at the upstream steady state, and presented a set of transcendental equations which could be solved numerically for the wave speed. Comparison of asymptotic wave speeds and numerical solutions showed good agreements, and we also presented a relation between the wave speed and the total number of virus particles in the system at steady state.

While continuum modelling approaches allow for significant analytic analysis, we saw that continuum assumption becomes invalid in the limit of low cell and particle numbers, such as the case of virus extinction phenomenon observed during the failure of treatment. By definition, such behaviour requires low concentrations of particles, which may invalidate the continuum assumptions used in deriving the governing equations from the chemical kinetics. Motivated by this, we consider a stochastic model describing the discrete behaviour same physical system in the hope of verifying the behaviour seen thus far.

Chapter 3

Stochastic simulation of tumour-virus system

In this chapter, we consider a discrete description of the tumour-virus interactions described previously (Chapter 2). After introducing the relevant theory of stochastic modelling and outlining its fundamental difference from the continuum description, we develop a compartment-based Monte Carlo algorithm describing the evolution, in space and time, of uninfected cells, infected cells and virus particles in a solid tumour. Typical parameter values, initial conditions and physically meaningful compartment sizes are shown, and a series of test cases for the model are presented. Comparing stochastic simulations to the solutions of equivalent continuum systems, we show the importance of compartment size choice, and discuss how to choose the reaction propensity for reaction-diffusion systems.

We show how this propensity affects key simulation outcomes such as wave speed and number of virus particles, and make recommendations for further use of the model.

3.1 Introduction

A common approach in analysing the time evolution of systems of chemically reacting molecules is to solve a set of coupled ordinary differential equations, with each equation representing the rate of change (in time) of the concentration of a particular species as a function of concentrations of all species present. This deterministic formulation, known as a set of reaction-rate equations, comes about from the law of averages, and is usually sufficiently accurate to describe the processes involved on the macroscopic scale. However, in certain situations, such as a system undergoing non-linear reactions in the neighbourhood of a chemical instability, this approach fails to recover the full qualitative behaviour when the system is affected by random perturbations occurring on discrete scales (McQuarrie,

1967). An alternative approach is to consider the physical system as a stochastic process where the reaction events are described probabilistically.

At a molecular level, reactions occur when two or more reacting molecules collide. Assuming the system is in thermal (but not necessarily chemical) equilibrium, a reaction may be thought of as occurring when the pair of molecules are both located within some reaction radius δr (generalised to a reaction volume δV), where they are sufficiently close to each other for a reaction to take place in time interval $(t, t + \delta t)$. However, as the reaction radius $\delta r \to 0$, the number of molecules within the reaction radius will drop to either 1 or 0, and as such, it is physically meaningless to talk about the number of molecules in this shrinking radius in the limit of $\delta t \to 0$ (Gillespie, 1977).

A more useful approach is to consider that the assumption of thermal equilibrium implies that the molecules will be randomly and uniformly distributed within the reaction volume δV. Now, collisions between molecules occur in a random manner, and instead of characterising reactions by their rates, we define a reaction probability per unit time, c_j, with the property that

$$\begin{aligned} c_j dt \quad = \quad & \text{probability that a randomly selected combination of} \\ & \text{reactant molecules at time } t \text{ will react accordingly} \\ & \text{in the next infinitesimal time interval } [t, t + dt). \end{aligned} \tag{3.1}$$

For a well-mixed system consisting of multiple species of molecules in a constant volume and at thermal equilibrium, the state of the system can be described by the molecular populations of each species, without specific knowledge of positions and velocities of the individual molecules. The probabilistic rates of reaction are functions of the total number of distinct combinations of reactant species within some defined reaction volume.

We define the time-dependent random variable $X(t) = \{X_1, X_2, \ldots, X_n\}$ to be the state vector of the system for molecules of species $\{1, \ldots, n\}$ at time t. Under the assumption that most of molecular collisions are non-reactive elastic collisions, the positions of molecules will be uniformly distributed throughout the volume. Now, by only considering reactions that change the populations of at least one of the species, the system can be represented exactly through a state-change vector v_{ij}, which represents the change in population of the i^{th} species due to the j^{th} reaction, and the propensity function a_j, which is defined such that $a_j dt$ gives the probability that the j^{th} reaction will occur in the infinitesimal time interval dt. This total probability of a specific reaction occurring is equivalent to multiplying (3.1) by the number of distinct combinations of molecules for the j^{th} reaction.

Since the transition from one state of the system to another is dependent only on the previous state, the evolution can be described as a discrete Markov process. Under the Markov assumption, the conditional probability of a system to be in state x at time t given it was at state $X(s)$ at time s depends only on $X(s)$ and $t - s$.

Physically, the number of molecules in a system is a discrete integer-valued random variable, and so the reaction process has to be described by the probability density of such a random variable. This description generalises the underlying physical processes, with the mean roughly corresponding with the solution to the deterministic model, and the variance describing the inherent statistical fluctuations about the mean. For a system consisting of discrete states, the probability of being a particular state can be described by considering the net transitions to and from all other states. This probabilistic interpretation yields a "chemical" master equation for the system.

3.1.1 Chemical master equation

Consider a system consisting of N distinct species, with the population of the i^{th} species, S_i at time t denoted by $X_i(t)$. For a system of M reactions, with the j^{th} reaction denoted by R_j, we can completely characterise each R_j by two quantities: the propensity function, a_j, and the associated state-change vector, ν_j. Given these definitions, the number of ways the system can reach state $X = \vec{x}$ at time $t + dt$ is given by

$$P(x, t+dt) = \sum_{j=1}^{M} P(x - \nu_j, t)\left(a_j(x - \nu_j)\, dt\right) + P(x,t)\left(1 - \sum_{j=1}^{M}\left(a_j(x)\, dt\right)\right). \quad (3.2)$$

In the limit $dt \to 0$, the above relation is reduced to a differential equation in probability density describing the time evolution of the probability of a system to be in one of a discrete set of state, known as the Chemical Master Equation (CME)

$$\frac{\partial P(x,t)}{\partial t} = \sum_{n=1}^{M}\left(a_j(x - \nu_j) P(x - \nu_j, t) - a_j(x) P(x,t)\right). \quad (3.3)$$

This governing equation describes the time evolution of the system exactly, but in practice it is very difficult to solve analytically for all but the simplest propensity functions $a_j(x)$. To illustrate this, we now look at exact solutions of the elementary first order unimolecular and second order bimolecular reaction, by deriving generating functions and comparing these to the continuum description.

3.1.1.1 Unimolecular reactions

In a system of unimolecular reactions, the transition probability of going from a state x to a new state $x - j$ depends linearly on x. For example, let us consider the simple decay reaction

$$\mathrm{A} \xrightarrow{k} \mathrm{B}, \quad (3.4)$$

and define $x = \begin{bmatrix} A \\ B \end{bmatrix}$ to be the state vector representing the number of molecules of species A and B, and $\nu = \begin{bmatrix} -1 & 1 \end{bmatrix}$ as the state-change vector representing the stoichiometry of (3.4).

Defining the random variable $X(t)$ to be the number of molecules of A in the system at time t, we introduce notation

$$P_x(t) = \text{Prob}\{X(t) = x\}, \tag{3.5}$$

to denote the probability of being in state $X(t) = x$ at time t. We assume that the probability of transition from state x to $x-1$ in the interval $(t, t+\Delta t)$ is $kx\Delta t + o(\Delta t)$, where k is constant, and the time interval is small enough such that only one molecule undergoes transition in this period. From this definition, we can write

$$P_x(t+\Delta t) = k(x+1)\Delta t P_{x+1}(t) + (1-kx\Delta t)P_x(t) + o(\Delta t). \tag{3.6}$$

Taking the limit as $\Delta t \to 0$ as in van Hove (1957), we obtain the differential-difference equation

$$\frac{dP_x}{dt} = k(x+1)P_{x+1}(t) - kxP_x(t). \tag{3.7}$$

To fully quantify the behaviour of the system, we derive the probability generating function and make use of its properties. By definition, the probability generating function of $F(s,t)$ is given by

$$F(s,t) = \sum_{n=0}^{\infty} P_n(t)\, s^n, \quad |s| < 1. \tag{3.8}$$

Taking the derivative with respect to time, we find that

$$\begin{aligned} \frac{\partial F}{\partial t} &= \sum_{x=0}^{\infty} \left(s^x \frac{dP_x(t)}{dt} \right) \\ &= \sum_{x=0}^{\infty} \left(s^x \left(k(x+1)P_{x+1}(t) - kxP_x(t) \right) \right) \\ &= k(1-s) \sum_{x=1}^{\infty} x s^{x-1} P_x(t) \\ &= k(1-s)\frac{\partial F}{\partial s}. \end{aligned} \tag{3.9}$$

Taking as the initial condition $F(s,0) = s^{x_0}$, where $X(0) = x_0$ is the initial number of

molecules of A, this partial differential equation has solution

$$F(s,t) = (1 + (s-1)\exp(ikt))^{x_0}. \tag{3.10}$$

From the properties of the probability generating function, the expected value of $X(t)$ is given by

$$\begin{aligned} E[X(t)] &= \overline{X}(t) \\ &= \sum xP_x \\ &= \left.\frac{\partial F}{\partial s}\right|_{s=1} \\ &= x_0 \exp(-kt), \end{aligned} \tag{3.11}$$

and the variance of $X(t)$ is given by

$$\begin{aligned} \mathrm{Var}[X(t)] &= E\left[\left(X - \overline{X}\right)^2\right] \\ &= \sum x^2 P_x - \overline{X}^2 \\ &= \left.\frac{\partial^2 F}{\partial s^2}\right|_{s=1} + \left.\frac{\partial F}{\partial s}\right|_{s=1} - \left(\left.\frac{\partial F}{\partial s}\right|_{s=1}\right)^2 \\ &= x_0 \exp(-kt)(1 - \exp(-kt)). \end{aligned} \tag{3.12}$$

From these calculations, we see that the mean value given by (3.11) is identical to the deterministic solution of the unimolecular reaction-rate equation $\frac{d[A]}{dt} = -k[A]$ (Connors, 1990, pp. 18).

3.1.1.2 Bimolecular reactions

We now consider the more complicated case of the bimolecular reaction

$$\mathrm{A} + \mathrm{B} \xrightarrow{k} \mathrm{C}. \tag{3.13}$$

We let $X(t)$ be the discrete random variable representing the number of molecules of C in the system at time t. Following the procedure from Ishida (1964), this yields the differential-difference equations

$$\begin{aligned} \frac{dP_0}{dt} &= -kabP_0(t), \\ \frac{dP_x}{dt} &= k(a-(x-1))(b-(x-1))P_{x-1}(t) - k(a-x)(b-x)P_x(t), \\ \frac{dP_{\tilde{c}}}{dt} &= k(a-(\tilde{c}-1))(b-(\tilde{c}-1))P_{\tilde{c}-1}(t), \end{aligned} \tag{3.14}$$

where a, b are the initial number of A and B, respectively, and $\tilde{c} = \min(a, b)$ is the maximum number of molecules of C, with

$$\sum_{n=0}^{\tilde{c}} P_n(t) = 1. \tag{3.15}$$

Taking the Laplace transform of (3.14) in time for initial condition $P_x(0) = \begin{cases} 1, & \text{for } x = 0 \\ 0, & \text{otherwise} \end{cases}$ results in the difference equations

$$\begin{aligned} -1 + zq_0(z) &= -kabq_0(z), \\ zq_x(z) &= k(a-(x-1))(b-(x-1))q_{x-1}(z) \\ &\quad -k(a-x)(b-x)q_x(z), \\ zq_{\tilde{c}}(z) &= k(a-(\tilde{c}-1))(b-(\tilde{c}-1))q_{\tilde{c}-1}(z), \end{aligned} \tag{3.16}$$

where $q_x(z)$ is the Laplace transform of $P_x(t)$.

Solving the resulting equations as in Ishida (1964) gives solution

$$q_x(z) = \binom{a}{x}\binom{b}{x}(x!)^2 k^x \prod_{n=0}^{x} \frac{1}{z - k(a-n)(b-n)}, \tag{3.17}$$

and after decomposing the product term into partial fractions, has Laplace inverse

$$\begin{aligned} P_x(t) &= (-1)^x \binom{a}{x}\binom{b}{x} \sum_{n=0}^{x} (-1)^n \left(1 + \frac{x-n}{a+b-x-n}\right) \\ &\quad \times \binom{x}{n}\binom{a+b-n}{x}^{-1} \exp(-k(a-n)(b-n)t). \end{aligned} \tag{3.18}$$

On introducing the probability generating function $F(s,t) = \sum_{n=0}^{\tilde{c}} P_n(t)\, s^n$, $|s| < 1$, it can be shown that this has the form

$$\begin{aligned} F(s,t) &= s^{\alpha} \sum_{n=a}^{0} (-1)^n (b-a+2n) \frac{a!\,(b!)}{(a-n)!\,(b+n)!} \\ &\quad \times \exp(-kn(b-a+n)t) \\ &\quad \times \frac{(b-a+n-1)}{n!\,(b-a)!} J_n\left(b-a, b-a+n+1, s^{-1}\right) \end{aligned} \tag{3.19}$$

where J_n are Jacobi polynomials (Abramowitz and Stegun, 1965, Ch. 22).

Making use of the properties of the probability generating function, the expectation value of the number of molecules C at any given time can be written in the relatively simple form

$$\begin{aligned} E[X(t)] &= \overline{X}(t) \\ &= a - \sum_{n=1}^{b-a} (b-a+2n) \left(\begin{array}{c} a \\ n \end{array} \right) \left(\begin{array}{c} b+n \\ n \end{array} \right)^{-1} \qquad (3.20) \\ &\quad \times \exp\left(-kn(b-a+n)t\right), \qquad (3.21) \end{aligned}$$

where a and b denote the initial populations of species A and B respectively.

Taking the derivative of (3.21) with respect to time and making use of (3.14), this can be written as

$$\frac{d}{dt}\left(E[X(t)]\right) = kE[a - X(t)]\,E[b - X(t)] + k\mathrm{Var}[X(t)], \qquad (3.22)$$

where $\mathrm{Var}[X(t)]$ denotes the variance. The first term is identical to the behaviour predicted from application of the law of mass action in the continuum model, with the second term denoting the stochastic fluctuations in the system. For the case where $E[a - X(t)]\,E[b - X(t)] \gg \mathrm{Var}[X(t)]$, the stochastic and continuum descriptions will be approximately consistent in the mean; however, as chemical reactions are random processes, this is often not the case, especially in small reaction systems. In these situations, the stochastic model can produce behaviour such as bistability of states which is not possible in the continuum model (Erban et al., 2007). Such behaviour is not always limited to the case of small reaction systems, and it has been shown that feedback processes can amplify the stochastic noise term to exhibit stochastic effects such as bistability on macroscopic scales (Samoilov et al., 2005).

The complexity of deriving analytic solutions to the CME, even in the case of relatively simple reaction leads us to seek approximations to the CME that simplify calculations while maintaining the qualitative behaviour of the system.

3.1.2 Exact stochastic simulation algorithms

Although the Chemical Master Equation is a useful starting point, analytic solutions are rarely found, and it is cumbersome to apply even in numerical simulations. Instead, numerical solutions of stochastic systems generally make use of Stochastic Simulation Algorithms (SSA), which are Monte Carlo procedures for numerically generating time trajectories of molecular populations in exact accordance with the underlying stochastic process.

One such algorithm is the Gillespie SSA, which is derived from the fundamental premise (3.1) without resorting to approximations, and while derived independently of the CME, it

is logically equivalent to it. This algorithm is a well-known example of a class known as "exact stochastic algorithms". These algorithms can be constructed from first principles, and have the added advantage of easily scaling to multiple spatial dimensions and complicated domains.

In the simplest implementation, known as the direct method, given an initial system state $X(t_0)$, we advance the system by determining which reaction R_j occurs next, and at what time this happens. The reaction and time are selected based on the propensity functions.

At each time step, we calculate propensities $a_j(x)$ for each reaction $j \in [1, M]$, as well as the total propensity of the system, defined to be $a_0(x) = \sum_{k=1}^{M} a_k(x)$. It can be shown (Gillespie, 1977) that the probability density function for the next reaction to be the j^{th} reaction at time t' is given by

$$P\left(t', j|x, t\right) = a_j(x) \exp\left(-a_0(x)\, t'\right), \tag{3.23}$$

where $t' > t$. The time to the next reaction t' is a waiting time, which is chosen from an exponentially distributed random variable with mean $1/a_0(x)$, while the reaction index j is chosen independently as an integer random variable with point probability $a_j(x)/a_0(x)$.

In the direct method, two uniformly distributed random numbers $r_1, r_2 \in [0, 1)$ are generated. The time to the next reaction is calculated by

$$t' = -\frac{1}{a_0} \ln(r_1), \tag{3.24}$$

and the next reaction R_j is chosen by finding index j satisfying

$$\sum_{k=1}^{j-1} \frac{a_k}{a_0} < r_2 \leq \sum_{k=1}^{j} \frac{a_k}{a_0}. \tag{3.25}$$

The populations of species are updated according to the state-change vector, and the current time is incremented by the time increment t'. We now apply this framework to construct a SSA for an inhomogeneous system of uninfected cells, infected cells and virus particles.

3.2 Formulation of SSA for tumour-virus system

At the fundamental level, interactions between virus particles and tumour cells occur in discrete units. While continuum modelling may be valid for certain parameter regimes, the cases of initial virus injection and the extinction of the infection wave are by definition reliant on low-population dynamics, suggesting that a discrete approach must be utilised.

We consider the physical model from the previous chapter, with the interactions between uninfected cells n, infected cells m and virus particles V described by the chemical reactions

$$\mathrm{n} + \mathrm{V} \overset{k_{react}}{\rightarrow} \mathrm{m}, \tag{3.26}$$

$$\mathrm{V} \overset{k_{death}}{\rightarrow} \emptyset, \tag{3.27}$$

where k_{react} is the rate of infection of virus particles and k_{death} is the rate of natural virus death. In addition to these reactions, which we model stochastically, we assume that infected cells burst and die after a (deterministic) time τ, releasing a fixed number, α, of virus particles each, given by

$$m|_{\mathrm{age}=\tau} \rightarrow \alpha V. \tag{3.28}$$

We introduce n, V and m to denote the number of uninfected cells, the number of virus particles, and the number of infected cells per unit age in the system, respectively.

The Stochastic Simulation Algorithm outlined previously assumes that the system is well-mixed, which simplifies greatly the number of reactions that need to be considered during a time interval. To extend this approach to spatially inhomogeneous systems, we implement what is known as an on-lattice approach, where the spatial domain is divided into a chain of well-mixed compartments, with interactions between each compartment corresponding to spatially inhomogeneous processes such as diffusion.

3.2.1 Inter-compartment diffusion

The diffusion-like random walk of particles in a compartment-based model can be described by a set of first-order reactions. In a one-dimensional discretised spatial domain, the diffusive motion of a generic cell g in compartment j to the left is described by the reaction

$$g_j \overset{p_{left}}{\rightarrow} g_{j-1}, \tag{3.29}$$

and the diffusive motions of cells at position j to the right corresponds with the reaction

$$g_j \overset{p_{right}}{\rightarrow} g_{j+1}, \tag{3.30}$$

where p_{left} and p_{right} are the rates of reaction to the left and right respectively, and are generally taken to be equal, if the random walk is unbiased.

Applying this formulation to the case of transitions of uninfected and infected cells

between compartments gives rise to the propensity functions

$$a_{n_D}(j) = pn_j, \tag{3.31}$$

$$a_{m_D}(j) = qm_j, \tag{3.32}$$

where p and q are the transition rates of the uninfected and infected cells respectively (with no preference to the left or right), and n, m are the numbers of uninfected and infected cells in the j^{th} compartment, respectively. We assume that virus particles do not diffuse, and the spread of infection is driven by the combination of the movement of infected cells and infected cell burst.

This approach to a random walk in space can be generalised to multiple spatial dimensions by including reaction terms for jump processes to each adjacent compartment. For a d-dimensional spatial domain, a minimum of $2d$ jump processes are required for a fully-connected domain, although additional jumps between diagonally-adjacent compartments could also be added. For simplicity, we choose the minimally-connected case (four neighbours in the two-dimensional case), which tends towards the higher-connected cases in the limit of shrinking compartment volume. The relationship between inter-compartment jump rates, p and q, and macroscopic diffusion coefficients, D_n and D_m, is discussed in Section 3.2.4.

3.2.2 Intra-compartment reactions

The natural death of virus particles in (3.27) is a zeroth-order process, which has a propensity function of the form

$$a_{death}(j) = k_{death} V_j, \tag{3.33}$$

where k_{death} is the rate of virus death.

In our discrete formulation, the death of an infected cell through virus bursting could be modelled by either a Poisson process with exponentially distributed waiting times or by a fixed, deterministic burst age. Although it is plausible that the physical system has some variation in the duration of infected cell lifetime, it is probably not true that a cell is equally likely to burst in any time interval, making the Markovian description inappropriate. Instead, we choose to implement a fixed burst-age, which is in keeping with the assumptions of the previous chapter. We derive the propensity function of the second-order infection reaction within a compartment governed by (3.26) from the number of possible combinations of reactions within the compartment. This suggests that the

propensity function of infection is

$$a_{react}(j) = k_{react} V_j n_j, \tag{3.34}$$

where j is the index of the compartment, k_{react} is the stochastic rate of infection, and V and n are the number of virus particles and uninfected cells in the compartment, respectively.

3.2.3 Initial and boundary conditions

As with the continuum model, we must specify physically meaningful initial and boundary conditions for the system. To mimic the initial conditions used in the continuum simulations, the uninfected cancer cells are uniformly distributed over all compartments, and the initial distribution of virus particles is restricted to a single compartment in the centre of the spatial domain. At the time of initialisation, no infected cancer cells are placed in the system.

In contrast to the continuum case, the boundary conditions relevant to the stochastic description do not require a well-mixed approximation at the edge of the domain, and can be replaced with reflective boundary conditions, as in Erban and Chapman (2007). This boundary condition is trivially implemented by checking whether cells in a boundary compartments are moving towards or away from the boundary, and "reflecting" them away from the boundary if they try to cross it. The ease of implementing complicated boundary geometries in rule-based algorithms serves to highlight the intuitive nature of implementing these algorithms.

3.2.4 Scaling of parameters

So far we have made use of the fundamental premise of reaction probability (3.1), without attempting to relate it to parameters that can be physically quantified using experimental data.

In Section 3.1, we considered the concept of reaction radius, and the requirement that the behaviour of the system should be independent of the arbitrary choice of this radius. This concept must also apply to compartment-based models, since for a finite number of particles in the system, decreasing the compartment size, h, would result in a reduction of poly-molecular intra-compartment reactions taking place. Similarly, the frequency of inter-compartment random walks would also be affected by the choice of compartment size. The propensity functions must therefore be modified in a way that adjusts for the choice of compartment size. This is done by specifying the stochastic reaction rates to be functions of compartment width, and scaling these accordingly.

From Erban et al. (2007), we find that the rate of inter-compartment jumps from Section 3.2.1 is related to the macroscopic diffusion coefficients of uninfected and infected

cells, D_n and D_m, by

$$p = \frac{D_n}{h^2}, \tag{3.35}$$

$$q = \frac{D_m}{h^2}. \tag{3.36}$$

For stochastic simulation in two spatial dimensions, compartments not on the boundary are connected to four neighbours, resulting in four possible inter-compartment reactions. This can be generalised, with the total propensity for jumping into any neighbouring compartment

$$a_{\text{total diff}}(j) = \begin{cases} \frac{2dD_n}{h^2} n_j, & \text{for uninfected cells} \\ \frac{2dD_m}{h^2} m_j, & \text{for infected cells} \end{cases},$$

where d is the number of spatial degrees of freedom.

Following from Bernstein (2005) and Higham (2008), we find that the stochastic and continuum rates for the bimolecular reaction (3.26) are related by compartment volume, h^3, resulting in the reaction propensity

$$a_{\text{react}}(j) = \frac{k_{react}}{h^3} V_j n_j. \tag{3.37}$$

Since unimolecular reactions, such as virus particle death, do not depend on a reaction radius, the stochastic rate constant is invariant of compartment width h, and is equivalent to the that of the continuum case (McQuarrie, 1967), with the propensity function for virus death given by

$$a_{\text{death}}(j) = k_{death} V_j. \tag{3.38}$$

3.2.5 Formulation of the Gillespie SSA

From the general outline of the Gillespie Stochastic Simulation Algorithm (SSA) in Section 3.1.2, we make use of the propensity functions formulated in Section 3.2.4 to implement the direct method of the Gillespie SSA.

One of the advantages of implementing a rule-based algorithm is the relative simplicity with which we can incorporate the time-delayed burst given by reaction (3.28). We introduce an additional internal state to track the birth time of each particle of the infected cell population m. Now, for every infection reaction R_{react} taking place, we set the associated burst state to time $t_{burst} = t_{current} + \tau$, and on generating each new exponentially distributed time increment Δt, we check to see if $t_{current} + \Delta t > t_{burst}$ for any of infected cell population m. If such a cell is found, then we discard the time increment τ as $t + \Delta t > t_{burst}$, and instead set the current time to the time of infected cell death,

$t_{new} = t_{burst}$. If $t_{current} + \Delta t < t_{burst}$ for all m, then no infected cells have burst in the time step, and we search continue with the Gillespie SSA as usual.

Combining the inter-compartment diffusion, intra-compartment reactions and deterministic infected cell bursts into a suitable SSA, we develop Algorithm 4 (Appendix A). This algorithm has been implemented in `C++` for a 2D domain, utilising a position-based map associative container to store uninfected cells, a position-based multi-map associative container to store unique infected cells, and a compartment-based map associative container to store virus particles in the system.

3.3 Choice of domain and typical parameters

In Section 3.2.1, we saw that spatially-dependent reactions can be modelled using SSA by introducing a series of connected, well-mixed compartments of width h. By definition, these reactions occur in 3D and reaction propensities depend on compartment volume, h^3 (Figure 3.1). However, due to the computationally-intensive nature of the exact SSA, where every reaction is simulated sequentially, we typically construct $N \times N \times 1$ compartment domains, corresponding to pseudo-2D solutions of inherently 3D systems (Figure 3.2a).

For the application of the SSA to modelling solid tumours, we consider two experimental scenarios: a 3D system initially consisting of densely packed uninfected cells, corresponding to a 3D in vitro culture (or a caricature of *in vivo* case without vasculature), and an initially sparse case, corresponding to an *in vitro* monolayer of cells on a Petri dish. For the dense case, each 2D simulation can be thought of as $L \times L \times h$ mm^3 slices of a solid tumour that is spatially invariant in the z-direction. The sparse case, on the other hand, describes a system that is effectively 2D, and provided the choice of compartment size h is sufficiently large to accommodate a monolayer of species, the $L \times L \times h$ domain describes the whole system.

Typically, solid tumours range from $600 - 2200$ mm^3 in volume (Heise et al., 1999), corresponding to a radius of $5 - 8$ mm for a spherical tumour. However, since a tumour of this size would almost certainly not be of uniform cell density, additional effects such as vascularization and growth would need to be considered at the periphery. In addition, key assumptions such as negligible virus diffusion would no longer be valid, requiring an extension to the model proposed. Instead, we focus on a 1 mm transport-limited, high-collagen content core region of the tumour where the effective diffusion of large particles such as adenovirus and herpes simplex virus is negligible (Baxter and Jain, 1989; Mok, 2007).

This high-density region of a tumour is typically quoted as having density 10^6 cells mm^{-3} (Wein et al., 2003; Chicoine and Silbergeld, 1995), which serves as the basis for our initial state for simulating the dense *in vivo* case. The sparse *in vitro* case, corresponding to a 2D monolayer such as a petri dish, is assumed to have similar parameter values except

the uninfected cell density. In a typical *in vitro* experiment, Bazan-Peregrino et al. (2008) count 20000 cells per well in a 96-well plate. Manufacturer specifications quote the typical growth surface area of such plates as $0.25 - 0.35$ cm^2, which allows a crude estimate of $550 - 800$ cells mm^{-2} for the *in vitro* case, a factor of 10 sparser than the equivalent *in vivo* monolayer.

The initial number of virus particles quoted in experimental studies varies by several orders of magnitude, with values ranging from $10^8 - 10^{12}$ pfu ml^{-1} (Kirn, 2001). This is further complicated by the fact that the spatial distribution of virus injections is not well studied. Taking best estimates from McKee et al. (2006) and Mok (2007), we set the typical virus injection area to be 10 μm, and the virus concentration to be 8×10^9 pfu ml^{-1}. While a typical infected cell burst can release thousands of virus particles, only a fraction of these are viable plaque forming units, and we thus follow the standard modelling technique of choosing burst size α to be 100 as in Bajzer et al. (2008) and Friedman et al. (2006).

In our simplified model, we treat the infection of cells by virus particles, (3.26), as a single reaction. In reality, this process is described by chain of complex internalization reactions, and a net rate for these is difficult to measure experimentally. From Pecora (2002) experimental data on fraction of cells successfully infected, Friedman et al. (2006) estimated the infection coefficient to be approximately 10^{-8} mm^{3}hr^{-1}vir^{-1}. Similarly, modelling the death rate of virus particles as a first-order death process in (3.27) amounts to a crude unification of immune effects, virus defects and a multitude of other potential processes resulting in virus particle clearance, estimated at 2.5×10^{-2} hr^{-1} by Friedman et al. (2006).

Finally, we estimate the diffusivity of uninfected cells via a macroscopic diffusion coefficient. As with the rate of reaction, this parameter is difficult to determine experimentally, as it varies with the density of the surrounding media. For the case of solid tumours, Matzavinos (2004) provide a lower bound for the diffusivity of cells to be 5×10^{-6} cm^{2}day^{-1}, but this estimate could potentially be several orders of magnitude larger for less dense regions of solid tumours.

A summary of these parameter estimates is given in Table 3.1.

3.4 Model validation

To test the validity of the (spatial) on-lattice SSA outlined in Algorithm 4 (in particular, appropriate relations between propensities and compartment sizes), we run simulations for simple cases, and compare numeric, and where appropriate, analytic solutions to the continuum model. In particular, we will compare the stochastic and continuum model for each process (diffusion, virus death, infection and infected cell burst) in turn, before finally combining all reactions to test the full model. In addition to testing the SSA, we

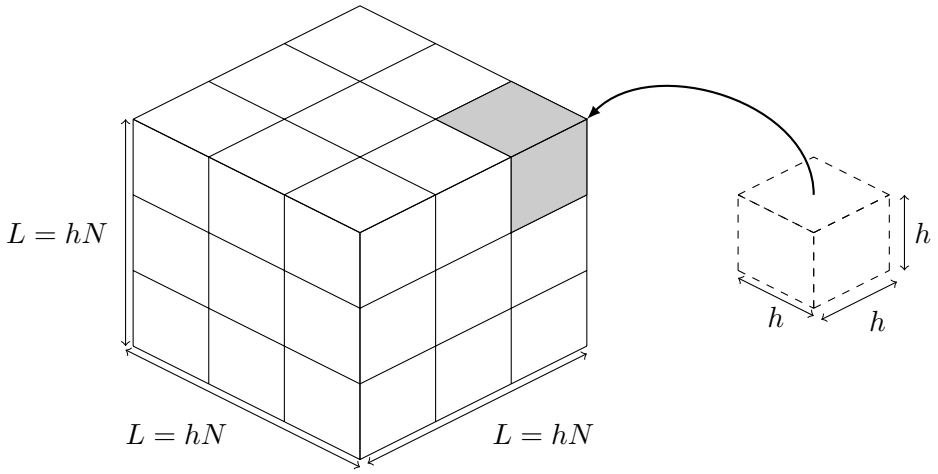

Figure 3.1: 3D domain of size $L \times L \times L$ mm, discretised into N compartments of volume h^3.

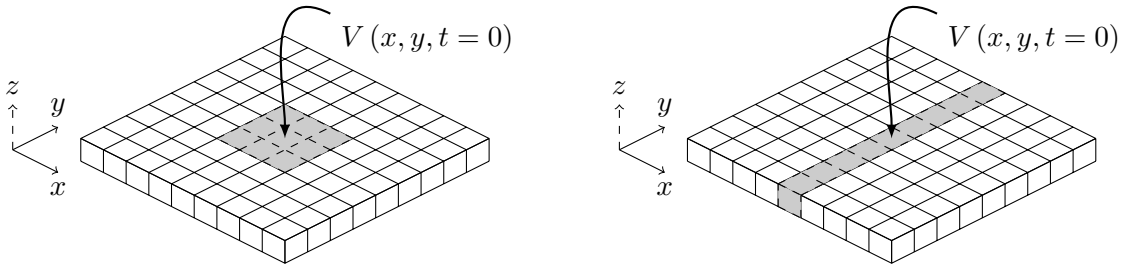

(a) y-dependent initial injection of virus particles in 3×3 central compartments (shaded).

(b) y-independent initial injection of virus particles in $N \times 1$ central compartments (shaded).

Figure 3.2: Comparison of pseudo-2D and pseudo-1D initial distributions of virus particles in a 2D domain.

Quantity	Notation	Value	Notes/Reference
Diffusion Ratio $^{D_m}/_{D_n}$ (PDE)	D	0.1	Arbitrary. Chosen to represent infected cells propagating slower that uninfected cells.
Uninfected Diffusion Coefficient	D_n	2.08×10^{-5} mm^{2}hr^{-1}	5×10^{-6} cm^{2}day^{-1} or greater (Matzavinos, 2004). This represent the smallest diffusion coefficient in solid tumours.
$\Delta x/\Delta y$	h	0.01 mm	Typical diameter of a cell (Paiva et al., 2009), representing the minimum compartment size.
Number Compartments		$100 \times 100 \times 1$ compartment domain	Corresponds to 1×1 mm^2 2D cross-section of depth 0.01 mm.
Burst Size	α	100	This represents viable virus particles; typical burst size may be $10^4 - 10^5$. Choosing burst size $50 - 100$ is common in mathematical models (cf. Friedman et al., 2006).
Virus Injection Area		5×5 compartments	McKee et al. (2006) show that typical area of virus spread in a 2D slice through fibrous tissue, 30 minutes after injection, is $5 - 10\mu$m^2.
Number of Virus Particles	$V(0)$	8000 particles per compartment	Kirn (2001)
Number of Uninfected Cells in $1 \times 1 \times 0.01$ mm slice	$N(0)$	10000 cells (*in vivo*)	1×10^6 cells mm^{-3} (Wein et al., 2003; Chicoine and Silbergeld, 1995) .
		1000 cells (*in vitro*)	Typical count of 20000 cells per well in a 96-well plate (Bazan-Peregrino et al., 2008), with surface area of plates $\approx 0.25 - 0.35$ cm^2. Rough estimate of 1000 cells mm^{-2}.
Burst Time	τ	$5 - 25$ hrs	Aghi and Martuza (2005).
Reaction Rate	k_{react}	10^{-8}mm^{3}hr^{-1}vir^{-1}	Friedman et al. (2006).
Virus Death Rate	k_{death}	2.5×10^{-2} hr^{-1}	Friedman et al. (2006); Paiva et al. (2009)
Max Time	$t_{\max}$	$\begin{cases} 500 \text{ hrs} & \text{for } \textit{in vivo} \text{ case} \\ 2000 \text{ hrs} & \text{for } \textit{in vitro} \text{ case} \end{cases}$	Typical experimental procedure is to re-administer therapy every 3–4 weeks (Kirn, 2001; Heise et al., 1999).

Table 3.1: Baseline parameters for virus-tumour model.

also use this opportunity to test our existing PDE Finite Difference-Fast Fourier Transform (FD-FFT) method (Section 2.4) for the same cases.

For the purposes of these tests, the generalised two-dimensional SSA is utilised, with a typical domain consisting of $N \times N \times 1$ compartments of width h. In spatially-varying cases where comparisons are made with one-dimensional solutions, the initial distributions of species are chosen to be spatially homogeneous in the y-direction (as illustrated by Figure 3.2b), and the solution then averaged over the total number of compartments in the y-direction: averaging over N compartments in the y-direction is equivalent to simulating N one-dimensional $N \times 1 \times 1$ simulations.

In the following test cases, a typical two-dimensional domain of 100×100 compartments, each of width $h = 0.01$ mm is used. This compartment size corresponds to the typical length-scale of a cell, and is therefore the smallest physically motivated compartment size we can choose. Furthermore, we use typical reaction rates, burst sizes and burst times outlined in Table 3.1 for the majority of the tests, unless otherwise specified.

The simplest of the test cases is the random walk of cells on a fixed lattice, and we compare the effects of compartment size on propensity scaling to the continuum diffusion case in the long-time limit.

3.4.1 Random walk and diffusion

The physical model described in Section 3.2 consisted of two motile species: uninfected and infected cells. Using the parameters in Table 3.1, we construct a two-dimensional $(N \times N \times 1)$ spatial domain, and consider two cases with initial distributions:

$$\begin{aligned} n_{ij}(0) &= \begin{cases} 1, & \text{for } (i,j) = (N/2, N/2) \\ 0, & \text{otherwise} \end{cases}, \\ m_{ij}(0) &= 0, \\ V_{ij}(0) &= 0, \end{aligned} \tag{3.39}$$

with $t \in [0, 500]$ and $\tau > 500$ hours, and

$$\begin{aligned} n_{ij}(0) &= 0, \\ m_{ij}(0) &= \begin{cases} 1, & \text{for } (i,j) = (N/2, N/2) \\ 0, & \text{otherwise} \end{cases}, \\ V_{ij}(0) &= 0. \end{aligned} \tag{3.40}$$

with $t \in [0, 4000]$ hours and $\tau > 4000$ hours. In both these cases, the absence of virus particles in the system, and a burst time $\tau > t_{max}$ means that the only reactions in the

system are the random walks of uninfected and infected cells, respectively.

Running 500 simulations on a $100 \times 100 \times 1$ compartment domain, we obtain a set of positions for the single uninfected and infected cell evolving in time. From theory (Berg, 1993, pp. 11), the expected relation between mean-squared displacement $\langle x^2 \rangle$ and time t to has the form

$$\langle x^2 \rangle = \left(\frac{2d}{h^2} D \right) t, \tag{3.41}$$

where d is the dimension ($d = 1$ for $N \times 1$ domain, $d = 2$ for $N \times N$ domain), and D is the macro-scale diffusivity of the species.

Figure 3.3 shows the mean squared displacement of the uninfected and infected cells from their initial position, averaged over the total number of simulations. As the x and y positions of the cell are independent of each other, the mean squared displacement relation in x and y (green and cyan, respectively in Figures 3.3a-3.3b) for each case equivalent to (3.41) in 1D. The radial displacement from initial distribution, given by coordinate $r = \sqrt{x^2 + y^2}$, depends on both coordinates, and so this is equivalent to the 2D case of (3.41). Comparing the gradient of lines of best-fit of mean squared displacement with the theoretically predicted relations, we see excellent agreement and recover the original diffusion coefficient D_n and D_m.

3.4.2 Homogeneous reaction (with random walk)

We now consider the test case of a purely reactive, homogeneous system, with the bimolecular reaction

$$\mathrm{n} + \mathrm{V} \overset{k_{react}}{\rightarrow} \mathrm{m}. \tag{3.42}$$

Using the law of mass action, we can write down the macroscopic model describing the evolution of n, m and V as

$$\begin{aligned} \frac{dn}{dt} &= -k_{react} V n, \\ \frac{dm}{dt} &= k_{react} V n, \\ \frac{dV}{dt} &= -k_{react} V n, \end{aligned} \tag{3.43}$$

with the initial conditions

$$\begin{aligned} n(0) &= n_0, \\ m(0) &= 0, \\ V(0) &= V_0, \end{aligned} \tag{3.44}$$

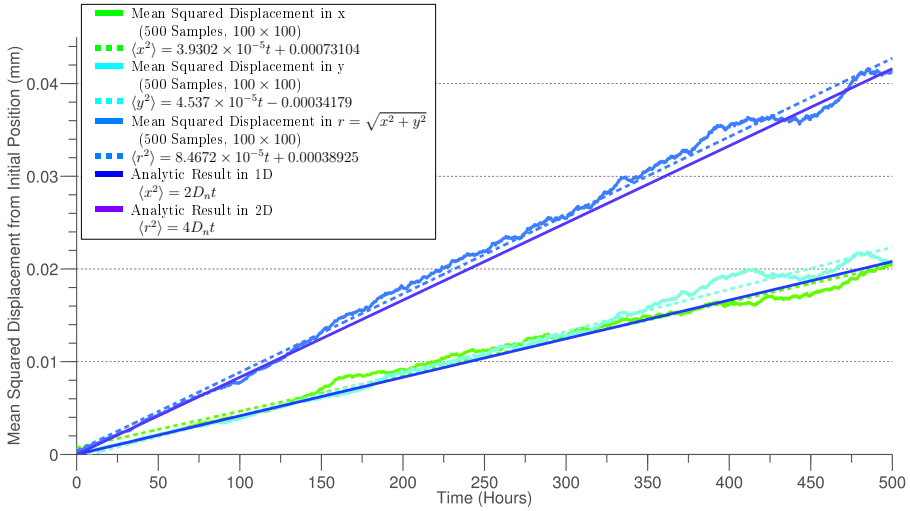

(a) Mean squared displacement of uninfected cell random walk with $D_n = 2.08 \times 10^{-5}\,\mathrm{mmhr}^{-1}$.

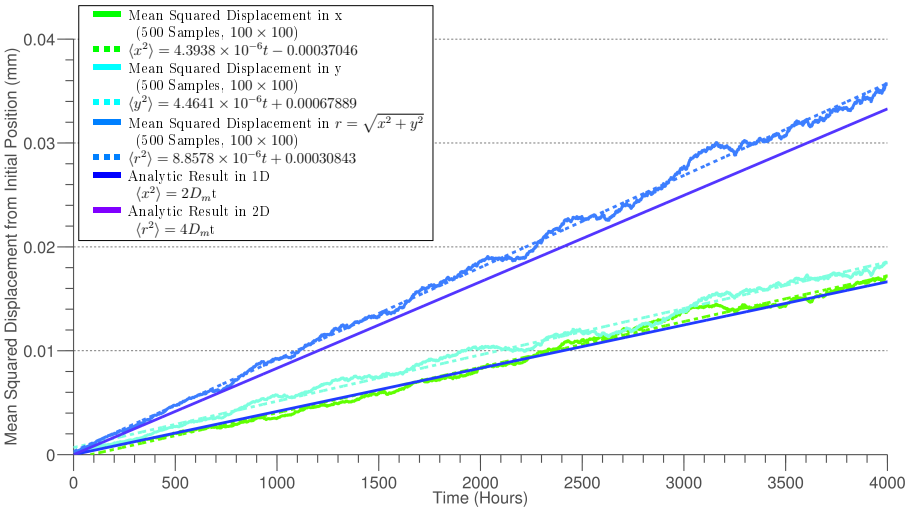

(b) Mean squared displacement of infected cell random walk with $D_m = 2.08 \times 10^{-6}\,\mathrm{mmhr}^{-1}$.

Figure 3.3: Mean squared displacement of uninfected and infected Cells in 2D for 500 samples, on a 100×100 compartment domain with $h = 0.01\,\mathrm{mm}$.

We solve the system (3.43) to give

$$\begin{aligned} n(t) &= \frac{n_0 - V_0}{1 - {}^{V_0}/_{n_0} \exp\left(-k_{react}\left(n_0 - V_0\right)t\right)}, && (3.45)\\ m(t) &= \frac{V_0\left(1 - \exp\left(-k_{react}\left(n_0 - V_0\right)t\right)\right)}{1 - {}^{V_0}/_{n_0} \exp\left(-k_{react}\left(n_0 - V_0\right)t\right)}, && (3.46)\\ V(t) &= \left(n_0 - V_0\right)\left(\frac{1}{1 - {}^{V_0}/_{n_0} \exp\left(-k_{react}\left(n_0 - V_0\right)t\right)} - 1\right). && (3.47) \end{aligned}$$

Algorithm 4 (Appendix A) can also be used in solving this system by setting the burst time $\tau > t_{max}$, and $k_{death} = 0$. If the typical experimental parameters outlined in Table 3.1 are used in this homogeneous case, the resultant virus concentration per compartment will be several orders of magnitude greater than the uninfected cell concentration. For the purpose of testing the SSA in the homogeneous case, we instead choose the virus and uninfected cell concentrations to be of the same order of magnitude. We pick a $100 \times 100 \times 1$ compartment grid with $h = 0.01$ mm, and we choose initial states for number of uninfected cells and virus particles per compartment, respectively, to be

$$\begin{aligned} \langle n_{ij}(0)\rangle &= 10 \text{ per compartment } \forall\,(i,j) \in \{100 \times 100\}, \\ V_{ij}(0) &= 80 \text{ per compartment } \forall\,(i,j) \in \{100 \times 100\}, && (3.48) \end{aligned}$$

where $\langle n_{ij}\rangle$ denotes mean number of particles of a species n at compartments $(i,j) \in \{N \times N\}$, such that the total number of particles in the system is given by $\sum_{i,j=1}^{N} n_{ij} = \langle n\rangle N^2$. Each particle is placed into compartment (i,j) at random, where i and j are sampled from a uniformly distributed random variable. Motivated by typical experimental parameters, we set $k_{react} = 10^{-8}$ mm^{3}hr^{-1}vir^{-1}, as outlined in the Section 3.3.

In addition to the SSA, our existing PDE Finite Difference-Fast Fourier Transform (FD-FFT) method in 1D (Section 2.4) can also be used to solve this problem. We choose the equivalent dimensionless parameters

$$\begin{aligned} k_B &= 0, \\ k_C &= \frac{1}{8}, \\ k_D &= 0, \\ \tau &= t_{max}, \\ [n]_0 &= \frac{10}{0.01^3}, \\ [V]_{max} &= \frac{80}{0.01^3}, && (3.49) \end{aligned}$$

and dimensionless initial conditions

$$\begin{aligned} [n](0) &= 1, \\ [m](0,a) &= 0, \\ [V](0) &= 1, \end{aligned} \tag{3.50}$$

for uninfected cell concentration $[n]$, infected cell concentration $[m]$ and virus particle concentration $[V]$.

Redimensionalising the 1D FD-FFT solution, and converting concentration into number of particles per compartment (of volume h^3). We compare the results of the SSA, analytic solution (3.45)-(3.47) and the FD-FFT solution for the number of particles per compartment in Figure 3.4. The choice of initial condition means that the uninfected cells are the limiting species in the reaction, and as expected, the number of virus particles reaches an equilibrium $V(t) \approx V(0) - n(0)$ for $t > 0$, once all uninfected cells have been used up in the bimolecular reaction.

This excellent agreement between four separate solutions suggests that the propensity scaling for the infection reaction in the SSA has been chosen appropriately, and further tests can now be performed for the remaining reactions.

3.4.3 Homogeneous reaction with virus death

We now look at a system with infection reaction (3.42) with an additional virus death reaction

$$\begin{aligned} \mathrm{n} + \mathrm{V} &\overset{k_{react}}{\rightarrow} \mathrm{m}, \\ \mathrm{V} &\overset{k_{death}}{\rightarrow} \emptyset. \end{aligned}$$

From the law of mass action, this system can be described in the continuous case by

$$\begin{aligned} \frac{dn}{dt} &= -k_{react} V n, \\ \frac{dm}{dt} &= k_{react} V n, \\ \frac{dV}{dt} &= -k_{react} V n - k_{death} V, \end{aligned} \tag{3.51}$$

which we consider for typical reaction rates

$$\begin{aligned} k_{react} &= 10^{-8}\ \mathrm{mm^3 hr^{-1} vir^{-1}}, \\ k_{death} &= 2.5 \times 10^{-2}\ \mathrm{hr^{-1}}, \end{aligned} \tag{3.52}$$

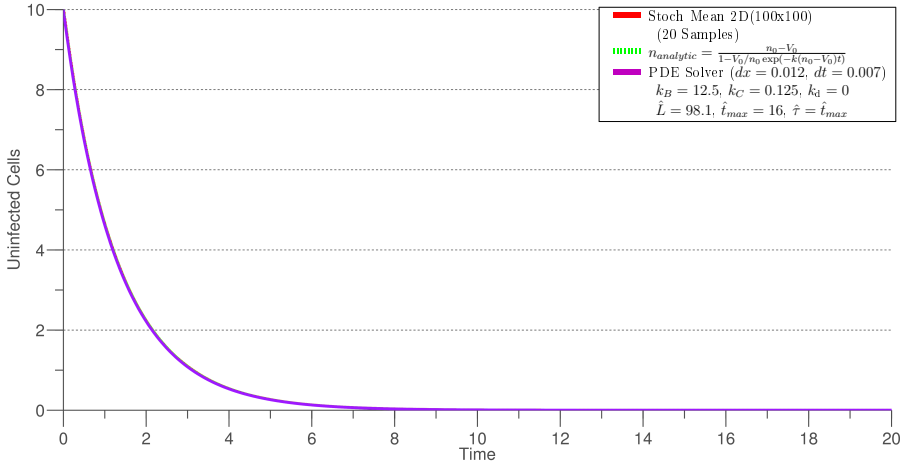

(a) Mean number of uninfected cells per compartment.

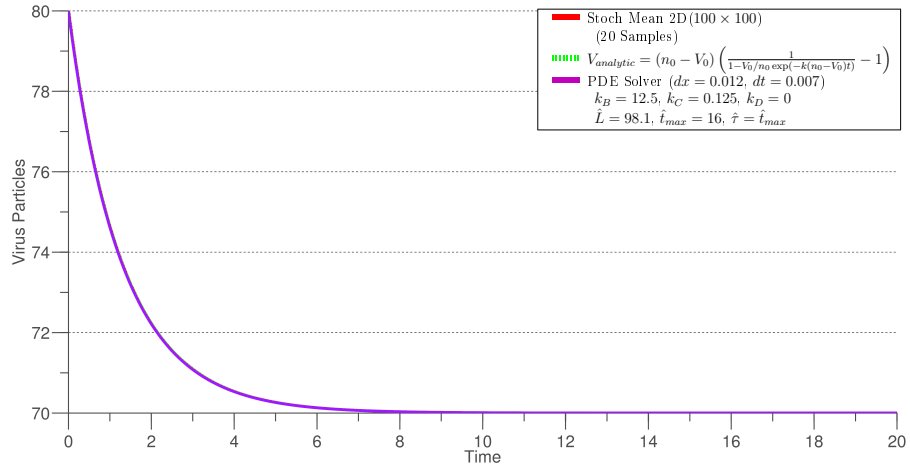

(b) Mean number of virus particles per compartment.

Figure 3.4: Comparison of SSA, FD-FFT PDE, and analytic solutions for homogeneous reaction with initial conditions $n(x, y, 0) = 10$, $V(x, y, 0) = 80$, $m(x, y, 0) = 0$, $k_{react} = {}^{10^{-8}}/_{h^3}\ \mathrm{mm^3 hr^{-1}}$, $h = 0.01\,\mathrm{mm}$.

as in Table 3.1. As before, we ignore the bursting of infected cells by setting the burst time $\tau > t_{max}$, and choose initial distributions for the SSA with $h = 0.01$ to be

$$\begin{aligned} \langle n_{ij}(0) \rangle &= 10 \text{ per compartment } \forall (i,j) \in \{100 \times 100\}, \\ V_{ij}(0) &= 80 \text{ per compartment } \forall (i,j) \in \{100 \times 100\}. \end{aligned} \tag{3.53}$$

Equations (3.51) no longer have a closed-form analytic solution for arbitrary initial conditions, but the equivalent system can be solved for concentration of species using MATLAB's inbuilt ODE solver, `ode45`.

We construct an equivalent continuum description for the FD-FFT solver by choosing initial conditions

$$\begin{aligned} [n](0) &= 1, \\ [m](0) &= 0, \\ [V](0) &= 1, \end{aligned} \tag{3.54}$$

for dimensionless concentrations of uninfected cells, infected cells and virus particles, respectively, and setting appropriate dimensionless parameters

$$\begin{aligned} k_B &= 0, \\ k_C &= \frac{1}{8}, \\ k_D &= \frac{2.5}{80}, \\ \tau &= t_{max}, \\ [n]_0 &= \frac{10}{0.01^3}, \\ [V]_{max} &= \frac{80}{0.01^3}. \end{aligned} \tag{3.55}$$

Redimensionalising the FD-FFT solution, and expressing the concentration of species as number of particles in the equivalent pseudo-1D system, we see that the results of 50 samples of the SSA agree perfectly with the FD-FFT solution, as well as a generic solution of (3.51) with MATLAB's inbuilt ODE solver, `ode45` from Figure 3.5. The presence of the additional virus death term in (3.51) results in removal of virus particles from the system even after all uninfected cells have reacted, and we find that $V(t) \approx V(10) \exp\left(-k_{death} t / h^3\right)$ for time $t > 10$.

Once again, perfect agreement between three separate methods of solution indicates that the propensity scaling for compartment width in the SSA are appropriate, and we now continue on to the test case with finite burst time in the next section.

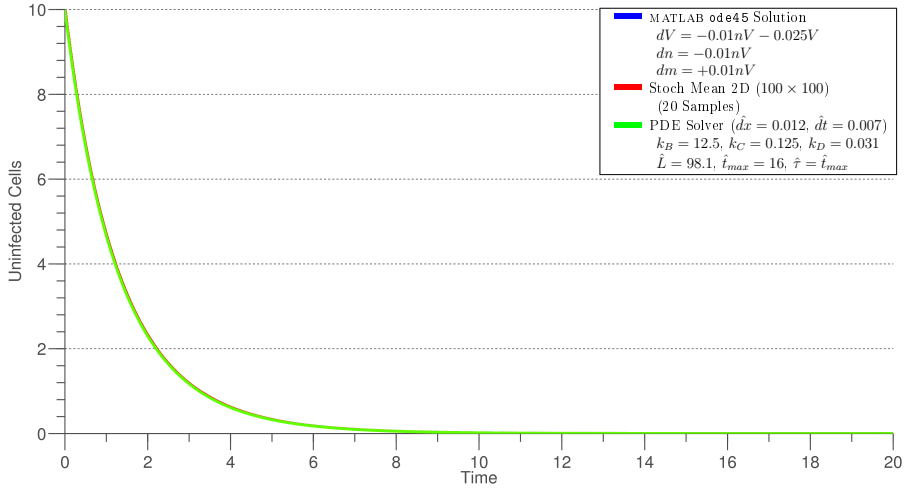

(a) Mean number of Uninfected Cells per compartment.

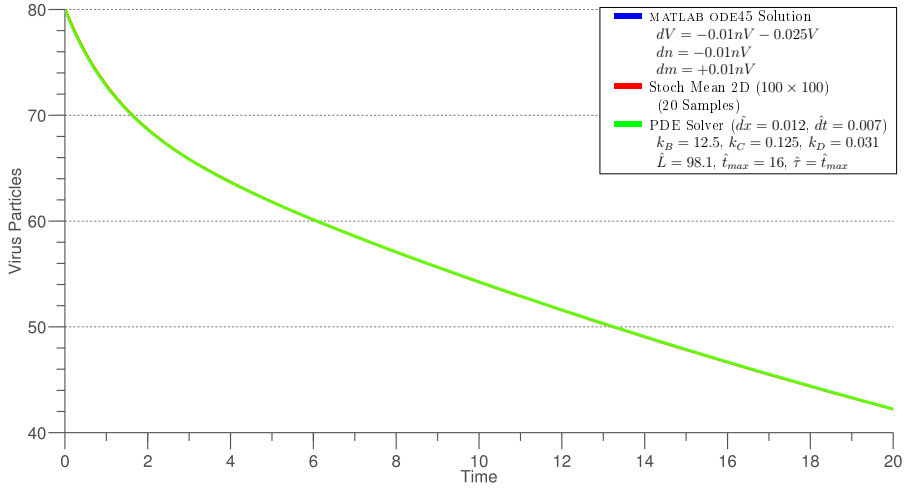

(b) Mean number of Virus Particles per compartment.

Figure 3.5: Comparison of SSA, FD-FFT and MATLAB `ode45` solution for homogeneous reaction with virus death with initial conditions $n(x, y, 0) = 10$, $V(x, y, 0) = 80$, $m(x, y, 0) = 0$, and $k_{react} = {}^{10^{-8}}/_{h^3}$ mm^{3}hr^{-1}, $k_{death} = 2.5 \times 10^{-2}$ hr^{-1}, $h = 0.01$ mm.

3.4.4 Reaction with burst

Finally, we consider the general case of virus-cell reactions outlined in (3.26)-(3.28) with a homogeneous initial condition on the number of virus particles, and random placement of uninfected cells. This is an extension of Section 3.4.3, incorporating the effects of infected cell burst, which adds α virus particles to the system at the final location of each infected cell of age τ, before removing the cell from the system. We choose a typical burst time of $\tau = 5$ hrs, and burst size $\alpha = 100$. A high number of virus particles are expected to be released from the first burst event, and so we choose the initial number of virus particles at $t = 0$ such that $\mathcal{O}(V) = \mathcal{O}(n)$, and choose initial distributions per compartment

$$\begin{aligned} \langle n_{ij}(0) \rangle &= 10 \text{ per compartment } \forall (i,j) \in \{100 \times 100\}, \\ V_{ij}(0) &= 8 \text{ per compartment } \forall (i,j) \in \{100 \times 100\}, \end{aligned} \tag{3.56}$$

where $\langle n \rangle$ denotes the mean number of particles of species n per compartment, with the total number of uninfected cells $\sum n(0) = N^2 \langle n(0) \rangle$, placed randomly in an $N \times N$ domain.

The dimensionless parameters for the continuum formulation of the equivalent system are

$$\begin{aligned} k_B &= 0, \\ k_C &= \frac{1}{8}, \\ k_D &= \frac{2.5}{8}, \\ \tau &= 0.4 t_{max}, \\ [n]_0 &= \frac{10}{0.01^3}, \\ [V]_{max} &= \frac{8}{0.01^3}, \end{aligned} \tag{3.57}$$

and initial conditions for dimensionless concentrations of uninfected cells, infected cells per unit age and virus particles

$$\begin{aligned} [n](0) &= 1, \\ [m](0,a) &= 0, \\ [V](0) &= 1. \end{aligned} \tag{3.58}$$

In the continuum formulation of this test case, no diffusion of uninfected or infected cells occurs. This implies that the Reaction Rate Equations describing (3.26)-(3.28) can be

written as

$$\begin{aligned} \frac{dn}{dt} &= -k_{react} V n, && (3.59) \\ \frac{dm}{dt} + \frac{dm}{da} &= 0, && (3.60) \\ \frac{dV}{dt} &= -k_{death} V - k_{react} V n + \alpha m\left(t, a = \tau\right), && (3.61) \end{aligned}$$

subject to initial conditions

$$\begin{aligned} n\left(0\right) &= n_0, \\ m\left(0, a\right) &= 0, \\ m\left(t, 0\right) &= k_{react} V\left(t\right) n\left(t\right), \\ V\left(0\right) &= V_0. \end{aligned} \qquad (3.62)$$

We solve (3.60) using the method of characteristics, and substitute for m into (3.61). Thus, the system is reduced to a set of Delay Differential Equations (DDE) with fixed delay, τ, of the form

$$\begin{aligned} \frac{dn}{dt} &= -k_{react} V n, \\ \frac{dV}{dt} &= -k_{death} V - k_{react} V n + \alpha V\left(t - \tau\right) n\left(t - \tau\right). \end{aligned} \qquad (3.63)$$

In addition to the our general FD-FFT PDE solver, this relatively simple system of DDEs can be solved using MATLAB's inbuilt `dde23` solver for fixed delay, τ. Comparing the SSA, FD-FFT and MATLAB `dde23` solutions for uninfected cells and virus particles per compartment (Figures 3.6a-3.6c), we initially see excellent agreement before the time of the first burst event at $t = \tau$, after which the number of remaining uninfected cells per compartment in the SSA is greater than that of the continuum solutions. As the continuum solutions given by the FD-FFT method and MATLAB's inbuilt delay differential equation solver, `dde23`, agree over the entire time interval, we focus on the compartment-based SSA in an attempt to understand the cause of the disagreement. It is important to note that the uninfected and infected cells solutions agree for $t \in [0, \tau]$, at which point the first generation of infected cells burst. Despite this, the number of virus particles per compartment agree with the continuum solutions for $t \in [\tau, 2\tau]$, implying that the discrepancy in uninfected cells is a consequence of a reduced rate of reaction between uninfected cells and virus particles in the SSA, caused by the release of virus particles at the first burst time $t = \tau$, and only becoming apparent in the virus concentration after the second generation of infected cells (added over $t \in [\tau, 2\tau]$) has burst.

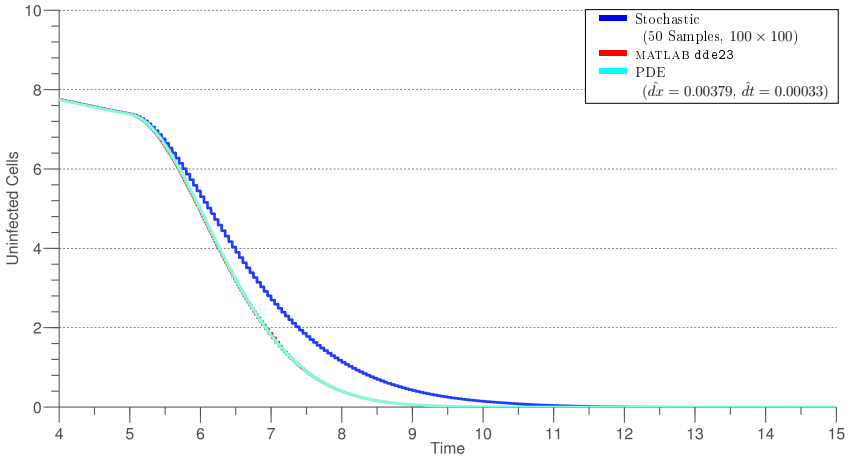

(a) Mean number of uninfected cells per compartment.

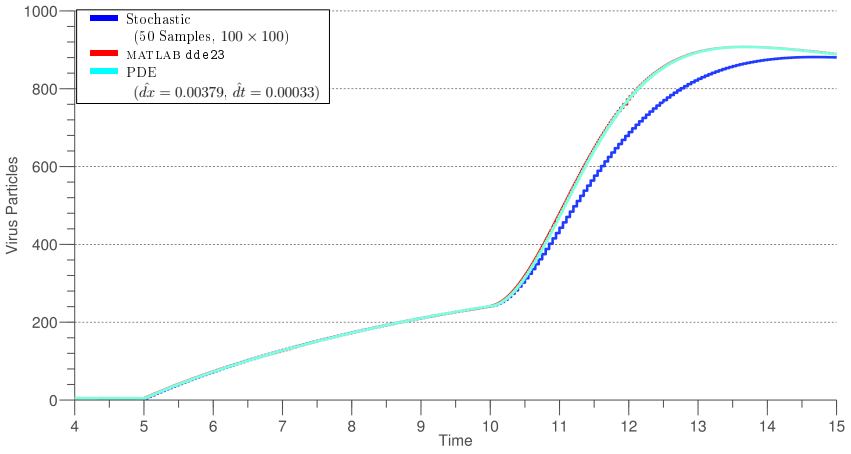

(b) Mean number of virus particles per compartment.

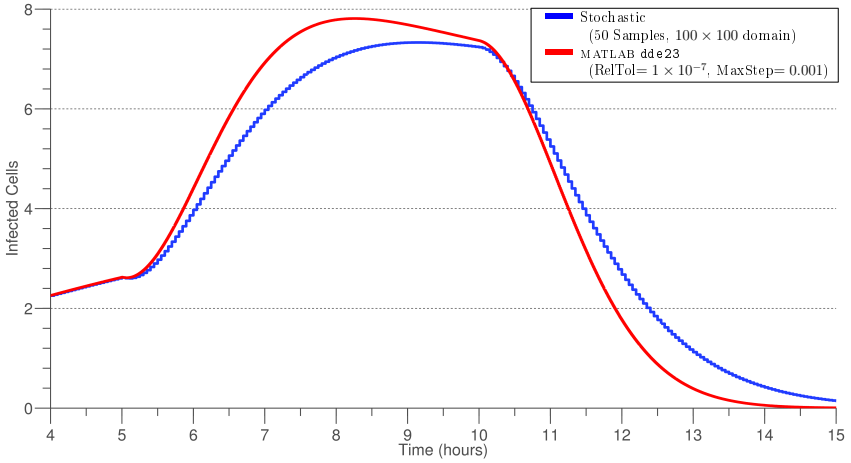

(c) Mean number of infected cells per compartment.

Figure 3.6: Comparison between SSA and MATLAB `dde23` solutions for homogeneous reaction with virus death and infected cell burst with initial state $V(0) = 8$, $n(0) = 10$ and $\tau = 5$, $k_{react} = {}^{10^{-8}}/_{h^3}$ mm^{3}hr^{-1}, $\alpha = 100$, $k_{death} = 2.5 \times 10^{-2}$ hr^{-1}, $h = 0.01$ mm.

3.4.4.1 Dependence on compartment size

So far, we have chosen the physically-motivated compartment size of $h = 0.01$ mm in our SSA simulations. We now look at the effects of varying compartment size in the previous test case in Section 3.4.4.

As each compartment has volume h^3, the 2D domain has total volume $Nh \times Nh \times h$. Therefore, by varying compartment size, we must adjust the initial states accordingly, so that particle number per unit volume is conserved. Running 50 simulations for $h = \{0.01, 0.02, 0.05\}$ mm on $\{100 \times 100, 50 \times 50, 20 \times 20\} \times 1$ compartment domains, respectively, we see that *increasing* compartment size results in better agreement with the continuum solution given by MATLAB's `dde23` solver (Figures 3.7a-3.7c), with the $h = 0.05$ mm results being nearly identical to the continuum solution.

From the compartment size comparison in Figure 3.7, we see that the effective rate of reaction between uninfected cells and virus particles in the SSA case changes with compartment size as soon as the system becomes inhomogeneous after the first burst event at time $t = \tau$. In the SSA, uninfected cells can either jump to an adjacent compartment or react with virus particles in the same compartment. This suggests that it is the local nature of burst events, where infected cells are removed and release many virus particles in the process, that results in a reduced reaction rate between uninfected cells and virus particles as compartment size is decreased. We test this hypothesis by modifying the SSA so that each virus particle created as a result of an infected cell burst is placed in random compartment, rather than the same compartment as the infected cell.

Running 50 simulations of a modified version of the SSA for $h = 0.01$ mm on a $100 \times 100 \times 1$ compartment domain where the location of virus particles released via burst events is chosen at random, we see perfect agreement between the SSA and MATLAB `dde23` continuum solutions (Figure 3.8). Although the burst of infected cells in the SSA is a deterministic process occurring after a fixed period of time, the time of infection, governed by the bimolecular reaction between uninfected cells and virus particles, is a random process. This introduces a level of inhomogeneity into the system, and since each infected cell releases α particles per burst, which is typically greater than the number of uninfected cells per compartment, the reaction propensity in each compartment becomes strongly dependent on the number of virus particles per compartment.

This is an inherent problem in using lattice-based simulations for reaction-diffusion systems, and Isaacson (2009) showed that in the limit $h \to 0$, the reaction propensity scaling breaks down to the point where no reactions will occur, recovering pure diffusion in the system.

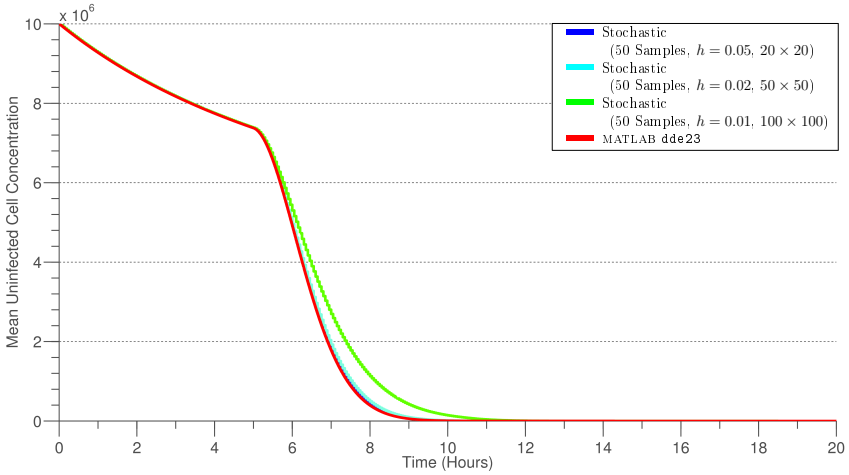

(a) Mean uninfected cell concentration per compartment.

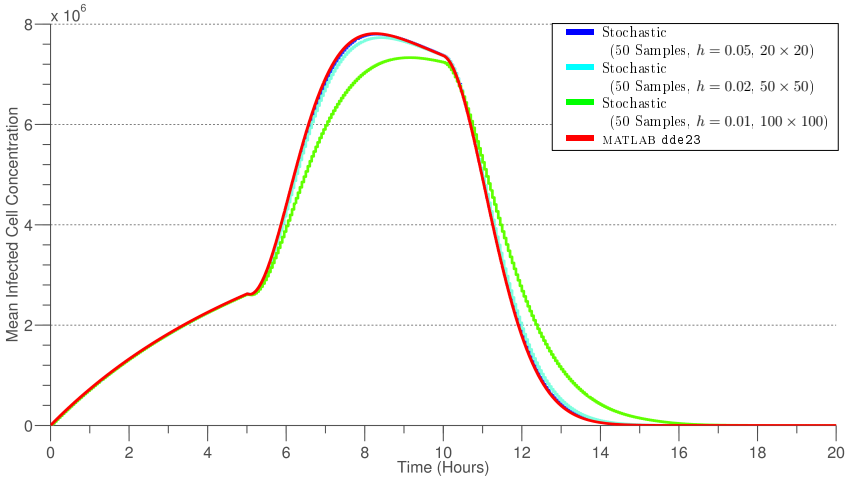

(b) Mean infected cell concentration per compartment.

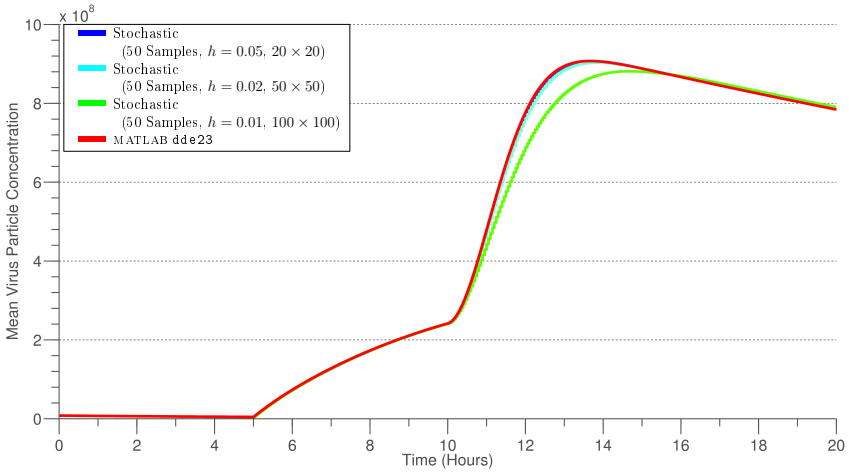

(c) Mean virus particle concentration per compartment.

Figure 3.7: Comparison of MATLAB `dde23` solution and SSA with $h = \{0.01\,\text{mm}, 0.02\,\text{mm}, 0.05\,\text{mm}\}$ with initial conditions ${}^{V(0)}/_{h^3} = 8 \times 10^6\ \text{mm}^{-3}$, ${}^{n(0)}/_{h^3} = 10 \times 10^6\ \text{mm}^{-3}$, and $\tau = 5$, $k_{react} = {}^{10^{-8}}/_{h^3}\ \text{mm}^3\text{hr}^{-1}$, $\alpha = 100$, $k_{death} = 2.5 \times 10^{-2}\text{hr}^{-1}$.

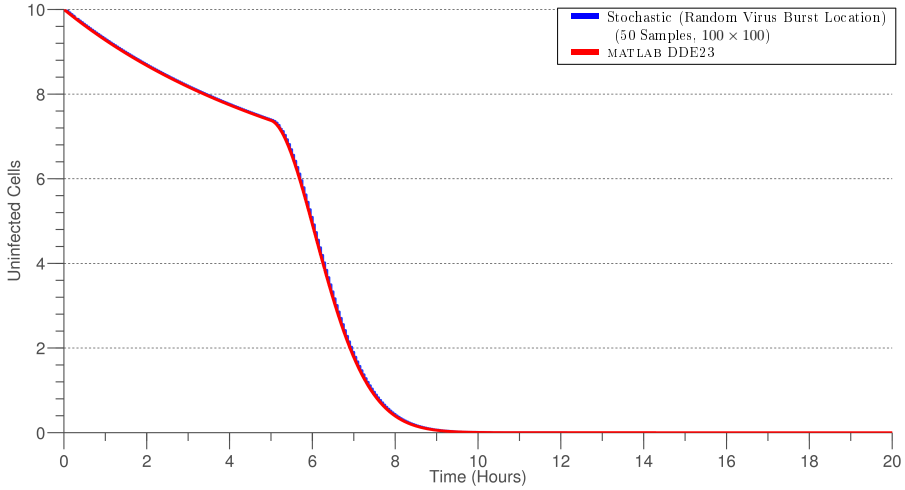

(a) Mean number of uninfected cells per compartment.

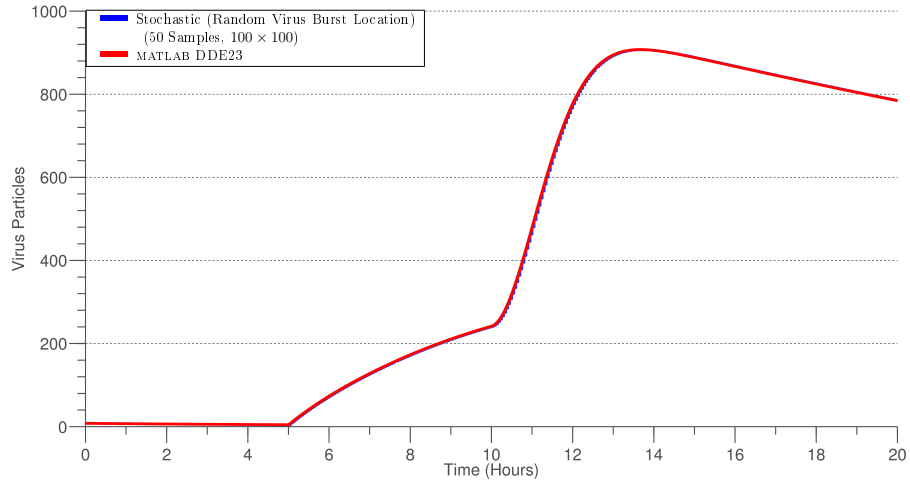

(b) Mean number of virus particles per compartment.

Figure 3.8: Comparison of SSA simulations and MATLAB `dde23` solution for random burst location with initial states $V(0) = 8$, $n(0) = 10$ and $\tau = 5$, $k_{react} = {}^{10^{-8}}/_{h^3}$ $\mathrm{mm}^{-3}\mathrm{hr}^{-1}$, $\alpha = 100$, $k_{death} = 2.5 \times 10^{-2}$ hr^{-1}.

3.5 Reconciling the continuum and stochastic models

For typical parameter values in Table 3.1, we have seen that the SSA simulations disagree with the FD-FFT solution to the equivalent continuum model. Previous work by Isaacson (2009) showed for compartment-based reaction-diffusion systems, no possible scaling of reaction propensity as a function of compartment size was possible in the limit $h \to 0$. Erban and Chapman (2009) extended this approach, and showed that for an on-lattice SSA representing an inhomogeneous system of bimolecular reactions of diffusing species, there exists a threshold compartment size h_{crit} such that for $h > h_{crit}$, the correct reaction propensity is

$$\lambda = \frac{D_n k}{D_n h^3 - \beta k h^2},$$

in the fully 3D case, where the spatial domain consists of 6-connected compartments. This scaling was shown to be a general case of (3.37), recovering the classical propensity scaling $\lambda = \frac{k}{h^3}$ in the limit $D_n h^3 \gg \beta k h^2$.

A similar result for 2D diffusion a system of 4-connected compartments is stated in Leier and Marquez-Lago (2011) without rigorous proof. In the following section, we make use of the derivation in Erban and Chapman (2009), to derive the equivalent correction term for the 2D case, where the spatial domain consists of 4-connected compartments.

3.5.1 Analytic reaction propensity correction in 2D

In the on-lattice SSA, particles undergo random walks by jumping between connected compartments. In the two-dimensional case of a domain of $N \times N \times 1$ compartments, each of width h, particles are connected to four neighbours. Following the method of Erban and Chapman (2009), we consider the system of reactions

$$\begin{aligned} \mathrm{n}_{ij} + \mathrm{V}_{ij} &\xrightarrow{\tilde{k}} \mathrm{m}_{ij} \\ \mathrm{n}_{ij} &\xrightarrow{D_n/h^2} \mathrm{n}_{ij+\vec{e}} \\ \mathrm{V}_{ij} &\xrightarrow{D_m/h^2} \mathrm{V}_{ij+\vec{e}} \\ \mathrm{m}_{ij}|_{a=\tau} &\xrightarrow{k_{burst}} \mathrm{V}_{ij} \end{aligned}$$

for compartment indices $(i,j) \in I_{\text{all}}$, 2D reaction rate $\tilde{k}$, inter-compartment jump rates D_n/h^2, D_m/h^2 and virus creation rate k_{burst} for uninfected cells, infected cells and virus particles n, m and V respectively, and jump offset vector $\vec{e} \in \vec{E}_{ij}$, the indice offset from the set of all neighbouring compartments into which a jump is possible in a 2D domain. Although virus particles do not move, we can consider the movement of infected cells, followed by an infected burst releasing virus particles to be equivalent to a net diffusion of virus particles with inter-compartment jump rate D_m/h^2.

We follow the exact procedure in Erban and Chapman (2009) to obtain the 2D propensity for a compartment-based reaction-diffusion system in Appendix B as

$$\lambda = \frac{(D_n + D_m)\, N^2 \tilde{k}}{(D_n + D_m) + \beta h^2 N^2 \tilde{k}}, \tag{3.64}$$

where $\tilde{k} = \frac{k_{react}}{h}$ is a reaction rate per unit z-direction, and β is given by

$$\beta = \frac{1}{2N^2} \sum_{(i,j)\neq(0,0)}^{N-1} \frac{1}{2 - \cos\left(i\pi/N\right) - \cos\left(j\pi/N\right)}, \tag{3.65}$$

which depends on number of compartments, N. This result agrees with the correction presented (but not rigorously derived) in Leier and Marquez-Lago (2011), and for our choice of $N = 100$, $\beta \approx -1.0569$.

In the limit $D_n \gg \beta\tilde{k}$, the correction term (3.64) recovers the classical propensity scaling k_{react}/h^3 outlined in Section 3.2.4.

Using the expression for corrected bimolecular reaction propensity in 2D for $D_n = 2.08 \times 10^{-5}$ mm^{2}hr^{-1}, $D_m = 0.1D_n$ and $k_{react} = 10^{-8}$ mm^{3}hr^{-1}, we find that even for the case of smallest compartment size $h = 0.01$, the corrected propensity value λ is only 5% greater than the value given by the classical k_{react}/h^3 scaling, which is insufficient in correcting the greatly reduced rate of reaction.

This result was confirmed numerically with a parameter sweep of the SSA for a range of values of k_{react} in the case of homogeneous initial distributions, and no value of k_{react} matched the continuum solutions for number of uninfected cells and virus particles in time. With this failure to predict the net reaction rate analytically, we move on to numerical simulations of the full model with inhomogeneous initial distributions, and the effects of compartment size on the behaviour of the model.

3.6 Inhomogeneous case in pseudo-1D

So far, we have looked at reconciling the effective reaction rates in the on-lattice discrete and continuum models for homogeneous initial conditions. We now look at full model: the inhomogeneous, pseudo-1D case of the SSA with spatial distribution of the initial injection of virus particles in the pseudo-1D SSA case chosen as in Figure 3.2b, allowing for comparison with the continuum model. For the remainder of this section, unless otherwise

stated, we will run simulations with the physical parameters

$$\begin{aligned} k_{react} &= 10^{-8}\ \text{mm}^3\text{hr}^{-1}\text{vir}^{-1}, \\ k_{death} &= 2.5 \times 10^{-2}\ \text{hr}^{-1}, \\ D_n &= 2.08 \times 10^{-5}\ \text{mm}^2\text{hr}, \\ D_m &= 0.1 D_n, \\ V &= 8 \times 10^9\ \text{vir mm}^{-3}, \\ n &= 1 \times 10^6\ \text{cells mm}^{-3}, \\ \tau &= 5\ \text{hrs}, \\ \alpha &= 100\ \text{vir per burst} \\ t_{max} &= 500\ \text{hrs}, \end{aligned} \tag{3.66}$$

as outlined in Table 3.1. When simulating this system with the SSA in Appendix A, we must also consider the width and number of compartments, corresponding to a choice of spatial domain. In addition to the compartment size choice of $h = 0.01$ mm, motivated previously, we also look at the case of $h = 0.02$ mm to determine the sensitivity of results to compartment size, on the basis of the results from Section 3.4.4. As the SSA simulates a 3D domain of volume $Nh \times Nh \times h$, the initial distributions for the $h = 0.01$ and $h = 0.02$ mm cases must be scaled to preserve concentration of virus particles. Because of the small number of compartments, particularly in the $h = 0.02$ mm case, we restrict the initial location of virus particles to a 0.02 mm width, allowing for comparison between the two discretizations, as well as with an equivalent PDE system. Therefore, in addition to these physical parameters, we choose

$$\begin{aligned} N &= 100\ \text{compartments}, \\ \langle n_{ij}(0) \rangle &= 1\ \text{per compartment}, \\ m_{ij}(0) &= 0\ \text{per compartment}, \\ V_{ij}(0) &= \begin{cases} 8000\ \text{per compartment} & \text{for } i \in [49, 50],\ j \in [1, N] \\ 0, & \text{otherwise} \end{cases}, \end{aligned} \tag{3.67}$$

for the $h = 0.01$ mm SSA case, and

$$\begin{aligned} N &= 50 \text{ compartments}, \\ \langle n_{ij}(0) \rangle &= 8 \text{ per compartment}, \\ m_{ij}(0) &= 0 \text{ per compartment}, \\ V_{ij}(0) &= \begin{cases} 64000 \text{ per compartment}, & \text{for } i = 25,\ j \in [1, N] \\ 0, & \text{otherwise} \end{cases} \end{aligned} \tag{3.68}$$

for the $h = 0.02$ mm SSA case, where $\langle n_{ij} \rangle$ denotes mean number of particles of a species n at compartments $(i, j) \in \{N \times N\}$. For the equivalent continuum model, we calculated dimensionless parameters as in Chapter 2, with dimensionless initial conditions for concentrations of species

$$\begin{aligned} [n](0, x) &= 1, \\ [m](0, x) &= 0, \\ [V](0, x) &= \begin{cases} 1, & \text{for } 0.49 \leq x \leq 0.51 \\ 0, & \text{otherwise} \end{cases}, \end{aligned} \tag{3.69}$$

where the [.] denotes concentration.

3.6.1 Compartment size dependence

The homogeneous test case in Section 3.4.4 illustrated that the compartment-based SSA for homogeneous initial distributions disagrees with the continuum model due to lower-than-expected reaction propensity for smaller choices of compartment size. We now briefly show the effects of compartment size on two key quantities: the speed of virus wave of propagation, and the number of particles in the system for inhomogeneous initial distributions of virus particles.

3.6.1.1 Travelling wave speed

The wave speed of virus particle propagation is one of the key observations of interest. However, determining an accurate value for the travelling wave speed of virus particles in SSA simulations is more difficult than in the continuum case due to the stochastic noise. For a typical set of parameters, s samples of the SSA run on a 2D $N \times N$ compartment grid with spatially-homogeneous initial distributions in the y-direction can be considered equivalent to sN 1D simulations, averaged along the y-axis. As the time to next reaction (as given by (3.24)) is random, each sample must be interpolated to a regular time grid

before a mean over s samples can be calculated. Once a mean of interpolated pseudo-1D samples has been calculated, the wave speed can be estimated by looking at the index of the compartment with the greatest number of virus particles. For an inhomogeneous initial distribution where virus particles are placed in the centre compartment, we find that the initial stripe of virus particles eventually separates into left-moving and right-moving travelling fronts. The point at which virus peak splits into left- and right-moving travelling fronts is found by searching for the time index corresponding to the maximum jump in peak virus position of interpolated pseudo-1D virus data. The peak virus position data is smoothed in time, and a line of best fit is calculated from the peak split position to the point where the gradient of the smoothed data begins to decrease (corresponding to boundary interactions in the system).

This procedure is illustrated in Figure 3.9, where lines of best fit (dashed) for virus displacement in time are plotted for the left- and right-moving virus waves, and boundary interactions are characterised by a decreasing gradient for times $t > 500$ hrs. We also note that due to the stochastic nature of the individual discrete simulations, the left- and right-moving fronts are not always symmetric within a simulation, and so the travelling wave speed, given by the gradient of the lines of best fit, can be biased towards a particular direction. An example of this can be seen in the case of $h = 0.01$ mm in Figure 3.9, where the right-moving wave is a factor of 1.8 times greater than the left-moving wave, most likely due to an asymmetry of virus particles early in the simulation resulting in a "die-out" scenario for the left-moving wave. As the net wave speed is calculated from the mean of the left- and right-moving waves, care must be taken when looking at mean behaviour of SSA simulations.

As with the homogeneous case, we find that choice of compartment size, h, affects the quantitative results of the simulations. For the case of the smallest physically-justified compartment size $h = 0.01$ mm, corresponding to the typical size of a cell, the wave speed is a factor of $2 - 4$ times less than that predicted by the continuum PDE solution. While doubling the compartment size to $h = 0.02$ mm recovers a wave speed within $10 - 15\%$ of that given by solution to the equivalent continuum model, the same cannot be said for the exact spatial distribution of virus particles (not shown). In general, we find that the width of each travelling front is less localised in the stochastic case, characterised by a larger full width half peak value than the more tightly bound continuum solution. This also affects the total number of virus particles in the system, as seen in the next section.

3.6.1.2 Number of particles in system

Although the wave speed in the $h = 0.02$ case roughly matches that of the PDE solution, there are still discrepancies between the inhomogeneous discrete and continuum models. Another useful metric for the progress of therapy is the number of virus particles in the

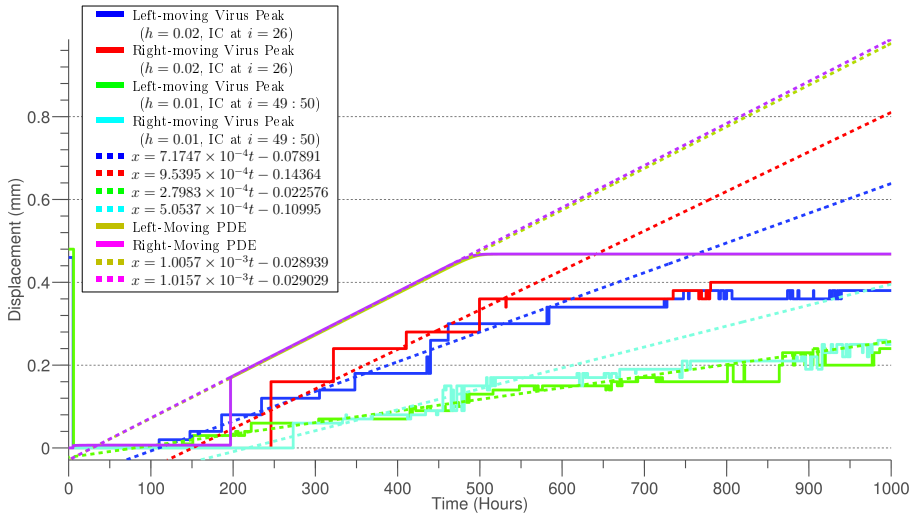

Figure 3.9: Comparison of mean displacement of virus peak between PDE solution and SSA with $h = \{0.01, 0.02\}$ mm.

system at any given time. Looking at the mean concentrations of uninfected cells and virus particles over the entire 1D domain (Figure 3.10), we see that there is a large discrepancy between the SSA and PDE results. Most notably, we see that the concentration of uninfected cells in the continuum case reduces at a constant rate, eventually resulting in the eliminations of uninfected cells in the system (Figure 3.10a). This rate of removal of uninfected cells is related to the steady state of virus particle concentration in the system, shown in Figure 3.10b. We also note that the mean virus particle concentration for the SSA cases with $h = \{0.01, 0.02\}$ mm is lower than the continuum case, and in contrast to the continuum case, does not appear to reach a steady state.

Qualitatively, the higher number of uninfected cell and lower virus particle concentrations in the inhomogeneous case agree with our previous conclusion of reduced effective reaction rate due to virus localization via infected cell bursts. This is further illustrated in the next section by removing the compartment dependence of virus particles by introducing a hybrid continuum-SSA.

3.6.2 Hybrid method

As illustrated in Section 3.4.4, the reduced effective reaction rate in the bimolecular reaction between uninfected cells and virus particles in the compartment-based SSA occurs due to virus burst localisation. In the homogeneous test case, this was verified by randomising the location of the virus particles entering the system from infected cell bursts. For the inhomogeneous case, the location of virus particles determines key behaviour in the system, such as the speed of wave propagation.

To illustrate this, we consider an artificial version of the SSA in which the number of virus particles in the system is given by the continuum solution. We solve the continuum

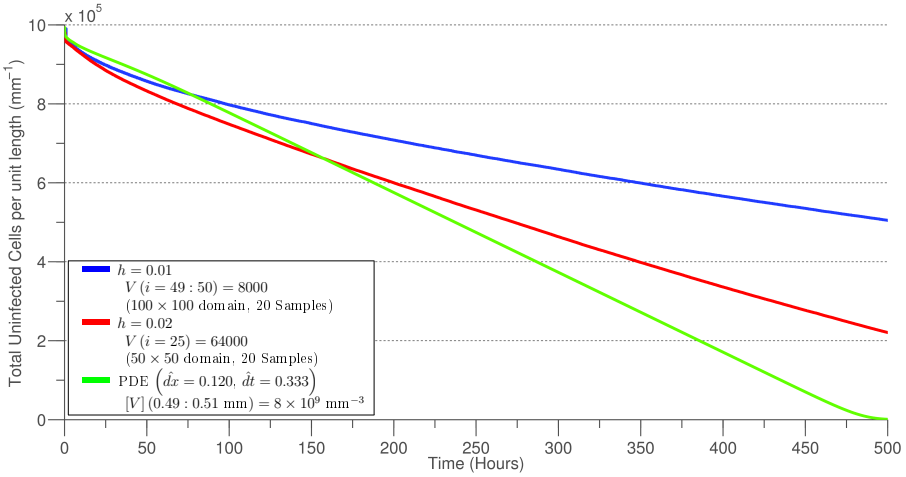

(a) Uninfected cell concentration in 1D for SSA with $h = 0.01$ mm (blue), $h = 0.02$ mm (red) and PDE (green).

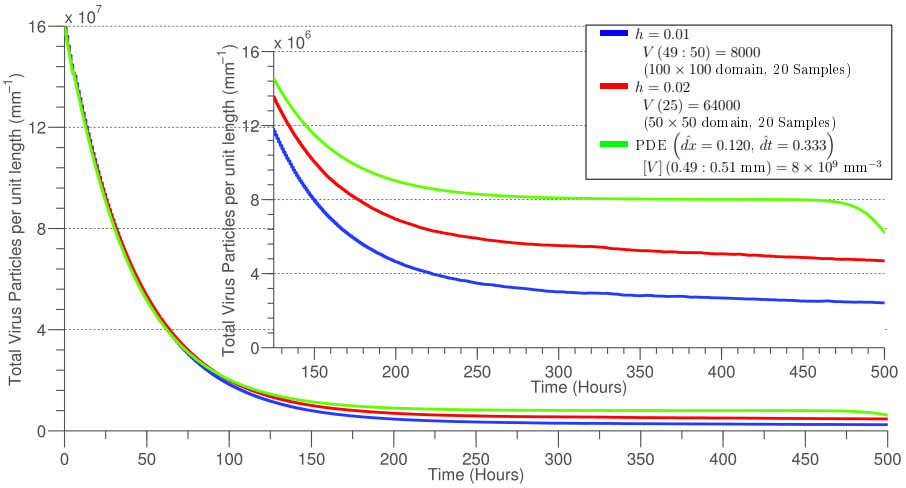

(b) Virus particle concentration in 1D for SSA with $h = 0.01$ mm (blue), $h = 0.02$ mm (red) and PDE (green), with magnified inset for $t \in [125, 500]$.

Figure 3.10: Comparison of 1D concentrations of SSA with $h = 0.01$ mm, $h = 0.02$ mm and FD-FFT solution to equivalent system of PDEs.

system of equations in Chapter 2 with the FD-FFT method for dimensionless parameters calculated from (3.66) and dimensionless initial conditions (3.69). The solution for the dimensionless concentration of virus particles is redimensionalised, and spatial domain changed to a histogram consisting of 100 compartments. This binned concentration is then converted to an equivalent number of particles in a $100 \times 100 \times 1$ compartment domain of compartment width $h = 0.01$, and saved at each time output.

By prescribing the number of virus particles in a compartment at given time t, the effective reactions required to be simulated by the SSA are reduced to

$$\begin{aligned} \mathrm{n}_i &\overset{2D_n/h^2}{\rightarrow} \mathrm{n}_{i\pm1}, \\ \mathrm{n}_i &\overset{V_i k_{react}/h^3}{\rightarrow} \mathrm{m}_i, \\ \mathrm{m}_i &\overset{2D_m/h^2}{\rightarrow} \mathrm{m}_{i\pm1}, \end{aligned} \tag{3.70}$$

where V_i is the number of virus particles in each compartment, as given by the binned FD-FFT solution. This is equivalent to reducing the bimolecular reaction between n and V to a decay reaction for n, with a weighted propensity for each compartment and time step. Plotting the distribution of uninfected cells in space for the hybrid SSA with $h = 0.01$ mm and continuum FD-FFT solutions (Figure 3.11), we see good agreement between the two approaches. Similarly, Figure 3.12 shows agreement between the solutions for mean concentration of uninfected cells in time. This is in stark contrast to the rate of change of uninfected cells for the regular SSA in Figure 3.10a, confirming that virus compartmentalization is the cause of the divergent solutions in the inhomogeneous case.

3.6.3 Wave speed dependence on reaction rate in PDE

Returning to the original SSA, we now focus on the case of $h = 0.01$ mm with a pseudo-1D initial distribution of virus particles. The comparison between compartment sizes in Figure 3.9 showed that the wave speed of virus propagation decreased for smaller compartment size, due to the lower than expected reaction propensity between uninfected cells and virus particles.

Calculating 20 samples of the SSA for a range of reaction rates $k_{react} = \{0.2, 0.4, 0.8, 1, 1.25, 1.5, 4, 8, 16, 25\} \times 10^{-8}$ mm^{3}hr^{-1}vir^{-1}, we obtain the mean peak virus particle positions shown in Figure 3.13, qualitatively showing that the wave speed increases with k_{react}, as expected. We calculate lines of best fit of the form $x = at + b$ using the methodology outline at the beginning of Section 3.5, with the results of this shown in Table 3.2.

Despite the difficulties in obtaining a precise value for the wave speed of SSA data, this parameter sweep in k_{react} shows that even for values of k_{react} an order of magnitude greater than the baseline value of 10^{-8} mm^{3}hr^{-1}vir^{-1} used in the equivalent continuum

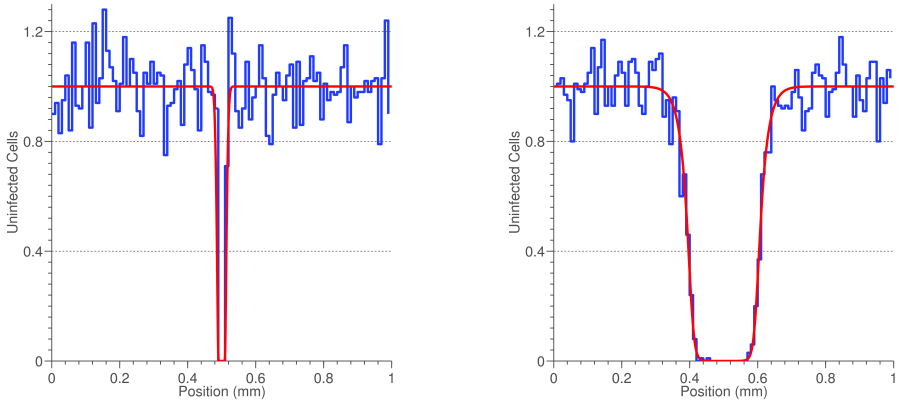

(a) Time $t = 1$ hrs. (b) Time $t = 101$ hrs.

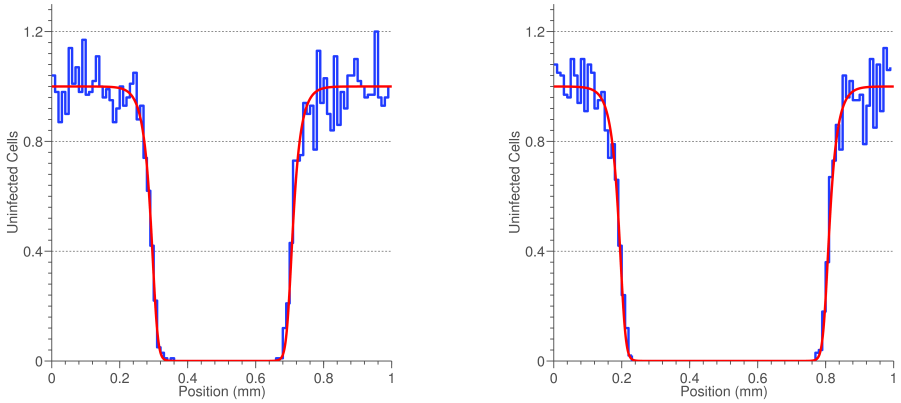

(c) Time $t = 201$ hrs. (d) Time $t = 301$ hrs.

Figure 3.11: Comparison of spatial distribution of uninfected cells in time for hybrid deterministic virus/SSA with $h = 0.01$ mm (blue) and PDE FD-FFT Solution (red).

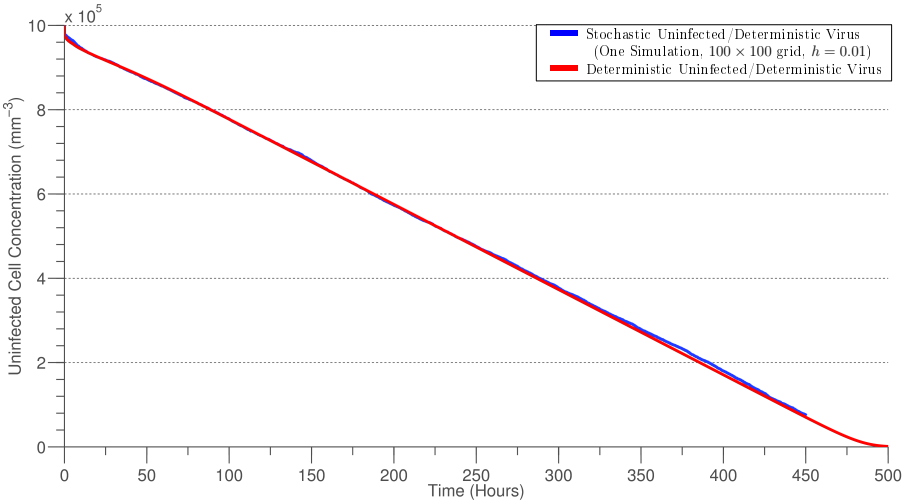

Figure 3.12: Comparison of mean uninfected cell concentration in system for hybrid deterministic virus/SSA with $h = 0.01$ mm (blue) and PDE FD-FFT solution (red).

model, the wave speed of from the SSA with compartment size $h = 0.01$ mm is still less than that predicted by the PDE model.

A similar parameter sweep in k_{react} for the equivalent PDE system showed that the wave speed increased logarithmically with k_{react} (Figure 3.14a), with a line of best fit for wave speed of the form $c = a\log(k_{react}) + b$ giving a good approximation to the data points. Extrapolating this fit to smaller values of k_{react}, we find that the effective reaction rate required in the continuum model to match the wave speed in the SSA for $k_{react} = 10^{-8}$ mm^{3}hr^{-1}vir^{-1} is in the interval $k_{react} = [0.875, 1.25] \times 10^{-9}$ mm^{3}hr^{-1}vir^{-1}.

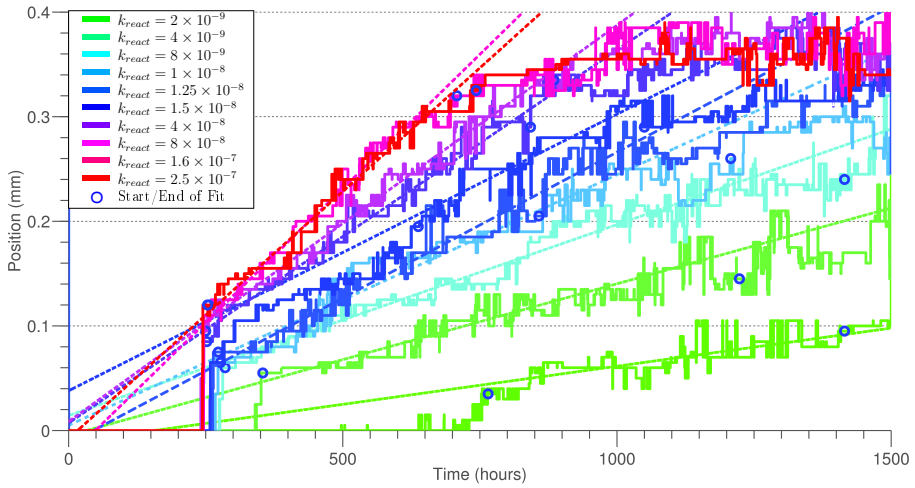

Figure 3.13: Mean displacement of virus particles over 20 samples (solid) and lines of best fit (dashed) in SSA on 100×100 compartment domain with $h = 0.01$ mm and pseudo-1D initial distribution $V(i = \{49, 50\}, j \in [1, N]) = 8000$.

k_{react} $\left(\text{mm}^3\text{hr}^{-1}\text{vir}^{-1}\right)$	Line of Best Fit $x = at + b$ for peak Virus displacement	
	a $\left(\text{mmhr}^{-1}\right)$	b (mm)
2×10^{-9}	7.2913×10^{-5}	-1.1462×10^{-2}
4×10^{-9}	1.4501×10^{-4}	-4.7600×10^{-3}
8×10^{-9}	1.8256×10^{-4}	1.4350×10^{-2}
1×10^{-8}	2.3954×10^{-4}	5.0116×10^{-3}
1.25×10^{-8}	2.7865×10^{-4}	-1.2590×10^{-2}
1.5×10^{-8}	2.6436×10^{-4}	3.8014×10^{-2}
4×10^{-8}	3.5661×10^{-4}	7.1866×10^{-3}
8×10^{-8}	3.7888×10^{-4}	8.5446×10^{-3}
1.6×10^{-7}	5.1281×10^{-4}	-2.4997×10^{-2}
2.5×10^{-7}	4.7248×10^{-4}	-7.7075×10^{-3}

Table 3.2: Lines of best fit for displacement of virus particles in time from Figure 3.13.

3.6.4 Empirical scaling of effective reaction rate

We have seen that the corrected propensity of the reaction-diffusion process given by the analytic expression in Section 3.5 fails to predict the true value of the reduced effective

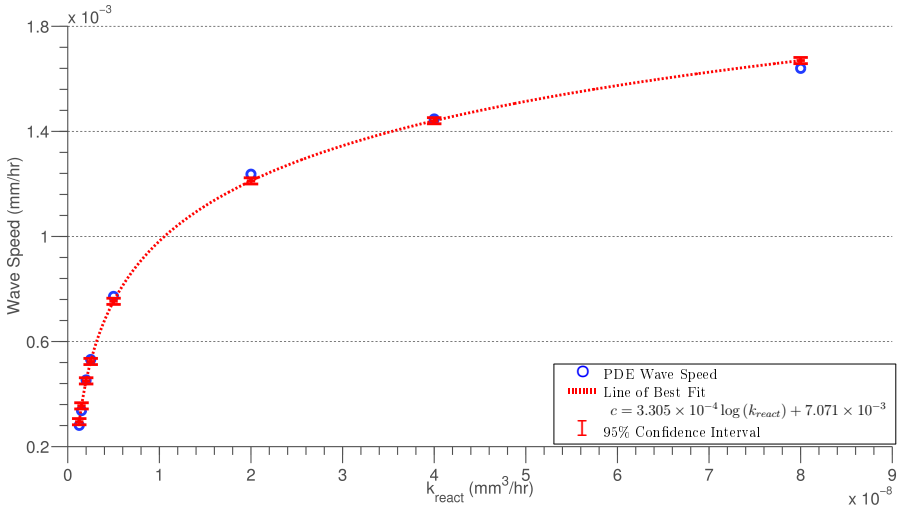

(a) Wave speed dependence on k_{react} given by FD-FFT solution to PDE system.

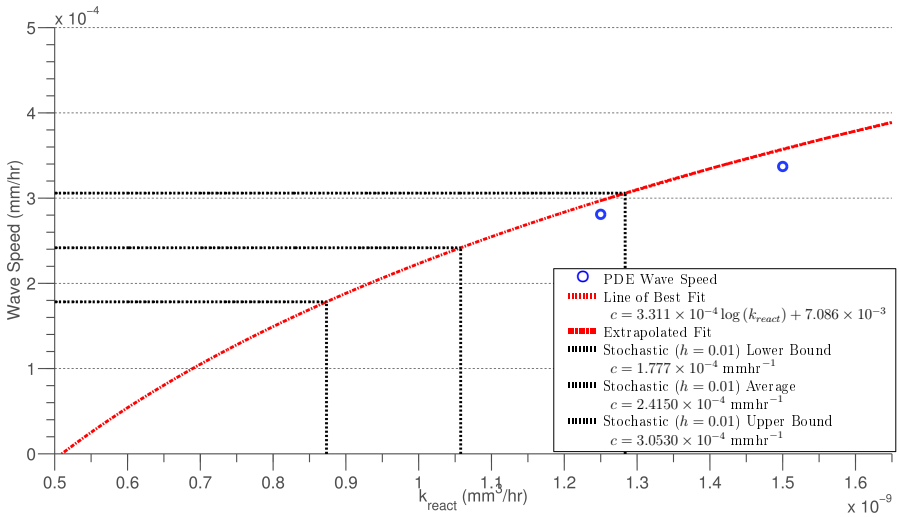

(b) Effective stochastic reaction rate estimate for $k_{react} = 10^{-8}$ mm^{3}hr^{-1}vir^{-1}, $h = 0.01$ mm.

Figure 3.14: Logarithmic dependence of wave speed on k_{react} for PDE system, with an extrapolated fit showing the predicted effective reaction rate for the $h = 0.01$ mm SSA case from Figure 3.9. The dashed lines represent the left- and right-moving wave speed, as well as the mean calculate wave speed.

reaction rate in the SSA. An alternative approach to determining this effective reaction rate for a given compartment size is to do a parameter sweep of the system using the SSA and FD-FFT solver and compare key outputs from each solution.

Motivated by the wave speed dependence on k_{react} in the continuum solution (Figure 3.14a), we look for a similar relation in the stochastic wave speed date presented in Table 3.2 for a SSA with compartment size $h = 0.01$ mm. Using this calculated wave speed, the semi-log plot of wave speed dependence on k_{react} in Figure 3.15b shows that a line-of-best-fit of the form $c = a \log(k_{react}) + b$ is once again the appropriate choice, despite the values at $k_{react} = \{16, 25\} \times 10^{-8}$ mm^{3}hr^{-1}vir^{-1} deviating from this curve. On comparison with the PDE model (Figure 3.14a), we find that there is no reaction propensity scaling of the form $\lambda = f(h)$ that will reconcile the wave speed between the continuum and discrete models for small compartment size. This is an interesting conclusion, and is contrary to the calculations in Section 3.5 that show that compartment size $h = 0.01$ mm is above the critical threshold h_{crit}, and that a scaling λ exists.

Another empirical observation from Figure 3.15a is that the wave speed determined by lines of best fit between the SSA with $h = 0.01$ mm and PDE follow the relation

$$c_{SSA} = 0.26 c_{PDE}, \tag{3.71}$$

which holds true for several orders of magnitude of $k_{react} \in \left[1 \times 10^{-9}, 2.5 \times 10^{-7}\right]$ mm^{3}hr^{-1}vir^{-1}.

3.7 Summary

In this chapter, we have outlined the fundamental differences between continuum and stochastic formulations of chemical and biological reactions, and the assumptions made in deriving each formulation. A theoretical framework resulting in the derivation of the chemical master equation describing the exact time evolution of a chemical system was presented, and we then introduced the Gillespie Stochastic Simulation Algorithm as a means of generating Monte Carlo trajectories of the Chemical Master Equation governing the time evolution of reactant species. We then considered the application of this algorithm to the stochastic simulation of the virus-cancer cell interaction model shown in Chapter 2, and discretised the spatial domain into a series of well-mixed compartments, developing a spatially-dependent algorithm based on the direct method variation of the Gillespie SSA.

Validating this algorithm for a series of known test cases, it was found that the inhomogeneity introduced by virus particles born from infected cell burst in each compartment caused disagreement between the equivalent age-structured continuum model and the SSA for the smallest physically-motivated choice of compartment size. Looking at the propensity scaling for the bimolecular reaction between uninfected cells and virus particles, we derived a 2D equivalent of the corrected scaling presented in Erban and Chapman

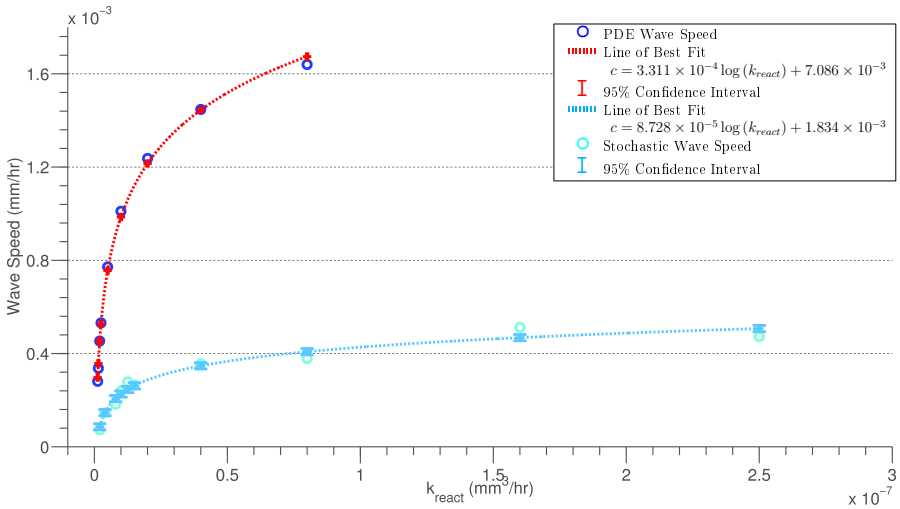

(a) Wave Speed Dependence on k_{react}.

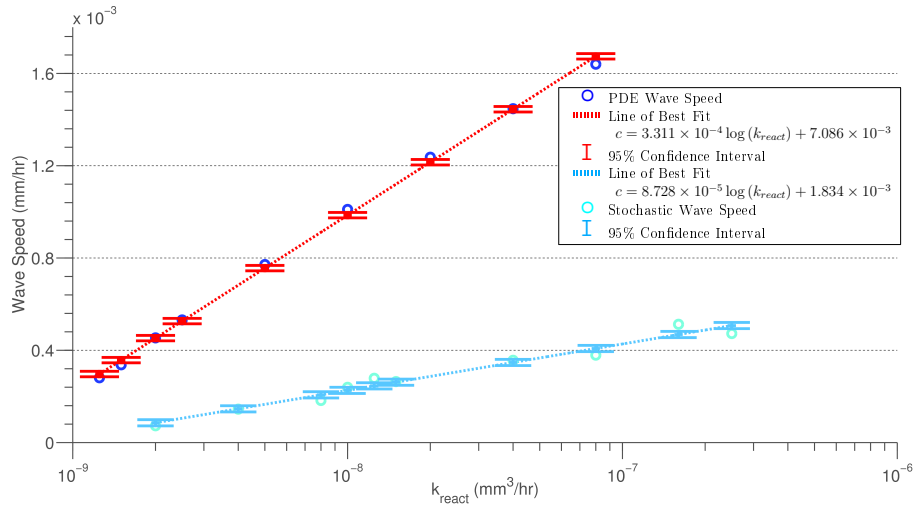

(b) Wave Speed Dependence on k_{react} (semi-log scale).

Figure 3.15: Comparison of wave speed dependence on k_{react} for PDE (Figure 3.14a) and SSA (Table 3.2) with $h = 0.01$ mm. From the lines-of-best-fit, we see that no trivial scaling of k_{react} as a function of compartment size h in the SSA case will recover the continuum wave speed.

(2009), but found that it was insufficient to reconcile the two models in the limit of small compartment size.

Relying on numerical solutions and SSA simulations, we saw that the calculated wave speed of virus propagation for a realistic set of parameters depended logarithmically on the reaction rate. This relation held true for both the continuum and small-compartment SSA case, and showed that no trivial scaling of reaction rate as a function of compartment size would reconcile the models. It was found that the small-compartment SSA case predicted a wave speed a factor of four smaller than that given by the continuum solution, but doubling the compartment size in the SSA was sufficient for the wave speed in the two models to agree. This is in stark contrast to numerical solutions of continuum models, where mesh size is typically decreased to satisfy convergence properties, and shows an important distinction between the two modelling approaches.

We also saw that, as predicted from travelling wave analysis of the continuum model, the wave speed of virus propagation was strongly related to the number of virus particles in the system. While doubling the compartment size was sufficient in matching predicted wave speeds of the SSA and continuum models, the same could not be said for the number of virus particles or their spatial distribution. Although this could be attributed to the transient state of the SSA simulations, requiring larger sample sizes, it is also possible that the large burst size results in the continuum model exhibit reignition behaviour from low concentrations that would indicate virus die out in a discrete model. This possibility is further supported by the fact that the continuum model reaches an equilibrium of virus particles for long time, whereas the mean of SSA samples continues a slow decay in time (not shown). This suggests that the equilibrium reached in the continuum case is not physically observed, showing the need for careful comparison between different discretizations.

These observations show the subtle difference in the continuum and discrete approaches to modelling biological systems, and illustrate the care that must be taken when choosing compartment sizes in on-lattice models. While the choice of larger compartment size brings the SSA results in line with continuum predictions, it also results in larger errors when calculating particle position (and hence wave speed), as well as placing restrictions on the type of initial distribution prescribed in the inhomogeneous system.

We have seen that the deterministic and stochastic approaches give qualitatively similar but quantitatively different results. We now move on the investigate the stochastic model in more detail. In the next chapter, we explore the effects of key experimentally varied parameters on the behaviour of the system. In particular, we devise a metrics for the success of therapy, consistency of simulation results, as well as looking at the mean time to tumour elimination and further wave speed analysis.

Chapter 4

Parameter analysis of stochastic model

In Chapter 3, we developed and tested a discrete, two-dimensional model for the interaction of virus particles with uninfected cells, based on the physical considerations outlined in Chapter 2. In this chapter, we exploit the model to examine the qualitative and quantitative effects of experimentally-controllable parameters on the outcome of therapy. We consider two general scenarios, corresponding to "dense" and "sparse" initial distributions of uninfected cells in the domain, perhaps corresponding to 2D cross-section of a tumour in an *in vivo* case, and a monolayer of cells on a Petri dish in an *in vitro* case.

4.1 Introduction

In this chapter, we consider a spatially-dependent, stochastic model for the spread of oncolytic virus throughout a solid tumour. We have previously seen several spatially-dependent mathematical models of replication-competent viruses in solid tumours in Chapter 1. PDE models such as those by Wein et al. (2003); Mok et al. (2009); Matzavinos (2004) considered the effects of diffusion coefficient and spatially varying initial conditions on the overall success of therapy. Spatial patterns and travelling waves were also shown in Matzavinos (2004), as well as the follow-up work by Chaplain (2008). However, as demonstrated in Chapter 3, discrete formulations of cell-virus interactions can result in significantly different behaviour due to the localisation of virus particles caused by the inherent discreteness of burst and extinction events.

Recent work by Reis et al. (2010); Wodarz (2013) explored spatial patterns in simple stochastic lattice models of cell-tumour systems. For a two-dimensional *in vitro* system consisting of a monolayer of uninfected cells, Wodarz et al. (2012); Wodarz (2013) formulated a compartment-based, probabilistic model of uninfected and infected cells. In this

model, each compartment has single-cell occupancy, and can either be empty or contain an uninfected or infected cell. At each time step, uninfected cells can replicate to a neighbouring empty compartment, become infected if adjacent to an infected cell, or die, and infected cells can either infect adjacent uninfected cells or die. In contrast to our model, where uninfected cells move into free space independent of cell density, this formulation does not allow for migration of uninfected cells into free space, and also incorporates cell crowding as well as regeneration of uninfected cells. The key parameter in the model was assumed to be the ratio of probability of infected cell death to infected cell transmission. Due to a lack of accurate experimental parameters, the authors performed a qualitative sensitivity analysis of this agent-based model for arbitrary parameter values, and compared these with limited experimental data as a proof of concept.

Our model incorporates two key physical processes neglected by existing models: the time delay in virus burst due to the duration of the lytic cycle, and the use of infected cell motility to spread virus particles. We now investigate the possible range of behaviour of this model, and compare the qualitative behaviour with that of existing models.

4.2 Typical system

The simulations presented in this chapter follow the physical parameters previously outlined in Section 3.3. The two-dimensional 1 mm $\times$ 1 mm domain is subdivided into cubic compartments of 0.01 mm in length, corresponding to the smallest physically plausible division; the size of a single cell.

We consider the effects of burst time, τ, diffusion ratio of infected-to-uninfected cells, D, initial distribution of virus particles in space, A, and burst size, α, for a range of values from the baseline parameter estimates in Table 3.1.

4.2.1 In vivo simulation

For the *in vivo* case, the 2D domain corresponds to a slice of a pseudo-3D solid tumour of uniform density in the z-direction (see Figure 3.2a from Section 3.3). Experimental and modelling data suggests that high-density regions of tumours contain 10^6 cells mm^{-3} (Wein et al., 2003; Chicoine and Silbergeld, 1995), corresponding to 10000 cells distributed throughout a $100 \times 100 \times 1$ compartment pseudo-2D domain.

Preliminary simulations for the base case parameter values (Table 3.1) showed sufficient numbers of virus particles and uninfected cells in the system to sustain a travelling wave of infection for the majority of simulations. No virus extinction was observed on typical time-scales of $\mathcal{O}\left(10^3\right)$ hours, and simulations exhibited sustained waves of infection with low variability. Because of this, an ensemble size of 20 simulations was chosen for each set of parameters in Table 4.1, the results of which are presented in Section 4.4.

Parameter	Values
τ	[5, 15, 25] hrs
D	[0.10, 0.25, 0.75, 1.0]
α	[10, 100, 1000]
A	$[1 \times 1,\ 5 \times 5,\ 11 \times 11]$ compartments

Table 4.1: Parameter range for *in vivo* (dense uninfected cell) simulations.

4.2.2 In vitro simulation

As with the *in vivo* case, the *in vitro* simulation domain of consisted of $100 \times 100 \times 1$ cubic compartments of unit length 0.01 mm. Physically, this now corresponds to a monolayer of cells in a petri dish rather than a cross-section of solid tumour, and the uninfected cell density is therefore reduced.

Typical experimental data from Bazan-Peregrino et al. (2008) states 20000 cells per well in a 96-well plate, with a typical growth surface area of each plate in the range $0.2 - 0.35$ cm^2. This corresponds to $550 - 1000$ cells mm^{-2}, and we take the upper value of 1000 cells distributed randomly throughout the simulation domain. With the exception of this uninfected cell initial condition, the baseline parameters from Table 3.1 are used once again.

This sparse initial condition of uninfected cells results in a limiting-reaction case, with virus particles often dying before having a chance to interact with the uninfected cell population. Preliminary simulations indicated that virus extinction was much more common, with many parameter sets that showed successful elimination of uninfected cells in the dense case resulting in trivial extinction in the sparse case.

As a result of these observations, less emphasis was put on investigating system behaviour for smaller increments of parameter values in the sparse, *in vitro* case (Table 4.2). Instead, we focussed computational efforts on an increasing the ensemble size to 50 simulations per parameter set, due to the greater variability observed between individual simulations.

Parameter	Values
τ	[5, 15, 25] hrs
D	[0.10, 0.75]
α	[100, 1000]
A	$[5 \times 5,\ 11 \times 11]$ compartments

Table 4.2: Parameter range for *in vitro* (sparse uninfected cell) simulations.

4.2.3 Qualitative comparison with Wodarz et al. (2012)

In preliminary simulations using the parameter ranges outlined in Sections 4.2.1–4.2.2, individual simulations were observed to have directionality of spread. This was due to

the equilibrium number of virus particles in the system being low, resulting in a small number of migrating infected cells. While the mean behaviour of the whole ensemble was radially symmetric, the individual variation in each simulation highlighted the inherent stochasticity in the system, and illustrated local extinction in some directions, which would not occur in a deterministic model.

Despite the crowding effects and lack of explicit infected cell motility of the Wodarz et al. (2012) model outlined in Section 4.1, the qualitative classification of spatial patterns presented by the authors provides a classification for the results of our model. As in our model from Chapter 3, reflective boundary conditions are chosen. Wodarz et al. (2012) chose an initial state of uninfected cells surrounded by empty space. A localised injection of virus particles is placed in the centre of the uninfected cells, and the system is allowed to evolve in time. From this initial state, the authors identified four possible physical outcomes:

1. Elimination of uninfected cells prior to infection wave-front reaching boundary
2. Elimination of uninfected cells after infection wave-front reaching boundary
3. Extinction of virus while uninfected cells persist
4. Coexistence of uninfected cells and virus

Of these behaviours, it can be argued that the coexistence of uninfected cells and virus is a transient state, and will tend to one of 1–3 in the long-time limit. Qualitatively, we find that our model is capable of exhibiting these physical outcomes, as well as the experimentally-observed spatial patterns published in this work.

4.2.3.1 Virus spatial patterns

For a square domain initially filled with uninfected cells, Wodarz et al. (2012) considered the case were virus particles were placed in the centre of the uninfected cells. Running multiple realisations for difference parameter values, four type of spatial patterns were identified:

1. Mixed expansion of virus and uninfected cells
2. Hollow ring expansion of virus with no uninfected cells behind wave front
3. Concentric ring expansion, with uninfected cells left behind at the site of virus initial condition
4. Expansion with sparse mixing of small number of virus

While all of these spatial patterns may be observed at some stage, extensive simulations show that Pattern 1 (mixed expansion of virus and uninfected cells) is not a stable state

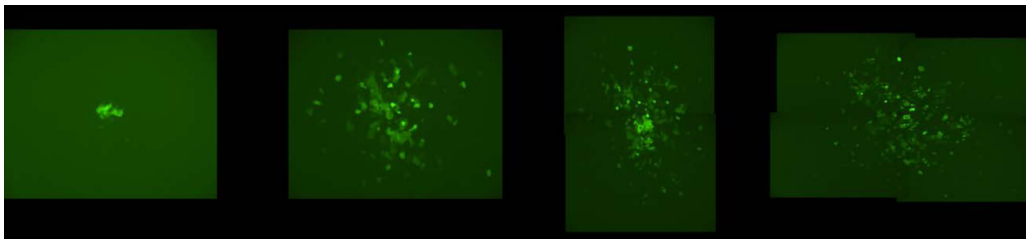

(a) Spatial pattern of adenovirus (AdEGFPuci) growth for the experiment that exhibits a disperse growth pattern. Snapshots in time are shown, representing days 7, 10, 11, and 12 post infection. The area of green fluorescence is shown, expressed by the infected cells, thus documenting the spatial spread of the virus through the population target cells arranged in a two dimensional setting (reproduced from Wodarz et al., 2012).

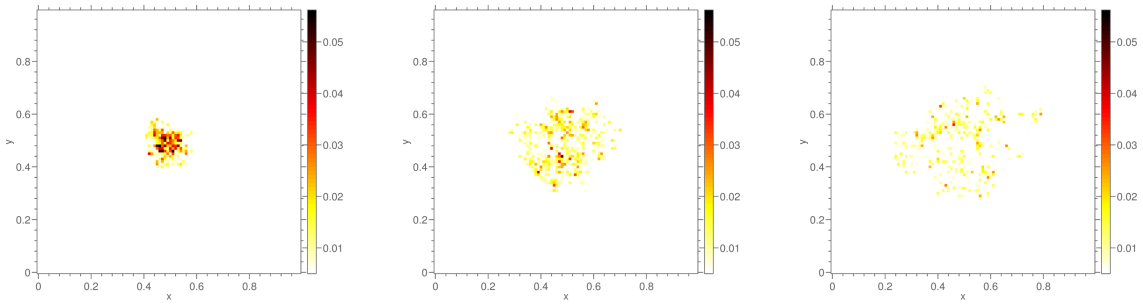

(b) Virus particles at $t = 500$. (c) Virus particles at $t = 1750$. (d) Virus particles at $t = 3000$.

Figure 4.1: Comparison of experimentally observed disperse structure of virus spread and numerical simulation with $\alpha = 10$, $D = 0.10$, $\tau = 25$ hrs, $A = 5 \times 5$ compartments (mean of 20 simulations with dense uninfected cell initial condition, and mean number of virus particles in each compartment indicated by colour bar). Other parameter values are given in Table 3.1

of the system. It corresponds to transient behavour, which either transition into Pattern 2 (hollow ring expansion case) or results in the eventual extinction of virus particles in the long-time limit. Pattern 4 (expansion with sparse mixing of virus particles) differs from Pattern 1 due to void space between uninfected and infected cells. It is typically an intermediate state, that is observed when viral spread kinetics are too low to maintain significant numbers of infected cells, and typically results in extinction of the infection.

In our simulations, we observe Patterns 1, 2 and 4, but have not been able to reproduce Pattern 3 (concentric ring expansion). As no experimental evidence has been found for this case, it is possible that it is also transient behaviour that occurs on a fast time-scale, and is not observed on the time-scales of our simulations.

Experimental data showing patterns 1 and 2 can be qualitatively reproduced by our model with dense uninfected cell initial condition (Figures 4.1–4.2). Unfortunately, due to the lack of parameter estimates, spatial scales and cell densities, only a qualitative comparison can be made.

4.2.3.2 Elimination of uninfected cells

The optimal outcome of therapy is the complete elimination of uninfected cells. Due to the single occupancy of compartments in the Wodarz et al. (2012) model, uninfected cells

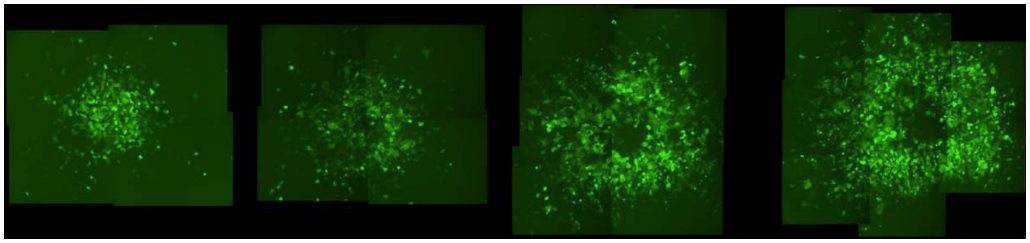

(a) Spatial pattern of adenovirus (AdEGFPuci) growth for the experiment that exhibits a ring structure. Snapshots in time are shown, representing days 7, 9, 11, and 13 post infection. The area of green fluorescence is shown, expressed by the infected cells, thus documenting the spatial spread of the virus through the population target cells arranged in a two dimensional setting (reproduced from Wodarz et al., 2012).

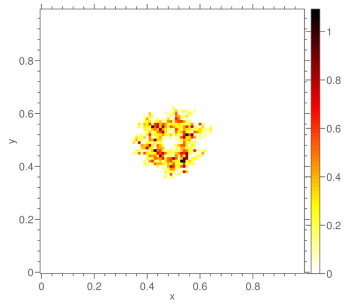

(b) Virus particles at $t = 500$.

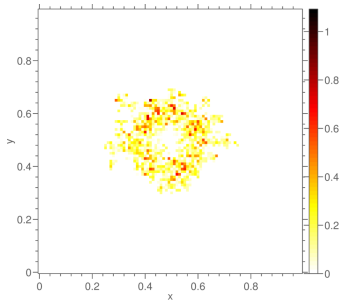

(c) Virus particles at $t = 1000$.

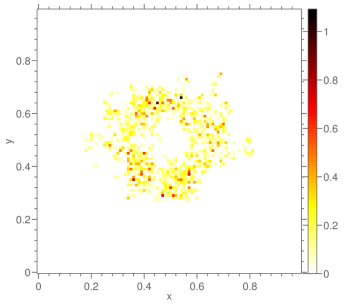

(d) Virus particles at $t = 1500$.

Figure 4.2: Comparison of experimentally observed ring structure of virus spread and numerical simulation with $\alpha = 100$, $D = 0.10$, $\tau = 15$ hrs, $A = 5 \times 5$ compartments (mean of 20 simulations with dense uninfected cell initial condition, and mean number of virus particles in each compartment indicated by colour bar). Other parameter values are given in Table 3.1

are placed in the centre of a larger (empty) domain. Virus particles were then placed in the centre of the uninfected cells, and the outcome of simulations was determined for a range of parameters. Reflective boundary conditions were implemented at the edges of the domain, and the authors then make the distinction between elimination of cells before or after reaching the boundary, with the latter case depending on the size of the domain.

The initial conditions on uninfected cells in our simulations did not leave free space in which to expand, but as crowding effects were not considered, this can be considered as equivalent to a long-time limit of the Wodarz et al. (2012) results. Furthermore, it is apparent that for equivalent initial conditions in our model, these two cases of elimination before or after reaching the boundary would simply correspond to values of diffusion ratio of $D < 1$ and $D > 1$. Working on the hypothesis that viruses reduce the available energy in infected cells, we only consider the physically motivated case of $D \leq 1$.

The elimination of uninfected cells after interactions with boundaries in our model for the dense *in vivo* case is shown in Figure 4.3. A long burst time of $\tau = 25$ hrs combine with a diffusion ratio of $D = 1.0$ results in the majority of uninfected cells removed from the system after $t = 625$ hours. Complete elimination of uninfected cells occurs at $t \approx 1000$ hours, with some virus particles still remaining in the system at this point.

This elimination behaviour is typical for the majority of parameters in the dense, *in vivo* case from Section 4.2.1, but due to the lack of experimental parameters in Wodarz et al. (2012), only a qualitative comparison can be made.

4.2.3.3 Coexistence of virus and uninfected cells

Another type of outcome identified was the coexistence of uninfected cells and virus particles (implicitly, through the presence of infected cells). This behaviour is a transient state, with the ultimate outcome being either the extinction of virus particles or a sustained wave of infection. However, this transient behaviour may occur on a sufficiently slow time-scale to be observed in experiments or simulations, and may therefore be of interest.

This transient behaviour was reproduced with our model for a range of parameter values that limit the total virus population and spread, such as the burst size or virus death rate. Figure 4.4 shows the coexistence of virus particles and uninfected cells in an dense, *in vivo* case for a low burst number, $\alpha = 10$, and long burst time, $\tau = 25$. This combination of parameters results in fewer virus particles to deplete the uninfected cell population and limit spread of virus, and the longer burst time allows for more uninfected cells to migrate into the reaction zone in between bursts. This coexistence occurs over a sufficiently long time interval to be observable, but the total virus population slowly decays in time, and so the eventual outcome of the simulations for this set of parameters is usually virus extinction.

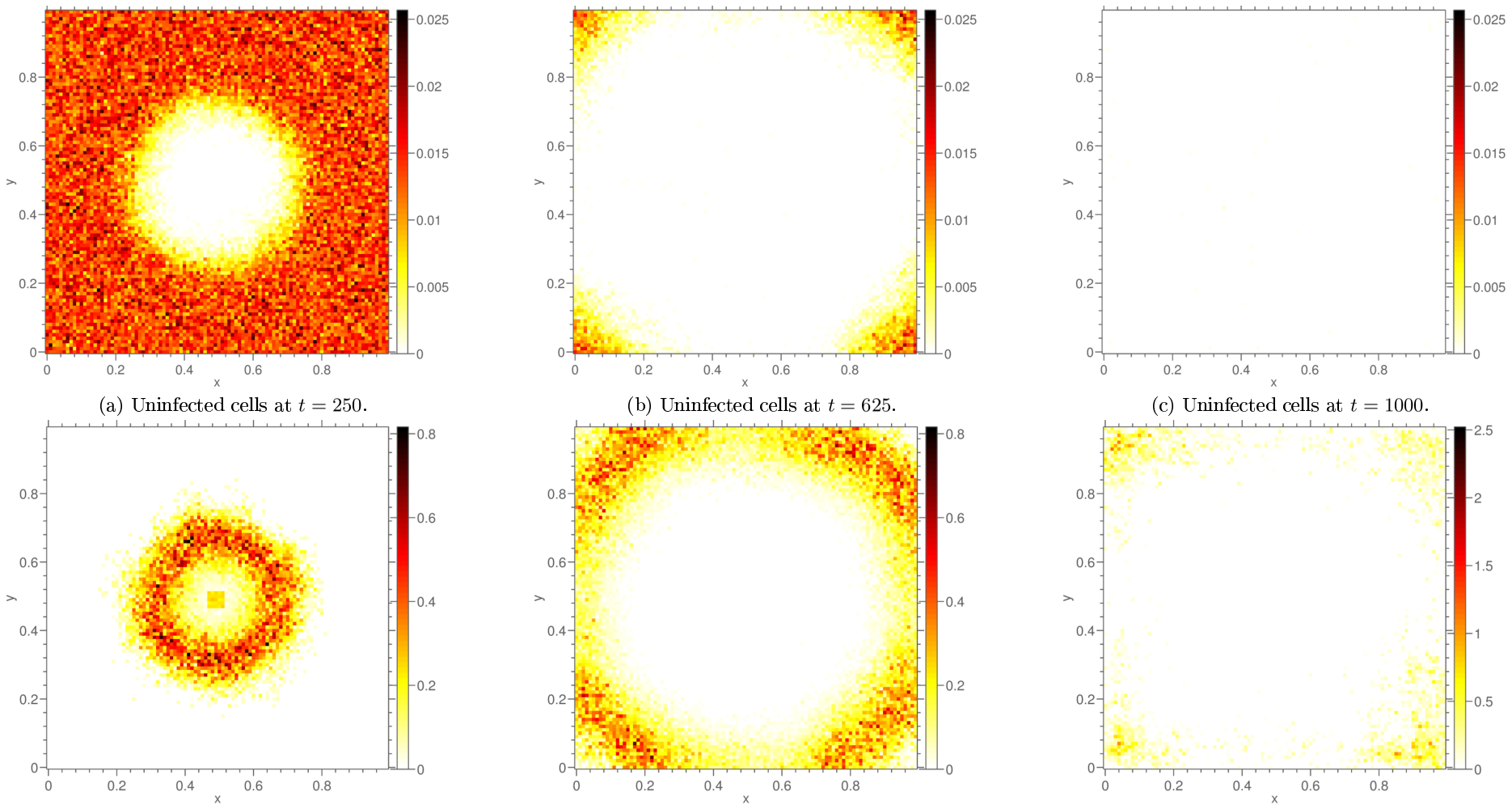

(a) Uninfected cells at $t = 250$.

(b) Uninfected cells at $t = 625$.

(c) Uninfected cells at $t = 1000$.

(d) Virus particles at $t = 250$.

(e) Virus particles at $t = 625$.

(f) Virus particles at $t = 1000$.

Figure 4.3: Elimination of uninfected cells for $\tau = 25$, $D = 1$ (mean of 20 simulations, with mean number of virus particles in each compartment indicated by colour bar). Other parameter values are given in Table 3.1

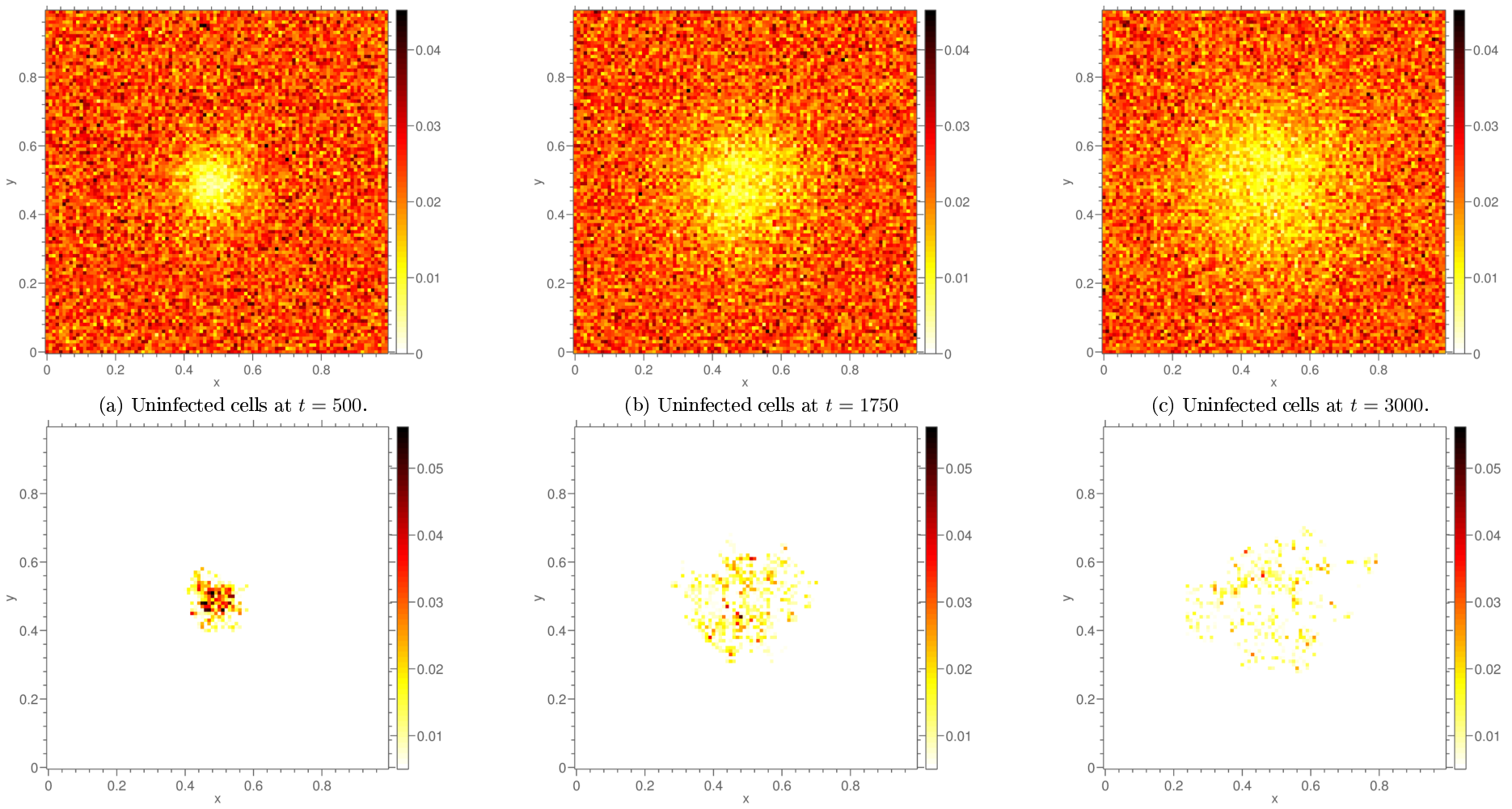

(a) Uninfected cells at $t = 500$.

(b) Uninfected cells at $t = 1750$

(c) Uninfected cells at $t = 3000$.

(d) Virus particles at $t = 500$.

(e) Virus particles at $t = 1750$.

(f) Virus particles at $t = 3000$.

Figure 4.4: Coexistence of uninfected cells and virus for $\tau = 25$, $\alpha = 10$ (mean of 20 simulations, with mean number of virus particles in each compartment indicated by colour bar). Other parameter values are given in Table 3.1.

4.2.3.4 Extinction of virus

The final observed outcome of simulations was the overall extinction of virus particles. This outcome is typically affected by the burst size of virus particles, burst time, as well as the density of uninfected cells in the system.

An example of virus extinction in the dense (*in vivo*) case with $\alpha = 5$ and $\tau = 5$ is shown in Figure 4.5. From a large initial number of virus particles, the relatively short burst time does not allow for uninfected cells to migrate into the reaction zone at a sufficient rate to sustain the reaction, and the low burst size results in the death of virus particles before they interact with migrating uninfected cells.

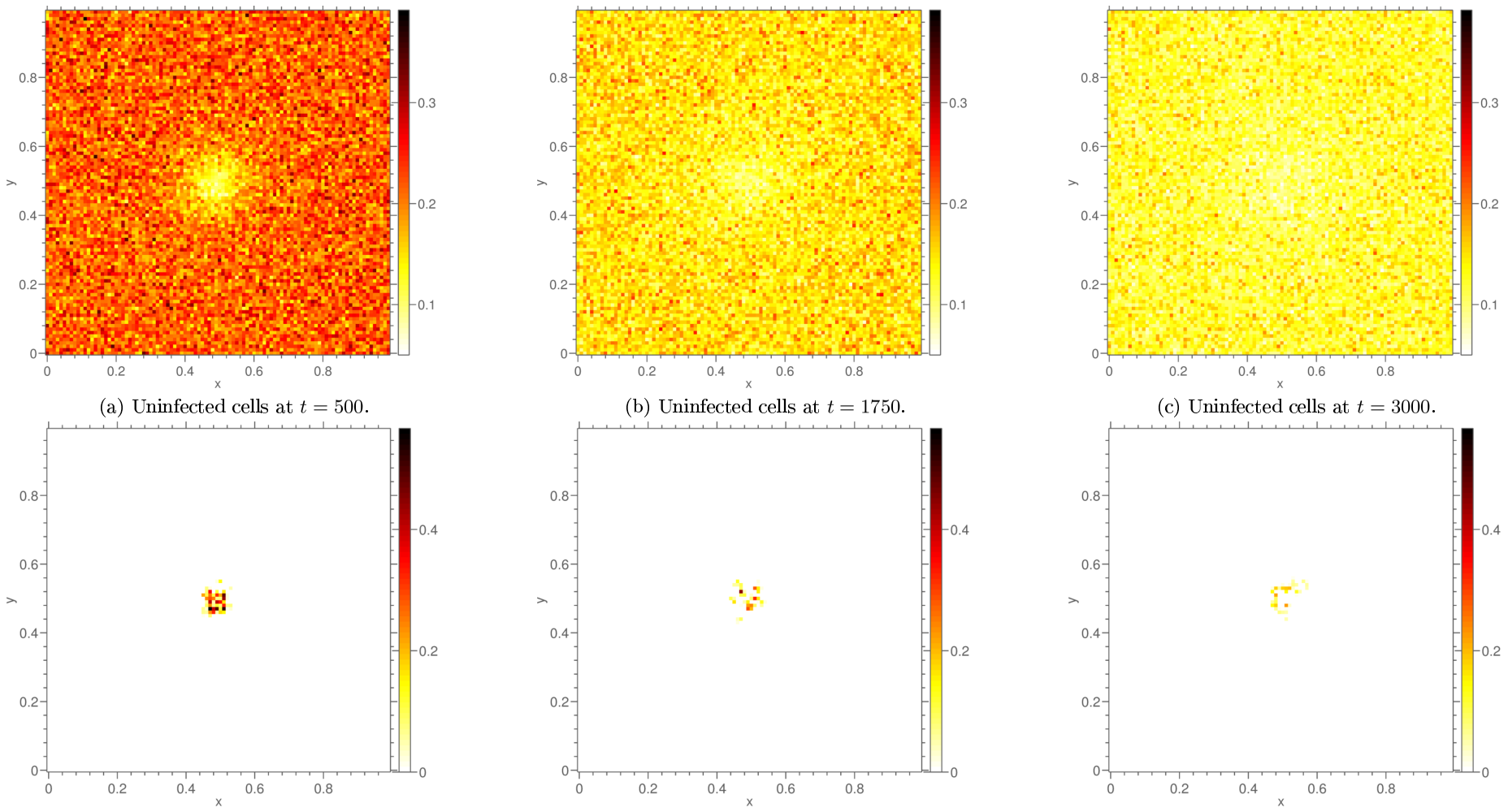

(a) Uninfected cells at $t = 500$.

(b) Uninfected cells at $t = 1750$.

(c) Uninfected cells at $t = 3000$.

(d) Virus particles at $t = 500$.

(e) Virus particles at $t = 1750$.

(f) Virus particles at $t = 3000$.

Figure 4.5: Extinction of virus for $\tau = 5$, $\alpha = 10$ (mean of 20 simulations, with mean number of virus particles in each compartment indicated by colour bar). Other parameter values are given in Table 3.1

4.2.4 Motivation and key questions

In both the dense (*in vivo*) and sparse (*in vitro*) cases, we are interested in performing a sensitivity analysis for a range of experimentally-controlled parameters; specifically those that depend on the physical properties of the oncolytic virus and initial conditions in the system. We aim to determine the effect that varying these key parameters will have on the propagation speed of infection, as well as overall success of therapy. We also want to quantify the variation in each ensemble of simulations to determine how consistent these results are for multiple realisations of the same set of parameters.

4.2.4.1 Burst time

The burst time, a measure of the life cycle of virus particles inside an infected cell prior to lysis, is a property of the specific virus strain used in oncolytic therapy. The viruses used in oncolytic virotherapy range from linear double-stranded DNA viruses, such as Adenovirus and HSV-1, single-stranded RNA viruses, such as Newcastle Disease, and segmented double-stranded RNA viruses, such as Reovirus. Following attachment to the cell surface, the virus must traverse the lipid bilayer surrounding the cell, before unpacking its genetic material for replication. For each of these viruses, the genome and physical size, morphology, coating (or lack thereof), as well as the replication site within the cell could all affect the duration of this lytic cycle.

In our model, the spread of virus is facilitated by the motility of infected cells prior to lysis, and we would therefore expect the speed of virus spread to depend on the length of time between initial infection and lysis. For a range of realistic burst times, $\tau = [5,\ 15,\ 25]$ hrs, we want to determine:

- Are spreading waves of infection with constant amplitude and speed observed?
- What are the typical speeds of infection waves for realistic burst times?
- How does the burst time affect the overall success of therapy?

Since the burst time is one of the most readily controlled experimental parameters, we will consider its effects in combination with all other parameter values.

4.2.4.2 Diffusion ratio

As part of the virus replication process, virus particles hijack the motor mechanism of the host, which results in reduced infected cell motility. As with the replication-dependent burst time, the physical properties of the specific virus species and strain dictate the extent to which the motor mechanism of the host is hijacked.

From an experimental point of view, it is difficult to obtain an accurate estimate of the effective motility coefficient of cells in a dense medium such as a solid tumour, and this is

therefore not typically an experimentally controlled parameter. In Chapter 2, the motility of infected and uninfected cells was related through the dimensionless ratio, $D = {}^{D_m}/_{D_n}$, and this becomes a convenient description for quantifying infected cell motility for different virus species and strains. Our assumption of virus particles hijacking the cellular motor mechanism of the host cell implies that $D \leq 1$, and we choose a range of values accordingly. For a range of diffusion ratios, $D = [0.1,\ 0.25,\ 0.75\ 1.0]$, we want to determine:

- How does the wave speed of infection depend on the diffusion ratio?
- Is there a non-trivial, optimal diffusion ratio to maximise success of therapy?
- Does increasing the diffusion ratio decrease the probability of extinction?

Preliminary simulations showed that the sparse uninfected cell initial case had limited success of virus infection, with little qualitative difference seen for similar values of diffusion ratio. For this reason, larger increments between parameter values was chosen for the range of diffusion ratios investigated.

4.2.4.3 Burst size

Another parameter of interest is the burst size; the number of viable virus particles released per infected cell at the end of the lytic cycle. Due to the broad range of oncolytic virus families and strains used in *in vivo* and *in vitro* experiments, this parameter is of significant experimental interest. Since the burst size refers to the production of "plaque forming units" (non-defective virus particles capable of infecting other cells), the burst size will be controlled by the efficiency of replication within the cell which, in turn, will depend on the genome size of the virus type, as well as the virulence of the particular virus strain.

Existing literature refers to a typical burst size in the range of $10 - 1000$ virus particle per burst (Section 3.3), and we therefore choose $\alpha = [10,\ 100,\ 1000]$. For this range of burst sizes, we want to determine:

- What is the minimum burst size to sustain an infection wave?
- Does a larger burst size increase the speed of propagation or effectiveness of therapy?
- Does the burst size affect variability between individual simulations in an ensemble?

Preliminary simulations showed that the sparse uninfected cell initial case showed uniform extinction of virus infection for $\alpha = 10$, and this result was subsequently omitted from the discussion of results in Section 4.5.

4.2.4.4 Injection area and virus concentration

One experimentally controllable parameter that does not directly relate to the type of virus used is the spatial distribution and concentration of the initial dose of virus particles. While experimental literature usually specifies the initial concentration of virus particles, the initial spatial distribution is not usually stated, possibly due to the difficulty of measuring this *in situ*.

In our model, virus particles are not explicitly considered to be a motile species, and so increasing the initial area of injection would increase the initial likelihood of interaction with a greater number of uninfected cells. For a fixed initial number of virus particles, we look at the effects of spreading this over a range of compartments (changing both the initial distribution and concentration of virus particles). In the absence of the required experimental data, we consider three arbitrary injection areas, $A = [1 \times 1,\ 5 \times 5,\ 11 \times 11]$ compartments of size $h = 0.01$ mm, choosing odd multiples of compartments to maintain spatial symmetry. For this range of injection areas, we wish to determine:

- Is the likelihood of virus extinction affected by the initial viral spread?
- Is speed of propagation dependent on initial virus concentration?
- Does increasing injection area change the number of uninfected cells removed from system in the long-time limit?

Preliminary simulations showed that the sparse uninfected cell initial case showed uniform extinction of virus infection for $A = 1 \times 1$ compartments, and this result was subsequently omitted from the discussion of results in Section 4.5.

4.2.4.5 Burst time versus motility coefficient

The motility of cells depends on a number of factors, such as the structure of the ECM, local concentration of cellular adhesion molecules, and presence of debris. While it is possible to control some of these factors experimentally in an *in vitro* study, this is usually not practical in an *in vivo* scenario.

In our model, the motility of infected cells is related to the uninfected cell motility through the dimensionless ratio, D, meaning that the physical properties of the domain will affect the speed of virus spread in the stochastic description of the physical system. In preliminary simulations, we observed that the burst time of infected cells has a similar qualitative effect as the motility coefficient of uninfected cells on the speed of propagation of infection throughout the domain. Since the burst time is a physical property of the domain, it may be the case that this is easier to control experimentally, and we therefore wish to determine whether these parameters are equivalent, and if a decrease in one parameter can be compensated for by an increase in the other.

To investigate the relative effects of these two parameters, we consider the baseline case of $D_n = 2.08 \times 10^{-5}$ mm^{2}hr^{-1} for burst times $\tau = [5,\ 15,\ 15]$ hrs, and compare this to a slower diffusion rate $D_n^\dagger = 1/2 D_n$ for longer burst times $\tau^\dagger = 2\tau$, while maintaining the baseline diffusion ratio, $D = 0.1$.

4.3 Analysis of simulations

To quantify the effect of key parameters on the simulations, we develop several metrics for each simulation ensemble: the rate of displacement of virus particles from their initial positions, the distribution of these displacements and the coefficient of variation for both the speed of spread and total number of uninfected cells. These concepts are later used in Sections 4.4–4.5 for analysing the results for the dense and sparse cases.

4.3.1 Mean displacement from initial condition

For the simulations presented in this chapter, we consider the spread of virus particles from a localised initial distribution in a two-dimensional domain with uniformly-distributed uninfected cells. In Section 3.6, we showed examples of travelling wave behaviour in the stochastic simulations. The wave speed was calculated by looking at the rate of change of displacement of virus particle from the central compartment of the initial distribution in time, and we apply the same methods to determine the mean speed of virus spread for the range of simulation ensembles.

Perhaps the simplest method for determining the overall wave speed of the set of simulations is to take the mean of the individual displacements over all simulations. This approach is adequate for ensembles that only have one steady state, and small variance from the mean of each individual simulation. However, in cases where two or more distinct states are possible, particularly the case of virus extinction, the displacement in time will be affected by simulations with zero net virus displacement. In the case of an ensemble with some extinct simulations, the displacement of non-extinct reactions may still be of interest. We therefore consider the weighted displacement of *ongoing* reactions, and only divide the sum of displacements by the number of simulations with $\sum_{x,y} V > 0$, as shown in Algorithm 2.

4.3.2 Distributions and bin sizing

As we outlined in Chapter 3, ODE models are often considered to be the mean of stochastic simulations in the limit of large sample sizes. However, these simulations also provide additional information in the form of variance between individual simulations. This can be visualised by plotting time histograms of quantities such as virus displacement, onset of extinction and mean numbers of virus particles and uninfected cells in the system.

Algorithm 2 Procedure for calculating the mean virus displacement of ongoing reactions.

1. For each simulation, i,

   (a) For each time step, t

      i. Calculate radial displacement of virus particle from central compartment,

$$\langle |\mathbf{x} - \mathbf{x}_0| \rangle^{(i)}(t) = \frac{\sum_{j,k} |\mathbf{x}_{j,k} - \mathbf{x}_0| V_{j,k}^{(i)}(t)}{\sum_{j,k} V_{j,k}(t)}$$

   (b) Interpolate virus displacement to uniformly-spaced time grid, $\hat{\mathbf{t}}$

   (c) Calculate extinction time for i^{th} reaction, $t_i^{\dagger}$, such that

$$\sum_{j,k} V_{j,k}^{(i)} \left(t > t_i^{\dagger} \right) = 0$$

2. Ongoing virus displacement is given by

$$\langle |\mathbf{x} - \mathbf{x}_0| \rangle^{(tot)}(t) = \frac{\sum_i \langle |\mathbf{x} - \mathbf{x}_0| \rangle^{(i)}(t)}{N - \sum_i \delta \left(t < t_i^{\dagger} \right)},$$

   where $\delta \left(t < t_i^{\dagger} \right) = \begin{cases} 1 & \text{if extinction time not reached} \\ 0 & \text{otherwise} \end{cases}$, and N is the total number of samples in the ensemble.

An important aspect of visualising histograms is the choice of bin size, as different bin sizes can reveal different features of the data, particularly for small sample sizes. There is no consensus on an "optimal" method for selecting the bin size, and the choice is often based on a guess of the underlying distribution of the data. These range from the simple rules-of-thumb, such as the square-root of sample size, $k = \sqrt{N}$, to Sturges' early work on binomial distributions, $k = (\log_2 N + 1)$ (Scott, 2009). For normally-distributed data, Scott (1979) derived a condition on the bin size that minimised the integrated mean-square error of the density estimate, with the bin size $k = 3.5\sigma N^{-1/3}$, where σ is the sample standard deviation. Freedman and Diaconis (1981) proposed using interquartile range instead of variance to reduce sensitivity to outliers in the data, giving the bin size estimate $k = 2\mathrm{IQR}(x) N^{-1/3}$. These methods are all derived using asymptotic methods, and are generally inaccurate in the case of small sample size.

More recently, Shimazaki and Shinomoto (2007) sought to find the optimal bin size for jagged data from neuron spikes by minimising the L^2 risk function. Using a similar initial approach to Scott (1979), the goodness of fit of the histogram to the underlying data was estimated through the mean integrated squared error. They proposed a bin size-dependent cost function

$$C_n(k) = \frac{2\overline{x} - \sigma^2}{(Nk)^2},$$

where n is the number of bins, N is the number of samples, $\overline{x} = \frac{1}{n}\sum_i^n x_i$, $\sigma^2 = \frac{1}{n}\sum_i^n (x_i - \overline{x})^2$, and x_i is the number of spikes in the i^{th} data set. Using this cost function, the optimal bin size can be found by determining the value k that minimises $C_n(k)$.

Due to the jump processes in our simulations, we make use of the Shimazaki and Shinomoto (2007) procedure for the selection of bin size.

4.3.3 Coefficient of variation

It remains to analyse the variability (or dispersion) of the individual simulations in time. Typical measures such as the standard deviation (or variance) are dimensional quantities that are only valid in the context of the overall mean of the data, making direct comparison between different ensembles with different means or units problematic.

A useful dimensionless measure of a distribution is the coefficient of variation, defined as the ratio of the standard deviation, σ, to the mean, μ, as

$$c_v = \frac{\sigma}{\mu}. \tag{4.1}$$

This quantity is an absolute, normalised measure of the spread of data, and can also be defined as the inverse of the signal-to-noise ratio. As it is a dimensionless quantity, it is scale invariant and shows the extent of variability in relation to mean of the population. This is in contrast to other measures of dispersion commonly used for analysing Brownian motion, such as the Index of Dispersion (the variance-to-mean ratio).

In the context of our stochastic simulations, we use the coefficient of variation to show the relative variability between distributions of total uninfected cells and displacement of virus particles. Significant changes in between time steps could indicate a qualitative change in simulations.

4.4 Dense case

4.4.1 Diffusion ratio

For values of diffusion ratio $D = [0.1, 0.25, 0.75, 1.0]$ in a sample of 20 simulations per parameter set, we find that the rate of change of displacement of virus particles increases with increasing diffusion ratio (Figure 4.6a). The rate of removal of uninfected cell removal from the system, shown in Figure 4.6b, also increases with diffusion ratio, with the simulations for $D = [0.75, 1]$ reaching the domain boundary, resulting in the elimination of uninfected cells. From the mean total virus particles in the system (Figure 4.6c), we see that these simulations failed to reach an equilibrium number of virus particles before the infection wave reached the edge of the computational domain. However, for shorter burst

times and lower diffusion ratios, we see the system reach an equilibrium number of virus particles, which is higher for larger values of the diffusion ratio.

Qualitatively, we see that increasing the diffusion ratio has a similar effect to increasing the burst time on the rate of virus spread. Similarly, the rate of clearance of uninfected cells from the system increases with both burst time and diffusion ratio. This suggests that the reduced mobility of uninfected cells in denser media can be compensated for by using viruses with longer burst times in an experimental setting.

The onset of virus extinction initially occurs for $t > 1000$, and only in the cases with the higher diffusion ratio and burst time, once the number of uninfected cells in the system approaches zero. Figure 4.7a shows no increase in the coefficient of variation of virus particle displacement for $t < 750$. This implies that the distribution of mean virus displacements of the ensemble remains unchanged, and combined with the small absolute value of the coefficient of variation, suggests that the ensemble mean virus displacement is representative of the individual simulations. There is no significant difference in the value of coefficient of variation for different diffusion ratios in Figure 4.7a for $t < 750$, although lower burst times appear to increase the absolute value slightly. On the other hand, Figure 4.7b shows that the coefficient of variation for the total number of uninfected cells remaining in the system increases steadily for larger values of D as the system becomes limited by the number of available uninfected cells. This is a key difference between increasing burst time and increasing diffusion ratio, as changing the burst time does not affect the variance from the mean of individual simulations, as seen in Figure 4.7b. One possible reason for this is that having a higher diffusion ratio (and hence infected cell motility coefficient) together with a lower burst time results in a narrower reaction zone for the travelling wave, whereas a longer burst time reduces the concentration of uninfected cells near the virus particles due to uninfected cells having a longer time in which to redistribute throughout the system.

Finally, we find that the set of parameters that achieves the fastest elimination of tumour, as well as the greatest virus displacement is when $D = 1.0$ and $\tau = 15$. However, the large coefficient of variation for total uninfected cells for $D = 1.0$ suggests that the mean is not wholly representative, and in absolute terms, there is negligible difference between the $\tau = 15$ and $\tau = 25$ cases when $D = 1.0$. When compared with the effects of increasing burst time for smaller values of the diffusion ratio, this shows that burst time has diminished effects on the wave speed for larger values of D. This suggests that there is a saturation in the speed of virus spread and rate of uninfected cell removal for increasing τ, beyond which the effects on the outcome of the simulation will be minimal.

4.4.2 Burst size

The burst size is another key experimental parameter: choosing more virulent virus strains or families significantly affects the results of simulations. Figure 4.8c shows that

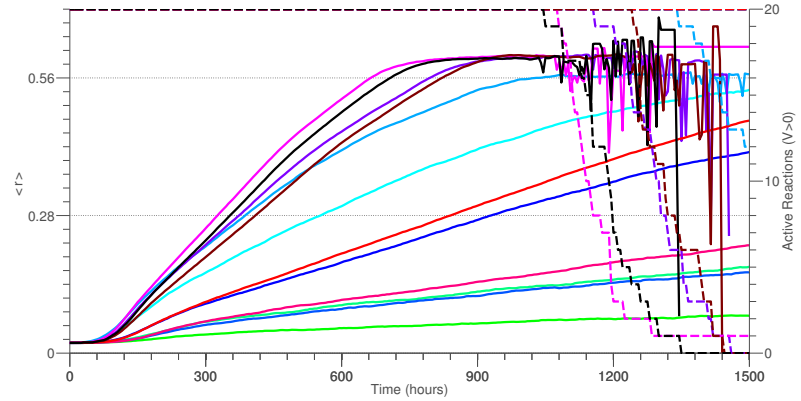

(a) Mean virus displacement for ongoing reactions for varying diffusion ratio in dense case.

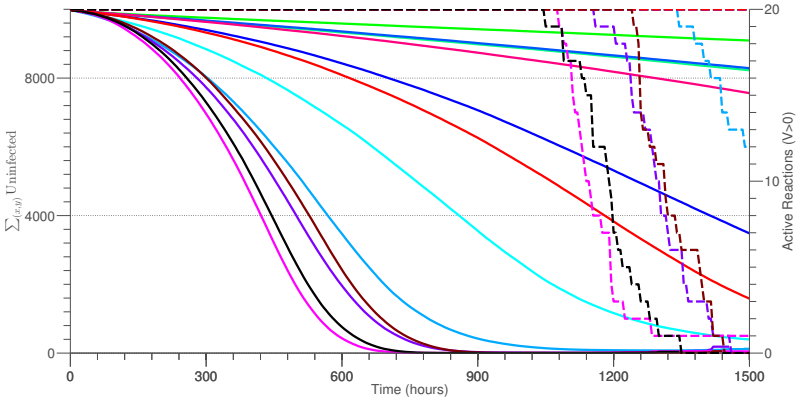

(b) Mean total uninfected cells for ongoing reactions for varying diffusion ratio in dense case.

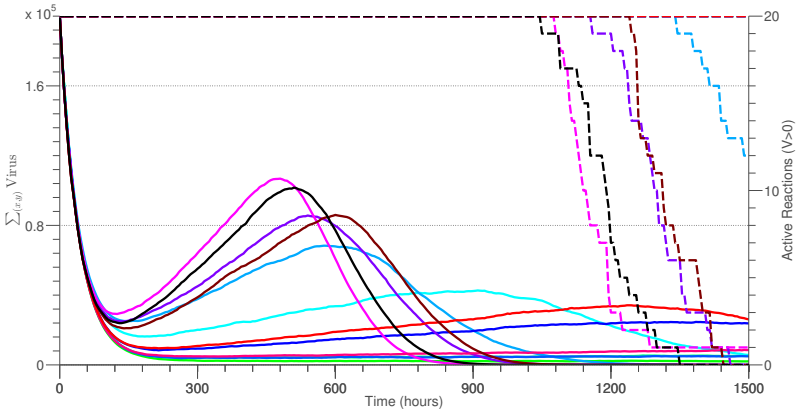

(c) Mean total virus particles for ongoing reactions for varying diffusion ratio in dense case.

D \ τ	5	15	25
0.10			
0.25			
0.75			
1.00			

(d) Plot legend.

D \ τ	5	15	25
0.10	0.4×10^{-4}	1.1×10^{-4}	1.4×10^{-4}
0.25	1.3×10^{-4}	2.9×10^{-4}	3.4×10^{-4}
0.75	4.7×10^{-4}	8.0×10^{-4}	7.8×10^{-4}
1.00	6.9×10^{-4}	9.3×10^{-4}	9.0×10^{-4}

(e) Wave speed best fit (mmhr^{-1}) from Figure 4.6a.

Figure 4.6: Mean virus displacement, total uninfected cells and total virus particles of ongoing reactions for varying diffusion ratio in dense case. Dashed lines indicate number of non-extinct simulations.

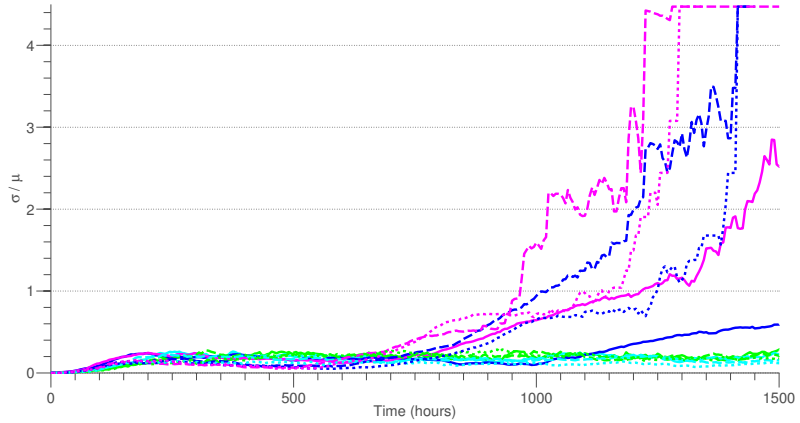

(a) Coefficient of Variation of Virus Displacement for diffusion ratio $D = [0.1, 0.25, 0.75, 1.0]$ (green, cyan, blue, purple) for $\tau = [5,\ 15,\ 25]$ hrs (solid, dashed, dotted) in dense case.

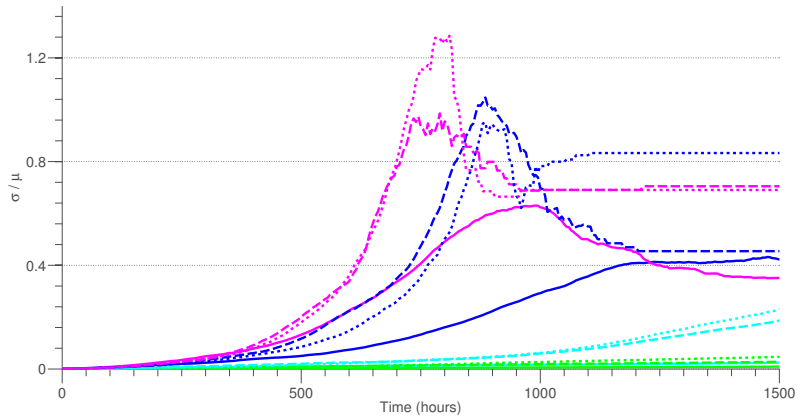

(b) Coefficient of Variation of total uninfected cells for diffusion ratio $D = [0.1, 0.25, 0.75, 1.0]$ (green, cyan, blue, purple) for $\tau = [5,\ 15,\ 25]$ hrs (solid, dashed, dotted) in dense case.

Figure 4.7: Variability of ensembles for varying diffusion ratio in dense case.

the burst size affects the mean number of virus particles in the system, which results in a greater number of uninfected cells removed (Figure 4.8b). The burst size also affects virus extinction: for burst size $\alpha = 10$, we see virus extinction of individual simulations in the $\tau = 5$ case for $t > 735$, with 30% of simulations extinct by $t = 1500$ hrs. Despite a non-zero number of virus particles for $t < 735$, Figure 4.8a shows negligible increase in the displacement of virus particles for ongoing reactions in the $\alpha = 10$, $\tau = 5$ case. This suggests that the reaction is not sustainable, and the ensemble is exhibiting transient behaviour en route to extinction.

Similarly, there is little difference in the rate of change of displacement in the $\tau = 15$ and $\tau = 25$ cases when $\alpha = 10$, even though all simulations in these ensembles have non-zero virus populations for $t \in [0, 1500]$. In contrast, we see a clear increase in wave speed for $\alpha = 100$ and $\alpha = 1000$, which implies that there is some threshold burst size, above which the reactions are sustainable, and the wave speed increases with larger bursts. Below this threshold, we see transient behaviour, and no significant change in wave speed.

This threshold effect is also seen in the coefficient of variation for virus displacement in Figure 4.9a. For the $\alpha = 10$ case, we see a steady increase in the coefficient of variation, compared to the $\alpha = 100$ and $\alpha = 1000$ cases, where the coefficient of variation remains constant for all $\tau \in [5, 15, 25]$. This is reflected in the coefficient of variation of total uninfected cells (Figure 4.9b), where the $\alpha = 100$ and $\alpha = 1000$ cases grow steadily in time, indicating greater removal of cells from the system.

4.4.3 Injection area and virus concentration

For several choices of initial distribution width, while conserving the total number of virus particles (and therefore varying the effective concentration), we find little effect on the results for the case of dense initial population of uninfected cells.

Although changing the width of the initial distribution alters the initial virus displacement, the rate of change is not affected by these initial conditions (Figure 4.10a), and observing simulations with narrower initial distributions of virus particles for a longer time would eventually result in the same net displacement.

Similarly, the equilibrium number of virus particles in the system is not affected by the initial condition size: although initially, the $A = 1 \times 1$ cases have fewer and the $A = 11 \times 11$ cases have greater numbers of mean particles than the $A = 5 \times 5$ case, they slowly tend towards the apparent equilibrium values over time (Figure 4.10c). Both these observations lead to the conclusion that the initial virus injection does not select a different equilibrium condition or travelling wave speed.

There are no extinction events in any simulations, and the mean of the virus displacements is representative of the individual simulations, with the coefficient of variation

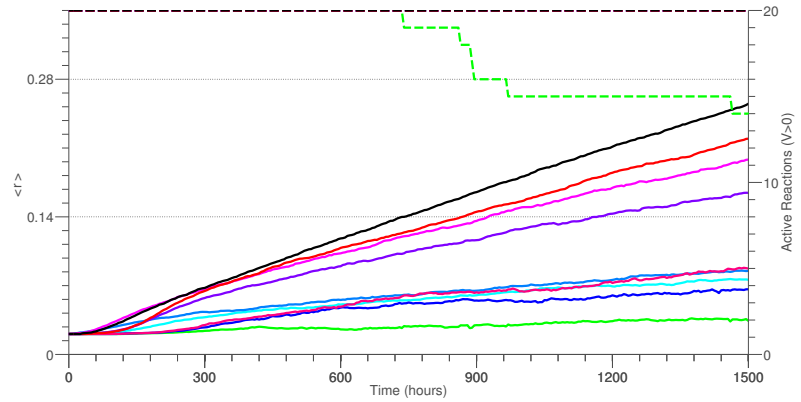

(a) Mean virus displacement for ongoing reactions for varying burst size in dense case.

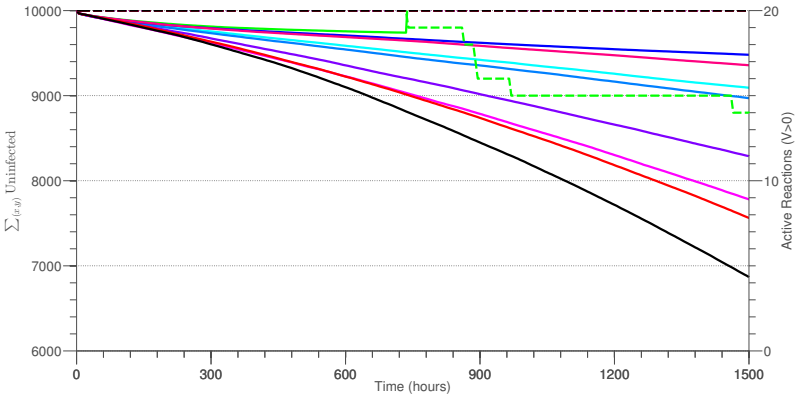

(b) Mean of total uninfected cells of ongoing reactions for varying burst size in dense case.

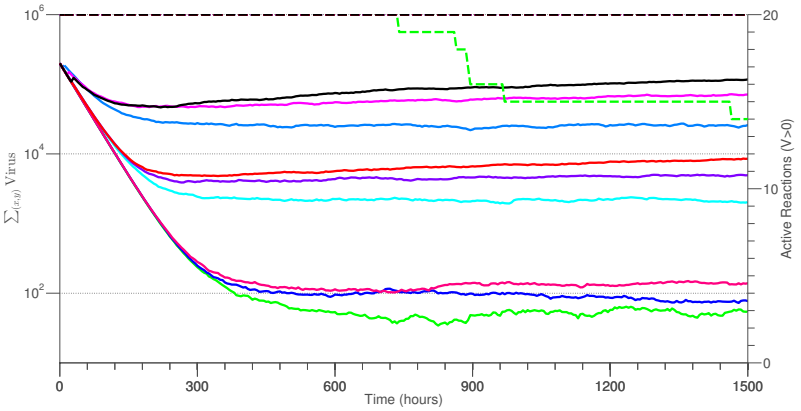

(c) Semi-log plot of mean total virus particles of ongoing reactions for varying burst size in dense case.

α \ τ	5	15	25
10			
100			
1000			

(d) Plot legend.

α \ τ	5	15	25
10	1.2×10^{-5}	3.9×10^{-5}	5.3×10^{-5}
100	4.1×10^{-5}	10.5×10^{-5}	14.3×10^{-5}
1000	4.0×10^{-5}	11.8×10^{-5}	16.1×10^{-5}

(e) Wave speed best fit (mmhr^{-1}) from Figure 4.8a.

Figure 4.8: Mean virus displacement, total uninfected cells and total virus particles of ongoing reactions for varying burst size in dense case. Dashed lines indicate number of non-extinct simulations.

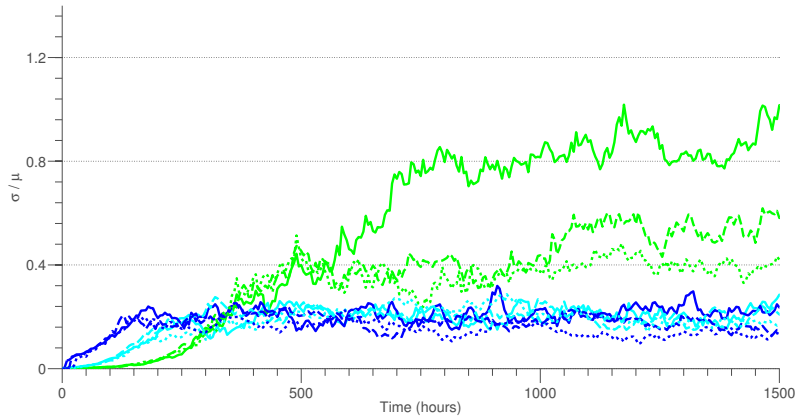

(a) Coefficient of Variation of Virus Displacement for $\alpha = [10,\ 100,\ 1000]$ (green, cyan, blue) for $\tau = [5,\ 15,\ 25]$ hrs (solid, dashed, dotted) in dense case.

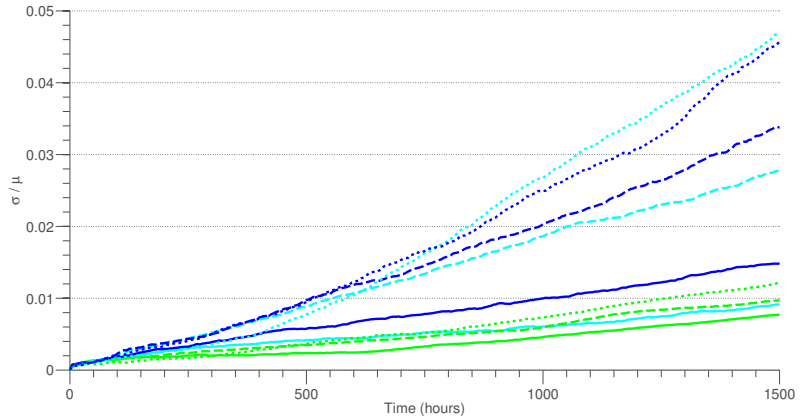

(b) Coefficient of variation for total uninfected cells for $\alpha = [10,\ 100,\ 1000]$ (green, cyan, blue) for $\tau = [5,\ 15,\ 25]$ hrs (solid, dashed, dotted) in dense case.

Figure 4.9: Variability of ensembles for varying burst size in dense case.

(Figure 4.11a) remaining constant in time. The coefficient of variation of total uninfected cells (Figure 4.11b) increases with time as a result of spatial spread of the infection wave, and we generally see no difference between the different initial conditions for equivalent burst times. The exception to this is the $A = 11 \times 11$, $\tau = 25$ case which experiences a sharp increase at $t = 600$, corresponding to a temporary increase in the total number of virus particles, as seen in Figure 4.10c.

On the basis of this data, we conclude that the initial virus distribution (and concentration) has minimal effect on the outcome of therapy in the dense case.

4.4.4 Burst time

In the analysis of Sections 4.4.1–4.4.3, we have presented the effects of parameters on simulations for a range of burst times. This analysis showed that the equilibrium number of virus particles in the system during a wave expansion, which was previously related to wave speed in Section 2.6, increases with burst time. This property of the virus species may be used to compensate for experimental scenarios with a high free virus death rate or smaller burst size.

We also saw that the speed of the infection wave (given by the rate of change of virus displacement) generally increased with burst time. However, the form of the wave speed dependence changes with the value of other parameters; in particular, the wave speed increases linearly with τ for small values of diffusion ratio, $D = [0.1, 0.25]$, while larger values of diffusion ratio, $D = [0.75, 1.0]$ resulted in a sub-linear increase. This eventually leads to a turning point for wave speed dependence on τ in the $D = 1.0$ case, where the largest observed wave speed was for $\tau = 15$, rather than $\tau = 25$. As the rate of removal of uninfected cells is closely linked to the speed of virus spread, this also increases linearly and then sub-linearly with burst time for larger D.

While this linear to sub-linear transition in the wave speed dependence on τ was also observed for different burst sizes, α, there was no turning point evident for $\alpha = [10, 100, 1000]$, and the increase in wave speed was monotonic for increasing burst time. This was also the case with the rate of removal of uninfected cells from the system.

Finally, the wave speed dependence for a range of initial virus particle distribution areas was linear and monotonically increasing with τ. The same is true for the rate of removal of uninfected cells from the system, as well the total number of virus particles at equilibrium.

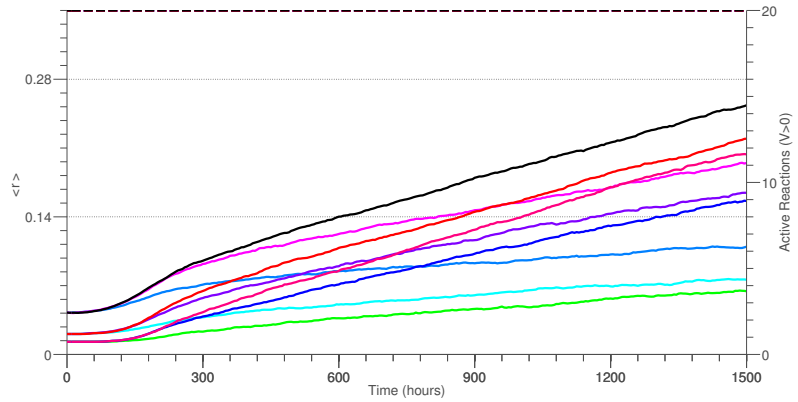

(a) Mean virus displacement for ongoing reactions for varying initial injection area in dense case.

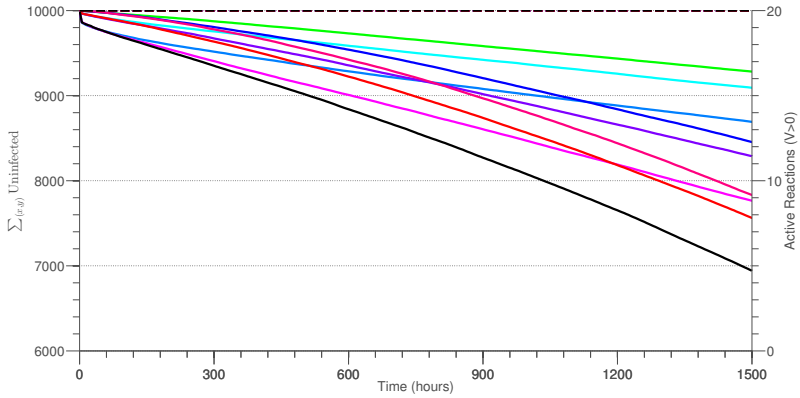

(b) Mean number of uninfected cells for ongoing reactions for varying initial injection area in dense case.

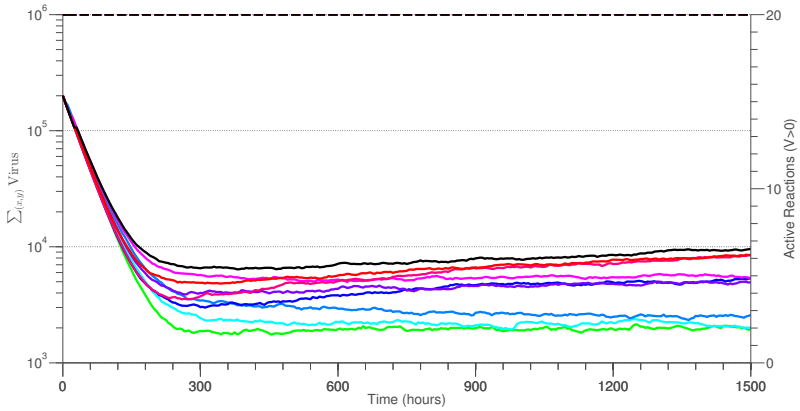

(c) Semi-log plot of mean total virus particles of ongoing reactions for varying initial injection in dense case.

A \ τ	5	15	25
1×1			
5×5			
11×11			

(d) Plot legend.

A \ τ	5	15	25
1×1	4.0×10^{-5}	1.1×10^{-5}	14.5×10^{-5}
5×5	4.1×10^{-5}	1.1×10^{-5}	14.3×10^{-5}
11×11	4.2×10^{-5}	1.0×10^{-5}	14.6×10^{-5}

(e) Wave speed fit (mmhr^{-1}) from Figure 4.10a.

Figure 4.10: Mean virus displacement, total uninfected cells and total virus particles of ongoing reactions for varying initial injection area in dense case. Dashed lines indicate number of non-extinct simulations.

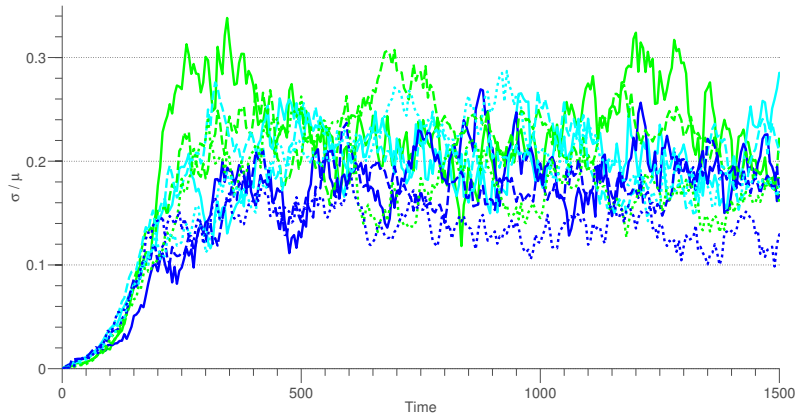

(a) Coefficient of Variation of virus particle displacement for $A = [1 \times 1,\ 5 \times 5,\ 11 \times 11]$ (blue, green, cyan) for $\tau = [5,\ 15,\ 25]$ hrs (solid, dashed, dotted) in dense case.

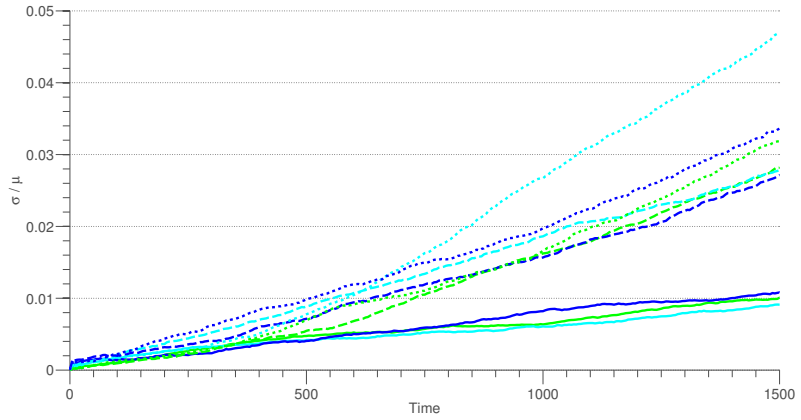

(b) Coefficient of variation for total uninfected cells for $A = [1 \times 1,\ 5 \times 5,\ 11 \times 11]$ (blue, green, cyan) for $\tau = [5,\ 15,\ 25]$ hrs (solid, dashed, dotted) in dense case.

Figure 4.11: Variability of ensembles for varying injection area in dense case.

4.4.5 Burst time versus motility coefficient

Having seen the qualitative effects of increasing burst time in Section 4.4.4, we tested the hypothesis that a reduced uninfected (and hence, infected) cell motility coefficient could be compensated for by a longer burst time. Using the baseline parameters outlined in Section 4.2.1 ($D_n^* = 2.08 \times 10^{-5}$ mm^{2}hr and $\tau^* = [5,\ 15,\ 25]$ hrs) as a control, we looked at the behaviour of a system with $D_n = 1/2 D_n^*$ and $\tau = 2\tau^*$.

In Figures 4.12a–4.12b, we see that there is a significant difference in the mean wave speed and rate of removal of uninfected cells between the two cases; the baseline case, (D_n^*, τ^*), resulted in both a faster wave speed and faster removal of uninfected cells than the corresponding $(1/2 D_n^*, 2\tau^*)$ cases. This is despite the fact that the mean total number of virus particles in the system, shown in Figure 4.12c, is an order of magnitude greater for $(1/2 D_n^*, 2\tau^*)$, and is likely due to decreased effects of the virus death term for longer burst times.

From the initial distribution of virus particles, the $(1/2 D_n^*, 2\tau^*)$ simulations show piecewise jumps in coefficient of variation of virus displacement compared to the smoother increases for (D_n^*, τ^*) for $t \in [0, 50]$ (Figure 4.13a). No extinction was observed in any simulations over time interval $t \in [0\ 1500]$, and the coefficient of variation of virus displacement fluctuated about a steady state for $t > 300$, corresponding to the system reaching a travelling wave state. This steady-state value of the coefficient of variation, $\sigma/\mu \approx 0.2$, was exhibited by all simulations and burst times. We therefore expect to see similar distribution of virus displacement between simulations in the long-time limit.

The coefficient of variation for total uninfected cells in the system, shown in Figure 4.13b, is small, and we expect a tightly bound distribution of total uninfected cells about the mean value. However, in relative terms, there is a significant relative difference in the coefficients of variation for total uninfected cells in the system between the (D_n^*, τ^*) and $(1/2 D_n^*, 2\tau^*)$ cases. While the rate of change for the $\tau^* = 5$ case is comparable to the corresponding $2\tau^*$ simulations, the rate of change of the coefficient of variation of total uninfected cells for baseline $\tau^* = [15,\ 25]$ simulations grow significantly faster than the corresponding $(1/2 D_n^*, 2\tau^*)$ cases.

The distributions of virus displacement and total uninfected cells at $t = 1000$, shown in Figure 4.14, confirm the conclusions from the coefficients of variation of the simulations. For $\tau^* = 5$, the distributions of virus displacement for (D_n^*, τ^*) and $(1/2 D_n^*, 2\tau^*)$ show similar deviation and are tightly bound around their respective means. In the $\tau^* = [15,\ 25]$ cases, the distribution of virus displacement for the (D_n^*, τ^*) simulations is spread over a broader range of displacements, and show a leading tail for larger values of τ^*. The distribution of total uninfected cells in the system for (D_n^*, τ^*) show similar spread for increasing τ^* compared to the $(1/2 D_n^*, 2\tau^*)$ simulations, with the formation of a tail for larger values of τ^*. The $(1/2 D_n^*, 2\tau^*)$ simulations do not show any significant changes in spread with increasing τ^*, and no tail or leading edge is formed.

The significant differences in mean wave speed and rate of removal of total uninfected cells in the long-time limits shows that the (D_n^*, τ^*) and $(1/2 D_n^*, 2\tau^*)$ cases are not equivalent. Moreover, the distributions of virus displacements and uninfected cells show that this is a qualitative difference between these parameter sets in the dense uninfected cells case.

4.4.6 Summary

The qualitative effects of burst time, diffusion ratio, burst size and initial condition on simulations for the dense uninfected cell case are shown in Table 4.3. On the basis of stochastic simulations for the parameter range outlined in Section 4.2.1, the following conclusions can be made:

- Complete failure of therapy due to virus extinction did not occur
- Wave speed generally increased for longer burst time, but reached a saturation point for large values
- Burst size exhibited threshold behaviour, above which the wave speed does not change
- The initial concentration of virus particles does not affect the properties of the travelling wave
- An increasing rate of change of coefficient of variation of virus displacement in time is accompanied by a constant coefficient of variation of total uninfected cells (and vice versa)

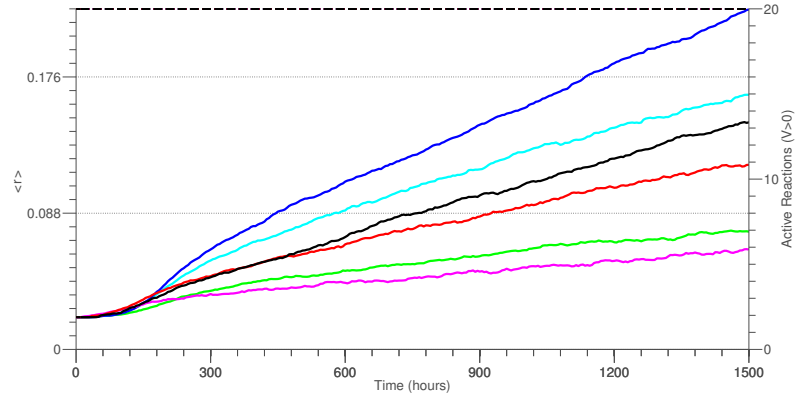

(a) Mean virus displacement for ongoing reactions for (D_n, τ) and $\left(\frac{1}{2}D_n, 2\tau\right)$ in dense case.

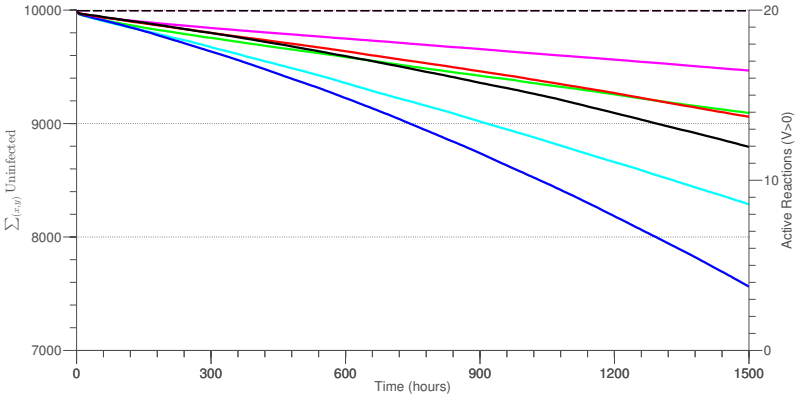

(b) Mean of total uninfected cells of ongoing reactions for (D_n, τ) and $\left(\frac{1}{2}D_n, 2\tau\right)$ in dense case.

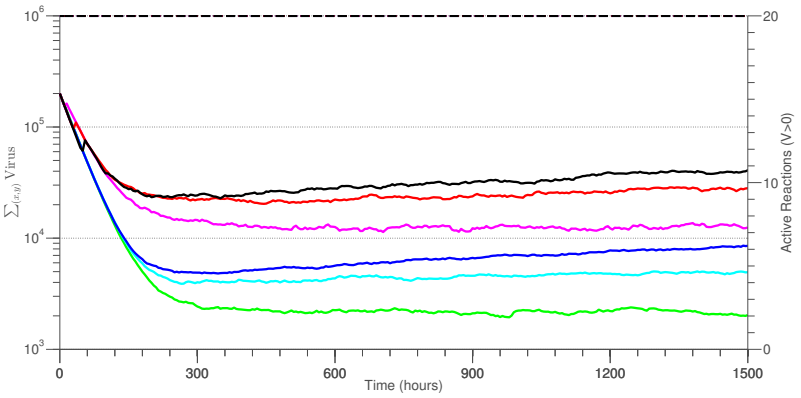

(c) Semi-log plot of mean total virus particles of ongoing reactions for (D_n, τ) and $\left(\frac{1}{2}D_n, 2\tau\right)$ in dense case.

	$D_n = 1.04 \times 10^{-5}$			$D_n = 2.08 \times 10^{-5}$		
	$\tau = 10$	$\tau = 30$	$\tau = 50$	$\tau = 5$	$\tau = 15$	$\tau = 25$

(d) Plot legend.

	$D_n = 1.04 \times 10^{-5}$			$D_n = 2.08 \times 10^{-5}$		
	$\tau = 10$	$\tau = 30$	$\tau = 50$	$\tau = 5$	$\tau = 15$	$\tau = 25$
c	2.6×10^{-5}	6.6×10^{-5}	8.2×10^{-5}	4.1×10^{-5}	1.1×10^{-5}	14.3×10^{-5}

(e) Wave speed fit (mmhr^{-1}) from Figure 4.12a.

Figure 4.12: Mean virus displacement, total uninfected cells and total virus particles of ongoing reactions for $(D_n,\ \tau)$ and $(1/2D_n,\ 2\tau)$ in dense case. Dashed lines indicate number of non-extinct simulations.

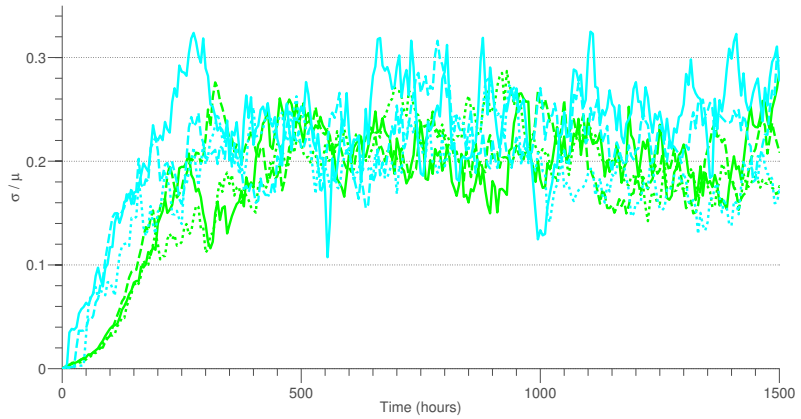

(a) Coefficient of Variation of virus particle displacement for $(D_n,\ \tau)$ (green) and $(1/2 D_n,\ 2\tau)$ (cyan) for $\tau^* = [5,\ 15,\ 25]$ hrs (solid, dashed, dotted) in dense case.

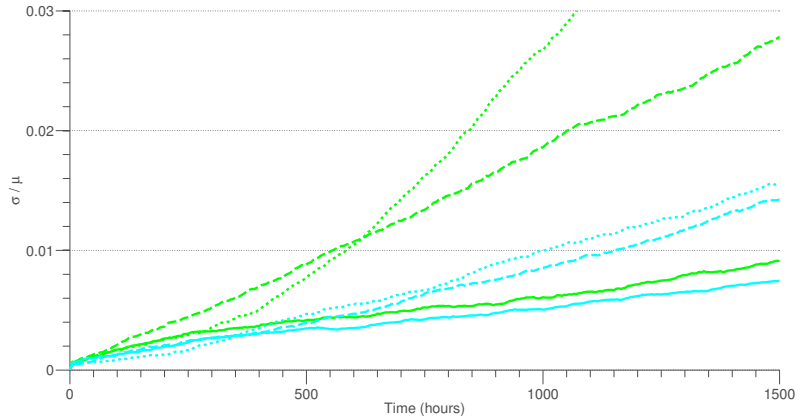

(b) Coefficient of variation for total uninfected cells for $(D_n,\ \tau)$ (green) and $(1/2 D_n,\ 2\tau)$ (cyan) for $\tau^* = [5,\ 15,\ 25]$ hrs (solid, dashed, dotted) in dense case.

Figure 4.13: Variability of ensembles for $(D_n,\ \tau)$ and $(1/2 D_n,\ 2\tau)$ for in dense case.

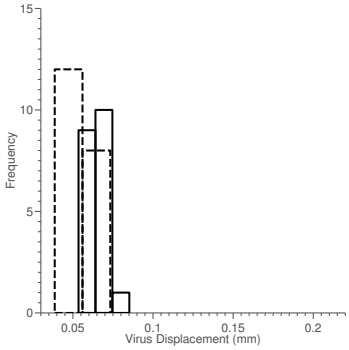

(a) Virus displacement at $t = 1000$ for $\tau^* = 5$.

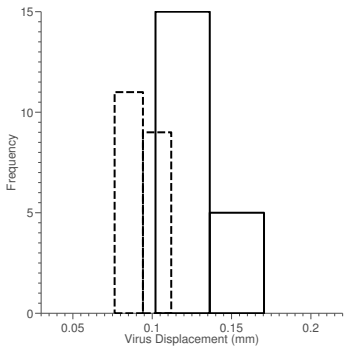

(b) Virus displacement at $t = 1000$ for $\tau^* = 15$.

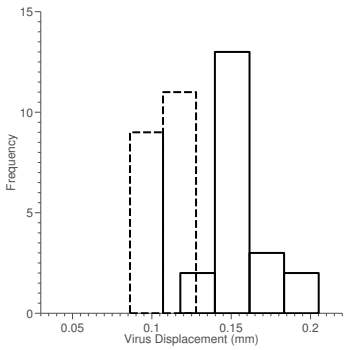

(c) Virus displacement at $t = 1000$ for $\tau^* = 25$.

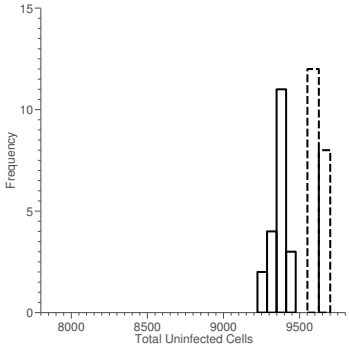

(d) Total uninfected cells at $t = 1000$ for $\tau^* = 5$.

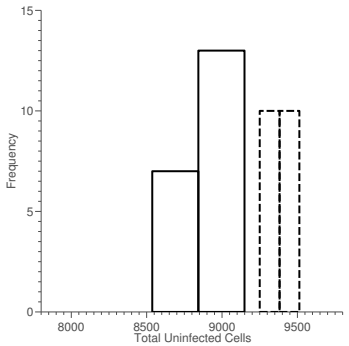

(e) Total uninfected cells at $t = 1000$ for $\tau^* = 15$.

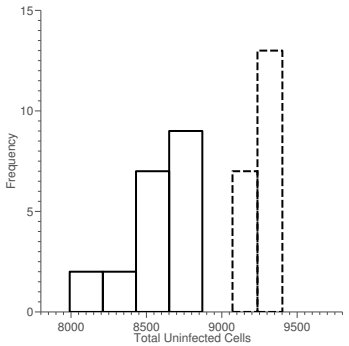

(f) Total uninfected cells at $t = 1000$ for $\tau^* = 25$.

Figure 4.14: Distribution of virus displacement and total uninfected cells for $D_n = D_n^*$, $\tau = \tau^*$ (solid) and $D_n = \frac{1}{2}D_n^*$, $\tau = 2\tau^*$ (dashed).

	Wave speed (c)	Rate of change of C.o.V. $\left(\frac{\Delta\left(\frac{\sigma}{\mu}\right)}{\Delta t}\right)$	Rate of uninfected cell removal $\left(\frac{\Sigma_{x,y} n_0 - \Sigma_{x,y} n}{\Delta t}\right)$	Equilibrium Virus particles $\left(\sum_{x,y} V_{eq}\right)$
$\tau \uparrow$				
$D \uparrow$				
$\alpha \uparrow$				
$A \uparrow$				

Table 4.3: Qualitative effects of key parameter in dense uninfected cell case. The arrows show qualitative trends in simulation metrics (wave speed, rate of change of C.o.V., rate of uninfected cell removal and total virus particles at equilibrium) for increasing values of independent parameters (τ, D, α, A). Solid lines denote strong sub-linear, linear or super-linear dependence, and dashed lines indicate weak dependence or a threshold condition.

4.5 Sparse case

In the sparse case, the number of uninfected cells (distributed randomly throughout the domain) is significantly less than the overall number of compartments, resulting in a large number of unoccupied compartments. In contrast to the dense case results in Section 4.4, the typical sparse system for parameters outline in Section 4.2.2 exhibits frequent virus extinction, and greatly increased variability between individual simulations. In addition to the rate at which individual simulations become extinct within an ensemble, we also consider the time of onset of extinction, which is the earliest time at which any simulation in the ensemble dies out.

4.5.1 Diffusion ratio

For diffusion ratio values $D = [0.10,\ 0.75]$ over 50 simulations, we find that the rate of change of displacement of virus particles increases with increasing diffusion ratio (Figure 4.15a). This increase in speed of propagation is coupled with a higher mean number of virus particles in the system for active reactions (Figure 4.15c). The rate of removal of uninfected cells, shown in Figure 4.15b, increases with diffusion ratio for $t < 500$, before the onset of the first extinctions in each ensemble, which results in a discontinuous jump in the weighted ongoing mean of uninfected cells.

The coefficient of variation of virus displacement (Figure 4.16a) increases steadily in time, with no significant difference between any set of parameters until the beginning of complete virus extinction in some simulations at $t = 500$. After this time, an increase in the rate of change of coefficient of variation for $D = 0.10$ is linked to an increased rate of simulation extinction in the ensemble (dashed line in Figure 4.15). This implies that a greater number of individual extinctions result in either an increase in the mean, or a decrease in standard deviation. Assuming that the wave of infection continues at constant speed, this means that either the distribution of virus displacements becomes narrower, or the mean behaviour in Figure 4.15a was dominated by the simulations that are the first to exhibit virus extinction.

The coefficient of variation for total uninfected cells in the system (Figure 4.16b) is an order of magnitude lower than in the dense case (due to the decrease in initial mean uninfected cells), but increases steadily for both values of D. With the beginning of complete virus extinction in some simulations at $t = 500$, the coefficient of variation for the $D = 0.10$ case approaches a constant value, but continues to increase in the $D = 0.75$ simulations. This suggests that the first few simulations to exhibit extinction were far from the mean and unlikely to ever sustain a viable reaction, despite contributing to the virus displacement.

The distribution of virus displacement at $t = 450$ (Figures 4.16c–4.16e), prior to the onset of extinction of individual simulations, show a qualitatively similar distribution for the $D = 0.10$ and $D = 0.75$ cases for $\tau = [5,\ 15]$. The distribution has a long tail, with the $D = 0.75$ case showing greater spread, particularly for $\tau = 15$. The distribution of virus displacements for the $\tau = 25$ simulations (Figure 4.16e) shows a smaller secondary peak in virus displacement at $\langle r \rangle = 0.08$ mm for $D = 0.75$, indicating a secondary wave speed steady state. The broader distribution of virus displacements for $D = 0.75$ is reflected in the variability of total uninfected cells removed from the system, as shown in Figure 4.16b.

4.5.2 Burst size

The burst size plays an important role in the sparse case. As with the dense case, the speed of virus particle propagation increases with burst size α (Figure 4.17a and 4.17e), and there is also a noticeable increase in the rate of change of wave speed for increasing τ in the $\alpha = 1000$ case, compared to $\alpha = 100$. The rate of simulation die-out also decreases significantly for higher burst size, with the number of non-extinct simulations at $t = 1000$ an order of magnitude greater than for $\alpha = 100$ (Figure 4.17b).

From the mean total of uninfected cells for ongoing reactions in Figure 4.17b, we see no difference in the rate of decay of uninfected cells for varying α and τ, but the onset of individual simulation die-out for $\alpha = 1000$ is delayed with increasing burst time, τ. This is

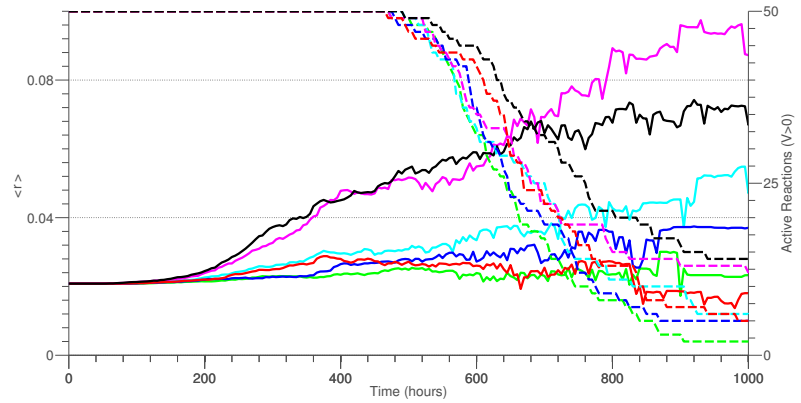

(a) Mean virus displacement for ongoing reactions for varying diffusion ratio in sparse case.

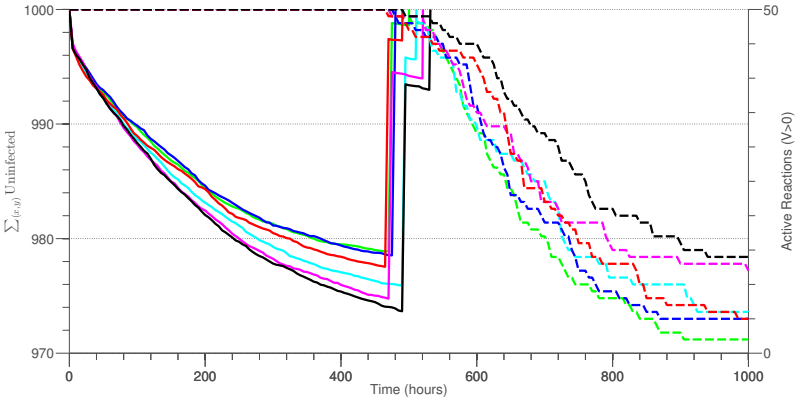

(b) Mean total uninfected cells for ongoing reactions for varying diffusion ratio in sparse case.

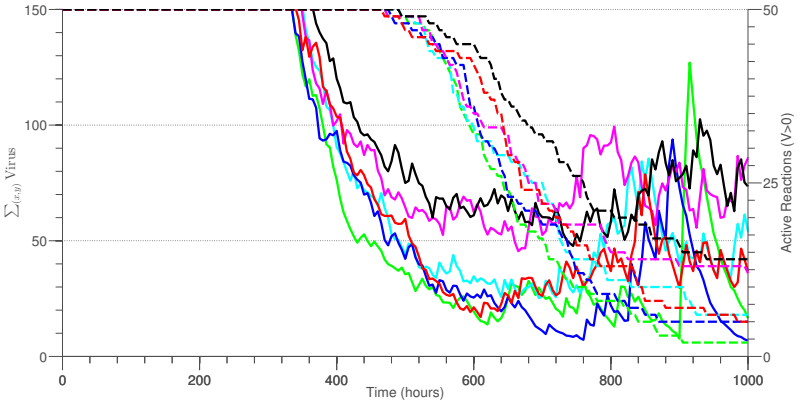

(c) Mean total virus particles for ongoing reactions for varying diffusion ratio in sparse case.

D \ τ	5	15	25
0.10			
0.75			

(d) Plot legend.

D \ τ	5	15	25
0.10	1.0×10^{-5}	1.7×10^{-5}	2.4×10^{-5}
0.75	3.2×10^{-5}	9.8×10^{-5}	10.2×10^{-5}

(e) Wave speed fit (mmhr^{-1}) from Figure 4.15a.

Figure 4.15: Mean virus displacement, total uninfected cells and total virus particles of ongoing reactions for varying diffusion ratio in sparse case. Dashed lines indicate number of non-extinct simulations.

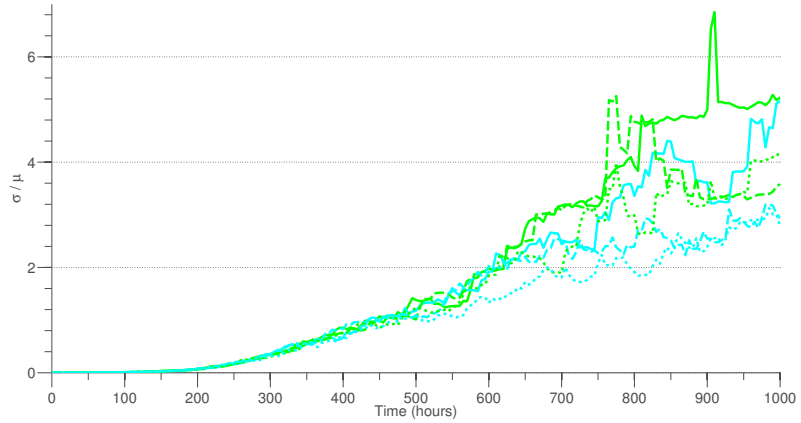

(a) Coefficient of Variation of Virus Displacement for diffusion ratio $D = [0.1, 0.75]$ (green, cyan) for $\tau = [5,\ 15,\ 25]$ hrs (solid, dashed, dotted) in sparse case.

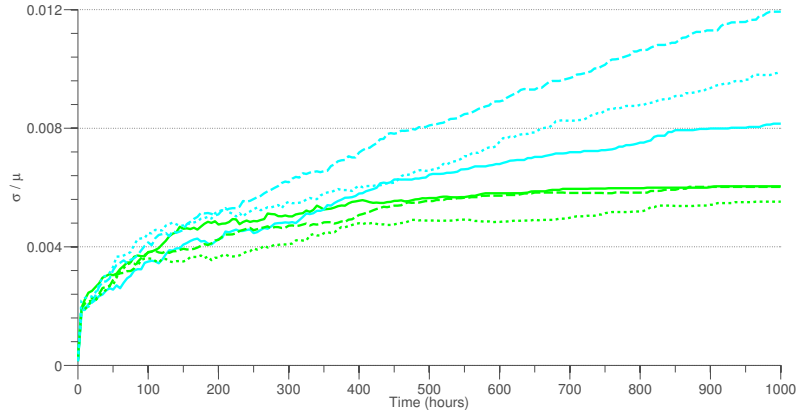

(b) Coefficient of Variation of total uninfected cells for diffusion ratio $D = [0.1, 0.75]$ (green, cyan) for $\tau = [5,\ 15,\ 25]$ hrs (solid, dashed, dotted) in sparse case.

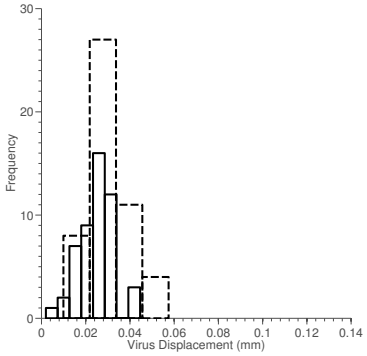

(c) Distribution of virus displacements at $t = 450$ for $\tau = 5$ for $D = [0.10,\ 0.75]$ (solid, dashed).

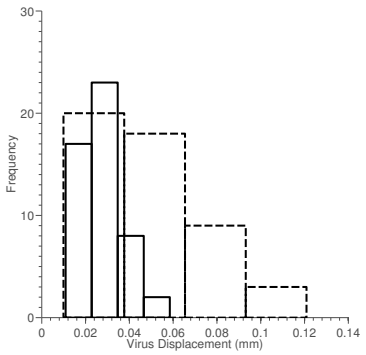

(d) Distribution of virus displacements at $t = 450$ for $\tau = 15$ for $D = [0.10,\ 0.75]$ (solid, dashed).

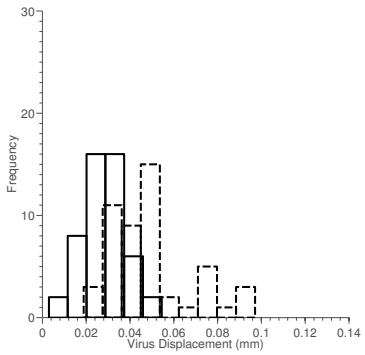

(e) Distribution of virus displacements at $t = 450$ for $\tau = 25$ for $D = [0.10,\ 0.75]$ (solid, dashed).

Figure 4.16: Variability of ensembles for varying diffusion ratio in sparse case.

in contrast to the $\alpha = 100$ case, where the first sets of reaction to exhibit virus extinction occur at $t \approx 500$, independent of τ, and this prolonged duration of simulations results in more uninfected cells removed from the system, despite identical rates of removal for $t < 300$.

The mean number of virus particles for ongoing reactions increases with the burst size, as shown in Figure 4.17c, where the $\alpha = 1000$ simulations reach an equilibrium number two orders of magnitude greater than the $\alpha = 100$ simulations. Combined with the mean virus displacement, this agrees with the analysis of the continuum model from Section 2.6.2, which related the total number of virus particles in the steady state to the wave speed.

The coefficient of variation for displacement of virus particles for $\alpha = 1000$ is initially greater than for the $\alpha = 100$ simulations due to discontinuous jumps in virus displacement associated with large burst events (Figure 4.18a). After this initial transient period, both sets of simulations settle into equilibrium behaviour, where we observe the rate of increase of coefficient of variation in time for $\alpha = 1000$ to be lower than that of $\alpha = 100$, with the intersection occurring at $t \approx 400$. After this point, the coefficient of variation for $\alpha = 1000$ flattens out, while the $\alpha = 100$ case continues to grow, until eventual extinction at $t \approx 1000$. The converse is true for the coefficient of variation of total uninfected cells (Figure 4.18b), with the rate of increase for $\alpha = 1000$ reaching constant increase for $t > 200$, while the $\alpha = 100$ simulation reach a constant coefficient of variation for $t > 750$.

The distribution of virus displacements prior to the first extinction event at $t = 450$ shows a similar shape between the $\alpha = 100$ and $\alpha = 1000$ cases for all values of τ examined (Figures 4.18c–4.18e). The larger burst $\alpha = 1000$ burst size has a greater mean value, shifting the distribution to the right compared to the $\alpha = 100$ case. In addition to this, the $\tau = 5$ and $\tau = 25$ cases show a small number of simulations with a significantly higher displacement of virus particles, suggesting that multiple steady states may be possible, with some supporting a much higher wave speed of infection.

4.5.3 Injection area and virus concentration

Changing the initial distribution (and hence concentration) of virus particles in the sparse uninfected cell case results in an increase in the rate of change of virus displacement (Figure 4.19a). As in Section 4.5.2, the rate of increase of displacement with increasing burst time is greater for the $A = 11 \times 11$ case compared to that of $A = 5 \times 5$.

The broader initial spread of virus particles in the $A = 11 \times 11$ simulations results in a higher rate of uninfected cell removal from the system than the $A = 5 \times 5$ initial condition (Figure 4.19b), but does not affect the onset or rate of individual simulation die-out. Similarly, Figure 4.19c shows that the initial distribution does not affect the mean number of virus particles in ongoing reactions, which is significantly smaller than the initial

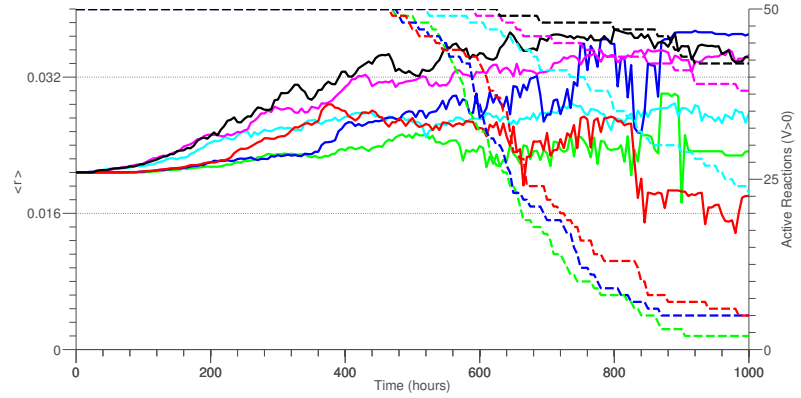

(a) Mean virus displacement for ongoing reactions for varying burst size in sparse case.

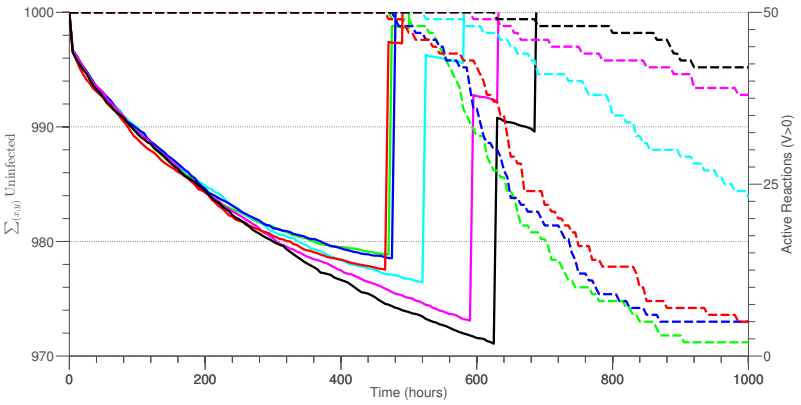

(b) Mean of total uninfected cells of ongoing reactions for varying burst size in sparse case.

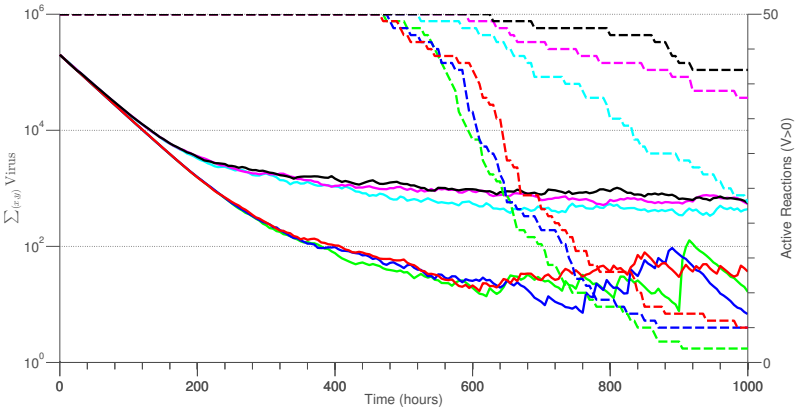

(c) Semi-log plot of mean total virus particles of ongoing reactions for varying burst size in sparse case.

α \ τ	5	15	25
100			
1000			

(d) Plot legend.

α \ τ	5	15	25
100	1.0×10^{-5}	1.7×10^{-5}	2.4×10^{-5}
1000	1.4×10^{-5}	2.4×10^{-5}	3.5×10^{-5}

(e) Wave speed fit (mmhr^{-1}) from Figure 4.17a.

Figure 4.17: Mean virus displacement, total uninfected cells and total virus particles of ongoing reactions for varying burst size in sparse case. Dashed lines indicate number of non-extinct simulations.

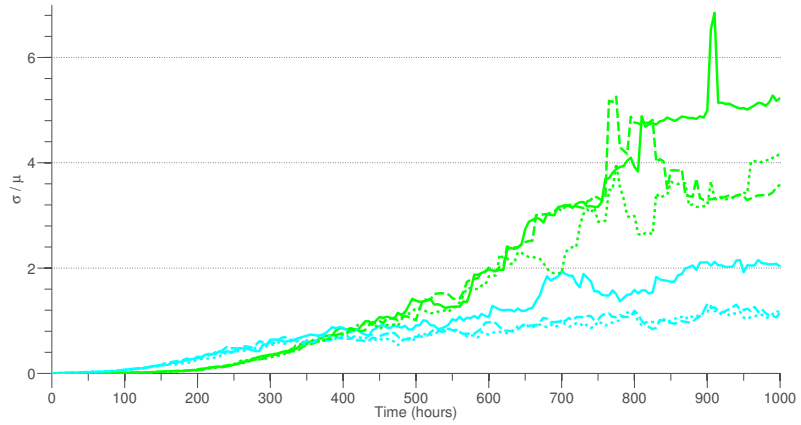

(a) Coefficient of Variation of Virus Displacement for burst size $\alpha = [100, 1000]$ (green, cyan) for $\tau = [5,\ 15,\ 25]$ hrs (solid, dashed, dotted) in sparse case.

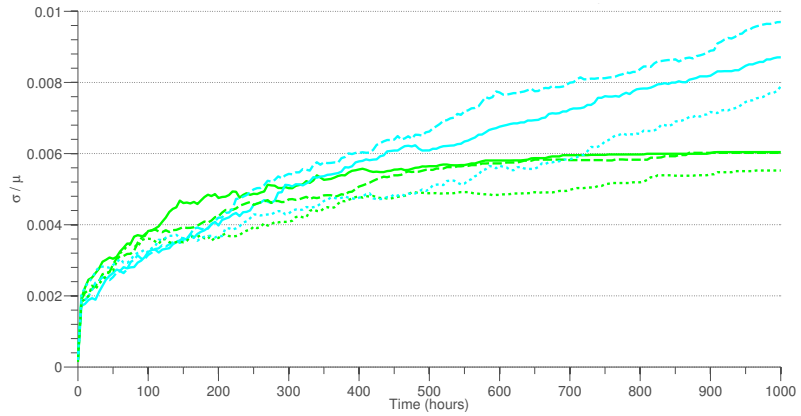

(b) Coefficient of variation for total uninfected cells for burst size $\alpha = [100, 1000]$ (green, cyan) for $\tau = [5,\ 15,\ 25]$ hrs (solid, dashed, dotted) in sparse case.

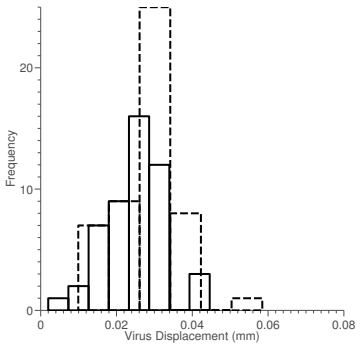

(c) Distribution of virus displacements at $t = 450$ for $\tau = 5$ for $\alpha = [100,\ 1000]$ (solid, dashed).

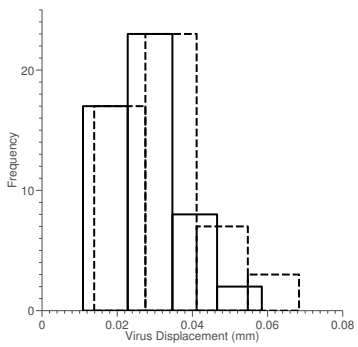

(d) Distribution of virus displacements at $t = 450$ for $\tau = 15$ for $\alpha = [100,\ 1000]$ (solid, dashed).

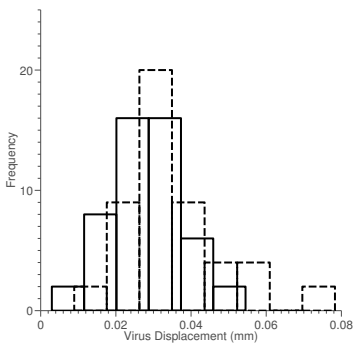

(e) Distribution of virus displacements at $t = 450$ for $\tau = 25$ for $\alpha = [100,\ 1000]$ (solid, dashed).

Figure 4.18: Variability of ensembles for varying burst size in sparse case.

number of virus particles in the system. The large decrease in virus population from initial distribution suggests that, for a fixed number of initial virus particles, a broad distribution of virus particles at a lower concentration would be a more effective treatment method for removing uninfected cells for a sparse initial condition.

There is no difference in the coefficient of variation of displacement of virus particles for different injection areas, with a linear increase in time for $t > 200$ (Figure 4.20a). At $t \approx 600$, the $\tau = 5$ and $\tau = 15$ cases of the $A = 11 \times 11$ simulations experience a discontinuous jump in the coefficient of variation due to the extinction of $10 - 20\%$ of simulations in a very short period of time.

The coefficient of variation for total uninfected cells in the system, shown in Figure 4.20b, increases at the same rate for both $A = 5 \times 5$ and $A = 11 \times 11$ cases. The difference in the size of the initial jump over $t \in [0,\ 25]$ is due to the greater spread of virus particles in the $A = 11 \times 11$ case, and this is reflected by a factor of 2.2 in the absolute value of the coefficient of variation. The decreasing rate of change for $t > 200$ in Figure 4.20b coincides with the increasing rate of change of coefficient of variation of virus displacement in Figure 4.20a, which is typical of bulk extinction. We can therefore conclude that the mean of total virus particles for ongoing reactions in Figure 4.19c for $t > 500$ is unlikely to be a true steady-state, and is more likely to be transient decay behaviour.

The distributions of virus displacement prior to the onset of extinction at $t = 450$, shown in Figures 4.20c–4.20e, confirm the qualitative similarities between the initial conditions. While there is a significant difference between the virus displacements in the two cases, this is equal to the difference in initial radial displacement, and the shape of the distributions does not change for burst times $\tau = 5$ and $\tau = 15$. When $\tau = 25$, the distribution of virus particles for $A = 11 \times 11$ appears to show a bimodal distribution. This peak separation suggests that it is possible for some reactions to keep propagating, despite most simulations experiencing extinction by $t = 1000$.

4.5.4 Burst time

The analysis in Sections 4.5.1–4.5.3 considered the effects of diffusion ratio, burst size and virus initial condition for a range of burst times. The wave speed of virus propagation increases with longer burst time, but in contrast to the dense case in Section 4.4, there is no significant change in the mean number of virus particles in the system. This is a consequence of the decreased uninfected cell density, and arises from the fact that virus particles need to travel further in the infected cell state to encounter uninfected cells. This is evident in Section 4.5.1, where the $\tau = 5$ and $\tau = 15$ cases for $D = 0.75$ show a significant jump in the mean number of virus particles, in contrast to the $D = 0.10$ case.

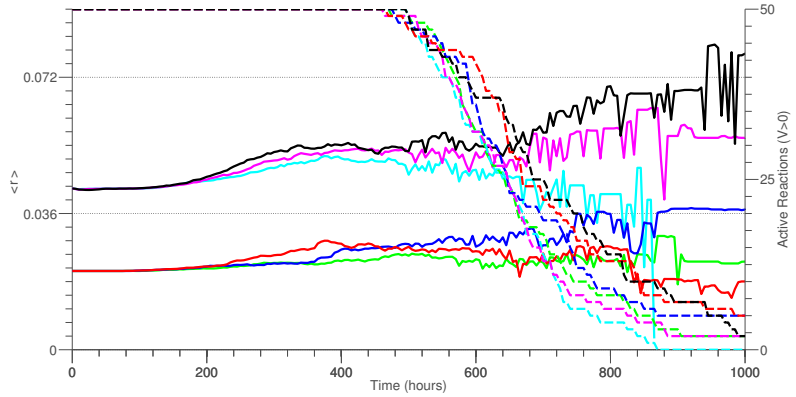

(a) Mean virus displacement for ongoing reactions for varying initial injection area in sparse case.

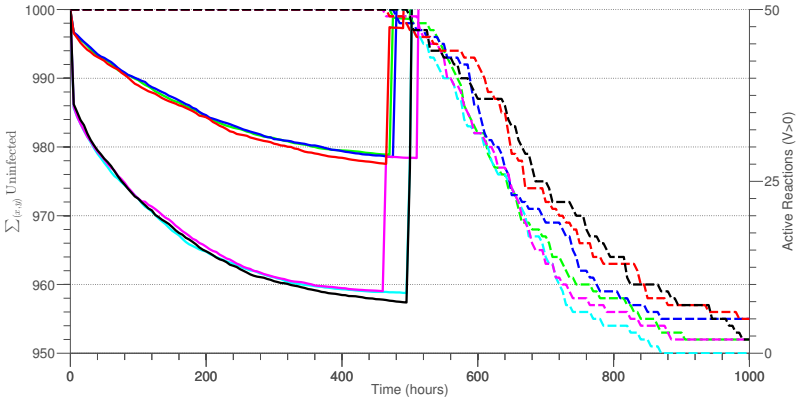

(b) Mean number of uninfected cells for ongoing reactions for varying initial injection area in sparse case.

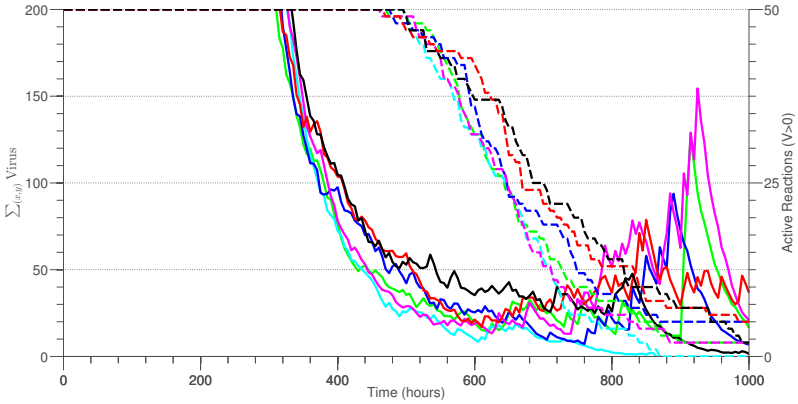

(c) Mean total virus particles of ongoing reactions for varying initial injection in dense case.

A \ τ	5	15	25
5×5			
11×11			

(d) Plot legend.

A \ τ	5	15	25
5×5	1.0×10^{-5}	1.7×10^{-5}	2.4×10^{-5}
11×11	3.7×10^{-5}	4.8×10^{-5}	6.3×10^{-5}

(e) Wave speed fit (mmhr^{-1}) from Figure 4.19a.

Figure 4.19: Mean virus displacement, total uninfected cells and total virus particles of ongoing reactions for varying initial injection area in sparse case. Dashed lines indicate number of non-extinct simulations.

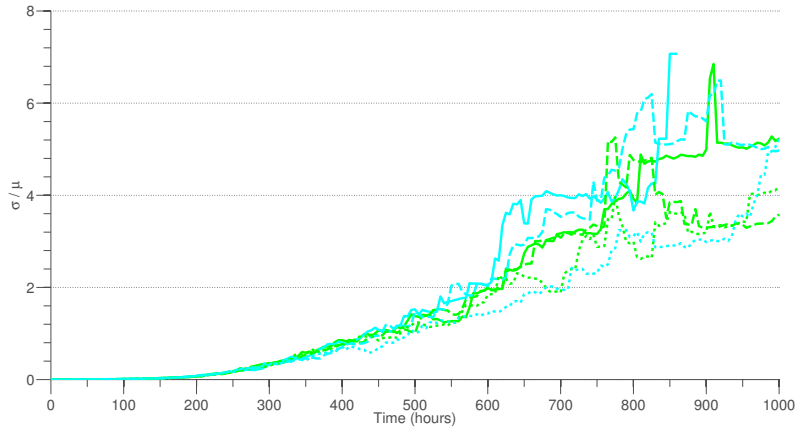

(a) Coefficient of Variation of virus particle displacement for $A = [5 \times 5,\ 11 \times 11]$ (green, cyan) for $\tau = [5,\ 15,\ 25]$ hrs (solid, dashed, dotted) in sparse case.

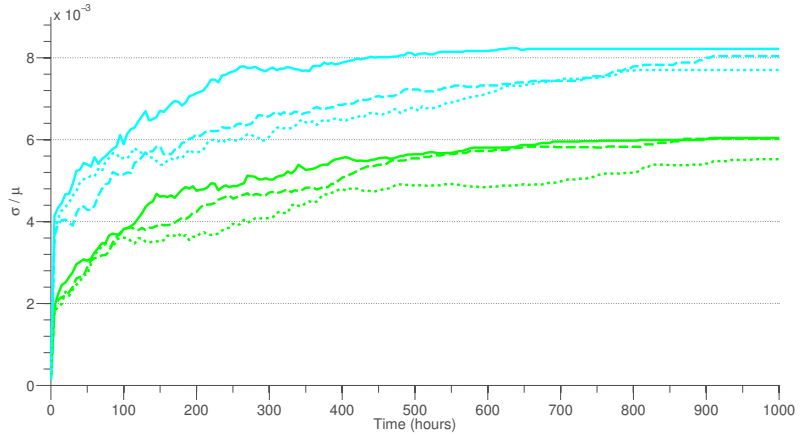

(b) Coefficient of variation for total uninfected cells for $A = [5 \times 5,\ 11 \times 11]$ (blue, green, cyan) for $\tau = [5,\ 15,\ 25]$ hrs (solid, dashed, dotted) in sparse case.

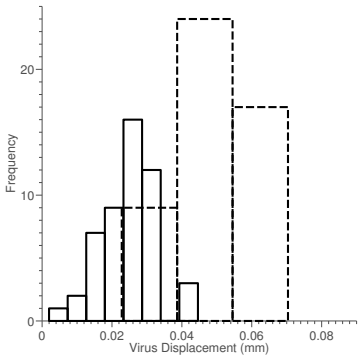

(c) Distribution of virus displacements at $t = 450$ for $\tau = 5$ for $A = [5{\times}5,\ 11{\times}11]$ (solid, dashed).

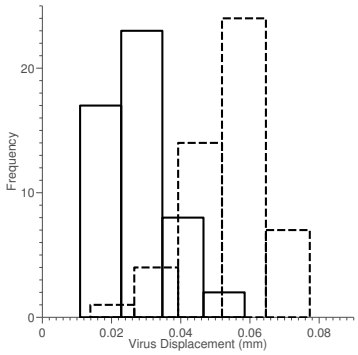

(d) Distribution of virus displacements at $t = 450$ for $\tau = 15$ for $A = [5{\times}5,\ 11{\times}11]$ (solid, dashed).

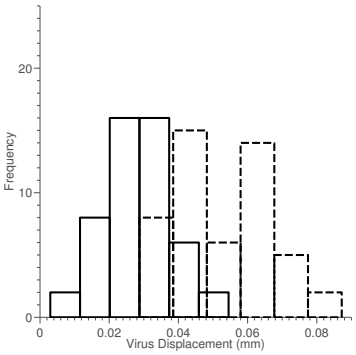

(e) Distribution of virus displacements at $t = 450$ for $\tau = 25$ for $A = [5{\times}5,\ 11{\times}11]$ (solid, dashed).

Figure 4.20: Variability of ensembles for varying injection area in sparse case.

In comparison to the dense case, the wave speed of infection in the sparse case is an order of magnitude smaller, and the large number of virus extinctions in individual simulations limits direct comparisons for the base parameter set. The mean wave speed increases linearly with burst time for $D = 0.10$, but transitions to a sub-linear dependence for $D = 0.75$, as in the dense case. Unlike the dense case, the mean wave speed dependence on burst time remains linear for the larger $\alpha = 1000$ case, most likely due to the lower concentration gradient of uninfected cells between the reaction zone and the remainder of the system.

No significant change in coefficient of variation of virus particles is observed between different burst times, implying that the effects of varying burst time in the simulations are qualitatively different from parameters such as the diffusion ratio. While the rate of simulation die-out was not affected by the burst time, the onset of extinction was delayed by longer burst times. This is not unexpected, as remaining in the infected cell state for a longer time allows the burst event to take place further from regions depleted of uninfected cells.

4.5.5 Burst time versus motility coefficient

In contrast to the dense uninfected cell in Section 4.4.5, we find that the mean wave speed of ongoing reaction for the $(1/2 D_n^*, 2\tau^*)$ simulations is consistently higher than the baseline (D_n^*, τ^*) case for sparse uninfected cell initial condition (Figure 4.21a). As with the dense case, the mean number of virus particles in the system, shown in Figure 4.21c, is greater for all $(1/2 D_n^*, 2\tau^*)$ simulations, with the increased burst time reducing the effects of the virus death term. Despite this increased wave speed and number of virus particles, the mean rate of removal of uninfected cells for $(1/2 D_n^*, 2\tau^*)$ is lower than the (D_n^*, τ^*) simulations for all τ^* (Figure 4.21b).

The first extinction happens in the $(1/2 D_n^*, 2\tau^*)$ simulations for $\tau^* = 25$ at $t = 450$, but in general, the rate of extinction is significantly slower for $(1/2 D_n^*, 2\tau^*)$ simulations compared to (D_n^*, τ^*) due to the greater number of virus particles in the system. Unlike the (D_n^*, τ^*) simulations, which exhibit the same initial onset time and extinction rates, the $(1/2 D_n^*, 2\tau^*)$ simulations show a delay in the onset of extinction for shorter burst time. This is a surprising result, and is in contrast to the burst size simulations for $\alpha = 1000$ in Section 4.5.2, where the onset of extinction was delayed for longer burst times. Despite the earliest onset of extinction occurring for $\tau^* = 25$ in the $(1/2 D_n^*, 2\tau^*)$ case, these simulations have the slowest rate of extinction overall, suggesting that this anomaly is due to variability between individual simulations.

The coefficient of variation of virus displacement (Figure 4.22a) increases in time for all parameter sets, with the $(1/2 D_n^*, 2\tau^*)$ simulations initially having a slightly greater absolute value, but a smaller rate of increase. The slower rate results in the (D_n^*, τ^*)

simulations reaching a greater absolute value of coefficient of variation of virus displacement around the time of the onset of virus extinction at $t \approx 450$. As is the case with all other sets of parameters examined, a greater rate of change of coefficient of variation of virus displacement is coupled with a smaller rate of change of the coefficient of variation of total uninfected cells (Figure 4.22b).

From the distributions of virus displacements prior to the onset of extinction at $t = 450$ (Figure 4.22c–4.22e), we see that while the (D_n^*, τ^*) distributions is typically symmetrical, the distributions for the $(1/2 D_n^*, 2\tau^*)$ case are more tightly bound for virus displacements smaller than the mean, and have a longer tails for displacements larger than the mean. In the case of $\tau^* = 25$, we also see a small secondary peak at $\langle r \rangle = 0.65$ in the $(1/2 D_n^*, 2\tau^*)$ case, which could be attributed to either a faster steady state or transient behaviour that would approach the mean value in the long-time limit if extinction did not occur.

4.5.6 Summary

The qualitative effects of burst time, diffusion ratio, burst size and initial condition on simulations for the sparse uninfected cell case are shown in Table 4.4. On the basis of stochastic simulations for the parameter range outlined in Section 4.2.2, the following conclusions can be made:

- Complete failure of therapy due to virus extinction was a typical outcome
- Increased burst size reduced the rate of therapy failure
- Failure of therapy was more likely for shorter burst times
- Broader initial distribution of virus particles increased total number of uninfected cells removed prior to extinction
- An increasing rate of change of coefficient of variation of virus displacement in time is accompanied by a constant coefficient of variation of total uninfected cells (and vice versa)

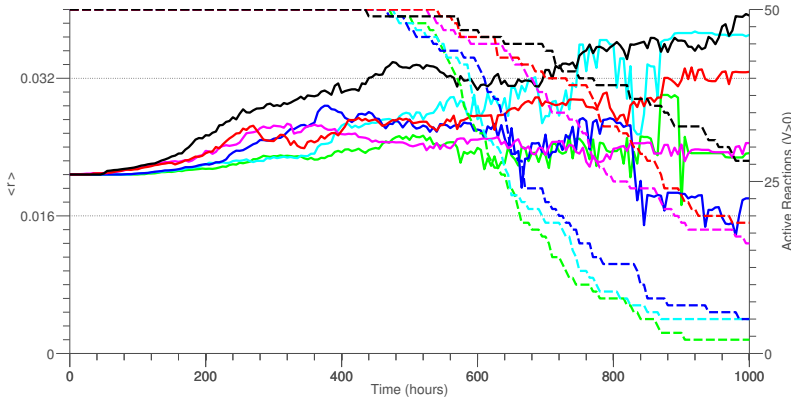

(a) Mean virus displacement for ongoing reactions for (D_n, τ) and $\left(\frac{1}{2}D_n, 2\tau\right)$ in sparse case.

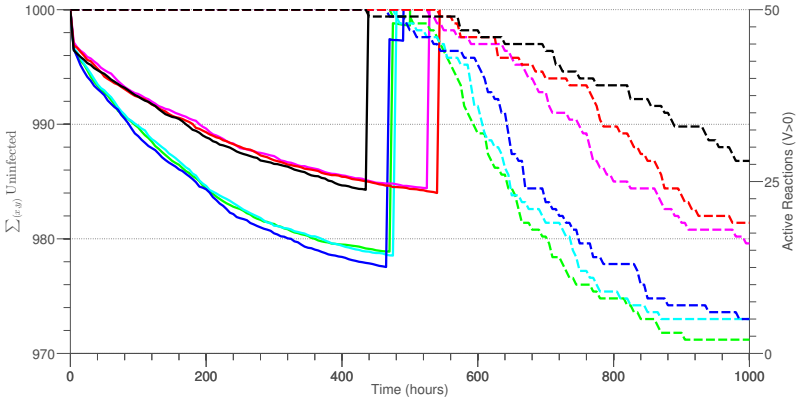

(b) Mean total uninfected cells for ongoing reactions for (D_n, τ) and $\left(\frac{1}{2}D_n, 2\tau\right)$ in sparse case.

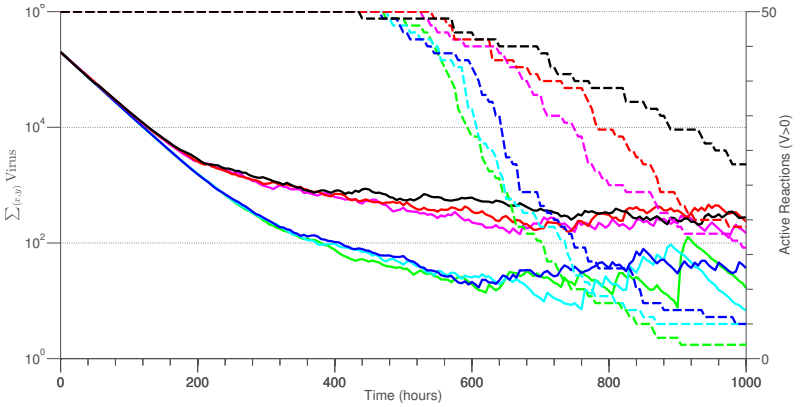

(c) Semi-log plot of mean total virus particles for ongoing reactions for (D_n, τ) and $\left(\frac{1}{2}D_n, 2\tau\right)$ in sparse case.

	$D_n = 1.04 \times 10^{-5}$			$D_n = 2.08 \times 10^{-5}$		
	$\tau = 10$	$\tau = 30$	$\tau = 50$	$\tau = 5$	$\tau = 15$	$\tau = 25$

(d) Plot legend.

	$D_n = 1.04 \times 10^{-5}$			$D_n = 2.08 \times 10^{-5}$		
	$\tau = 10$	$\tau = 30$	$\tau = 50$	$\tau = 5$	$\tau = 15$	$\tau = 25$
c	1.15×10^{-5}	1.26×10^{-5}	2.38×10^{-5}	0.65×10^{-5}	1.03×10^{-5}	1.40×10^{-5}

(e) Wave speed fit (mmhr^{-1}) from Figure 4.21a.

Figure 4.21: Mean virus displacement, total uninfected cells and total virus particles of ongoing reactions for (D_n, τ) and $\left(\frac{1}{2}D_n, 2\tau\right)$ in sparse case. Dashed lines indicate number of non-extinct simulations.

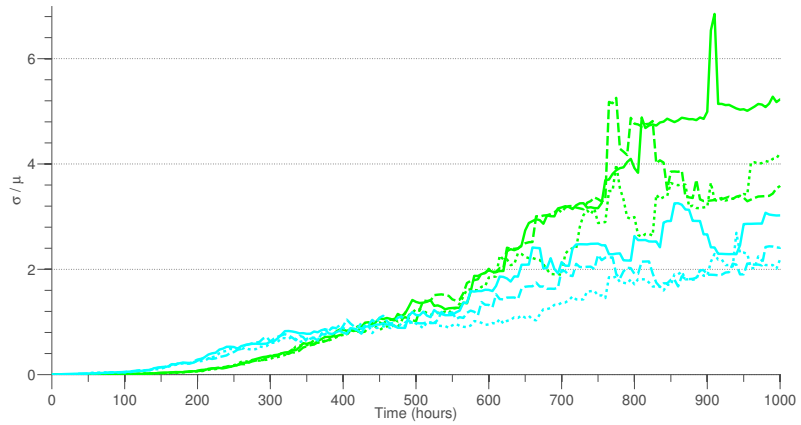

(a) Coefficient of Variation of virus particle displacement for $(D_n^*,\ \tau^*)$ (green) and $(1/2D_n^*,\ 2\tau^*)$ (cyan) in sparse case for $\tau^* = [5,\ 15,\ 25]$ (solid, dashed and dotted, respectively).

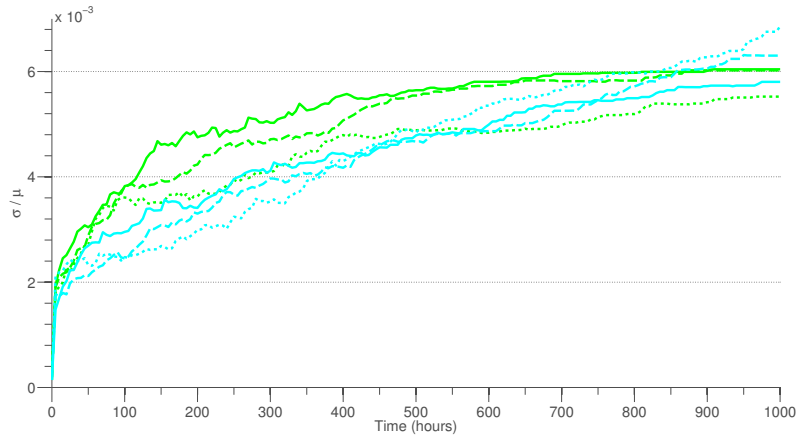

(b) Coefficient of variation for total uninfected cells for $(D_n^*,\ \tau^*)$ (green) and $(1/2D_n^*,\ 2\tau^*)$ (cyan) in sparse case for $\tau^* = [5,\ 15,\ 25]$ (solid, dashed and dotted, respectively).

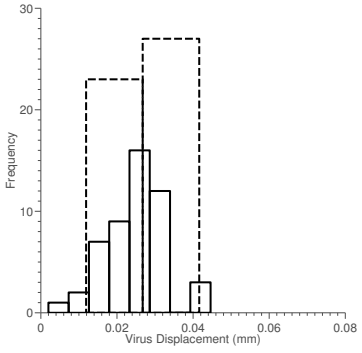

(c) Distribution of virus displacements at $t = 450$ for $\tau = 5$, $D_n = D_n^*$ (solid) and $\tau = 10$, $D_n = \frac{1}{2}D_n^*$ (dashed).

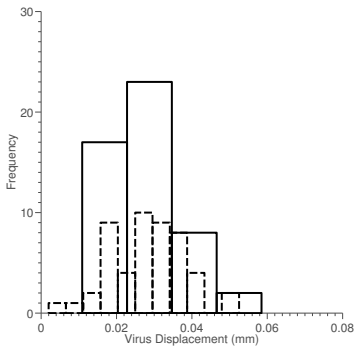

(d) Distribution of virus displacements at $t = 450$ for $\tau = 15$, $D_n = D_n^*$ (solid) and $\tau = 30$, $D_n = \frac{1}{2}D_n^*$ (dashed).

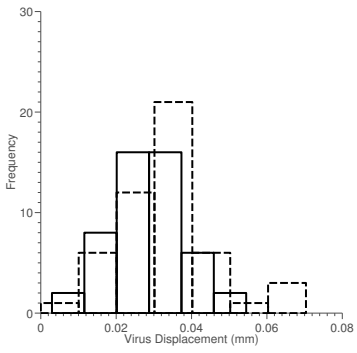

(e) Distribution of virus displacements at $t = 450$ for $\tau = 25$, $D_n = D_n^*$ (solid) and $\tau = 50$, $D_n = \frac{1}{2}D_n^*$ (dashed).

Figure 4.22: Variability of ensembles for $(D_n,\ \tau)$ and $(1/2D_n,\ 2\tau)$ for in sparse case.

	Wave speed (c)	Rate of change of C.o.V. $\left(\frac{\Delta\left(\frac{\sigma}{\mu}\right)}{\Delta t}\right)$	Rate of uninfected cell removal $\left(\frac{\Sigma_{x,y} n_0 - \Sigma_{x,y} n}{\Delta t}\right)$	Equilibrium Virus particles $\left(\sum_{x,y} V_{eq}\right)$	Onset and rate of die-out	
$\tau \uparrow$						
$D \uparrow$						
$\alpha \uparrow$						
$V_0 \uparrow$						

Table 4.4: Qualitative effects of key parameter in sparse uninfected cell case. The arrows show qualitative trends in simulation metrics (wave speed, rate of change of C.o.V., rate of uninfected cell removal and total virus particles at equilibrium) for increasing values of independent parameters (τ, D, α, A). Solid lines denote strong sub-linear, linear or super-linear dependence, and dashed lines indicate weak dependence or a threshold condition.

4.6 Summary

In this chapter, we investigated the behaviour of the stochastic model developed in Chapter 3 for a range of experimentally-controlled parameters for both dense and spare uninfected cell initial conditions. Comparisons with existing agent-based models (and experimental data within) showed that for the chosen ranges of parameters, our model was capable of reproducing all families of spatial patterns, with the exception of spatial oscillations.

Further quantitative analysis for varying diffusion ratio, burst size, virus initial condition and burst time showed that the dense uninfected cell initial condition sustained a travelling wave for most parameter values tested, with the exception of very small values of burst size, with low variability between individual simulations. For small burst sizes, virus extinction was a typical result of individual simulations, and there were indications of a minimum burst size required to sustain a travelling wave, which was not observed in the continuum model. In general, the wave speed of propagation and number of virus particles at equilibrium increased with larger values of diffusion ratio, burst time and burst size, but reached a saturation point for larger values of these parameters. Varying the initial spatial distribution of virus particles did not affect the wave speed of equilibrium number of virus particles for the travelling wave, suggesting a single steady state in the system.

The sparse uninfected cell initial condition simulations resulted in much more frequent virus extinction in individual simulations, highlighting the stochastic nature of the model.

The rate of extinction of individual simulations was decreased by larger burst sizes, while the onset of extinction was weakly linked to the burst size and burst time, which was due to the increased available time in which virus particles could react. The spread of virus particles was limited by the number of uninfected cells, and in contrast to the dense case, a broader initial spread of virus particles resulted in a greater number of uninfected cells removed from the system.

Overall, the travelling wave speeds observed in the dense case were significantly higher than the sparse case, but still lower than those predicted by the continuum PDE model. As seen in the previous chapter, this disagreement is due to the discrete nature of the stochastic model, as well as the localisation of the burst term in the compartment representation.

We have illustrated that for a range of plausible physical values, our model can replicate existing experimental results, and exhibit travelling waves of infection. However, without meaningful estimates of key parameters such as uninfected cell motility coefficient and initial virus distribution, direct comparisons with experimental data are not possible. For these reasons, additional effects such as cellular crowding were not explicitly considered in the full model, and were assumed to be incorporated in the effective motility coefficient. Since it may not be practical to measure the effective motility coefficient of uninfected cell in a dense medium, we develop a model to derive the bulk properties of the medium based on its microscopic structure in the following chapter.

Chapter 5

Effective medium approximations in continuum models

In this chapter, we address the experimental difficulties of determining the effective motility coefficient of tumour cells in a dense environment by considering a simple model of motility of a species through a heterogeneous medium of obstacles. Assuming a regular, periodic structure of impenetrable obstacles, we apply the method of asymptotic homogenisation to determine the effective diffusivity of cells for an equivalent homogeneous description. We compare these results with those from literature for a range of obstacle sizes and shapes, and show that this description is also valid for sufficiently small reaction terms.

Comparing the heterogeneous and effective, homogeneous descriptions in the stochastic model, we illustrate the limits of the continuum approach, which are addressed in the next chapter.

5.1 Introduction

In Chapters 2–3, we developed a model for the spatio-temporal evolution of virus particles in a dense tumour. For simplicity, this model only considered three species: uninfected cells, virus particles and infected cells created by the reaction of the former two species.

Solid tumours consist of two interconnected compartments: malignant cells and the stroma in which they are dispersed (Mok, 2007, pp. 23). The stroma is induced by tumour-host interaction, and is required for tumour growth and survival. The primary components of the stroma include leaked plasma, interstitial collagen, fibrin, fibronectin and connective tissue cells such as fibroblasts (Bhowmick and Moses, 2005). These

components often form long fibres, which can act as barriers to motile particles, limiting diffusive and convective properties (Ramanujan et al., 2002).

By omitting additional non-reactive objects such as cellular debris, connective tissue such as fibroblasts or simply species that move on a slower time-scale to cells, the effects of these components on the primary species was implicitly incorporated into the appropriate rate constants. While certain rate constants can be measured *in situ*, the motility of cells through a medium with obstacles has proven hard to determine (Ramanujan et al., 2002). Instead, the structure of the ECM, along with the diffusivity in free space, can be used to estimate the effective diffusivity of the medium.

In this chapter, we illustrate the methodology for determining the effective properties of motile cells in an idealised heterogeneous domain of obstacles. In our idealised model, the motility of cells in two dimensions is described by the diffusion equation, and the distribution of obstacles (representing the cross-sections of long fibres) is considered to be periodic. If the period of the obstacles is short compared with the overall size of the domain, corresponding to a large number of obstacles, we can make use of the method of multiple scales to obtain the bulk behaviour of the medium on the macroscopic scale. While similar methods exist for the case of random obstacle placement (Saxton, 1996), we only consider the case of periodic obstacles.

Effective medium theory has application in physical problems such as heat transfer, elasticity, electrical conductivity, magnetic permeability, and flow in strongly heterogeneous multiphase materials (see Batchelor, 1974 and Milton, 2002 for a more extensive list). One common feature shared in these various applications is that the governing equations involve rapidly oscillating coefficients due to the microscopic heterogeneity of the material. These rapid oscillations mean that a numerical solution is often not tractable, and analytic methods are helpful in reducing the complexity of the problem. The simplest approach in determining the effective properties is with a weighted average, a first-order perturbation theory, and can be thought of as a consequence of the law of large numbers. A more rigorous and accurate method is that of periodic homogenisation, a second-order perturbation method derived as a consequence of the central limit theorem (Pavliotis, Grigorios A and Stuart, 2008, pp. 6–7).

Generally speaking, this method exploits the multiple scales in the problem by parametrising in terms of the scaling ratio of micro- and macroscopic lengthscales, $\epsilon = \frac{\mathbf{y}}{\mathbf{x}}$, and then examining what happens as the limit of this ratio tends to zero. An extensive review of the theory of periodic homogenisation is given by Papanicolaou et al. (1979); Sánchez-Palencia (1980); Allaire (1992), and provide a rigorous basis for the method. This analysis can be extended to higher powers in ϵ and thereby obtain a solution that captures the correct asymptotic behaviour as ϵ (Milton, 2002). A number of sophisticated techniques, such as G-convergence and H-convergence, have been developed to apply homogenisation techniques to the case of non-periodic coefficients. In addition to this, the more general theory

of Γ-convergence has also been developed for non-linear cases (Cioranescu and Donato, 1999, pp. 241).

In Section 5.2, we review existing empirical and asymptotic expressions for diffusion in a multi-phase medium. In Section 5.3, we consider the simple case of homogenisation of a linear parabolic equation with periodically varying coefficients, and apply the method of multiple scales to obtain an analytic expression for the effective medium in terms of the free diffusivity and inclusion shape. In Section 5.4.1, we compare asymptotic results for effective media from literature (Section 5.2) to numerical results of diffusivity in a medium consisting of periodic obstacles, obtained from homogenisation theory (Section 5.3). The effective description is then compared to the obstacle problem using the stochastic model proposed in Chapter 3, and the validity of the continuum effective medium approximation is then discussed.

5.2 Existing results from literature

Composite media have been studied extensively in the literature, as far back as Poisson, Maxwell and Rayleigh, and the theory has since been developed, often independently, in many fields of physics, engineering and biology (Milton, 2002; Papanicolaou et al., 1979). A common aim is to simplify the physical problem by approximating the heterogeneous domain with an homogeneous one with equivalent macroscopic properties. As a result of the parallel development of this field, it is often referred to by different names, such effective medium theory, mixing theory, composite medium theory, homogenization or constitutive relations.

The similarity between these various fields arises from the fact that for many simple problems, the underlying physical processes are described by either the Heat equation, or its steady-state equivalent, Laplace's equation. An illustrative list of equivalent problems, as well as the physical interpretation of the variables, is shown in Table 5.1.

To illustrate this in one dimension, we define

$$j(x) = D(x)\, c(x), \tag{5.1}$$

and considering the differential equation

$$\nabla \cdot j = 0. \tag{5.2}$$

For example, writing $c(x) \equiv -\nabla u(x)$, (5.2) becomes the steady-state heat equation, where $D(x)$ can be interpreted as spatially-varying diffusion coefficient. Alternatively, by re-labelling $c(x) \equiv h(x)$ and $D(x) \equiv \mu(x)$, (5.1)–(5.2) describe the magnetic field b for magnetic permeability μ. While the solution of the problem of course depends on the

Problem	$j(x) = D(x)\,c(x)$	$c(x)$	D
Electrical Conduction	Electrical conduction current, j	Electric field, e	Electrical conductivity, σ
Dielectrics	Displacement field, d	Electric field, e	Electric permittivity, ϵ
Magnetism	Magnetic induction, b	Magnetic field, h	Magnetic permeability, μ
Thermal Conduction	Heat current, q	Temperature gradient, $-\nabla T$	Thermal conductivity, κ
Diffusion	Particle current	Concentration gradient, $-\nabla u$	Diffusivity, D

Table 5.1: Interpretation of physical quantities for related problems (adapted from Milton, 2002, pp.19).

boundary conditions (Jönsson et al., 1986), the techniques used to derive these are usually transferable.

Various analytic and empirical expressions relating the heterogeneous and effective homogeneous domains exist, and in this section, we give a brief overview of existing results relevant to effective medium descriptions of diffusion in the presence of obstacles.

Homogenization and related averaging techniques typically consider two physical cases: random and periodic structures (Batchelor, 1974). For the former, the effective properties are usually expressed in terms of upper and lower bounds, whereas the latter case can result in either asymptotic or closed-form solutions. For results from electrical conduction literature, the effective conductivity is usually defined in the range $1 < \sigma_{eff} < \infty$, and correspond to the reciprocal of the equivalent properties in diffusion or optics problems (Perrins et al., 1979b).

5.2.1 Empirical approximation

Empirical approximations for the effective diffusion in constricted media are often used in the context of porous media and gels. These generally consider the effects of curved pores lumped together in the form of an effective diffusivity.

For fluid-filled pores of a solid composite, the effective diffusion is often expressed through the empirical relation

$$D_{eff} = D_{free}\frac{\Omega_{free}}{\tau^2}, \tag{5.3}$$

where D_{free} is the diffusion coefficient in the bulk space of size Ω_{free}, and τ is the tortuosity of the pores (Cussler, 1997, pp. 191). The tortuosity is a measure of the increased mean path length due to curvature of pores, and typically has values between 2 and 6. Because the solid phases are impermeable, diffusion occurs over a smaller cross-sectional area than is available in a homogeneous material. The effective diffusivity is typically lower than

in the corresponding bulk space due to the reduced volume fraction of free space, as well as the longer distance travelled in the pores, characterised by the tortuosity (Westrin and Axelsson, 1991).

Unfortunately, Equation (5.3) has limited predictive value, since τ cannot be measured easily in a direct way (Ramanujan et al., 2002). Instead, tortuosity is often empirically defined as a function of Ω_{free}, depending on the specific geometry considered (van Brakel and Heertjes, 1974). Attempts have been made to derive analytic expressions for tortuosity from the specific shape of pores, with a value $\tau = \sqrt{2}$ obtained for a two-dimensional periodic network of squares (Hrabe et al., 2004).

5.2.2 Spherical inclusions

As we will see in Section 5.3, a composite domain consisting of two or more different materials can be reduced to an effective macroscopic description that depends on both the geometry and volume of the inclusions. Analytic determination of this type goes back to J.C. Maxwell and Lord Rayleigh, who computed the effective conductivity of composites consisting of a matrix with regular spherical inclusions (Hashin, 1983).

This work was extended and generalised, and related expressions are now known under various names in different fields; the Maxwell-Garnett mixing rule for effective permittivity, its analogues in gases, the Clausius–Mossotti relation, and the Lorenz–Lorentz equation for the refractive index in optics (Landauer, 1978; Monecke, 1987).

Most closed form expressions consider isotropic mixtures of spheres, although these can also be extended to ellipses. Similarly, the expressions for two-phase (binary) mixing commonly cited in literature can be generalised to multiphase mixtures (Sihvola, 2013).

For a two-phase, d-dimensional medium of spherical inclusions in an infinite domain, Maxwell expressed the effective coefficient (in our case, the diffusivity), D_{eff}, in terms of the pure phase coefficients of the domain and spheres, D_b and D_s, and volume fraction of the sphere, ϕ_s, as

$$\frac{D_{eff}}{D_b} = 1 + d\phi_s \frac{D_b - D_s}{D_b + (d-1)\, D_s} + \mathcal{O}\left(\phi_s\right), \tag{5.4}$$

and as each sphere was considered as a single entity, this result is strictly valid only in the dilute limit of sparse spheres, $\phi_s \ll 1$, beyond which corrections of $\mathcal{O}\left(\phi_s^2\right)$ are required to account for interactions between adjacent spheres (Markov, 2000). The related Clausius-Mossotti or Maxwell-Garnett mixing rules

$$\frac{D_{eff} - D_s}{D_{eff} + (d-1)\, D_s} = \phi_s \frac{D_b - D_s}{D_b + (d-1)\, D_s}. \tag{5.5}$$

are a direct result of (5.4), and are more commonly used (Merrill et al., 1999).

An improvement on the Maxwell-Garnett approximation was made by Bruggeman, when he developed an expression for the effective electrical properties of a composite system that treats the two composites in a symmetrical fashion, giving the relation

$$(1-\phi_s)\,\frac{D_b - D_{eff}}{D_b + (d-1)\,D_{eff}} + \phi_s \frac{D_s - D_{eff}}{D_s + (d-1)\,D_{eff}} = 0. \tag{5.6}$$

This result (also known as the Bottcher, Polder-van Santen or Effective Medium Approximation) came from intuition that the total polarization of an electric field is zero throughout the homogenised composite medium, and has the property that it treats the inclusions and the environment symmetrically, with no difference between the two phases. Intuitively, this symmetry in (5.6) can be interpreted as a weighted mixing of the unknown effective medium using the volume fraction of each component as weight, and is in stark contrast with the Maxwell-Garnett approach, which is inherently non-symmetric (Sihvola, 2000). While the Maxwell-Garnett mixing rule only holds for the dilute composite media, the Bruggeman rule has a wider applicability, and is valid for larger volume fractions. This is because it correctly interpolates between the diffusion coefficients D_b and D_s at $\phi_s = 0$ and $\phi_s = 1$, as well as between the derivatives $\frac{dD_{eff}}{d\phi_s}\Big|_{\phi_s=0}$ and $\frac{dD_{eff}}{d\phi_s}\Big|_{\phi_s=1}$ (Monecke, 1987; Landauer, 1978).

Another well-known formula, often used in the study of wave propagation in random media is the Coherent Potential formula (Landauer, 1978; Sihvola, 2000). For spherical inclusions in a d-dimensional domain, to $\mathcal{O}(\phi_s)$, this is stated as

$$D_{eff} = D_b + \phi_s\,(D_s - D_b)\,\frac{dD_{eff}}{dD_{eff} + (1-\phi_s)\,(D_s - D_b)}. \tag{5.7}$$

The Maxwell-Garnett, Bruggeman and Coherent Potential mixing rules given in (5.5), (5.6) and (5.7) can be stated in the form of the Unified Mixing formula

$$\frac{D_{eff} - D_s}{D_{eff} + (d-1)\,D_s + \nu\,(D_{eff} - D_s)} = \phi_s \frac{D_b - D_s}{D_b + (d-1)\,D_s + \nu\,(D_{eff} - D_b)}, \tag{5.8}$$

where $\nu = 0$ for the Maxwell-Garnett, $\nu = 2$ for the Bruggeman and $\nu = 3$ for the Coherent Potential approximations (Kristensson, 2003; Sihvola, 2000). It is worth noting that all classical mixture formulae have their domain of validity for small volume fractions $\phi_s \ll 1$, with a perturbation expansion of (5.8) giving

$$D_{eff} \approx D_b + d\phi_s \frac{D_s - D_b}{D_s + (d-1)\,D_b}, \tag{5.9}$$

to $\mathcal{O}(\phi_s)$, and the parameter ν affecting the $\mathcal{O}\left(\phi_s^2\right)$ corrections.

Composites consisting of two or more materials of very different properties are known as high-contrast composites, and correspond to the asymptotic limit $\frac{D_b}{D_s} \gg 1$. In the case

of the Maxwell-Garnett formula (5.5), Perrins et al. (1979b) derive the limiting case of impenetrable cylinders in two dimensions as

$$D_{eff} = D_b \frac{1-\phi}{1+\phi}, \tag{5.10}$$

where ϕ is the volume fraction of the cylinder.

In the context of conductivity, there exists a reciprocal relation linking the effective properties of a high contrast conductor to that of a composite with the same phase geometry, but with an electrical contact resistance at phase interfaces (Lipton, 1997), such that

$$\sigma_{eff}\left(\phi_s, \frac{\sigma_s}{\sigma_b}\right)\sigma_{eff}\left(\phi_s, \frac{\sigma_b}{\sigma_s}\right) = 1, \tag{5.11}$$

for effective conductivity σ_{eff} as a function of inclusion fraction ϕ_s and conductivities σ_s, σ_b. This result was proven by Keller (1963) for composites with rectangular symmetry, and was later applied to the average conductivity of a statistically homogeneous, isotropic random distribution of cylinders (Keller, 1964). While there is no equivalent physical interpretation of the resistivity in the context of diffusion, this result allows us to apply results derived for perfect conductors to study diffusion in the presence of impenetrable obstacles.

5.2.3 Bounds on diffusion

So far, we have considered the case of ordered media. For the case of disordered media, the lack of a microscopic unit cell limits the information about the internal structure of a medium. Instead, the effective properties of the medium are expressed in terms of upper and lower bounds. The most widely used of these are known as the Wiener bounds (also known as Voigt-Reuss bounds in elasticity literature), and the Hashin-Shtrikman bounds.

The simplest of these bounds was first derived by Wiener in the context of conductivity. These were derived by looking at the best and worst cases for conductivity, and assuming that the phases in a composite system are lumped in either series or parallel layers. The effective properties for these cases were then found using the analogy of an equivalent electrical circuit using a series model for the lower limit and a parallel model for the upper limit (Das et al., 2010). In the context of diffusion in a two-phase medium, this results in a bound on the effective diffusivity, D_{eff},

$$\left(\frac{\phi_1}{D_1} + \frac{\phi_2}{D_2}\right)^{-1} \leq D_{eff} \leq \phi_1 D_1 + \phi_2 D_2, \tag{5.12}$$

where D_i and ϕ_i are the diffusion coefficients and volume fractions of the i^{th} phase, respectively. These bounds define an interval within which the effective properties of the heterogeneous medium should lie, independently on the details of the internal arrangement. These depend solely on the phase volume fractions, and are valid for arbitrary micro-structures, and both isotropic and anisotropic media. We also note that (5.12) are inclusive bounds, and there exist heterogeneous media whose effective properties equal the limit upper- and lower-bound cases, notably laminate or fibre media (Markov, 2000).

With further assumptions, the Wiener bounds can be improved. By assuming that the composite is macroscopically isotropic, in addition to being statistically homogeneous, Hashin and Shtrikman used a variational principle to obtain greatly improved bounds on D_{eff}. For a two-phase medium, these bounds are given by

$$D_1 + \frac{\phi_2}{\frac{1}{D_2 - D_1} + \frac{\phi_1}{3D_1}} \leq D_{eff} \leq D_2 + \frac{\phi_1}{\frac{1}{D_1 - D_2} + \frac{\phi_2}{3D_2}}, \tag{5.13}$$

for $D_1 < D_2$. The Hashin-Shtrikman bounds are valid for any two-phase composite and describe the possible eigenvalues of the effective diffusivity matrix. The authors were able to show that, for the two-phase system, these are also the best obtainable bounds if one assumes only homogeneity and isotropy. For spherical inclusions, the upper bound of (5.13) reduces to the Maxwell formula (5.4), while the lower bound corresponds to the inverse case of the same expression, where $D_2 > D_1$ (Sihvola, 2013).

A comparison of the tightness of the Wiener and Hashin-Shtrikman bounds can be seen in Figure 5.1, where the range of possible values of the effective diffusivity is indicated by the shaded area. The Hashin-Shtrikman bounds, enclosing the shaded area, provide a tighter bound on the effective diffusivity than the Wiener bounds, with the exception of the extreme layered media, where the bounds are equal. The exact shape enclosed by the Hashin-Shtrikman bounds depends on the relative ratios of D_1 and D_2, with looser bounds for higher contrasting materials. If one of the phases is the void phase, such as a medium filled with impenetrable obstacles, $D_1 \to 0$ and the lower bounds of both the Wiener and Hashin-Shtrikman expressions degenerate to zero.

5.2.4 Square inclusions

Despite useful asymptotic results, such as those shown in Section 5.2.2, few closed-form solutions exist, even for the relatively simple case of two-phase media (Craster and Obnosov, 2001). One special case of micro-structures in two dimensions is that of the periodic checkerboard, a doubly-periodic medium consisting of two distinct squares, arranged in an

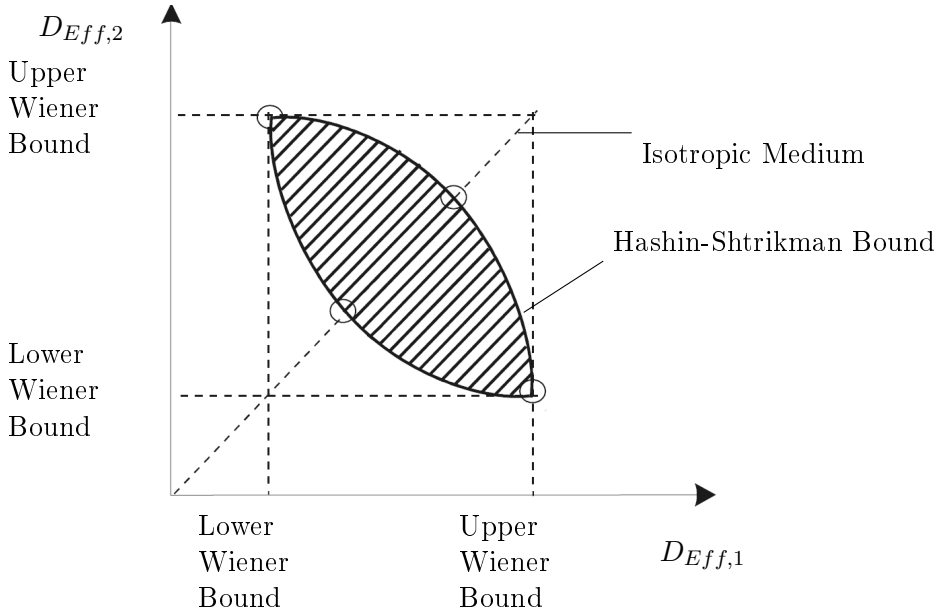

Figure 5.1: Bounds on effective diffusion in phase space, with optimal points indicated by circles. $D_{Eff,1}$ and $D_{Eff,2}$ are the diagonal elements of the diffusivity tensor (adapted from Meidell, 2001).

alternating manner. Using a duality argument, Keller (1964) found that a two-phase checkerboard with squares of diffusivity (or conductivity), D_1 and D_2, has effective coefficient

$$D_{eff} = \sqrt{D_1 D_2}. \tag{5.14}$$

This solution was later used to show that the effective diffusivity of a three-dimensional, face centred cubic checkerboard in the limiting case of $\frac{D_2}{D_1} \gg 1$ has diffusivity $D_{eff} = \sqrt{D_1 D_2}$ (Milton, 2001).

The asymptotic case $\frac{D_2}{D_1} \gg 1$ is of particular interest when studying diffusion through media with obstacles. However, the simple two-dimensional periodic checkerboard is of limited use, as the case $D_1 = 0$ result in a trivial solution. An extension of this model is the four-phase periodic checkerboard, assembled by lining 2×2 squares of equal area, each with diffusion coefficients D_1, D_2, D_3 and D_4. In 1985, Mortola and Steffe proposed a conjecture for the effective conductivity of this structure. This conjecture was proven independently by Milton (2001) and Craster and Obnosov (2001), and gives the closed form solution for effective diffusivity

$$\begin{aligned} D_{eff} &= \sqrt{\frac{(D_2 + D_3)(D_4 + D_1)}{(D_1 + D_2)(D_3 + D_4)}} \\ &\quad \times \sqrt{\frac{D_1 D_2 D_3 + D_1 D_2 D_4 + D_1 D_3 D_4 + D_2 D_3 D_4}{D_1 + D_2 + D_3 + D_4}}. \end{aligned} \tag{5.15}$$

Finally, Lu (1995) derived an asymptotic relation for square cylinders in a two-dimensional

square array, analogous to the round cylinder case of Perrins et al. (1979a).

5.3 Parabolic equations

5.3.1 Heat equation

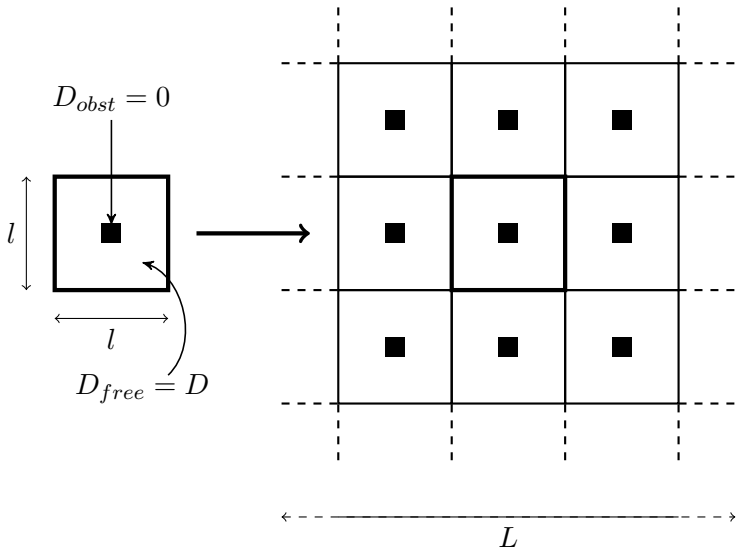

Figure 5.2: Heterogeneous domain with periodic structure.

We consider the simplest model of cell motility in a heterogeneous environment: diffusion in a two-dimensional domain containing impermeable, axisymmetric obstacles, arranged in an a periodic manner (see Figure 5.2). For simplicity, we suppose that the motility coefficient does not change in the free space, although this can be extended to a spatially-varying motility coefficient using the same techniques.

The two-dimensional, $L \times L$ domain illustrated in Figure 5.2 is composed of periodic cells of size $l \times l$. In each unit period, species u diffuses in free space, Ω, with motility tensor $\vec{D_{free}}$, and the impermeable obstacle is represented by a region of space with motility coefficient $D_{obst} = 0$. The motility tensor, $\vec{D_{free}}$, is constant, but not necessarily isotropic. The spatio-temporal evolution of species u in free space, Ω, is given by the Heat equation

$$\frac{\partial u(\mathbf{X},t)}{\partial t} = \nabla \cdot \left(\vec{D_{free}} \nabla u(\mathbf{X},t) \right) \quad \text{in } \Omega, \tag{5.16}$$

in space, $\mathbf{X}$, and time, t, subject to a no-flux boundary condition at the obstacle interface, Γ, given by

$$-\vec{D_{free}} \nabla u(\mathbf{X},t) \cdot \mathbf{n} = 0 \quad \text{on } \Gamma, \tag{5.17}$$

where $\mathbf{n}$ is the unit normal to Γ.

Making use of the periodic structure in the system, we define the dimensionless length scales

$$\mathbf{x} = \frac{\mathbf{X}}{L}, \tag{5.18}$$

$$\mathbf{y} = \frac{\mathbf{X}}{l}, \tag{5.19}$$

which can be related through the aspect ratio

$$\epsilon = \frac{l}{L}, \tag{5.20}$$

such that

$$\mathbf{y} = \epsilon^{-1}\mathbf{x}. \tag{5.21}$$

Assuming that $l \ll L$ for closely-packed obstacles in a large domain, the length scales $\mathbf{x}$ and $\mathbf{y}$ may be interpreted as the macroscopic and microscopic length scales of the system, respectively. Although these variables are related through the small parameter, $\epsilon \ll 1$, it becomes convenient to use separation of scales to formulate the governing equations in terms of both these variables, which are treated as being independent of each other from now on.

Making use of this separation of scales, we write $u \equiv u(\mathbf{x}, \mathbf{y}, t)$ and expand asymptotically in powers of ϵ as

$$u(\mathbf{x}, \mathbf{y}, t) = u_0(\mathbf{x}, \mathbf{y}, t) + \epsilon u_1(\mathbf{x}, \mathbf{y}, t) + \epsilon^2 u_2(\mathbf{x}, \mathbf{y}, t) + \mathcal{O}\left(\epsilon^3\right), \tag{5.22}$$

where each $u_{(i)}(\mathbf{x}, \mathbf{y}, t)$ is $\mathbf{y}$-periodic, such that

$$u_{(i)}(\mathbf{x}, \mathbf{y} + \epsilon\mathbf{e}_j, t) = u_{(i)}(\mathbf{x}, \mathbf{y}, t), \tag{5.23}$$

where $\mathbf{e}_j$ are unit vectors in the j^{th} direction, and $j \in [1, 2]$.

Using (5.21) and applying the chain rule, the gradient operator with respect to original spatial variable, $\mathbf{X}$, can be rewritten in terms of the macro- and microscopic length scales as

$$\nabla \equiv \nabla_{\mathbf{x}} + \epsilon^{-1}\nabla_{\mathbf{y}}, \tag{5.24}$$

where $\nabla_{\mathbf{x}} \equiv \frac{\partial}{\partial x_1}\hat{x}_1 + \frac{\partial}{\partial x_2}\hat{x}_2$ and $\nabla_{\mathbf{y}} \equiv \frac{\partial}{\partial y_1}\hat{y}_1 + \frac{\partial}{\partial y_2}\hat{y}_2$ are the gradient operators with respect to new variables $\mathbf{x}$ and $\mathbf{y}$, with corresponding unit vectors $\hat{x}_i$ and $\hat{y}_i$, respectively.

Substituting (5.22) and (5.24) into (5.16), and grouping like orders of ϵ, the first three

terms governing the evolution of u in free space Ω are

$$0 = \nabla_{\mathbf{y}} \cdot \left(\vec{D_{free}} \nabla_{\mathbf{y}} u_0 \right), \qquad \text{at } \mathcal{O}\left(\epsilon^{-2}\right) \tag{5.25}$$

$$0 = \nabla_{\mathbf{y}} \cdot \left(\vec{D_{free}} \nabla_{\mathbf{x}} u_0 + D_{free} \nabla_{\mathbf{y}} u_1 \right) + \nabla_{\mathbf{x}} \cdot \left(D_{free} \nabla_{\mathbf{y}} u_0 \right), \text{ at } \mathcal{O}\left(\epsilon^{-1}\right) \tag{5.26}$$

$$\begin{aligned} \frac{\partial u_0}{\partial t} &= \nabla_{\mathbf{y}} \cdot \left(\vec{D_{free}} \nabla_{\mathbf{x}} u_1 + D_{free} \nabla_{\mathbf{y}} u_2 \right) \\ &\quad + \nabla_{\mathbf{x}} \cdot \left(\vec{D_{free}} \nabla_{\mathbf{x}} u_0 + D_{free} \nabla_{\mathbf{y}} u_1 \right), \qquad \text{at } \mathcal{O}(1), \end{aligned} \tag{5.27}$$

Similarly, the corresponding boundary conditions on Γ, given by (5.17), become

$$-\vec{D_{free}} \left(\nabla_{\mathbf{y}} u_0 \right) \cdot \mathbf{n} = 0, \text{ at } \mathcal{O}\left(\epsilon^{-1}\right) \tag{5.28}$$

$$-\vec{D_{free}} \left(\nabla_{\mathbf{x}} u_0 \right) \cdot \mathbf{n} - \vec{D_{free}} \left(\nabla_{\mathbf{y}} u_1 \right) \cdot \mathbf{n} = 0, \text{ at } \mathcal{O}(1) \tag{5.29}$$

$$-\vec{D_{free}} \left(\nabla_{\mathbf{x}} u_1 + \nabla_{\mathbf{y}} u_2 \right) \cdot \mathbf{n} = 0, \text{ at } \mathcal{O}(\epsilon) \tag{5.30}$$

At $\mathcal{O}\left(\epsilon^{-2}\right)$, Equations (5.25), (5.28) and (5.23) imply a solution

$$u_0(\mathbf{x}, \mathbf{y}, t) \equiv u_0(\mathbf{x}, t), \tag{5.31}$$

which is independent of micro-scale, $\mathbf{y}$. This solution is unique up to an additive constant, and applying the Fredholm Alternative Theorem, we impose the additional condition

$$\iint_{\Omega} u_0(\mathbf{x}, \mathbf{y}, t)\, d\mathbf{y} = \text{constant}, \tag{5.32}$$

on the microscale to ensure uniqueness.

Substituting (5.31) into (5.26), the $\mathcal{O}\left(\epsilon^{-1}\right)$ terms imply that

$$\nabla_{\mathbf{y}} \cdot \left(\vec{D_{free}} \nabla_{\mathbf{x}} u_0 + \vec{D_{free}} \nabla_{\mathbf{y}} u_1 \right) = 0, \tag{5.33}$$

subject to corresponding boundary condition (5.29). Using separation of variables, we rewrite $u_1(\mathbf{x}, \mathbf{y}, t)$ as

$$u_1(\mathbf{x}, \mathbf{y}, t) = \vec{\chi}(\mathbf{y}) \cdot \nabla_{\mathbf{x}} u_0(\mathbf{x}, t) + \bar{u}_1(\mathbf{x}, t), \tag{5.34}$$

where $\overline{u}_1(\mathbf{x}, t)$ is an arbitrary function of $\mathbf{x}$ and t only, and cell functions $\chi_j(\mathbf{y})$, $j \in [1, 2]$

are chosen to satisfy the related cell problem

$$-\nabla_{\mathbf{y}}\left(\vec{D_{free}}\left(\mathbf{e}_j+\nabla_{\mathbf{y}}\chi_j\left(\mathbf{y}\right)\right)\right) = 0 \text{ in } \Omega, \tag{5.35}$$

$$-\mathbf{n}\cdot\left(\vec{D_{free}}\left(\mathbf{e}_j+\nabla_{\mathbf{y}}\chi_j\left(\mathbf{y}\right)\right)\right) = 0 \text{ on } \Gamma, \tag{5.36}$$

where each $\chi_j\left(\mathbf{y}\right)$ are y-periodic, and have the property

$$\iint_{\Omega}\chi_j\left(\mathbf{y}\right)d\mathbf{y}=0, \tag{5.37}$$

to ensure uniqueness. The solution of (5.35)–(5.37) for cell function $\vec{\chi}\left(\mathbf{y}\right)$ allows us to express u_1 terms in terms of u_0 through (5.34). We now seek to relate u_2 to u_0 by considering the $\mathcal{O}\left(1\right)$ terms in (5.27).

Integrating (5.27) over a unit cell, Ω, we find that

$$\begin{aligned}\iint_{\Omega}\frac{\partial u_0}{\partial t}d\mathbf{y} &= \iint_{\Omega}\nabla_{\mathbf{y}}\cdot\left(\vec{D_{free}}\nabla_{\mathbf{x}}u_1+D_{free}\nabla_{\mathbf{y}}u_2\right)d\mathbf{y}\\ &\quad+\iint_{\Omega}\nabla_{\mathbf{x}}\cdot\left(\vec{D_{free}}\nabla_{\mathbf{x}}u_0+D_{free}\nabla_{\mathbf{y}}u_1\right)d\mathbf{y}.\end{aligned} \tag{5.38}$$

Using Green's theorem (or divergence theorem for the three-dimensional case), the double integral over the unit cell can be replace by a line integral, giving

$$\begin{aligned}\frac{\partial u_0}{\partial t}\iint_{\Omega}d\mathbf{y} &= \oint_{\Gamma}\mathbf{n}\cdot\left(\vec{D_{free}}\nabla_{\mathbf{x}}u_1+D_{free}\nabla_{\mathbf{y}}u_2\right)d\mathbf{s}\\ &\quad+\nabla_{\mathbf{x}}\cdot\iint_{\Omega}\left(\vec{D_{free}}\nabla_{\mathbf{x}}u_0+D_{free}\nabla_{\mathbf{y}}u_1\right)d\mathbf{y},\end{aligned} \tag{5.39}$$

where $\vec{n}$ is the unit normal to the contour. Applying the boundary conditions (5.30) on the unit cell, this reduces to

$$\frac{\partial u_0}{\partial t}\iint_{\Omega}d\mathbf{y}=\nabla_{\mathbf{x}}\cdot\iint_{\Omega}\left(\vec{D_{free}}\nabla_{\mathbf{x}}u_0+D_{free}\nabla_{\mathbf{y}}u_1\right)d\mathbf{y}, \tag{5.40}$$

and substituting (5.34) relates the macroscopic solution $u_0\left(\mathbf{x}\right)$ to the cell problem $\vec{\chi}$ as

$$\frac{1}{|\Omega|}\frac{\partial u_0}{\partial t}=\nabla_{\mathbf{x}}\cdot\iint_{\Omega}\vec{D_{free}}\left(\nabla_{\mathbf{x}}u_0+\nabla_{\mathbf{y}}\left(\vec{\chi}\left(\mathbf{y}\right)\cdot\nabla_{\mathbf{x}}u_0+\bar{u}_1\left(\mathbf{x}\right)\right)\right)d\mathbf{y}, \tag{5.41}$$

where $|\Omega|$ is the area of the unit cell. Since $\overline{u}_1\left(\mathbf{x}\right)$ is independent of the microscale, $\mathbf{y}$, the gradient of the last term in (5.41) is zero, and the macroscopic equation simplifies to

$$\frac{1}{|\Omega|}\frac{\partial u_0}{\partial t}=\nabla_{\mathbf{x}}\cdot\iint_{\Omega}\vec{D_{free}}\left(\nabla_{\mathbf{x}}u_0+\nabla_{\mathbf{y}}\left(\vec{\chi}\left(\mathbf{y}\right)\cdot\nabla_{\mathbf{x}}u_0\right)\right)d\mathbf{y}. \tag{5.42}$$

Given this form of the integral expression, we can define the effective diffusivity tensor as

$$\vec{D^*_{ij}} = \frac{1}{|\Omega|}\iint_\Omega \left(D_{free,ij} + \left(\vec{D_{free}}\nabla_{\mathbf{y}}\chi_i(\mathbf{y})\right)\cdot e_j\right)d\mathbf{y} \tag{5.43}$$

$$= \frac{1}{|\Omega|}\iint_\Omega \vec{D_{free}}\left(\mathbf{e}_i + \nabla_{\mathbf{y}}\chi_i(\mathbf{y})\right)\cdot\left(\mathbf{e}_j + \nabla_{\mathbf{y}}\chi_j(\mathbf{y})\right)d\mathbf{y}, \tag{5.44}$$

where notation A_{ij} indicates i^{th} row and j^{th} column of tensor A. The first term of (5.43) can be interpreted as the mean diffusivity of the unit cell, and the second term as a higher-order corrector. Substituting this definition into the governing equation for the macroscopic evolution of $u_0(\mathbf{x},t)$, the macroscopic governing equation reduces to

$$\psi\frac{\partial u_0}{\partial t} - \nabla_{\mathbf{x}}\cdot\left(\vec{D^*}\nabla_{\mathbf{x}}u_0\right) = 0, \tag{5.45}$$

where $\psi = \frac{|\Omega\backslash\Omega_{obst}|}{|\Omega|}$ is the porosity of the unit cell.

For symmetric obstacles in a domain with a constant, isotropic diffusion coefficient, $\vec{D_{free}} = D_{free}\mathbf{I}$, the effective diffusivity becomes

$$\frac{D_{free}}{|\Omega|}\iint_\Omega\left(1+\frac{\partial\chi_1}{\partial y_1}\right)d\mathbf{y} = D_{eff} = \frac{D_{free}}{|\Omega|}\iint_\Omega\left(1+\frac{\partial\chi_2}{\partial y_2}\right)d\mathbf{y}. \tag{5.46}$$

5.3.2 Extension to reaction-diffusion system

While we have only considered the case of diffusion only, it should be noted that the homogenisation procedure from Section 5.3.1 can be extended to incorporate a reaction term. The addition of a small linear reaction term with rate constant $k \sim \epsilon^2$ to (5.16), the governing equation

$$\frac{\partial u(\mathbf{X},t)}{\partial t} = \nabla\cdot\left(\vec{D_{free}}\nabla u(\mathbf{X},t)\right) - ku \quad \text{in } \Omega, \tag{5.47}$$

yields the effective macroscopic equation

$$\psi\frac{\partial u_0}{\partial t} - \frac{\partial}{\partial x_i}\left(\vec{D^*}\frac{\partial u_0}{\partial x_j}\right) + \psi k u_0 = 0, \tag{5.48}$$

where $\vec{D^*}$and ψ are defined as in Section 5.3.1. The assumption of an $\mathcal{O}\left(\epsilon^2\right)$ reaction rate implies that this term only appears in the $\mathcal{O}(1)$ balance in (5.27), and does not affect the solution of the cell function. Rewriting the reaction constant as

$$k = k^* v, \tag{5.49}$$

this simple extension can be applied to the study slow reactions of u with a spatially uniform distribution of species v.

More general methods for the homogenisation of reaction-diffusion equations in high contrast media have been developed, including non-linear reaction terms (Pankratov et al., 2003) and reaction-driven changes to the micro-structure (Meier, 2008).

5.4 Numerical results and comparison

As we have seen in Section 5.2, the shape of inclusions strongly affects the macroscopic properties of the effective domain, particularly for the case of dense obstacles. In this section, we calculate the effective diffusivity of squares and rounded squares using the homogenisation approach derived in Section 5.3, and compare these with existing theory and discrete simulations of random walks on a lattice.

5.4.1 Shape of obstacles

The asymptotic homogenisation method derived in Section 5.3 expressed the effective properties of an infinite medium with periodic obstacles in terms of a local cell problem (5.35)–(5.37). This non-trivial system of equations for $\chi_1(\mathbf{y}, t)$ and $\chi_2(\mathbf{y}, t)$ can be solved numerically using a Finite Element solver such as COMSOL.

We considered a unit cell $\Omega : [0, 1] \times [0, 1]$, with free space diffusivity $D_{free} = 1$ and an impenetrable obstacle centred about $\mathbf{y} = (0.5, 0.5)$. The range of obstacle shapes, shown in Figure 5.3, was created by rounding corners of a square using COMSOL's Fillet tool, with the area of the inclusion given by

$$A_{obst} = \left((2r)^2 - \pi \left(p_{fillet} r\right)^2\right), \tag{5.50}$$

where $2r$ is the width of the square, and $0 \leq p_{fillet} < 0.5$ is the fillet fraction, with the value $p_{fillet} = 0.5$ corresponding to a circle of radius r.

Figure 5.3: Obstacle shapes with increasing percentage of corner rounding.

To implement the zero-mean condition (5.37) numerically, the cell problem (5.35)–

(5.37) was reformulated as the time-varying initial-value problem

$$\frac{\partial \chi_i(\mathbf{y},t)}{\partial t} = D_{free}\left(\frac{\partial^2 \chi_i}{\partial y_1^2} + \frac{\partial^2 \chi_i}{\partial y_2^2}\right) \text{ in free space,} \tag{5.51}$$

$$\mathbf{n}\cdot(\nabla\chi_i) = -\hat{n}_{yi}, \text{ at obstacle interface} \tag{5.52}$$

$$\chi_i|_{y_1=0} = \chi_i|_{y_1=1}\,, \tag{5.53}$$

$$\chi_i|_{y_2=0} = \chi_i|_{y_2=1}\,, \tag{5.54}$$

$$\chi_i(t=0) = 0, \tag{5.55}$$

where $\hat{n}_{yi}$ is the unit normal in the y_i direction. Solving this over time interval $t \in [0, 10]$ on COMSOL's predefined "Fine" mesh setting, the solutions of χ_1 and χ_2 converged to a solution for $t < 1$ for all cases tested. The resulting long-time solution was used to evaluate the effective diffusivity through (5.46) for fillet ratios $p_{fillet} = [0, 0.1, 0.2, 0.3, 0.4]$ and $2r \in [0.025, 0.95]$. The numerical results for effective diffusivity are shown in Figure 5.4.

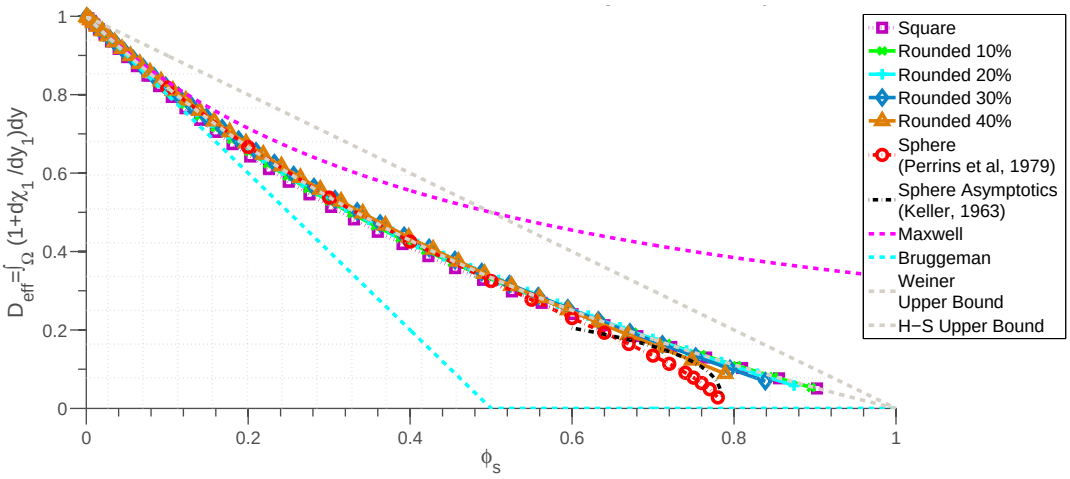

Figure 5.4: Comparison of effective diffusivity for square and rounded square obstacles from homogenisation and effective medium theory. These are contained within the Weiner Bounds (horizontal shade) and Hashin-Shrikman Bounds (vertical shade). Non-square obstacles show a percolation threshold as $r \to 0.5$

The analytic expressions for effective diffusion coefficients in Section 5.2 converge to the same result in the limit of small obstacle size, $\phi_s < 0.2$. The Maxwell and Bruggeman rules diverge for $\phi_s > 0.2$, with the latter providing a slightly more accurate bound. These errors arise due to the breakdown of the dilute phase assumptions, and have previously been reported in literature (Hui and Ke-da, 1992).

With increasing obstacle size, the shape of inclusions becomes important (Kalnin et al., 2002). In the case of circular inclusions, the effective diffusivity in Figure 5.4 approaches zero as radius $r \to 0.5$ and obstacle area $\phi_s \to \frac{\pi}{4}$, corresponding to the percolation threshold

of obstacles touching their neighbours. While there is still free space in the corners of the unit cell, the diffusivity is limited by the narrow channel, and Li et al. (2002) show that the asymptotic behaviour tends to

$$D_{eff} = \frac{2\left(\pi/4 - \phi\right)}{\pi^{\frac{3}{2}}}, \ \frac{\pi}{4} - \phi_s \ll 1. \tag{5.56}$$

This percolation phenomenon becomes less prominent as the obstacle shape tends to a square, in which case $D_{eff} \to 0$ only as $\phi_s \to 1$. As expected, the upper Hashin-Shtrikman bound matches the square obstacles case, and all numerical results lie within the regions specified by this, as well as the looser Wiener bounds.

5.4.2 Stochastic simulation comparison

The compartment-based Stochastic Simulation Algorithm from Chapter 3 can be extended to incorporate obstacles in the interior of the domain. Compartments with obstacles are set to behave in the same way as boundaries, with any inter-compartment jumps from a neighbouring compartment reflected, corresponding to a no-flux condition (Section 3.2.3). This rule-based approach can be further extended to model crowding effects of particles by introducing a maximum compartment occupancy, with full compartments acting as (time-dependent) obstacles. However, this extension is beyond the scope of our work, and we only consider the case of static obstacles.

For the two-dimensional, square lattice domain considered in Chapter 3, blocked compartments behave as square obstacles from Section 5.4.1. In theory, curvature can be approximated by reducing the compartment size and forming obstacle aggregates, but as discussed in Section 3.5, there would be limits to the minimum compartment choice when inter-compartment reactions are considered.

Using the effective diffusion coefficient calculated in Section 5.4.1, we now compare the obstacle and effective medium approximation for simple random walk in two dimensions in the discrete case. For two choices of compartment size, $h = 0.01$ mm and $h = 0.05$ mm, we consider a periodic checkerboard arrangement of 0.05×0.05 mm obstacles in a two-dimensional domain (Figure 5.5).

The checkerboard arrangement in Figure 5.5 corresponds to a 0.1×0.1 mm periodic unit cell, with 25% of the area occupied by obstacles. The stochastic inter-compartment jump rate from Section 3.2.4 is given by

$$k_{jump} = \frac{2d}{h^2} D, \tag{5.57}$$

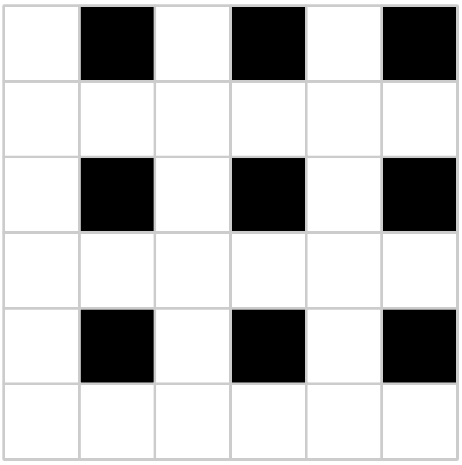

(a) 3×3 tiling of unit cells for $h = 0.05$.

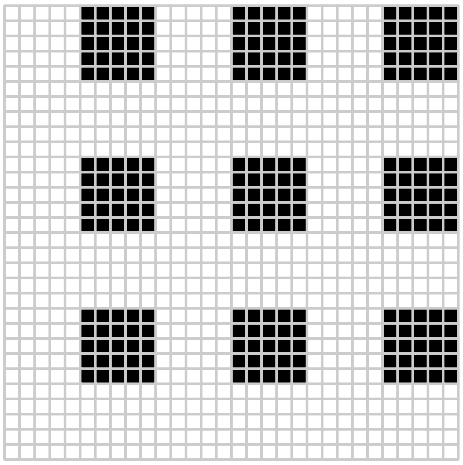

(b) 3×3 tiling of unit cells for $h = 0.01$.

Figure 5.5: Equivalent stochastic simulation domains for two discretisations.

where h is the compartment width and $d = 2$ in the two-dimensional situation. The asymptotic homogenisation method from Section 5.3 reduced the diffusion equation (5.16) in a domain with obstacles to the scaled diffusion equation (5.45) with reduced diffusivity. Due to the porosity term multiplying the $\frac{\partial}{\partial t}$ term in (5.45), the effective diffusivity from (5.46) must be divided by the porosity to put the problem in the equivalent random walk problem, giving

$$\begin{aligned} D &= \frac{D_{free}}{|\Omega \setminus \Omega_{obst}|} \iint_{\Omega} \left(1 + \frac{\partial \chi_1}{\partial y_1}\right) d\mathbf{y} \\ &\approx 0.771 \end{aligned}$$

for $D_{free} = 1$. The jump rate for the effective medium case is then calculated using this value. For a 2×2 mm domain with an initial condition of a single cell at $\mathbf{x} = (1, 1)$, 10000 simulations were run for $D_{free} = 1$ and $D_{eff} = 0.771$ for compartment size $h = 0.01$ and $h = 0.05$ mm over time interval $t \in [0, 1]$. The radial mean-squared displacement of these simulations, plotted in Figure 5.6, shows a linear relationship in time, agreeing with established results for the limiting case of a random walk (Berg, 1993, pp. 11).

The observed diffusion constant for each case (Table 5.2), shows excellent agreement between the effective medium cases for both $h = 0.01$ and $h = 0.05$ discretisations, with the values within 2% and 3%, respectively, of the expected value $D_{eff} = 0.771$. The observed diffusion coefficient for the obstacle domain for compartment size $h = 0.01$ is slightly less than the analytically-derived value, but roughly agrees with the both the effective case, and similar results reported by Holcman et al. (2011) for square obstacles. However, the analogous obstacles case for compartment size $h = 0.05$ shows a significantly reduced

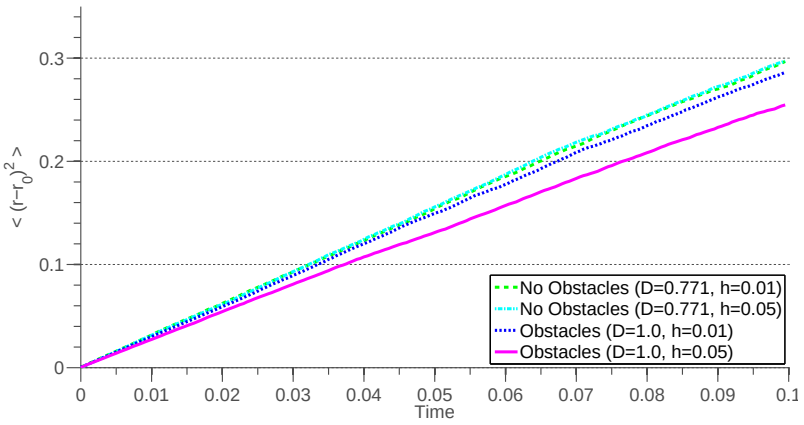

Figure 5.6: Radial mean-squared displacement of 10000 simulations for a random walk on a 0.05×0.05 mm checkerboard domain with $D_{free} = 1$ and effective medium with $D_{eff} = 0.771$ for compartment sizes $h = [0.01,\ 0.05]$.

	Slope of Mean-Square Displacement, m	Macroscopic Diffusion, $D = \frac{m}{2d}$
$h = 0.01$, Effective Medium	3.00	0.75
$h = 0.05$, Effective Medium	2.90	0.76
$h = 0.01$, Obstacles	3.03	0.73
$h = 0.05$, Obstacles	2.56	0.64

Table 5.2: Observed diffusion constant from Figure 5.6.

diffusion coefficient, with a value 17% smaller than the expected value of $D_{eff} = 0.771$. This suggests that the choice of compartment size affects the macroscopic properties of random walks on the lattice, despite representing seemingly equivalent domains.

This discrepancy between the effective medium and obstacle cases in the stochastic model is due to the relative size of obstacles to minimum jump distance (equal to compartment size, h). The asymptotic homogenization method from Section 5.3 converges to the effective diffusion in the limit $\epsilon \to 0$, and the Taylor series expansion (5.22) is valid for $\epsilon \ll 1$. However, this expansion implicitly relies on the micro-scale variable, y, being continuous, and is only valid when the mean-free path of particles (or alternatively, the particle size) is much smaller than obstacle spacing. These effects have previously been shown by Gauthier et al. (2004), who found that the use of discrete compartment sizes comparable with the size of the obstacles (or the particle) themselves will not lead to the same quantitative dynamical properties as a continuous-time, off-lattice Brownian Dynamics simulation of the same system.

Mercier et al. (1999) have shown that the correct effective diffusion limit for obstacles in an on-lattice model is recovered as $h \to 0$, but it has previously been noted that the inclusion of inter-compartment reactions to the Stochastic Simulation Algorithm enforces a minimum compartment size (Erban and Chapman, 2009). In the context of modelling cell interactions, the choice of minimum compartment size is also limited by the size of the cell, corresponding to $h = 0.01$ mm (Section 3.3).

From the results of these stochastic simulations, we conclude that classical (continuum) homogenisation approaches are insufficient in describing the macroscopic properties of domain with periodic obstacles of the same order as particles, and a new approach is required to determine the effective diffusivity in the system.

5.5 Summary

In this chapter, we have considered a simplified theoretical framework to estimate the effective motility of cells in a heterogeneous domain filled with periodic obstacles. In the limit of closely packed obstacles in a sufficiently large domain, we made use of the method of multiple scales to derive the effective motility coefficient in terms of a single unit period. This was then solved numerically using a finite element solver for symmetrical square and rounded obstacle cross-sections.

After presenting existing asymptotic approximations, as well as upper and lower bounds for the effective diffusivity in domains filled with periodic cylindrical and square obstacles, we compared these with our numerical results, and found excellent agreement with theory. The calculated motility for square obstacles was used to compare the effective medium approach with the obstacle case in the lattice-based stochastic model. The observed diffusion coefficient, calculated from the mean-squared displacement, demonstrated the breakdown

of the continuum "effective medium" approach in the discrete case for larger choices of compartment size. The reduced observed diffusion was attributed to the jump size being comparable with the obstacle size, with Taylor series expansion no longer being valid on the micro-scale due to the breakdown of the continuum assumption.

This limiting case suggests the need for a discrete analogue of the method of multiple scales, which is addressed in the next chapter.

Chapter 6

Effective transport properties of random walks on lattices

In this chapter, we develop techniques for determining the effective transport properties of a heterogeneous medium with periodic obstacles in cases where the microscale interactions are discrete. By considering the case of a random walk on a lattice with spatially-dependent transition rates, we present a method for determining whether the macroscopic behaviour is drift- or diffusion-dominated, and calculating the effective macroscopic governing equation.

6.1 Introduction

In Chapter 5, we saw how periodic, heterogeneous composite media could be approximated with a homogeneous, effective medium that takes into account the variations on the microscale. This idea is generally known as homogenisation, and several techniques exist for determining these effective properties. All these approaches depend on a separation of scale, where the heterogeneities are small relative to the global dimensions of the medium.

Various techniques exist to determine the effective properties of media. In a continuum description, various perturbation method approaches are used. Writing the system as a function of both the microscopic and macroscopic length-scales related by the ratio of the micro- and macroscopic length-scales, ϵ, the governing equations are then expanded asymptotically in powers of the small parameter ϵ. Matching solutions at orders of ϵ and making use of the periodicity of the system, the leading-order behaviour of the system can be expressed in terms of an integral of the microscopic unit cell, which describes the specific geometry of the system (as demonstrated in Section 5.3.1).

Most solids are crystalline, and what is often referred to as diffusion in such structures actually occurs by atomic hops in a lattice. There exists a separation of time-scales between the elementary jump process of particles between neighbouring lattice sites and

the succession of steps that lead to macroscopic diffusion (Mehrer, 2007). In fact, many properties of these two formulations are equivalent on macroscopic length-scales or in the slow-time limit. However, this correspondence does not always hold, particularly when the quantities of interest depend on distances comparable to the lattice constant (Blumen and Zumofen, 1981). In the case of continuum approaches to homogenisation, the microscopic scale is treated as a continuous variable to make use of Taylor expansions. As we saw in Section 5.4.2, this approach is no longer valid when the period of the microscopic variations is of the same order of magnitude as the lattice spacing, and in this case, other techniques must be used.

These limitations are often seen in solid state physics (Haus and Kehr, 1987) and lattice gas dynamics (Kutner, 1981). To overcome continuum limitation, it is common to consider jump-diffusion processes of single particles on the microscopic scale as probabilistic random walks on an ordered lattice, or in the case of a one-dimensional random walk, a periodic potential well (Zwerger and Kehr, 1980). In statistical mechanics, the Brownian motion of particles in a periodic potential well is described by Langevin equations. Using linear response theory, it is possible to derive the Kubo-Green relation relating the diffusion coefficient to the velocity autocorrelation, or an ensemble average of the second moment. Typically, this approach only allows for the calculation of the effective diffusion coefficient in the over-damped limit, as this is the limit in which only single jumps occur. It has also been noted that the Kubo-Green formula is invalid when the probe size is of the order of the applicable scale length for the lattice gas (Uebing et al., 1996).

Effective medium approximations of continuous time random walks on a lattice have also been treated using generating functions approaches by Montroll and Weiss (1965), and later applied to the study of disordered media. These approaches make use of Lattice Green functions, constructed from discrete Fourier transforms of single-step transition probabilities, expressing the effective diffusion coefficient in terms of the zeroth and second moment of the hopping probability (Scher and Lax, 1973). A thorough description of this method, as well as related techniques, can be found in reviews by Bouchaud and Georges (1990); Havlin and Ben-Avraham (1987); Kehr et al. (1998).

The Montroll-Weiss method was used by Kehr and Haus (1978) to determine the effective transport in a material with traps, such as charge transport in semiconductors and diffusion of particles in metals with defects. The general procedure, summarised in Braun and Sholl (1998); Koza (1999) is

1. Reduce infinite system to single elementary cell with periodic boundary conditions.

2. Write down Master equation.

3. Calculate steady-state properties of this system; in particular, the steady-state site occupation probabilities.

4. Using this information, find effective drift, ν, and effective diffusion coefficient, D.

Applying this result to the effective conductivity in an n-state trapping model, Kehr and Haus (1978) confirmed an existing result of frequency-independent effective conductivity, originally proposed by Tunaley (1974).

A method of determining effective diffusion coefficient, D, in arbitrary periodic lattice systems satisfying the detailed balance condition was then proposed by Braun and Sholl (1998). Building on the methods of Kutner and Sosnowska (1977); Kehr et al. (1978), the authors looked at the joint probability master equation for occupation of states on a lattice. Taking Fourier and Laplace transforms in space and time, respectively, the authors constructed an eigenvalue problem in terms of a transfer matrix and Boltzmann distribution for equilibrium occupation of sites. Defining the eigenvector and eigenvalues of the transformed system as continuous functions of wavelength, $\mathbf{k}$, the lowest eigenvector was Taylor expanded about $\mathbf{k} = 0$. The coefficients of this expansion were then related to the mean-squared displacement, and shown to be equivalent to the diffusion coefficient.

While this method is mathematically consistent, it does not give adequate physical meaning to the derived quantities. Furthermore, the effective macroscopic transport equations are not derived explicitly, but rather, the derived coefficient is shown to satisfy the effective equations through substitution.

In this chapter, we develop a more rigorous method for the derivation of effective transport equations of random walks on discrete lattices. Our derivation mirrors classical multi-scale homogenisation, and consequently, each step has physical interpretation. The resultant effective transport equations are shown as a direct consequence of the derivation, and agree with the results of Braun and Sholl (1998). Although we consider the simple case of transitions between adjacent nodes, it should be noted that the method derived here is equally valid for non-Markov processes.

6.2 Toy problem

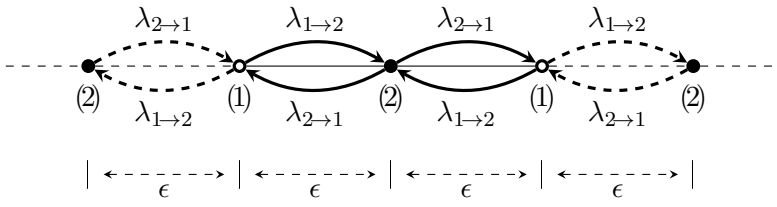

Figure 6.1: One-step transition for a one-dimensional, periodic Markov chain consisting of two distinct node types, separated by distance ϵ.

To illustrate the general approach, we start by considering the simplest case: a one-dimensional Markov chain, consisting of two distinct type of nodes separated by distance ϵ, arranged in a periodic, alternating manner (Figure 6.1). We define spatial coordinate

$x = n\epsilon$, where n is the node index $n \in \mathbb{Z}$, and node type $i \in [1,2]$, where the node type of the current position is given by $i = \mod(n-1,2)+1$. In contrast to continuum homogenisation techniques where the micro- and macroscopic length-scales are continuous variables expressed in terms of each other, the microscopic length-scale in our system is accounted for by the discrete node index, i. The Markov chain formulation implies that transitions can only occur between adjacent nodes, and writing $\lambda_{n\to n\pm1}$ to denote transition rates left and right from node n, we see that $\lambda_{n+1} = \lambda_{n-1}$ in the two-node case. Due to the periodicity of the chain, we only need to consider a single unit period of the Markov chain to characterise the overall properties of the system.

The conditional probability of being at position x in node type $i \in [1,2]$ at time $t+\Delta t$ is given by

$$\begin{aligned} P_1^{(t+\Delta t)}(x, t+\Delta t|x,t) &= \lambda_{2\to1}\Delta t P_2^{(t)}(x-\epsilon;\epsilon) + \lambda_{2\to1}\Delta t P_2^{(t)}(x+\epsilon;\epsilon) \\ &\quad + (1-2\lambda_{1\to2}\Delta t)\, P_1^{(t)}(x;\epsilon) \\ P_2^{(t+\Delta t)}(x, t+\Delta t|x,t) &= \lambda_{1\to2}\Delta t P_1^{(t)}(x-\epsilon;\epsilon) + \lambda_{1\to2}\Delta t P_1^{(t)}(x+\epsilon;\epsilon) \\ &\quad + (1-2\lambda_{2\to1}\Delta t)\, P_2^{(t)}(x;\epsilon)\,. \end{aligned} \tag{6.1}$$

For a random walk on a Markov chain consisting of a single node type, the probability $P^{(t)}(x\pm\epsilon)$ would be expanded as a Taylor series in space about x, and the $\mathcal{O}(1)$ and $\mathcal{O}(\epsilon)$ terms cancel, reducing to the Heat equation in the limit of continuous time and space. In the two-node case, $P_1^{(t)}$ and $P_2^{(t)}$ vary on the fast-scale, and therefore, the cross-terms representing transitions from adjacent states cannot be trivially expressed in terms of each other. Considering node of type i at position x, we approximate the probability of being in an adjacent state by Taylor expanding $P_{i\pm1}^{(t)}(x\pm\epsilon;\epsilon)$ in the neighbourhood of x by

$$P_{i\pm1}^{(t)}(x\pm\epsilon;\epsilon) = P_{i\pm1}^{(t)}(x;\epsilon) \pm \epsilon\frac{\partial P_{i\pm1}^{(t)}}{\partial x} + \frac{\epsilon^2}{2}\frac{\partial^2 P_{i\pm1}^{(t)}}{\partial x^2} + \mathcal{O}\left(\epsilon^3\right), \tag{6.2}$$

and (6.1) becomes

$$\begin{aligned} \frac{P_1^{(t+\Delta t)} - P_1^{(t)}}{\Delta t} &\approx -2\lambda_{1\to2}P_1^{(t)}(x;\epsilon) + 2\lambda_{2\to1}P_2^{(t)}(x;\epsilon) + \epsilon^2\lambda_{2\to1}\frac{\partial^2 P_2^{(t)}}{\partial x^2} \\ \frac{P_2^{(t+\Delta t)} - P_2^{(t)}}{\Delta t} &\approx 2\lambda_{1\to2}P_1^{(t)}(x;\epsilon) - 2\lambda_{2\to1}P_2^{(t)}(x;\epsilon) + \epsilon^2\lambda_{1\to2}\frac{\partial^2 P_1^{(t)}}{\partial x^2}. \end{aligned} \tag{6.3}$$

Taking the continuum time limit $\Delta t \to 0$, (6.3) is reduced to the system of Master equations

$$\frac{\partial}{\partial t}\mathbf{P} = A\mathbf{P} + \epsilon B\mathbf{P} + \frac{\epsilon^2}{2}C\mathbf{P}, \tag{6.4}$$

where $\mathbf{P}=\begin{bmatrix} P_1(x,t;\epsilon) & P_2(x,t;\epsilon) \end{bmatrix}^T$, $A=\begin{bmatrix} -2\lambda_{1\to 2} & 2\lambda_{2\to 1} \\ 2\lambda_{1\to 2} & -2\lambda_{2\to 1} \end{bmatrix}$, $B=\begin{bmatrix} 0 & 0 \\ 0 & 0 \end{bmatrix}$ and $C=\begin{bmatrix} 0 & 2\lambda_{2\to 1}\frac{\partial^2}{\partial x^2} \\ 2\lambda_{1\to 2}\frac{\partial^2}{\partial x^2} & 0 \end{bmatrix}$.

Taking an analogous approach to that used in classical homogenisation techniques, we assume that the transition probability vector, $\mathbf{P}$, can be written in the form of an asymptotic expansion in small parameter, ϵ, as

$$\mathbf{P}(x,t;\epsilon) = \mathbf{P}^{(0)}(x,t;\epsilon) + \epsilon\mathbf{P}^{(1)}(x,t;\epsilon) + \epsilon^2\mathbf{P}^{(2)}(x,t;\epsilon) + \mathcal{O}\left(\epsilon^3\right), \tag{6.5}$$

and introduce this into (6.4) to balance corresponding powers of ϵ. As we are interested in the macroscopic behaviour of the system, we seek to rescale time to balance the higher-order corrections in ϵ. For the two-node case, the drift matrix $B = \mathbf{0}$, and so no $\mathcal{O}(\epsilon)$ terms will appear in (6.4). The appropriate balance occurs at $\mathcal{O}\left(\epsilon^2\right)$, and we apply the scaling $t = \epsilon^{-2}\hat{t}$ to obtain

$$\epsilon^2\frac{\partial}{\partial \hat{t}}\mathbf{P}^{(0)} = A\left(\mathbf{P}^{(0)} + \epsilon^2\mathbf{P}^{(2)}\right) + \frac{\epsilon^2}{2}C\mathbf{P}^{(0)} + \mathcal{O}\left(\epsilon^3\right). \tag{6.6}$$

The transition matrix, A, is singular regardless of the choice of transition rates $\lambda_{1\to 2}$ and $\lambda_{2\to 1}$. At $\mathcal{O}(1)$, the (6.6) implies that

$$A\mathbf{P}^{(0)} = \mathbf{0}. \tag{6.7}$$

We use separation of variables to write the leading order term as a product of the slow- and fast-scale variables

$$\mathbf{P}^{(0)}\left(x,\hat{t};\epsilon\right) = \mathbf{u}f\left(x,\hat{t}\right), \tag{6.8}$$

where $\mathbf{u} = \begin{bmatrix} \lambda_{1\to 2}^{-1} & \lambda_{2\to 1}^{-1} \end{bmatrix}^T$ is an eigenvector of A, representing the stationary distribution on the fast-scale, and scalar function $f\left(x,\hat{t}\right)$ varies slowly on the macroscopic scale, and independent of the rapid variation of the unit Markov chain.

Balancing the $\mathcal{O}\left(\epsilon^2\right)$ terms in (6.6) relates $\mathbf{P}^{(2)}$ to $\mathbf{P}^{(0)}$ through the relation

$$A\mathbf{P}^{(2)} = \mathbf{b}, \tag{6.9}$$

where $\mathbf{b} = \frac{\partial}{\partial \hat{t}}\mathbf{P}^{(0)} - \frac{1}{2}C\mathbf{P}^{(0)}$. However, since matrix A is singular, there is no unique solution to (6.9). By the Fredholm Alternative Theorem, if there exists a left eigenvector, $\mathbf{v}^T$, such that $\mathbf{v}^TA = \mathbf{0}^T$, then a solution $\mathbf{P}^{(2)}$ can only exist if $\mathbf{b}$ is orthogonal to $\mathbf{v}$. A suitable left eigenvector of matrix A is $\mathbf{v}^T = \begin{bmatrix} 1 & 1 \end{bmatrix}$, and applying solvability condition

$\mathbf{v}^T\mathbf{b} = 0$, we require that

$$\mathbf{v}^T \frac{\partial}{\partial \hat{t}} \left(\mathbf{u} f\left(x, \hat{t}\right) \right) = \frac{1}{2} \mathbf{v}^T C \left(\mathbf{u} f\left(x, \hat{t}\right) \right). \tag{6.10}$$

The eigenvector $\mathbf{u}$ is independent of time, allowing us to write the governing equation for macroscopic variable $f\left(x, \hat{t}\right)$ as

$$\frac{\partial f}{\partial \hat{t}} = \left(\frac{2}{\frac{1}{\lambda_{1\to 2}} + \frac{1}{\lambda_{2\to 1}}} \right) \frac{\partial^2 f}{\partial x^2}, \tag{6.11}$$

and identify the macroscopic diffusion coefficient $D = \frac{2}{\frac{1}{\lambda_{1\to 2}} + \frac{1}{\lambda_{2\to 1}}}$ on the slow-scale.

6.3 Generalization

6.3.1 N-node case in one dimension

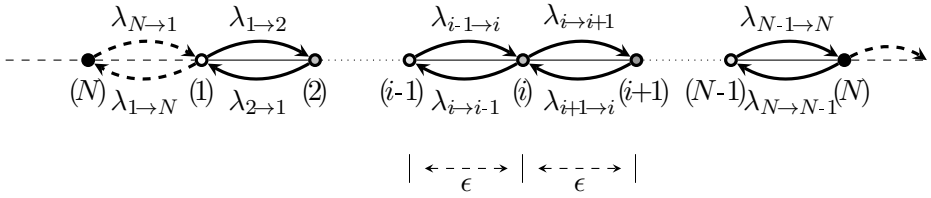

Figure 6.2: One-step transition for a one-dimensional, periodic Markov chain consisting of N distinct node types, separated by distance ϵ.

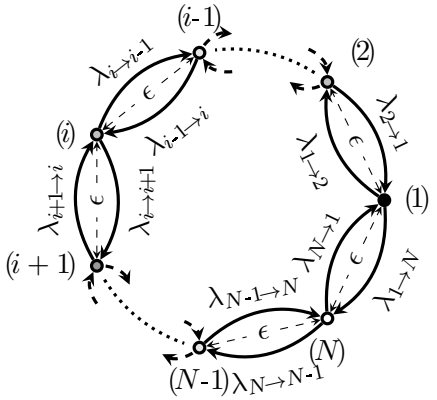

Figure 6.3: Circular queue representation of N-node periodic unit Markov chain from Figure 6.2.

We now consider the general case of a one-dimensional Markov chain consisting of an N-node unit period (Figure 6.2), of which the illustrative example from Section 6.2 is

a special case. For $N > 2$, the transition rates left and right are not necessarily equal, allowing for drift-dominant behaviour on the macroscopic scale. Such a one-dimensional chain can be pictured as a circular queue of N nodes of type $i \in [1, N]$, and current position, x, describing the number of net rotations from the initial position (Figure 6.3).

Introducing circular indexing notation $\overline{i \pm 1} \equiv \mod (i \pm 1 - 1, N) + 1$ to denote nodes adjacent to index $i \in [1, N]$, the one-step probability of being in state i at time $t + \Delta t$ is given by

$$\begin{aligned} P_i^{(t+\Delta t)}(x, t+\Delta t | x, t) &= \lambda_{\overline{i\text{-}1} \to i} \Delta t P_{\overline{i\text{-}1}}^{(t)}(x - \epsilon; \epsilon) + \lambda_{\overline{i+1} \to i} \Delta t P_{\overline{i+1}}^{(t)}(x + \epsilon; \epsilon) + \\ &\quad \left(1 - \left(\lambda_{i \to \overline{i\text{-}1}} + \lambda_{i \to \overline{i+1}}\right) \Delta t\right) P_i^{(t)}(x; \epsilon). \end{aligned} \tag{6.12}$$

Taylor expanding each $P_i^{(t)}(x \pm \epsilon)$ about x and taking continuum limit $\Delta t \to 0$, the system of Master equations for the $1 \times N$-node unit chain can be written as

$$\frac{\partial}{\partial t}\mathbf{P} = A\mathbf{P} + \epsilon B\mathbf{P} + \frac{\epsilon^2}{2} C\mathbf{P}, \tag{6.13}$$

where vector $\mathbf{P} = \begin{bmatrix} P_1 & \dots & P_N \end{bmatrix}^T$. Matrices A, B and C are $N \times N$ tridiagonal matrices with corners, and can be written as

$$\begin{aligned} A &= M_N \mathrm{diag}\left(\lambda_{i \to \overline{i+1}}\right) - \mathrm{diag}\left(\lambda_{i \to \overline{i-1}} + \lambda_{i \to \overline{i+1}}\right) + M_N^T \mathrm{diag}\left(\lambda_{i \to \overline{i+1}}\right), \\ B &= \left(M_N \mathrm{diag}\left(-\lambda_{i \to \overline{i+1}}\right) + M_N^T \mathrm{diag}\left(\lambda_{i \to \overline{i+1}}\right)\right) \frac{\partial}{\partial x}, \\ C &= \left(M_N \mathrm{diag}\left(\lambda_{i \to \overline{i+1}}\right) + M_N^T \mathrm{diag}\left(\lambda_{i \to \overline{i+1}}\right)\right) \frac{\partial^2}{\partial x^2}, \end{aligned} \tag{6.14}$$

where $M_N = \left[\begin{array}{c|c} 0 & 1 \\ \hline \mathbf{I}_{N-1} & 0 \end{array}\right]$ is the $N \times N$ cyclic permutation matrix.

As with the two-node case in Section 6.2, the transition matrix A is singular, as conservation of probability implies that each column sums to zero for any choice of $\lambda_{j \to i}$. From this, we identify $\mathbf{v}^T = \mathbf{1}_{1 \times N}$ as a suitable left-eigenvector for any general transition matrix A.

Following the same procedure as in Section 6.2, we write an asymptotic expansion of $\mathbf{P}(x, t; \epsilon)$ in terms small parameter ϵ as

$$\mathbf{P}(x, t; \epsilon) = \mathbf{P}^{(0)}(x, t; \epsilon) + \epsilon \mathbf{P}^{(1)}(x, t; \epsilon) + \epsilon^2 \mathbf{P}^{(2)}(x, t; \epsilon) + \mathcal{O}\left(\epsilon^3\right), \tag{6.15}$$

and (6.13) becomes

$$\begin{aligned}\frac{\partial}{\partial t}\left(\mathbf{P}^{(0)}+\epsilon\mathbf{P}^{(1)}+\epsilon^2\mathbf{P}^{(2)}\right) &= A\mathbf{P}^{(0)}+\epsilon\left(A\mathbf{P}^{(1)}+B\mathbf{P}^{(0)}\right)\\ &\quad+\epsilon^2\left(A\mathbf{P}^{(2)}+B\mathbf{P}^{(1)}+\frac{1}{2}C\mathbf{P}^{(0)}\right)+\mathcal{O}\left(\epsilon^3\right). \quad (6.16)\end{aligned}$$

In contrast to the two-node case, the drift matrix B is generally non-zero, and thus diffusion arising from $\mathcal{O}\left(\epsilon^2\right)$ terms is not necessarily the dominant behaviour on the slow-scale. We seek to rescale time as $t=\epsilon^{-k}\hat{t}$, where $k\in\mathbb{Z}^+$ is the smallest integer such that (6.16) is non-trivial at $\mathcal{O}\left(\epsilon^k\right)$.

At $\mathcal{O}(1)$, (6.16) with substitution $t=\epsilon^k\hat{t},\ k\in\mathbb{Z}^+$ gives the balance

$$A\mathbf{P}^{(0)}=0. \quad (6.17)$$

Using separation of variables, we write $\mathbf{P}^{(0)}\left(x,\hat{t};\epsilon\right)$ as a product of the slow- and fast-scale variables

$$\mathbf{P}^{(0)}\left(x,\hat{t};\epsilon\right)=\mathbf{u}f\left(x,\hat{t}\right), \quad (6.18)$$

where $\mathbf{u}$ is an eigenvector of A, representing the stationary distribution on the fast-scale, and scalar function $f\left(x,\hat{t}\right)$ varies slowly on the macroscopic scale, and independent of the rapid variation of the unit Markov chain. In theory, the eigenvector $\mathbf{u}$ can be solved for analytically. However, with the exception of some special cases (discussed in Section 6.4), the analytic form of $\mathbf{u}$ is non-trivial, and would usually be solved for numerically.

At $\mathcal{O}(\epsilon)$, (6.16) gives the balance

$$A\mathbf{P}^{(1)}=\mathbf{b}, \quad (6.19)$$

where $\mathbf{b}=-B\frac{\partial}{\partial x}\left(\mathbf{u}f\left(x,\hat{t}\right)\right)$. Since matrix A is singular, $A\mathbf{P}^{(1)}=\mathbf{b}$ does not have a unique solution for $k\geq 2$. By the Fredholm Alternative Theorem, we require $\mathbf{v}^T\mathbf{b}=0$ for all solutions of $A^T\mathbf{v}$ in order for a solution solution $\mathbf{P}^{(1)}$ to exist at $\mathcal{O}(\epsilon)$. This means that either

$$\mathbf{v}^TB\mathbf{u}=0, \quad (6.20)$$

and no further information about $f\left(x,\hat{t}\right)$ is gained, or

$$\frac{\partial f}{\partial x}=0, \quad (6.21)$$

From (6.14), we see that the solvability condition (6.20) can be written as

$$\sum_{i}^{N} u_i \left(\lambda_{i\to\overline{i-1}} - \lambda_{i\to\overline{i+1}}\right) \neq 0. \tag{6.22}$$

If (6.20) is non-zero, then the requirement that $\mathbf{v}^T\mathbf{b} = 0$ implies that $\frac{\partial f}{\partial x} = 0$. In this case, the dominant behaviour occurs at $\mathcal{O}(\epsilon)$, and we choose time scaling $t = \epsilon^{-1}\hat{t}$ to balance the terms in (6.16). Solving the equation

$$\mathbf{v}^T\left(\mathbf{u}\frac{\partial f}{\partial t} - B\frac{\partial}{\partial x}\left(\mathbf{u}f\left(x,\hat{t}\right)\right)\right) = 0, \tag{6.23}$$

gives the governing equation for the time evolution of macroscopic function, $f\left(x,\hat{t}\right)$, as

$$\frac{\partial f}{\partial t} = \nu\frac{\partial f}{\partial x}, \tag{6.24}$$

where the macroscopic drift coefficient, ν, is given by

$$\nu = \frac{\mathbf{v}^T B\mathbf{u}}{\mathbf{v}^T\mathbf{u}}. \tag{6.25}$$

If solvability condition (6.20) is zero, then $\frac{\partial f}{\partial x} \neq 0$ in general, and the $\mathbf{P}^{(1)}$ terms in (6.13) must satisfy

$$A\mathbf{P}^{(1)} = -B\mathbf{u}\frac{\partial f}{\partial x}. \tag{6.26}$$

Since $v^T B\mathbf{u} = 0$, there exists a constant vector,$\mathbf{w}$, such that

$$A\mathbf{w} = -B\mathbf{u}, \tag{6.27}$$

which determines a solution

$$\mathbf{P}^{(1)} = \mathbf{w}\frac{\partial f}{\partial x}. \tag{6.28}$$

Since $A\mathbf{u} = 0$, the solution (6.28) is not unique, as adding any multiple of $\mathbf{u}$ will also satisfy (6.26). Therefore, the general solution for $\mathbf{P}^{(1)}$ can be written as

$$\mathbf{P}^{(1)} = \mathbf{w}\frac{\partial f}{\partial x} + \mathbf{u}g\left(x,\hat{t}\right), \tag{6.29}$$

for arbitrary scalar function $g\left(x,\hat{t}\right)$. In order to determine $f\left(x,\hat{t}\right)$, we need to consider the next order of (6.16).

Choosing time scaling $t = \epsilon^{-2}\hat{t}$, we find that at $\mathcal{O}\left(\epsilon^2\right)$, this gives

$$A\mathbf{P}^{(2)} = \frac{\partial}{\partial \hat{t}}\mathbf{P}^{(0)} - \frac{1}{2}C\frac{\partial^2}{\partial x^2}\mathbf{P}^{(0)} - B\mathbf{P}^{(1)}. \tag{6.30}$$

Applying the Fredholm Alternative Theorem at $\mathcal{O}\left(\epsilon^2\right)$, the solvability condition implies that

$$\mathbf{v}^T\left(\frac{\partial}{\partial \hat{t}}\left(\mathbf{u}f\left(x,\hat{t}\right)\right)\right) = \mathbf{v}^T\left(\frac{1}{2}C\mathbf{u}f\left(x,\hat{t}\right) - B\mathbf{w}\frac{\partial f}{\partial x}\right), \tag{6.31}$$

which is satisfied for any Markov chain with at least one non-zero transition rate. The time evolution of scalar function $f\left(x,\hat{t}\right)$ on the slow time-scale can now be written as the advection-diffusion equation

$$\frac{\partial f}{\partial \hat{t}} = D\frac{\partial^2 f}{\partial x^2} - \nu\frac{\partial f}{\partial x}, \tag{6.32}$$

where macroscopic diffusion coefficient, D, is given by

$$D = \frac{\mathbf{v}^T C\mathbf{u}}{2\mathbf{v}^T\mathbf{u}}, \tag{6.33}$$

and additional macroscopic advection coefficient, ν, is given by

$$\nu = \frac{\mathbf{v}^T B\mathbf{w}}{\mathbf{v}^T\mathbf{u}}. \tag{6.34}$$

6.3.2 Generalization to $N \times N$-node case in two-dimensions

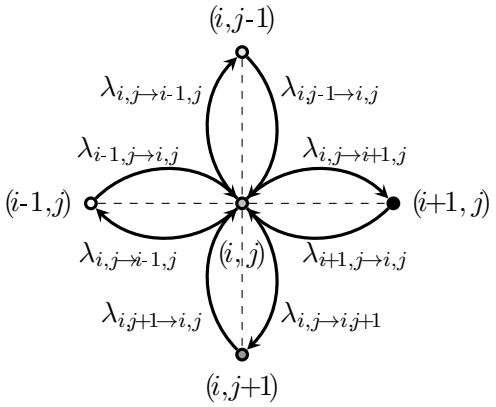

Figure 6.4: One-step transition for a two-dimensional, periodic Markov chain consisting of $N \times N$ distinct node types, each separated by distance ϵ.

The approach outlined in Section 6.3.1 can be generalised to a two-dimensional, $N \times N$-node Markov chain. This extension is of particular interest in real-world applications, as it allows us to represent a structured domain with obstacles (via a zero transition rate in the unit Markov chain), while retaining non-zero macroscopic drift or diffusion in the system.

Introducing notation $\lambda_{i,j\to k,l}$ to denote transition rate from node type (i,j) to (k,l), we consider a four-connected system where valid transitions only occur between adjacent nodes, $(k,l) = \left(i, \overline{j \pm 1}\right)$ or $(k,l) = \left(\overline{i \pm 1}, j\right)$, as shown in Figure 6.4. We Taylor expand the discrete-time transition probabilities $P^{(t)}_{\overline{i\pm1},j}(x \pm \epsilon, y; \epsilon)$ and $P^{(t)}_{i,\overline{j\pm1}}(x, y \pm \epsilon; \epsilon)$ in the neighbourhood of x, and take the continuum time limit $\Delta t \to 0$, resulting in the two-dimensional Master equation

$$\frac{\partial}{\partial t}\mathbf{P} = A\mathbf{P} + \epsilon B\mathbf{P} + \frac{\epsilon^2}{2}C\mathbf{P}, \tag{6.35}$$

which is written in vectorised form by defining

$$\mathbf{P} = \begin{bmatrix} P_{1,1} & \cdots & P_{1,N} & P_{2,1} & \cdots & P_{2,N} & \cdots & \cdots & P_{N,N} \end{bmatrix}^T.$$

In this formulation, matrices A, B and C are $N^2 \times N^2$ block tridiagonal matrices with corners (with $N \times N$ tridiagonal corner matrices on the main diagonal), of the form

$$\begin{aligned}
A &= M_{N^2}\mathrm{diag}\left(\vec{\lambda}_{\mathbf{i}\to\overline{\mathbf{i+1}}}\right) + M^T_{N^2}\mathrm{diag}\left(\vec{\lambda}_{\mathbf{i}\to\overline{\mathbf{i-1}}}\right) \\
&\quad + \mathrm{diag}\left(M_N\mathrm{diag}\left(\lambda_{i,j\to i,\overline{j+1}}\right) - \mathrm{diag}\left(\lambda_{i,j\to i,\overline{j\pm1}} + \lambda_{i,j\to\overline{i\pm1},j}\right) + M^T_N\mathrm{diag}\left(\lambda_{i,j\to i,\overline{j+1}}\right)\right) \\
B &= M_{N^2}\mathrm{diag}\left(-\vec{\lambda}_{\mathbf{i}\to\overline{\mathbf{i+1}}}\right)\frac{\partial}{\partial x} + M^T_{N^2}\mathrm{diag}\left(\vec{\lambda}_{\mathbf{i}\to\overline{\mathbf{i-1}}}\right)\frac{\partial}{\partial x} \\
&\quad + \mathrm{diag}\left(M_N\mathrm{diag}\left(-\lambda_{i,j\to i,\overline{j+1}}\right)\frac{\partial}{\partial y} + M^T_N\mathrm{diag}\left(\lambda_{i,j\to i,\overline{j+1}}\right)\frac{\partial}{\partial y}\right), \\
C &= M_{N^2}\mathrm{diag}\left(\vec{\lambda}_{\mathbf{i}\to\overline{\mathbf{i+1}}}\right)\frac{\partial^2}{\partial x^2} + M^T_{N^2}\mathrm{diag}\left(\vec{\lambda}_{\mathbf{i}\to\overline{\mathbf{i-1}}}\right)\frac{\partial^2}{\partial x^2} \\
&\quad + \mathrm{diag}\left(M_N\mathrm{diag}\left(\lambda_{i,j\to i,\overline{j+1}}\right)\frac{\partial^2}{\partial y^2} + M^T_N\mathrm{diag}\left(\lambda_{i,j\to i,\overline{j+1}}\right)\frac{\partial^2}{\partial y^2}\right),
\end{aligned} \tag{6.36}$$

where $M_{N^2} = \left[\begin{array}{c|c} \mathbf{0}_{N\times N} & \mathbf{1}_{N\times N} \\ \hline \mathbf{I}_{(N^2-N)} & \mathbf{0}_{N\times N} \end{array}\right]$ is the $N^2 \times N^2$ block-cyclic permutation matrix, $M_N = \left[\begin{array}{c|c} 0 & 1 \\ \hline \mathbf{I}_{N-1} & 0 \end{array}\right]$ is a regular $N\times N$ cyclic permutation matrix, and $\vec{\lambda}_{\mathbf{k}\to\mathbf{l}} = \begin{bmatrix} \lambda_{k,1\to l,1} & \cdots & \lambda_{k,N\to l,N} \end{bmatrix}^T$.

As expected, transition matrix A conserves mass, and the left-eigenvector is given by $\mathbf{v}^T = \mathbf{1}_{1\times N^2}$. The general procedure for determining the macroscopic properties of the system are analogous to the one-dimensional case, and the general procedure is outlined in Algorithm 3.

Algorithm 3 General procedure for determining macroscopic diffusion and advection coefficients of periodic Markov chains.

1. Write down one-step transition probabilities.

2. Taylor expand $P^{(t)}_{\mathbf{i}\pm\mathbf{1}}(\mathbf{x}\pm\epsilon;\epsilon)$ terms about $\mathbf{x}$.

3. Take continuum limit $\Delta t \to 0$ and write governing equation of the form

$$\frac{\partial}{\partial t}\mathbf{P} = A\mathbf{P} + \epsilon B\mathbf{P} + \frac{\epsilon^2}{2}C\mathbf{P} + \mathcal{O}\left(\epsilon^3\right).$$

4. Calculate $\mathbf{b} = \mathbf{v}^T B\mathbf{u}$.

   (a) If $\mathbf{b} = 0$, then rescale time to advection-diffusion timescale $t = \epsilon^{-2}\hat{t}$.

   (b) If $\mathbf{b} \neq 0$, then rescale time to advection timescale $t = \epsilon^{-1}\hat{t}$.

5. Expand $\mathbf{P}$ as a power series in small parameter ϵ

$$\mathbf{P} = \mathbf{P}^{(0)} + \epsilon\mathbf{P}^{(1)} + \epsilon^2\mathbf{P}^{(2)} + \ldots$$

6. Calculate $\mathbf{u}$, an eigenvector of A, and write

$$\mathbf{P}^{(0)} = \mathbf{u}f\left(\mathbf{x},\hat{t}\right),$$

   where $f\left(\mathbf{x},\hat{t}\right)$ is independent of fast-scale ϵ.

   (a) If $\mathbf{b} \neq 0$ and $B \neq \mathbf{0}$, write

$$\mathbf{P}^{(1)} = \mathbf{w}\frac{\partial}{\partial \mathbf{x}}f\left(x,\hat{t}\right) + \mathbf{u}g\left(\mathbf{x},\hat{t}\right),$$

   where $g\left(\mathbf{x},\hat{t}\right)$ is independent of fast-scale ϵ, and solve

$$A\mathbf{w} = -B\mathbf{u},$$

   to obtain $\mathbf{w}$.

7. Match next order of ϵ, and apply Fredholm Alternative Theorem using orthogonal vector $\mathbf{v}^T = \begin{bmatrix}1 & \cdots & 1\end{bmatrix}$.

   (a) Advection-dominated ($\mathbf{b} \neq 0$)

$$\frac{\partial f}{\partial \hat{t}} = \frac{1}{\mathbf{v}^T\mathbf{u}}\left(\mathbf{v}^T B\mathbf{u}\right)\nabla f.$$

   (b) Advection-Diffusion-dominated ($\mathbf{b} = 0$)

$$\frac{\partial f}{\partial \hat{t}} = \frac{1}{2\mathbf{v}^T\mathbf{u}}\left(\mathbf{v}^T C\mathbf{u}\right)\nabla^2 f - \frac{\mathbf{v}^T B\mathbf{w}}{\mathbf{v}^T\mathbf{u}}\nabla f.$$

6.4 Results

6.4.1 Source-dependent transition rates

One special case of unit Markov chain that has a tractable analytic form for the eigenvector, u, is a source-driven jump process, where the transition rate $\lambda_{\mathbf{i}\to\mathbf{j}}$ only depends on the current node type $\mathbf{i}$, and has no dependence on the destination. Such a restriction is typical in physical cases such as particles trapped in a potential well, and in the effective diffusion calculations for crystalline structures with impurities in solid-state physics. In this formulation, transition rates (which are typically of temperature-dependent, Arrhenius type) relate to the energy required to overcome the trapping potential, and may be thought of as the inverse mean time to escape from a given well. Once this energy is overcome, the particle is free to move isotropically, resulting in purely diffusive macroscopic behaviour. Variations of this, such as the tilted washboard potentials found in Josephson junctions and molecular ratchets, result in asymmetric potentials where the transition probabilities depend on the jump direction (Tatarkova et al., 2003; Pavliotis and Vogiannou, 2008). This introduces a bias in the system, which results in a macroscopic drift.

In two dimensions, we define the jump rate from node (i, j) to any adjacent node as $\lambda_{i,j}$, such that $\lambda_{i,j\to\overline{i\pm1},j} = \lambda_{i,j\to i,\overline{j\pm1}} = \lambda_{i,j}$. Following the general approach from Algorithm 3, we find that eigenvector $\mathbf{u}$ has the analytic form

$$u_{ij} = \frac{1}{\lambda_{i.j}}, \tag{6.37}$$

and since the transition rates are isotropic, the solvability condition $\mathbf{v}^T B\mathbf{u} = 0$. Solving the equation

$$A\mathbf{w} = B\mathbf{u}, \tag{6.38}$$

we find that $\mathbf{w} = \mathbf{u}$ in the source-dependent case. This implies that the drift term, ν, becomes

$$\begin{aligned} \nu &= \frac{\mathbf{v}^T A\mathbf{u}}{\mathbf{v}^T\mathbf{u}} \\ &= 0. \end{aligned} \tag{6.39}$$

The time evolution on the macroscopic scale in two dimensions is therefore given by

$$\frac{\partial f}{\partial t} = \left(\frac{4}{\sum_{i,j} {}^1\!/\lambda_{i,j}}\right) \nabla^2 f\left(x, y, t\right). \tag{6.40}$$

As expected, there is no anisotropy in this system. This is to be expected, as there is no bias in the transitions to any adjacent nodes. It is possible to obtain trapping states by

setting $\lambda_{k,l} \to 0$ for some nodes, but such a configuration would not violate the isotropic properties of the system on the macroscopic scale.

The application of source-dependent transition rates to trapping states in heterogeneous (non-Bravais) lattices has been studied extensively by Haus and Kehr (1987); Kutner (1981); Dieterich et al. (1980) in solid-state conductors and charge transport in semiconductors. Using Lattice Greens functions, Kehr et al. (1978) derive the effective diffusion coefficient

$$D_{\text{eff}} = \frac{n}{2d}\frac{a^2}{\langle\tau\rangle}, \tag{6.41}$$

where $\langle\tau\rangle$ is the residence time averaged over all sites, n is the number of nearest neighbour sites and a is the lattice constant. The transition rates $\lambda_{i,j}$ can be considered as proportional to the inverse of residence time at site (i,j), and so this expression agrees with our result.

To illustrate these trapping states, we consider the case of a 2×2-node periodic unit cell with purely source-dependent transitions, placed in a checkerboard such that $\lambda_{1,1} = \lambda = \lambda_{2,2}$ and $\lambda_{1,2} = \mu = \lambda_{2,1}$. Figure 6.5 shows the mean squared displacement of a particle undergoing a random walk for the case of $\mu = \frac{1}{\lambda}$ and $\mu =$ constant as $\lambda \to 0$. As expected, the effective diffusion coefficient in the x and y directions are equal, and agree perfectly with the analytic prediction given by discrete homogenisation. We also see that in the limiting case of $\lambda \to 0$, the $\mu = \frac{1}{\lambda}$ and $\mu =$ constant cases converge at the same rate, indicating a trapping state which is independent of the transition rate of its neighbours.

6.4.2 Destination-dependent transition rates

Another important type of periodic unit Markov chain is one where the transition rate $\lambda_{i,j\to k,l}$ depends purely on the destination node, such that $\lambda_{i,\overline{j\pm1}\to i,j} = \lambda_{i,j} = \lambda_{\overline{i\pm1},j}$. In contrast to the source-driven case, where the transition rates represented an energy trap binding the particle to its current node, the destination-dependent case represents a barrier to overcome on arriving to a new node. This has important physical application in biology, where spatial heterogeneities such as layered media can be modelled with varying λ, or porous media in the limiting case of $\lambda_{i,j} \to 0$ (Olveczky and Verkman, 1998; Posnansky and Shah, 2008; Aliev and Tikhonov, 2004; Saxton and Jacobson, 1997), and in solid-state physics, where diffusion process across a step edge is known to differ from diffusion on a terrace. Such interlayer diffusion processes are usually characterised by an additional barrier, the Ehrlich-Schwoebel (ES) barrier, added to the activation energy for diffusion on a terrace (Rabbering et al., 2009).

On formulating the general destination-dependent problem in 2D, we find that eigenvector $\mathbf{u}$ has the analytic form

$$u_{ij} = \lambda_{i,j}, \tag{6.42}$$

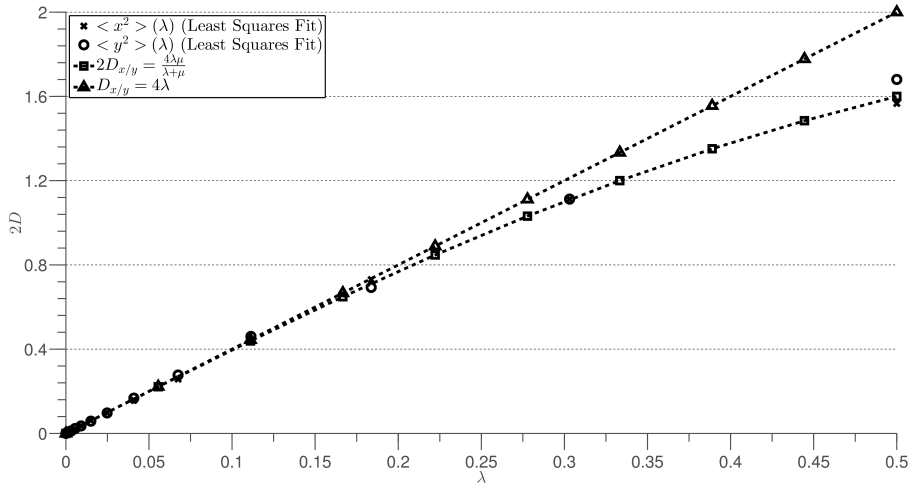

(a) $\mu = \frac{1}{\lambda}$.

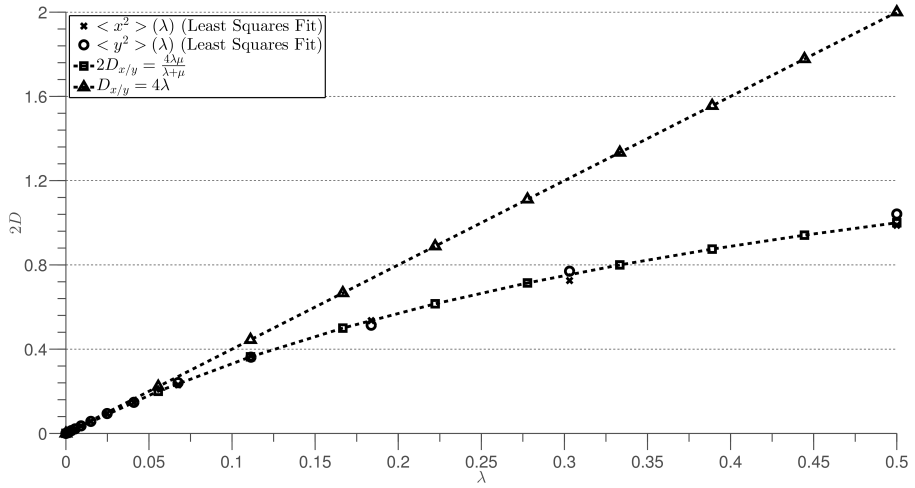

(b) $\mu = \frac{1}{2}$.

Figure 6.5: Effective diffusion coefficient for 2×2 source-driven transition with $\lambda_{1,1} = \lambda = \lambda_{2,2}$ and $\lambda_{1,2} = \mu = \lambda_{2,1}$.

with solvability condition

$$\mathbf{v}^T B\mathbf{u} = 0, \tag{6.43}$$

satisfied for arbitrary choice of destination-dependent transition rates. This indicates that the dominant transport process on the macro-scale is advection-diffusion, and following the method outline in Algorithm 3, we find that in 2D, the form of macroscopic transport equation is

$$\frac{\partial f}{\partial \hat{t}} = D_x \frac{\partial^2 f}{\partial x^2} + D_y \frac{\partial^2 f}{\partial y^2} + \nu_x \frac{\partial f}{\partial x} + \nu_y \frac{\partial f}{\partial y}. \tag{6.44}$$

The diffusion coefficients, D_x and D_y, have the closed-form expression

$$\begin{aligned} D_x &= \frac{2\left(\sum_{i,j} \lambda_{i,j}\lambda_{i+1,j}\right)}{\left(\sum_{i,j} \lambda_{i,j}\right)^2}, \\ D_y &= \frac{2\left(\sum_{i,j} \lambda_{i,j}\lambda_{i,j+1}\right)}{\left(\sum_{i,j} \lambda_{i,j}\right)^2}. \end{aligned} \tag{6.45}$$

The advection terms ν_x and ν_y are generally non-zero, but without a closed-form solution for vector $\mathbf{w}$, these are to be determined numerically from Algorithm 3. In contrast to the source-dependent jump rates, the diffusion (and advection) coefficients in the destination-dependent case are not necessarily equal, and now depend on the specific structure of $N \times N$ unit cell. An exception to this is the special 2×2-node case, where $B = \mathbf{0}$ and no advection terms appear, but anistropic diffusion may still be present.

To illustrate this, we consider the simple case of a 2×2-node periodic Markov chain with an obstacle at position $(1, 2)$ such that $\lambda_{i,j\to 1,2} = 0$. The analytic expression for the diffusion coefficients becomes

$$\begin{aligned} D_x &= 2\left(\frac{\lambda_{2,1}\lambda_{2,2}}{\lambda_{1,1} + \lambda_{2,1} + \lambda_{2,2}}\right), \\ D_y &= 2\left(\frac{\lambda_{1,1}\lambda_{2,1}}{\lambda_{1,1} + \lambda_{2,1} + \lambda_{2,2}}\right). \end{aligned} \tag{6.46}$$

Comparing this result to the mean squared displacement in x and y for 1000 Monte-Carlo simulations of a destination-dependent checkerboard with $\lambda_{\to 1,1} = \frac{1}{8}$, $\lambda_{\to 2,1} = \frac{1}{4}$ and $\lambda_{\to 2,2} = \frac{1}{2}$ in Figure 6.6, we see excellent agreement between our predicted effective properties and the numerical results.

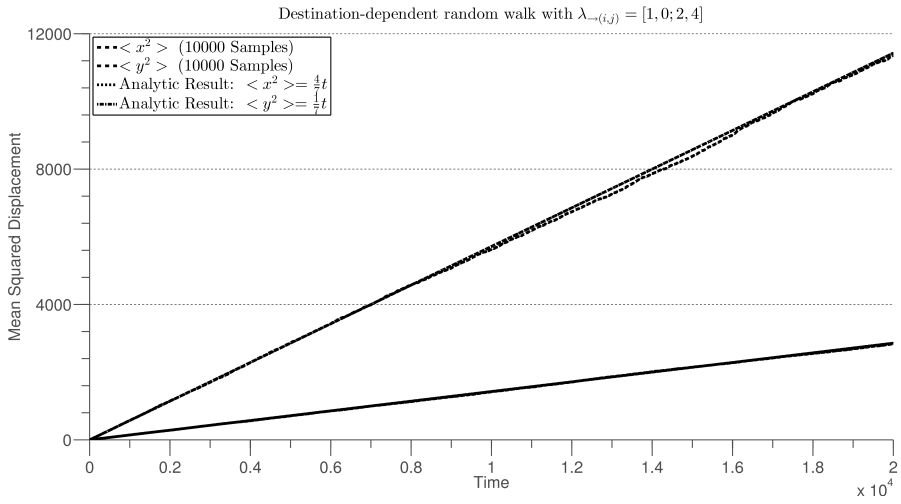

Figure 6.6: Mean Squared Displacement for 2×2-node destination-driven Markov chain with obstacle at $(1, 2)$ and $\lambda_{\to 1,1} = \frac{1}{8}$, $\lambda_{\to 2,1} = \frac{1}{4}$ and $\lambda_{\to 2,2} = \frac{1}{2}$.

6.4.3 Four-phase checkerboard with barrier

In the theory of electrical conductivity of composite materials, the four-phase checkerboard consisting of a 2×2 tiling of different materials is one of the few known cases with a closed-form analytic solution for effective conductivity (Milton, 2001), given by the Mortola-Steffe formula reviewed in Section 5.2

$$\left(\overline{\lambda}_{ij}\right) = \begin{bmatrix} \overline{\lambda}_{11} & 0 \\ 0 & \overline{\lambda}_{22} \end{bmatrix}, \tag{6.47}$$

where

$$\begin{aligned} \lambda_{11} &= \sqrt{\frac{(\alpha+\gamma)(\beta+\delta)}{(\alpha+\beta)(\gamma+\delta)}} \times \sqrt{\frac{\alpha\beta\gamma+\alpha\beta\delta+\alpha\gamma\delta+\beta\gamma\delta}{\alpha+\beta+\gamma+\delta}}, \\ \lambda_{22} &= \sqrt{\frac{(\alpha+\beta)(\gamma+\delta)}{(\alpha+\gamma)(\beta+\delta)}} \times \sqrt{\frac{\alpha\beta\gamma+\alpha\beta\delta+\alpha\gamma\delta+\beta\gamma\delta}{\alpha+\beta+\gamma+\delta}}, \end{aligned} \tag{6.48}$$

and α, β, γ and δ are the effective conductivities of each material (Craster and Obnosov, 2001).

For general transition rates that depend on both the source and destination node, the form of eigenvector $\mathbf{u}$ is non-trivial. However, it is possible to write in closed-form for certain special cases. Consider the four-phase checkerboard with an obstacle at position $(1, 2)$, but with general transition rates that may depend on both source and destination nodes. Setting $\lambda_{1,1\to 1,2} = 0$, $\lambda_{2,2\to 1,2} = 0$ and $\lambda_{1,2\to 1,1} = 0$, $\lambda_{1,2\to 2,2} = 0$, the eigenvector,

$\mathbf{u}$, is given by

$$\mathbf{u} = \left[\frac{\lambda_{2,1\to1,1}^2\lambda_{2,2\to2,1}^2}{\lambda_{1,1\to2,1}^2\lambda_{2,1\to2,2}^2} \quad 0 \quad \frac{\lambda_{2,1\to1,1}\lambda_{2,2\to2,1}^2}{\lambda_{1,1\to2,1}\lambda_{2,1\to2,2}^2} \quad \frac{\lambda_{2,1\to1,1}\lambda_{2,2\to2,1}}{\lambda_{1,1\to2,1}\lambda_{2,1\to2,2}}\right]^T, \tag{6.49}$$

and solvability condition $\mathbf{v}^T B\mathbf{u}$ becomes

$$\begin{aligned} 2\Bigg(&-\frac{\lambda_{2,1\to1,1}^2\lambda_{2,2\to2,1}^2}{\lambda_{1,1\to2,1}\lambda_{2,1\to2,2}^2}\frac{\partial}{\partial y} - \frac{2\lambda_{2,1\to1,1}\lambda_{2,2\to2,1}^2}{\lambda_{1,1\to2,1}\lambda_{2,1\to2,2}}\frac{\partial}{\partial x} \\ &+\frac{2\lambda_{2,1\to1,1}^2\lambda_{2,2\to2,1}^2}{\lambda_{1,1\to2,1}\lambda_{2,1\to2,2}^2}\frac{\partial}{\partial y} + \frac{\lambda_{2,1\to1,1}\lambda_{2,2\to2,1}^2}{\lambda_{1,1\to2,1}\lambda_{2,1\to2,2}}\frac{\partial}{\partial x}\Bigg) = 0. \end{aligned} \tag{6.50}$$

Therefore, the dominant behaviour of the system on the macro-scale is diffusion, with governing equation

$$\frac{\partial f}{\partial \hat{t}} = D_x\frac{\partial^2 f}{\partial x^2} + D_y\frac{\partial^2 f}{\partial x^2}, \tag{6.51}$$

with effective diffusion coefficients

$$\begin{aligned} D_x &= 2\left(\frac{\lambda_{2,1\to1,1}}{\lambda_{1,1\to2,1}\lambda_{2,1\to2,2}} + \frac{1}{\lambda_{2,1\to2,2}} + \frac{1}{\lambda_{2,2\to2,1}}\right)^{-1}, \\ D_y &= 2\left(\frac{\lambda_{2,1\to2,2}}{\lambda_{2,1\to1,1}\lambda_{2,2\to2,1}} + \frac{1}{\lambda_{1,1\to2,1}} + \frac{1}{\lambda_{2,1\to1,1}}\right)^{-1}. \end{aligned} \tag{6.52}$$

Figure 6.7 shows the mean squared displacement for 1000 Monte-Carlo realizations of a four-phase system with obstacle at $(1,2)$ and general transition rates $\lambda_{1,1\to2,1} = \frac{1}{8}$, $\lambda_{2,1\to1,1} = \frac{1}{16}$, $\lambda_{2,1\to2,2} = \frac{1}{4}$ and $\lambda_{2,2\to2,1} = \frac{1}{2}$. As in the previous cases, this shows excellent agreement with the analytic results of $D_x = \frac{1}{4}$ and $D_y = \frac{1}{16}$.

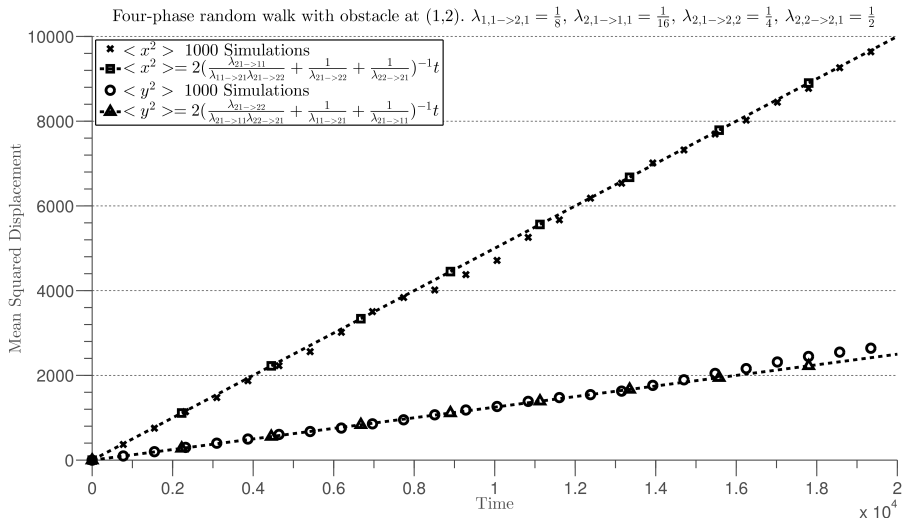

Figure 6.7: Mean Squared Displacement for 2×2-node Markov chain with obstacle at $(1,2)$ and general transition rates $\lambda_{1,1\to2,1} = \frac{1}{8}$, $\lambda_{2,1\to1,1} = \frac{1}{16}$, $\lambda_{2,1\to2,2} = \frac{1}{4}$ and $\lambda_{2,2\to2,1} = \frac{1}{2}$.

6.5 Summary

In this chapter, we have developed a method for determining the macroscopic transport properties of an infinite periodic Markov chains or lattice, with spatially-dependent transition rates. By Taylor expanding the conditional probability of each node in a unit chain on the microscale, we constructed a matrix equation governing the time evolution of node occupation probabilities. Using a perturbation expansion from classical homogenisation theory, the Fredholm Alternative Theorem was applied to construct a solvability condition for the system. This condition on the eigenvector of the transition rate matrix, determined whether drift or diffusion was the dominant behaviour on the macroscale. The effective drift or diffusion coefficient was shown to be a simple analytic expression dependent on the product of the transition rate matrix and eigenvector. While, in theory, the eigenvector could be solved analytically, in practice, numerical methods would be used to trivially solve for the solvability condition and effective governing equation with little computational cost.

The effective Markov chain approach was then extended to a two-dimensional lattice. Analytic solutions for two special forms of transitions were then derived. For transition rates that depend only on the current location, the macroscopic behaviour was shown to be isotropic diffusion, with the effective diffusivity equal to the harmonic mean of the transition rates. For transition rates that depend only on the target jump location, the macroscopic was shown to be advection-diffusion, with the effective diffusivity proportional to the sum of product pairs of adjacent transition rates, and effective drift calculated from the eigenvector of transition rates. In general, the effective diffusion coefficient was not isotropic, and a non-zero drift term appeared in the macroscopic equation, with the exact values dependent on the forms of transition rates. Numerical simulations for heterogeneous lattices were in perfect agreement with their effective homogeneous counterparts.

For the random walks of particles in the presence of obstacles, initially considered in Section 5.4.2, the destination-dependent formulation can be utilised when the obstacle size is comparable to the jump size. The analytic expression for a 2×2 grid from Section 6.4.2 predicts an effective diffusivity $D_x = \frac{2}{3} = D_y$ for transition rate $\lambda_{1,1} = \lambda_{2,1} = \lambda_{2,2} = 1$ and $\lambda_{1,2} = 0$. This agrees with the results from stochastic simulations of $D = 0.73$ and $D = 0.64$, for lattice spacings $h = 0.01$ and $h = 0.05$, respectively.

More generally, the method developed in this chapter is also valid for non-Markov periodic unit chains and lattices. Allowing transitions to non-adjacent states would result in additional terms in the Taylor expansion of the conditional probabilities in the Master equation, and alter the form of the transition matrix. Rather than being a tridiagonal matrix, this would now become $(2n+1)$-diagonal, where $n \in \mathbb{N}$ is maximum neighbour jump distance. While this would increase the computational cost of determining the eigenvector of the matrix, the orthogonal matrix $\mathbf{v}^T$ would be unchanged, and the solvability condition would be equally valid in this more general case.

In addition to addressing the limitations of classical homogenisation techniques for large obstacles shown in Chapter 5, we have developed a general procedure that has applications in the study of crystalline solids, lattice gas dynamics and conductivity of impure metals.

Chapter 7

Conclusion

In this chapter, we give a brief summary of this thesis. We then consider possible avenues for further extension, both from a theoretical and experimental standpoint.

7.1 Review of thesis

In Chapter 1, we presented a biological introduction to oncolytic virotherapy, the lytic cycle and the physical properties of avascular solid tumours. An overview of current modelling approaches for virus-cell interaction in solid tumours was given, and the physical limitations of the various models were discussed.

In Chapter 2, we derived a spatially-dependent, aged-structured reaction-diffusion system of PDEs, describing the interaction between uninfected cells, infected cells and virus particles in a solid tumour. Uninfected cells were considered to be motile, and reacted with virus particles to form infected cells. Once infected, these cells would continue to move around, albeit at a different rate, before dying after some fixed burst time, at which point they release multiple virus particles at their new location. Crucially, virus particles were assumed to be static (due to the dense tumour environment), and viral spread was facilitated purely by the motility of infected cells. Immune effects were modelled by incorporating a death rate for free virus particles, and it was assumed that virus particles inside infected cells were unaffected by the immune clearance.

Numerical solutions of the system of PDEs showed evidence of travelling waves of sustained viral spread. Reformulating the system in travelling wave coordinates, we performed an asymptotic analysis of the equations at the upstream boundary to derive an analytic expression for the wave speed in terms of the dimensionless parameters of the model. This was shown to agree with numerical solutions of the PDE system. Further numerical solutions of the full system for other sets of parameters showed reignition cases, where the virus population recovered from concentrations corresponding to fractions of

virus particles, suggesting a breakdown of the continuum hypothesis when dealing with extinction events.

In Chapter 3, we addressed the continuum breakdown of the model in Chapter 2 at low concentrations. An equivalent discrete, probabilistic formulation of virus-cell interactions on a mesoscopic, cellular scale was formulated via a compartment-based approach, which was implemented with a Gillespie Stochastic Simulation Algorithm (SSA). The physical domain was divided into a lattice of connected compartments, with cells undergoing a random walk between adjacent compartments. Virus particles could react with uninfected cells in the same compartment with a fixed probability, and infected cell bursts released virus particles into their current compartment after a deterministic period of time. This particle-interaction description was derived from more realistic physical principles than the empirically-derived reaction-rate equations from the continuum model. The compartment-based formulation allowed for easier implementation of complicated geometries, but came at a higher computational cost, with multiple realisations of the same parameters required to adequately describe the stochastic system.

Validating the model against known test cases, we demonstrated that the inhomogeneity introduced by virus particles born from infected cell burst in each compartment caused disagreement between the equivalent age-structured continuum model and the SSA for the smallest physically-motivated choice of compartment size. Further investigation showed that no empirical correction to the reaction rate would reconcile the two models in the limit of small compartment size, suggesting that this phenomenon was a fundamental property of discrete interactions.

In Chapter 4, we considered the qualitative behaviour of the stochastic model from Chapter 3, and analysed the effects of key experimental parameters on the success or failure of therapy, speed of viral spread and variability between simulations. Comparing our model with the simple agent-based model proposed by Wodarz (2013), we were able to replicate all qualitative forms of behaviour, and the majority of spatial patterns. We then studied the effects of burst time, diffusion ratio of infected to uninfected cells, burst size and initial viral spread on the behaviour of the system for a range of realistic parameter values. For a domain consisting of a dense initial population of uninfected cells, the SSA showed little variation between individual simulations, and, with the exception of small burst size, the general result was the complete removal of uninfected cells, corresponding to successful treatment. Travelling fronts of infection were observed, and larger values of diffusion ratio resulted in a greater equilibrium number of virus particles in the system. For a domain consisting of a sparse initial population of uninfected cells, we observed much greater variability between individual simulations compared to the dense cell case. The majority of simulations showed virus extinction, corresponding to partial failure of therapy. The only notable exception was in the case of larger burst sizes, which prolonged the overall duration of therapy, and hence, the total number of uninfected cells removed

from the system. The wave speed in the dense case was found to be significantly greater than for the sparse case for equivalent parameters, although the initial spread of virus particles did not affect the wave speed of infection. A lack of accurate parameter estimates meant that a quantitative comparison could not be undertaken, and we instead considered methods to improve these estimates, in particular, the motility coefficient of cells.

In Chapter 5, we addressed the experimental difficulty of measuring the effective motility of cells *in situ* by considering effective medium approximations of diffusion through heterogeneous environments. Assuming an idealised tumour with periodic arrangement of impermeable fibres on the microscale, we considered the diffusion problem in a two-dimensional domain filled with periodic obstacles. Using the method of asymptotic homogenisation, we showed how the macroscopic behaviour of this heterogeneous domain was reduced to a diffusion problem in a homogeneous domain, with the effective diffusivity given by the solution of a related problem, dependent on the geometry of the obstacle. We briefly considered the effects of adding a linear reaction term to this domain, and showed bounds on the maximum rate of reaction for which the effective properties would be the same.

Numerical solutions for effective diffusivity showed excellent agreement with existing asymptotic expressions from literature for both dilute and densely-packed square and round obstacles. Finally, we considered the case of diffusion in a checkerboard domain of square obstacles. Using the compartment-based stochastic model from Chapter 3, the mean squared displacement of the obstacle domain was compared with the effective medium case, using the numerically-determined effective properties from continuum theory. We saw that when the minimum jump distance, governed by the compartment size, was of the same order of magnitude as the obstacles, continuum homogenization techniques failed to adequately describe the effective medium. This suggested that a new approach to homogenisation on the microscale was needed in this limiting case.

In Chapter 6, we considered effective medium approximations when the microscopic length-scale could not be treated as a continuous variable. Looking at the case of a random walk on a periodic Markov chain or lattice with spatially-dependent transition probabilities, we treated the macro- and microscopic length-scale as continuous and discrete variables, respectively. The time evolution of a particle undergoing a random walk in this system was given by Master equations for the conditional probability of occupying each node. Drawing parallels with classical homogenisation theory, we applied a discrete multiple-scales expansion of the system on the microscale to obtain a governing matrix equation, grouped in powers of lattice spacing. Applying the Fredholm alternative, we derived a solvability condition in terms of the eigenvector of the transition matrix, which determined whether the macroscopic of the system behaviour was drift- or diffusion-dominated. A continuum effective transport equation was derived, describing the macroscopic time evolution of the discrete, heterogeneous chain or lattice, and the effective drift or diffusion coefficient was

given by an analytic expression in terms of matrix products of eigenvector and transition matrix.

For the special case of transition rates that depended only on the source-node (such as particles trapped in a potential well), we showed that the macroscopic behaviour was always isotropic diffusion, and gave a closed-form expression for the effective diffusion coefficient. For the related case of destination-dependent transition rates (such as random walks on a lattice with obstacles), we showed that the macroscopic behaviour was diffusive, and was generally anisotropic except in specific cases of the transition matrix. Numerical results showed perfect agreement for the mean-squared displacement of random walks on heterogeneous and effective lattices for general cases of source- and destination-dependent transition rates.

This technique was found to be equally valid for the case of non-local transitions, and, as a result, could be applied to fields such as semiconductor conductivity, gas lattice dynamics, and other related areas of physics dealing with discrete transport processes.

7.2 Future work

In this thesis, we have considered spatially-dependent continuum and discrete formulations of a three-species model of oncolytic virotherapy. These models incorporated important physical effects, such as a delayed infected cell burst due to the lytic cycle, as well as cell motility. While this model is a useful starting point for *in silico* studies of avascular tumours, there is scope for including additional physical behaviour, as well as experimental validation. We therefore conclude with some areas of potential work.

7.2.1 Modelling extensions

- In the continuum and discrete models in Chapters 2–3, cells were implicitly assumed to be infinitesimally small, and therefore, cell motility neglected excluded-volume effects. While cellular crowding is trivial to implement in the discrete, compartment-based model, a continuum formulation of this would limit the extent to which analytic approaches could be used.

- For simplicity, both the continuum and discrete models assumed that the infection of cells was a result of a single virus particle and uninfected cell, with no reaction between virus particles and already-infected cells possible. While we do not expect multiple viral infection to change either the burst time or burst size due to the exponential reproduction of virus particles in the host cell, this behaviour may be important in a low viral concentration scenario.

- By incorporating uninfected cell growth and an additional species representing the spread of nutrients throughout the system, the avascular model could be applied to larger, vascular tumours. Furthermore, the addition of oxygen gradients and blood supply would expand the applicability of the model. These would be relatively straight-forward extensions of the model, and could be implemented within both the stochastic and deterministic model frameworks, at the cost of increased computational demands.

- The homogenisation technique in Chapter 5 neglected reaction terms of the same order of magnitude as the diffusion coefficient, and did not consider the case of non-linear reaction terms. These extensions have previously been studied in literature, and could be applied to this problem. In addition to this, the approach could be applied to the full age-structured system of equations from Chapter 2. Finally, the assumption of periodic obstacles could be relaxed, and the case of random obstacle placement could be considered with extended homogenisation methods.

7.2.2 Experimental validation

- The greatest source of uncertainty in our model is the lack of an accurate estimate for the effective motility of cells, which is difficult to measure *in vivo*. A better approximation could be obtained by combining experimental data on the volume fraction and periodicity of collagen fibres in solid tumours with the homogenisation techniques from Chapter 5. Such techniques have previously been applied to the study of effective properties of gels, and these techniques could be applied to the study of avascular tumours

- While it was assumed that the motility of infected cells was different from that of uninfected cells, no experimental data was available to estimate the diffusion ratio, D. This parameter was shown to affect both the travelling wave speed, as well as the probability of success or failure of therapy, and experimental estimates are needed for any quantitative applications of the model.

- Due to a lack of adequate experimental data, the spatial distribution of the initial viral injection was chosen arbitrarily. Presumably, this would not be difficult to determine experimentally, and would allow for a more realistic sensitivity analysis of the three species model.

- While travelling waves have been observed experimentally, few estimates of the speed of *in vivo* viral spread have been published. This may be due to technical limitations, and is currently a major obstacle to validating the model with experimental results.

7.3 Final words

In conclusion, by formulating novel models of oncolytic virotherapy in solid tumours, we have shown fundamental differences in discrete and continuum descriptions of viral spread and extinction. These models provide a building block for the fundamental understanding of virus-cell interaction in solid tumours, and are a useful first step in developing *in silico* models for oncolytic therapy. As better experimental estimates of parameter values become available, our model will have important implications for optimal design and dosage of oncolytic agents in a clinical setting.

Appendix A

Gillespie stochastic simulation algorithm

Algorithm 4 Pseudo-code for Gillespie SSA applied to virus-tumour system.

SET Initial Conditions, Parameters
SET number of Virus Particles in central compartment to initial condition
for each uninfected cell specified by initial condition **do**
    GENERATE random x & y coordinate from uniform distribution
    SET Uninfected Cell position to (x,y)
end for
SET Total Uninfected Cell Propensity to number Uninfected Cells * Uninfected Diffusion Rate
SET Total Infected Cell Propensity to number Infected Cells * Infected Diffusion Rate
SET Total Virus Death Propensity to number of Virus Particles * Virus Death Rate
for each compartment **do**
    SET Reaction Propensity for current compartment to number Virus Particles in compartment * number Uninfected Cells at compartment position * Reaction Rate
end for
SET Total Reaction Propensity to sum of Reaction Propensity at each compartment
SET Total Propensity to Sum of Total Uninfected, Infected, Virus Death and Reaction Propensities
GENERATE Random Number between 0 and 1 from uniform distribution
SET Time to Next Event to (Current Time + Log(1/Random Number)/Total Propensity)
while Current Time $<$ Maximum Time **do**
    if Time to Next Event $>$ Burst Time of any Infected Cells **then**
        ADD Burst Size number of Virus Particles in compartment corresponding to Infected Cell position
        REMOVE Infected Cell
        UPDATE Reaction Propensity at compartment, Total Reaction Propensity, Total Virus Death Propensity, Total Infected Diffusion Propensity and Total Propensity
        SET Current Time to Burst Time
    else
        GENERATE Random Number between 0 and Total Propensity
        FIND which individual propensity interval within Total Propensity the Random Number falls into
        SET Next Event accordingly

Algorithm 4 Pseudo-code for Gillespie SSA applied to virus-tumour system (continued).

```
27:         if Next Event is Uninfected Diffusion then
28:             CHOOSE an Uninfected Cell at random
29:             GENERATE Random Number between 0 and 1
30:             if Random Number < 0.25 then Uninfected Cell is trying to move left then
31:                 if not at left boundary then
32:                     SET Uninfected Cell x coordinate to x-1
33:                 else
34:                     DO Nothing
35:                 end if
36:             else if Random Number < 0.5 then Uninfected Cell is trying to move right
    then
37:                 if not at right boundary then
38:                     SET Uninfected Cell x coordinate to x+1
39:                 else
40:                     DO Nothing
41:                 end if
42:             else if Random Number < 0.75 then Uninfected Cell is trying to move up
    then
43:                 if not at top boundary then
44:                     SET Uninfected Cell y coordinate to y-1
45:                 else
46:                     DO Nothing
47:                 end if
48:             else Uninfected Cell is trying to move down
49:                 if not at bottom boundary then
50:                     SET Uninfected Cell y coordinate to y+1
51:                 else
52:                     DO Nothing
53:                 end if
54:             end if
55:             UPDATE Total Uninfected Diffusion Propensity
56:             if Uninfected Cell has moved then
57:                 UPDATE Reaction Propensity at compartment corresponding to old
    position
58:                 UPDATE Reaction Propensity at compartment corresponding to new
    position
59:                 UPDATE Total Reaction Propensity
60:             end if
```

Algorithm 4 Pseudo-code for Gillespie SSA applied to virus-tumour system (continued).

```
61:         else if Next Event is Infected Diffusion then
62:             CHOOSE an Infected Cell at random
63:             GENERATE Random Number between 0 and 1
64:             if Random Number < 0.25 then Infected Cell is trying to move left then
65:                 if not at left boundary then
66:                     SET Infected Cell x coordinate to x-1
67:                 else
68:                     DO Nothing
69:                 end if
70:             else if Random Number < 0.5 then Infected Cell is trying to move right
    then
71:                 if not at right boundary then
72:                     SET Infected Cell x coordinate to x+1
73:                 else
74:                     DO Nothing
75:                 end if
76:             else if Random Number < 0.75 then Infected Cell is trying to move up then
77:                 if not at top boundary then
78:                     SET Infected Cell y coordinate to y-1
79:                 else
80:                     DO Nothing
81:                 end if
82:             else Infected Cell is trying to move down
83:                 if not at bottom boundary then
84:                     SET Infected Cell y coordinate to y+1
85:                 else
86:                     DO Nothing
87:                 end if
88:             end if
89:             UPDATE Total Infected Diffusion Propensity
```

Algorithm 4 Pseudo-code for Gillespie SSA applied to virus-tumour system (continued).

```
90:         else if Next Event is Reaction then
91:             GENERATE new random number between 0 and Total Reaction Propensity
92:             SUM Compartment propensities until random number < running sum to determine reaction compartment
93:             REMOVE a Virus Particle at compartment and an Uninfected Cell at compartment position
94:             ADD Infected Cell at current position
95:             SET Infected Cell Burst Time to Current Time + Burst Age
96:             UPDATE Total Number Uninfected Cells, Total Number Infected Cells, Total Number Virus Particles
97:             UPDATE Reaction Propensity at compartment
98:             UPDATE Total Reaction Propensity, Total Uninfected Propensity, Total Infected Propensity, Total Propensity
99:         else Next Event is Virus Death
100:            GENERATE random x & y coordinate
101:            while number of Virus Particles at (x,y) compartment is 0 do
102:                GENERATE new random x & y coordinate
103:            end while
104:            SET number of Virus Particles at (x,y) compartment to current number - 1
105:            UPDATE Total Virus Death Propensity
106:            UPDATE Reaction Propensity at (x,y)
107:            UPDATE Total Reaction Propensity
108:        end if
109:    end if
110:    UPDATE Total Propensity
111: end while
```

Appendix B

Derivation of 2D corrected propensity for reaction-diffusion

Defining I_{all} as the set of all possible compartment indices in 2D domain of size $[0, L] \times [0, L] \times h$, and $\vec{E}$ as the jump vector showing index offsets to neighbouring 4-connected compartments to which molecules can jump to, we consider the set of reactions

$$\begin{aligned} n_{ij} + V_{ij} &\overset{\tilde{k}}{\rightarrow} m_{ij} \\ n_{ij} &\overset{D_n/h^2}{\rightarrow} n_{ij+\vec{e}} && \text{(B.1)} \\ V_{ij} &\overset{D_m/h^2}{\rightarrow} V_{ij+\vec{e}} && \text{(B.2)} \\ \emptyset &\overset{k_{burst}}{\rightarrow} V_{ij} && \text{(B.3)} \end{aligned}$$

for $(i, j) \in I_{all}$ and $\vec{e} \in \vec{E}_{ij}$, where h is the compartment width, D_n is the diffusion coefficient of species n, D_m is the diffusion coefficient of species m, which is responsible for the transport of species V via virus burst, $\tilde{k} = k_{react}/h$ is a reaction rate per unit z-direction, and k_{burst} is the rate of virus creation as a result of infected cell burst.

Defining the stationary distribution for a system of $N = \frac{L}{h}$ compartments as

$$\phi(\vec{s}) = \lim_{t \to \infty} p_{\vec{s}}(t) \qquad \text{(B.4)}$$

where $\vec{s}$ is the vector representing number of molecules of each species in the system, Erban and Chapman (2009) showed that in certain cases, the standard choice of propensity function $a_{ij} = k_{react} n_{ij} V_{ij}$ results in a stationary distribution that is dependent on the number of compartments. As the choice of domain discretization is an artificial concept introduced in the SSA, rather than an inherent property of the physical system, this result

poses a contradiction. As we expect the stationary distribution to be independent of N, we want to find the effective propensity, λ, to minimise the error between ϕ_N and ϕ_1.

Defining the joint probability

$$P\left(\vec{n},\vec{V}\right) \equiv \text{Prob}\left\{\mathrm{n}_{ij}\left(t\right)=n_{ij},\mathrm{V}_{ij}\left(t\right)=V_{ij}\right\}, \tag{B.5}$$

and the jump operator

$$J_{ij}^{\vec{e}}\left(\vec{a}\right)=\left\{q_{uv}\mid\left(u,v\right)\in I_{all}\right\}, \tag{B.6}$$

where

$$q_{uv}=\begin{cases} a_{uv}+1 & \text{for } (u,v)=(i,j) \\ a_{uv}-1 & \text{for } (u,v)=(i,j)+\vec{e} \\ a_{uv} & \text{otherwise} \end{cases} \tag{B.7}$$

The time evolution of the reactions is described by the Reaction-Diffusion Master Equation (RDME)

$$\begin{aligned} \frac{\partial P\left(\vec{n},\vec{m},t\right)}{\partial t} &= \frac{\tilde{k}}{h^2}\sum_{(i,j)}\left\{\left(n_{ij}+1\right)\left(V_{ij}+1\right)P\left(\vec{n}+\vec{\delta}_{ij},\vec{V}+\vec{\delta}_{ij}\right)-n_{ij}V_{ij}P\left(\vec{n},\vec{V}\right)\right\} \\ &\quad +k_{burst}h^3\sum_{(i,j)}\left\{\left(V_{ij}+1\right)P\left(\vec{n},\vec{V}+\vec{\delta}_{ij}\right)-V_{ij}P\left(\vec{n},\vec{V}\right)\right\} \\ &\quad +\frac{D_n}{h^2}\sum_{(i,j)}\sum_{\vec{e}\in\vec{E}_{ij}}\left\{\left(n_{ij}+1\right)P\left(J_{ij}^{\vec{e}}\left(\vec{n}\right),\vec{V}\right)-n_{ij}P\left(\vec{n},\vec{V}\right)\right\} \\ &\quad +\frac{D_n}{h^2}\sum_{(i,j)}\sum_{\vec{e}\in\vec{E}_{ij}}\left\{\left(V_{ij}+1\right)P\left(\vec{n},J_{ij}^{\vec{e}}\left(\vec{V}\right)\right)-V_{ij}P\left(\vec{n},\vec{V}\right)\right\}. \end{aligned} \tag{B.8}$$

For the case $n_0=1$ (single molecule at location $\vec{b}=(b_1,b_2)$, the RDME for the equivalent model of (B.8) where n is considered to be stationary and V has diffusion coefficient (D_n+D_m) reduces to

$$\begin{aligned} \frac{\partial P\left(\vec{V},t\right)}{\partial t} &= \frac{\tilde{k}}{h^2}\left\{\left(V_{\vec{b}}+1\right)P\left(\vec{V}+\vec{\delta}_{\vec{b}}\right)-n_{\vec{b}}P\left(\vec{V}\right)\right\} \\ &\quad +k_{burst}h^3\sum_{(i,j)}\left\{P\left(\vec{V}-\vec{\delta_{ij}}\right)-P\left(\vec{V}\right)\right\} \\ &\quad +\frac{D_n+D_m}{h^2}\sum_{(i,j)}\sum_{\vec{e}\in\vec{E}_{ij}}\left\{\left(V_{ij}+1\right)P\left(J_{ij}^{\vec{e}}\left(\vec{V}\right)\right)-n_{ij}P\left(\vec{V}\right)\right\}. \end{aligned} \tag{B.9}$$

Our goal is to minimise the error between the stationary distributions ϕ_1 and ϕ_N by calculating an "effective" rate constant λ to replace $\frac{k_{react}}{h^3}$. The stationary distribution is valid as $t\to\infty$, so let $P_S\left(\vec{V}\right)=\lim_{t\to\infty}P\left(\vec{V},t\right)$.

Multiplying the RDME by $\vec{V}$ and summing, we have

$$0 = \begin{cases} k_{burst}h^3 + \frac{D_n+D_m}{h^2}\sum_{\vec{e}\in\vec{E_{ijk}}}\left\{M_{ij+\vec{e}} - M_{ij}\right\} & \text{, for } (i,j) \neq \vec{b} \\ -\lambda M_{\vec{b}} + k_{burst}h^3 + \frac{D_n+D_m}{h^2}\sum_{\vec{e}\in\vec{E}_b}\left\{M_{\vec{b}+\vec{e}} - M_{\vec{b}}\right\} & \text{, for } (i,j) = \vec{b} \end{cases}, \tag{B.10}$$

where $M_{ij}(t) = \sum_{\vec{V}} V_{ij} P_S\left(\vec{V}\right) = \sum_{n00=0}^{\infty}\sum_{n01=0}^{\infty}\cdots\left(V_{ij}P_S\left(\vec{V}\right)\right)$ is the mean number of particles at (i,j) at time t, as when $(i,j) \neq \vec{b}$, the probability of reaction is zero.

Choosing a basis function $\psi^{i'j'}$ of the form

$$\psi^{i'j'} \propto \cos\left(\frac{i'\left(i-1/2\right)\pi}{N}\right)\cos\left(\frac{j'\left(j-1/2\right)\pi}{N}\right), \tag{B.11}$$

the orthogonality condition is then given by

$$\begin{aligned} \sum_{i,j=1}^{N}\psi_{ij}^{i'j'}\psi_{ij}^{i''j''} &= \frac{N^2}{4} \\ \sum_{i=1,j=0}^{N}\psi_{ij}^{i'j'}\psi_{ij}^{i''j''} &= \frac{N^2}{2} \\ \text{or} &= N^2 \text{ if } i,j=0, \end{aligned} \tag{B.12}$$

implying that the normalisation for the basis function has the form

$$\sqrt{\psi\psi} = \begin{cases} \frac{\sqrt{4}}{\sqrt{N^2}} & \text{for } i,j>0 \\ \frac{\sqrt{2}}{\sqrt{N^2}}, & \text{for one of } i,j=0\cdot \\ \frac{1}{\sqrt{N^2}}, & \text{for both } i,j=0 \end{cases} \tag{B.13}$$

Now writing the mean number of particles in compartment (i,j) as

$$M_{ij} = \sum_{i',j'=0}^{N-1}\tilde{M}_{i'j'}\psi_{ij}^{i'j'}, \tag{B.14}$$

the RDME (B.10) becomes

$$\begin{aligned} k_{burst}h^3 + \frac{D_n+D_m}{h^2}\sum_{\vec{e}\in\vec{E}_{ij}}\sum_{i',j'}^{N-1}\tilde{M}_{i'j'}\left\{\psi_{ij+\vec{e}}^{i'j'} - \psi_{ij}^{i'j'}\right\} &= 0, \text{ for } (i,j)\neq\vec{b} \\ k_{burst}h^3 + \frac{D_n+D_m}{h^2}\sum_{\vec{e}\in\vec{E}_{ij}}\sum_{i',j'}^{N-1}\tilde{M}_{i'j'}\left\{\psi_{\vec{b}+\vec{e}}^{i'j'} - \psi_{ij}^{i'j'}\right\} &= \lambda M_{\vec{b}}. \end{aligned} \tag{B.15}$$

Making use of the basis function

$$\psi_{ij}^{i'j'} = \cos\left(\frac{i'\left(i-1/2\right)\pi}{N}\right)\cos\left(\frac{j'\left(j-1/2\right)\pi}{N}\right), \tag{B.16}$$

the RDME becomes

$$\begin{aligned} k_{burst}h^3 + \frac{D_n+D_m}{h^2}\sum_{i',j'=0}^{N-1}\tilde{M}_{i'j'}c^{i'j'}\psi_{ij}^{i'j'} &= 0, \text{ for } (i,j)\neq\vec{b} \\ k_{burst}h^3 + \frac{D_n+D_m}{h^2}\sum_{i',j'=0}^{N-1}\tilde{M}_{i'j'}c^{i'j'}\psi_{\vec{b}}^{i'j'} &= \lambda M_{\vec{b}}, \end{aligned} \tag{B.17}$$

where $c^{ij} = 2\left(\cos\left(\frac{i\pi}{N}\right)+\cos\left(\frac{j\pi}{N}\right)-2\right)$.

Multiplying (B.17) by $\psi_{ij}^{i''j''}$, applying orthonormality conditions (B.12) and summing the resulting equations

$$\begin{aligned} k_{burst}\nu &= \lambda M_{\vec{b}}, \\ \frac{D_n+D_m}{h^2}c^{i''j''}\tilde{M}_{i''j''} &= \lambda M_{\vec{b}}\psi_{\vec{b}}^{i''j''} \text{ for } \left(i'',j''\right)\neq(0,0), \\ \therefore \tilde{M}_{i''j''} &= \frac{\lambda h^2 M_{\vec{b}}\psi_{\vec{b}}^{i''j''}}{\left(D_n+D_m-k_{burst}h^5\right)c^{i''j''}}, \\ &\quad \text{for } \left(i'',j''\right)\neq(0,0) \end{aligned} \tag{B.18}$$

where $\nu = N^2h^3$ is the volume of the 2D domain.

Now, we can write

$$\tilde{M}_{i''j''} = \frac{k_{burst}\nu h^2\psi_{\vec{b}}^{ij}}{\left(D_n+D_m\right)c^{i''j''}}, \tag{B.19}$$

and applying (B.14), this implies that

$$\begin{aligned} M_{\vec{b}} &= \sum_{i',j'=0}^{N-1}\tilde{M}_{i'j'}\psi_{\vec{b}}^{i'j'} \\ &= \sum_{i',j'}^{N-1}\frac{k_{burst}\nu h^2\psi_{\vec{b}}^{i'j'}\psi_{\vec{b}}^{i'j'}}{\left(D_n+D_m\right)c^{i'j'}} \\ &= N^{-1}\tilde{M}_{00} - \beta_{\vec{b}}\frac{k_{burst}\nu h^2}{\left(D_n+D_m\right)}, \end{aligned} \tag{B.20}$$

where

$$\beta_{\vec{b}} = - \sum_{\substack{i,j=0 \\ (i,j)\neq(0,0)}} \frac{\left(\psi_{\vec{b}}^{ij}\right)^2}{c^{ij}}. \tag{B.21}$$

Substituting this form of $M_{\vec{b}}$ into (B.18), we obtain

$$\frac{k_{burst}\nu}{\lambda} = N^{-1}\tilde{M}_{00} - \beta_{\vec{b}}\frac{k_{burst}\nu h^2}{(D_n + D_m)}. \tag{B.22}$$

The average number of molecules is given by $A_s \equiv \sum_{i,j}^{N} M_{ij}$. We want to choose $A_s = M_s$, where M_s is the mean number of particles given by the stationary distribution. For the well-stirred case, Erban and Chapman (2009) show this to be

$$M_s = \frac{k_{burst}\nu}{\tilde{k}n_0}. \tag{B.23}$$

Setting $A_s = M_s$ for the case of $n_0 = 1$ gives

$$\begin{aligned} \frac{k_{burst}\nu}{N\tilde{k}} &= \tilde{M}_{00} \\ &= \frac{k_{burst}\nu N}{\lambda} + \beta_{\vec{b}}\frac{k_{burst}\nu N h^2}{(D_n + D_m)}, \end{aligned} \tag{B.24}$$

and for 2D reaction volume $\nu = N^2h^3$, this gives the corrected reaction propensity

$$\lambda = \frac{(D_n + D_m)\, N^2\tilde{k}}{(D_n + D_m) + \beta h^2 N^2 \tilde{k}}. \tag{B.25}$$

This expression is independent of k_{burst}, and depends only on compartment size h and total number of compartments, N, in the domain. The 2D reaction rate $\tilde{k}$ is effectively a reaction rate per unit z-direction, and is related to the 3D reaction rate by $\tilde{k} = {}^{k_{react}}/_{h}$.

Bibliography

M. Abramowitz and I. A. Stegun. Handbook of mathematical functions with formulas, graphs, and mathematical tables. *Dover Books on Advanced Mathematics*, 1965.

M. Aghi and R. Martuza. Oncolytic viral therapies-the clinical experience. *Oncogene*, 2005 **24**(52):7802–7816. ISSN 0950-9232.

J. Al-Omari and S. a. Gourley. Monotone travelling fronts in an age-structured reaction-diffusion model of a single species. *Journal of mathematical biology*, 2002 **45** (4):294–312. ISSN 0303-6812.

M. K. Aliev and A. N. Tikhonov. Random walk analysis of restricted metabolite diffusion in skeletal myofibril systems. *Molecular and Cellular Biochemistry*, 2004 **256** (1/2):257–266. ISSN 0300-8177.

G. Allaire. Homogenization and two-scale convergence. *SIAM Journal on Mathematical Analysis*, **23**(6):1482–1518, 1992.

U. Ascher and L. Petzold. The numerical solution of delay-differential-algebraic equations of retarded and neutral type. *SIAM journal on numerical analysis*, **32**(5):1635–1657, 1995.

Z. Bajzer, T. Carr, K. Josić, S. J. Russell, and D. Dingli. Modeling of cancer virotherapy with recombinant measles viruses. *Journal of theoretical biology*, 2008 **252** (1):109–22. ISSN 1095-8541.

G. K. Batchelor. Transport Properties of Two-Phase Materials with Random Structure. *Annual Review of Fluid Mechanics*, 1974 **6**(1):227–255. ISSN 0066-4189.

L. T. Baxter and R. K. Jain. Transport of fluid and macromolecules in tumors. I. Role of interstitial pressure and convection. *Microvascular Research*, **37**(1):77–104, 1989.

M. Bazan-Peregrino, R. C. Carlisle, R. Hernandez-Alcoceba, R. Iggo, K. Homicsko, K. D. Fisher, G. Halldén, V. Mautner, Y. Shen, and L. W. Seymour. Comparison of molecular strategies for breast cancer virotherapy using oncolytic adenovirus. *Human Gene Therapy*, 2008 **19**(9):873–886. ISSN 1557-7422.

H. C. Berg. *Random Walks in Biology.* Princeton University Press, 1993. ISBN 0691000646.

D. Bernstein. Simulating mesoscopic reaction-diffusion systems using the Gillespie algorithm. *Physical Review E - Statistical, Nonlinear and Soft Matter Physics*, 2005 **71**(4 Pt 1):041103. ISSN 1539-3755.

N. A. Bhowmick and H. L. Moses. Tumor-stroma interactions. *Current opinion in genetics & development*, 2005 **15**(1):97–101. ISSN 0959-437X.

D. Birk and R. Trelstad. Extracellular compartments in tendon morphogenesis: collagen fibril, bundle, and macroaggregate formation. *The Journal of cell biology*, **103** (July):231–240, 1986.

A. Blumen and G. Zumofen. Energy transfer as a random walk on regular lattices. *The Journal of Chemical Physics*, **75**(2):892, 1981. ISSN 00219606.

J. Bouchaud and A. Georges. Anomalous diffusion in disordered media: statistical mechanisms, models and physical applications. *Physics reports*, **195**(4-5):127–293, 1990.

Y. Boucher, L. T. Baxter, and R. K. Jain. Interstitial pressure gradients in tissue-isolated and subcutaneous tumors: implications for therapy. *Cancer research*, 1990 **50** (15):4478–84. ISSN 0008-5472.

J. Brábek, C. T. Mierke, D. Rösel, P. Veselý, and B. Fabry. The role of the tissue microenvironment in the regulation of cancer cell motility and invasion. *Cell communication and signaling : CCS*, 2010 **8**:22. ISSN 1478-811X.

O. Braun and C. Sholl. Diffusion in generalized lattice-gas models. *Physical Review B*, 1998 **58**(22):14870–14879. ISSN 0163-1829.

E. Brown, T. McKee, E. DiTomaso, A. Pluen, B. Seed, Y. Boucher, and R. K. Jain. Dynamic imaging of collagen and its modulation in tumors in vivo using second-harmonic generation. *Nature medicine*, 2003 **9**(6):796–800. ISSN 1078-8956.

D. Burstein, M. L. Gray, a. L. Hartman, R. Gipe, and B. D. Foy. Diffusion of small solutes in cartilage as measured by nuclear magnetic resonance (NMR) spectroscopy and imaging. *Journal of orthopaedic research : official publication of the Orthopaedic Research Society*, 1993 **11**(4):465–78. ISSN 0736-0266.

H. M. Byrne, T. Alarcon, M. R. Owen, S. D. Webb, and P. K. Maini. Modelling aspects of cancer dynamics: a review. *Philosophical transactions. Series A, Mathematical, physical, and engineering sciences*, 2006 **364**(1843):1563–78. ISSN 1364-503X.

S. L. Campbell. Singular linear systems of differential equations with delays. *Applicable Analysis*, 1980 **11**(2):129–136. ISSN 0003-6811.

M. Chaplain. Modelling aspects of cancer growth: insight from mathematical and numerical analysis and computational simulation. In V. Capasso and M. Lachowicz, editors, *Multiscale Problems in the Life Sciences*, pages 147–200. Springer Berlin Heidelberg, 2008. ISBN 978-3-540-78360-2.

T. B. Chaston and B. a. Lidbury. Genetic 'budget' of viruses and the cost to the infected host: a theory on the relationship between the genetic capacity of viruses, immune evasion, persistence and disease. *Immunology and cell biology*, 2001 **79**(1):62–6. ISSN 0818-9641.

M. Chicoine and D. Silbergeld. Assessment of brain tumor cell motility in vivo and in vitro. *Journal of neurosurgery*, **82**(4):615–622, 1995.

D. Cioranescu and P. Donato. *An introduction to homogenization*. Oxford University Press, New York, NY, 1999. ISBN 0198565542.

K. A. Connors. *Chemical Kinetics: The Study of Reaction Rates in Solution*. John Wiley & Sons, 1990. ISBN 1560810068.

R. Craster and Y. Obnosov. Four-phase checkerboard composites. *SIAM Journal on Applied Mathematics*, **61**(6):1839–1856, 2001.

D. Cross and J. Burmester. Gene therapy for cancer treatment: past, present and future. *Clinical medicine & research*, **4**(3):218–227, 2006.

S. Cudmore, I. Reckmann, and M. Way. Viral manipulations of the actin cytoskeleton. *Trends in microbiology*, 1997 **5**(4):142–8. ISSN 0966-842X.

C. M. Cuesta and J. R. King. Front Propagation in a Heterogeneous Fisher Equation: The Homogeneous Case is Non-Generic. *The Quarterly Journal of Mechanics and Applied Mathematics*, 2010 **63**(4):521–571. ISSN 0033-5614.

E. L. Cussler. *Diffusion: Mass Transfer in Fluid Systems*. Cambridge University Press, 1997. ISBN 0521564778.

P. K. Das, X. Li, and Z.-S. Liu. Effective transport coefficients in PEM fuel cell catalyst and gas diffusion layers: Beyond Bruggeman approximation. *Applied Energy*, 2010 **87** (9):2785–2796. ISSN 03062619.

C. d. L. Davies, D. A. Berk, A. Pluen, and R. K. Jain. Comparison of IgG diffusion and extracellular matrix composition in rhabdomyosarcomas grown in mice versus in vitro as spheroids reveals the role of host stromal cells. *British journal of cancer*, 2002 **86**(10):1639–44. ISSN 0007-0920.

W. Dieterich, P. Fulde, and I. Peschel. Theoretical models for superionic conductors. *Advances in Physics*, 1980 **29**(3):527–605. ISSN 0001-8732.

D. Dingli, M. D. Cascino, K. Josić, S. J. Russell, and Z. Bajzer. Mathematical modeling of cancer radiovirotherapy. *Mathematical biosciences*, 2006 **199**(1):55–78. ISSN 0025-5564.

R. Eftimie, J. L. Bramson, and D. J. D. Earn. Interactions between the immune system and cancer: a brief review of non-spatial mathematical models. *Bulletin of Mathematical Biology*, 2011 **73**(1):2–32. ISSN 1522-9602.

R. Erban and S. J. Chapman. Stochastic modelling of reaction-diffusion processes: algorithms for bimolecular reactions. *Physical Biology*, 2009 **6**(4):046001.

R. Erban and S. Chapman. Reactive boundary conditions for stochastic simulations of reaction-diffusion processes. *Physical Biology*, **4**(1):16–28, 2007.

R. Erban, J. Chapman, and P. Maini. A practical guide to stochastic simulations of reaction-diffusion processes. *Arxiv preprint arXiv07041908*, 2007 page 35.

K. Fisher and L. W. Seymour. Viral hijacking of infected cell motor mechanism. Private Communication, 2009.

A. C. Fowler. Asymptotic methods for delay equations. *Journal of Engineering Mathematics*, 2005 **53**(3-4):271–290. ISSN 0022-0833.

D. Freedman and P. Diaconis. On the histogram as a density estimator: L2 theory. *Zeitschrift für Wahrscheinlichkeitstheorie und Verwandte Gebiete*, 1981 **57**(4):453–476. ISSN 0044-3719.

A. Friedman and Y. Tao. Analysis of a model of a virus that replicates selectively in tumor cells. *Journal of mathematical biology*, **423**:391–423, 2003.

A. Friedman, J. Tian, G. Fulci, E. Chiocca, and J. Wang. Glioma virotherapy: effects of innate immune suppression and increased viral replication capacity. *Cancer research*, 2006 **66**(4):2314–2319. ISSN 0008-5472.

M. G. Gauthier, G. W. Slater, and K. D. Dorfman. Exact lattice calculations of dispersion coefficients in the presence of external fields and obstacles. *The European physical journal. E, Soft matter*, 2004 **15**(1):71–82. ISSN 1292-8941.

D. Gillespie. Exact stochastic simulation of coupled chemical reactions. *The journal of physical chemistry*, **93555**(1):2340–2361, 1977.

Z. S. Guo, S. H. Thorne, and D. L. Bartlett. Oncolytic virotherapy: molecular targets in tumor-selective replication and carrier cell-mediated delivery of oncolytic viruses. *Biochimica et biophysica acta*, 2008 **1785**(2):217–31. ISSN 0006-3002.

B. a. C. Harley, H.-D. Kim, M. H. Zaman, I. V. Yannas, D. a. Lauffenburger, and L. J. Gibson. Microarchitecture of three-dimensional scaffolds influences cell migration behavior via junction interactions. *Biophysical journal*, 2008 **95**(8):4013–24. ISSN 1542-0086.

Z. Hashin. Analysis of Composite Materials-A Survey. *Journal of Applied Mechanics*, **50** (3):481, 1983. ISSN 00218936.

J. Haus and K. Kehr. Diffusion in regular and disordered lattices. *Physics Reports*, **6**: 263–406, 1987.

S. Havlin and D. Ben-Avraham. Diffusion in disordered media. *Advances in Physics*, 1987 **36**(6):695–798. ISSN 0001-8732.

C. Heise, A. Williams, J. Olesch, and D. Kirn. Efficacy of a replication-competent adenovirus (ONYX-015) following intratumoral injection: intratumoral spread and distribution effects. *Cancer gene therapy*, **6**(6):499–504, 1999.

D. J. Higham. Modeling and simulating chemical reactions. *SIAM Review*, **50**(2):347, 2008.

D. Holcman, N. Hoze, and Z. Schuss. Narrow escape through a funnel and effective diffusion on a crowded membrane. *Physical Review E*, 2011 **84**(2):021906. ISSN 1539-3755.

J. Hrabe, S. Hrabetová, and K. Segeth. A model of effective diffusion and tortuosity in the extracellular space of the brain. *Biophysical journal*, 2004 **87**(3):1606–17. ISSN 0006-3495.

L. Hui and B. Ke-da. Effective conductivity in a checkerboard geometry at high conductance ratio and high concentration. *Physical Review B*, **46**(14):1–4, 1992.

S. Isaacson. The reaction-diffusion master equation as an asymptotic approximation of diffusion to a small target. *SIAM Journal on Applied Mathematics*, **70**(1):77–111, 2009.

K. Ishida. Stochastic Model for Bimolecular Reaction. *The Journal of Chemical Physics*, **41**(8):2472, 1964.

R. K. Jain. Vascular and interstitial barriers to delivery of therapeutic agents in tumors. *Cancer metastasis reviews*, 1990 **9**(3):253–66. ISSN 0167-7659.

R. K. Jain. Delivery of molecular medicine to solid tumors: lessons from in vivo imaging of gene expression and function. *Journal of Controlled Release*, **74**(1-3):7–25, 2001.

R. Jain. Transport of molecules, particles, and cells in solid tumors. *Annual review of biomedical engineering*, (96):241–263, 1999.

S. H. Jang, M. G. Wientjes, D. Lu, and J. L. S. Au. Drug delivery and transport to solid tumors. *Pharmaceutical Research*, **20**(9):1337–1350, 2003.

B. Jönsson, H. Wennerström, P. G. Nilsson, and P. Linse. Self-diffusion of small molecules in colloidal systems. *Colloid & Polymer Science*, 1986 **264**(1):77–88. ISSN 0303-402X.

J. Kalnin, E. Kotomin, and J. Maier. Calculations of the effective diffusion coefficient for inhomogeneous media. *Journal of physics and chemistry of solids*, **63**:449–456, 2002.

K. W. Kehr, D. Richter, and R. H. Swendsen. The influence of impurities on interstitial diffusion. *Journal of Physics F: Metal Physics*, 1978 **8**(3):433–446. ISSN 0305-4608.

K. Kehr and J. Haus. On the equivalence between multistate-trapping and continuous-time random walk models. *Physica A: Statistical Mechanics and its Applications*, 1978 **93**(3-4):412–426. ISSN 03784371.

K. Kehr, K. Mussawisade, T. Wichmann, and W. Dieterich. Nonlinear Mobility of Particles in Nonsymmetric Potentials under Strong Bias Conditions. *physica status solidi (b)*, 1998 **205**(1):73–76. ISSN 03701972.

J. B. Keller. Conductivity of a Medium Containing a Dense Array of Perfectly Conducting Spheres or Cylinders or Nonconducting Cylinders. *Journal of Applied Physics*, **34**(4):991, 1963. ISSN 00218979.

J. B. Keller. A Theorem on the Conductivity of a Composite Medium. *Journal of Mathematical Physics*, **5**(4):548, 1964. ISSN 00222488.

J. R. King. Wavespeed selection in the heterogeneous Fisher equation: Slowly varying inhomogeneity. *Networks and Heterogeneous Media*, 2013 **8**(1):343–378. ISSN 1556-1801.

D. Kirn, R. L. Martuza, and J. Zwiebel. Replication-selective virotherapy for cancer: Biological principles, risk management and future directions. *Nature Medicine*, **7**(7):781–787, 2001.

D. Kirn. Oncolytic virotherapy for cancer with the adenovirus dl1520 (Onyx-015): results of phase I and II trials. *Expert opinion on biological therapy*, 2001.

Z. Koza. General technique of calculating the drift velocity and diffusion coefficient in arbitrary periodic systems. *Journal of Physics A: Mathematical and General*, 1999 **32** (44):7637–7651. ISSN 0305-4470.

G. Kristensson. Homogenization of Spherical Inclusions. *Progress In Electromagnetics Research*, **42**:1–25, 2003. ISSN 1559-8985.

R. Kutner. Chemical diffusion in the lattice gas of non-interacting particles. *Physics Letters A*, **81**(4):239–240, 1981.

R. Kutner and I. Sosnowska. Thermal neutron scattering from a hydrogen-metal system in terms of a general multi-sublattice jump diffusion model-I. *Journal of Physics and Chemistry of Solids*, 1977 **38**(7):741–746. ISSN 00223697.

R. Landauer. Electrical conductivity in inhomogeneous media. In *AIP Conference Proceedings*, **40**, pages 2–45. AIP, 1978.

A. Leier and T. Marquez-Lago. Correction factors for boundary diffusion in reaction-diffusion master equations. *The Journal of chemical physics*, 2011 **135**(13):134109. ISSN 1089-7690.

B. R. Lester and J. B. McCarthy. Tumor cell adhesion to the extracellular matrix and signal transduction mechanisms implicated in tumor cell motility, invasion and metastasis. *Cancer metastasis reviews*, 1992 **11**(1):31–44. ISSN 0167-7659.

J. Levick. Flow through interstitium and other fibrous matrices. *Experimental Physiology*, 1987.

S. Li, L. J. Lee, and J. Castro. Effective Mass Diffusivity in Composites. *Journal of Composite Materials*, 2002 **36**(14):1709–1724. ISSN 0021-9983.

L. A. Liotta. Tumor invasion and metastases–role of the extracellular matrix: Rhoads Memorial Award lecture. *Cancer research*, 1986 **46**(1):1–7. ISSN 0008-5472.

R. Lipton. Reciprocal Relations, Bounds, and Size Effects for Composites with Highly Conducting Interface. *SIAM Journal on Applied Mathematics*, 1997 **57**(2):347–363. ISSN 0036-1399.

T.-C. Liu, T. Zhang, H. Fukuhara, T. Kuroda, T. Todo, R. L. Martuza, S. D. Rabkin, and A. Kurtz. Oncolytic HSV armed with platelet factor 4, an antiangiogenic agent, shows enhanced efficacy. *Molecular therapy : the journal of the American Society of Gene Therapy*, 2006 **14**(6):789–97. ISSN 1525-0016.

T.-C. Liu, E. Galanis, and D. Kirn. Clinical trial results with oncolytic virotherapy: a century of promise, a decade of progress. *Nature Clinical Practice Oncology*, 2007 **4**(2):101–117. ISSN 1743-4262.

T. Liu and D. Kirn. Gene therapy progress and prospects cancer: oncolytic viruses. *Gene therapy*, 2008 **7**(1):2–8. ISSN 1476-5462.

S.-Y. Lu. The Effective Thermal Conductivities of Composites with 2-D Arrays of Circular and Square Cylinders. *Journal of Composite Materials*, 1995 **29**(4):483–506. ISSN 0021-9983.

K. Z. Markov. Elementary Micromechanics of Heterogeneous Media. In L. Markov, Konstantin and Preziosi, editor, *Heterogeneous Media*, pages 1–162. Birkhäuser Boston, 2000. ISBN 978-1-4612-7098-0.

A. Matzavinos. Mathematical modelling of the spatio-temporal response of cytotoxic T-lymphocytes to a solid tumour. *Mathematical Medicine and Biology*, 2004 **21**(1):1–34. ISSN 1477-8599.

P. Mcauliffe, W. Jarnagin, P. Johnson, K. Derlman, H. Federoff, and Y. Fong. Effective treatment of pancreatic tumors with two multimutated herpes simplex oncolytic viruses. *Journal of Gastrointestinal Surgery*, 2000 **4**(6):580–588. ISSN 1091255X.

T. D. McKee, P. Grandi, W. Mok, G. Alexandrakis, N. Insin, J. P. Zimmer, M. G. Bawendi, Y. Boucher, X. O. Breakefield, and R. K. Jain. Degradation of fibrillar collagen in a human melanoma xenograft improves the efficacy of an oncolytic herpes simplex virus vector. *Cancer research*, 2006 **66**(5):2509–13. ISSN 0008-5472.

D. McQuarrie. Stochastic approach to chemical kinetics. *Journal of Applied Probability*, **4**(3):413–478, 1967.

H. Mehrer. *Diffusion in solids: Fundamentals, Methods, Materials, Diffusion-Controlled Processes*. Springer, Berlin, Heidelberg, 2007. ISBN 978-3-540-71486-6.

A. Meidell. *Homogenization and computational methods for calculating effective properties of some cellular solids and composite structures*. PhD thesis, Norwegian University of Science and Technology, 2001.

S. Meier. *Two-scale models for reactive transport and evolving microstructure*. PhD thesis, University of Bremen, 2008.

J.-F. Mercier, G. W. Slater, and H. L. Guo. Numerically exact diffusion coefficients for lattice systems with periodic boundary conditions. I. Theory. *The Journal of Chemical Physics*, **110**(12):6050, 1999. ISSN 00219606.

W. Merrill, R. Diaz, M. LoRe, M. Squires, and N. Alexopoulos. Effective medium theories for artificial materials composed of multiple sizes of spherical inclusions in a host continuum. *IEEE Transactions on Antennas and Propagation*, **47**(1):142–148, 1999. ISSN 0018926X.

G. W. Milton. Proof of a conjecture on the conductivity of checkerboards. *Journal of Mathematical Physics*, **42**(10):4873, 2001. ISSN 00222488.

G. W. Milton. *The Theory of Composites*. Cambridge University Press, Cambridge, 2002. ISBN 9780511613357.

W. Mok. *Improving the delivery and efficacy of a cancer therapeutic via extracellular matrix modification.* PhD thesis, MIT, 2007.

W. Mok, T. Stylianopoulos, Y. Boucher, and R. K. Jain. Mathematical modeling of herpes simplex virus distribution in solid tumors: implications for cancer gene therapy. *Clinical cancer research : an official journal of the American Association for Cancer Research*, 2009 **15**(7):2352–60. ISSN 1078-0432.

J. Monecke. Material constants of composites. I. General theory for the dielectric constant. *physica status solidi (b)*, **279**(I), 1987.

E. W. Montroll and G. H. Weiss. Random Walks on Lattices. II. *Journal of Mathematical Physics*, **6**(2):167, 1965. ISSN 00222488.

J. D. Murray. *Mathematical Biology: I. An Introduction.* Springer, 2002. ISBN 0387952233.

S. Nagano, J. Y. Perentes, R. K. Jain, and Y. Boucher. Cancer cell death enhances the penetration and efficacy of oncolytic herpes simplex virus in tumors. *Cancer research*, 2008 **68**(10):3795–802. ISSN 1538-7445.

P. a. Netti, D. a. Berk, M. a. Swartz, a. J. Grodzinsky, and R. K. Jain. Role of extracellular matrix assembly in interstitial transport in solid tumors. *Cancer research*, 2000 **60**(9):2497–503. ISSN 0008-5472.

B. P. Olveczky and a. S. Verkman. Monte Carlo analysis of obstructed diffusion in three dimensions: application to molecular diffusion in organelles. *Biophysical journal*, 1998 **74**(5):2722–30. ISSN 0006-3495.

L. R. Paiva, C. Binny, S. C. Ferreira, and M. L. Martins. A multiscale mathematical model for oncolytic virotherapy. *Cancer research*, 2009 **69**(3):1205–11. ISSN 1538-7445.

L. Pankratov, A. Piatnitskii, and V. Rybalko. Homogenized model of reaction-diffusion in a porous medium. *Comptes Rendus Mécanique*, **331**:253–258, 2003.

G. Papanicolaou, A. Bensoussan, and J.-L. Lions. *Asymptotic Analysis of Periodic Structures*, **46**. North-Holland Publishing Company, Amsterdam/New York, 1979. ISBN 9780080875262.

K. a. Parato, D. Senger, P. a. J. Forsyth, and J. C. Bell. Recent progress in the battle between oncolytic viruses and tumours. *Nature reviews. Cancer*, 2005 **5**(12): 965–76. ISSN 1474-175X.

G. A. Pavliotis and A. Vogiannou. Diffusive transport in periodic potentials: underdamped dynamics. *Fluctuation and Noise Letters*, 2008 **08**(02):L155–L173. ISSN 0219-4775.

A. M. Pavliotis, Grigorios A and Stuart. *Multiscale methods: averaging and homogenization*. Springer Science+ Business Media, New York, NY, 2008.

A. L. Pecora. Phase I Trial of Intravenous Administration of PV701, an Oncolytic Virus, in Patients With Advanced Solid Cancers. *Journal of Clinical Oncology*, 2002 **20** (9):2251–2266. ISSN 0732183X.

W. T. Perrins, D. R. McKenzie, and R. C. McPhedran. Transport Properties of Regular Arrays of Cylinders. *Proceedings of the Royal Society A: Mathematical, Physical and Engineering Sciences*, 1979 **369**(1737):207–225a. ISSN 1364-5021.

W. Perrins, R. McPhedran, and D. McKenzie. Optical properties of dense regular cermets with relevance to selective solar absorbers. *Thin Solid Films*, **57**(1979):321–326, 1979b.

A. Ploubidou and M. Way. Viral transport and the cytoskeleton. *Current opinion in cell biology*, 2001 **13**(1):97–105. ISSN 0955-0674.

A. Pluen, Y. Boucher, S. Ramanujan, T. D. McKee, T. Gohongi, E. di Tomaso, E. B. Brown, Y. Izumi, R. B. Campbell, D. A. Berk, and R. K. Jain. Role of tumor-host interactions in interstitial diffusion of macromolecules: cranial vs. subcutaneous tumors. *Proceedings of the National Academy of Sciences of the United States of America*, 2001 **98**(8):4628–33. ISSN 0027-8424.

O. P. Posnansky and N. J. Shah. On the problem of diffusivity in heterogeneous biological materials with random structure. *Journal of biological physics*, 2008 **34**(6): 551–67. ISSN 0092-0606.

A. T. Power, J. Wang, T. J. Falls, J. M. Paterson, K. a. Parato, B. D. Lichty, D. F. Stojdl, P. a. J. Forsyth, H. Atkins, and J. C. Bell. Carrier cell-based delivery of an oncolytic virus circumvents antiviral immunity. *Molecular therapy : the journal of the American Society of Gene Therapy*, 2007 **15**(1):123–30. ISSN 1525-0024.

F. Rabbering, H. Wormeester, F. Everts, and B. Poelsema. Quantitative understanding of the growth of Cu/Cu(001) including the determination of the Ehrlich-Schwoebel barrier at straight steps and kinks. *Physical Review B*, 2009 **79**(7):075402. ISSN 1098-0121.

S. Ramanujan, A. Pluen, T. D. Mckee, E. B. Brown, Y. Boucher, and R. K. Jain. Diffusion and Convection in Collagen Gels : Implications for Transport in the Tumor Interstitium. *Biophysical Journal*, **83**(3):1650–1660, 2002. ISSN 0006-3495.

C. L. Reis, J. M. Pacheco, M. K. Ennis, and D. Dingli. In silico evolutionary dynamics of tumour virotherapy. *Integrative biology : quantitative biosciences from nano to macro*, 2010 **2**(1):41–5. ISSN 1757-9708.

M. Samoilov, S. Plyasunov, and A. P. Arkin. Stochastic amplification and signaling in enzymatic futile cycles through noise-induced bistability with oscillations. *Proceedings of the National Academy of Sciences of the United States of America*, 2005 **102**(7):2310–5. ISSN 0027-8424.

E. Sánchez-Palencia. *Non-Homogeneous Media and Vibration Theory*, **127** of *Lecture Notes in Physics*. Springer-Verlag, Berlin, Heidelberg, 1980. ISBN 978-3-540-10000-3.

H. Sauthoff, J. Hu, C. Maca, M. Goldman, S. Heitner, H. Yee, T. Pipiya, W. N. Rom, and J. G. Hay. Intratumoral spread of wild-type adenovirus is limited after local injection of human xenograft tumors: virus persists and spreads systemically at late time points. *Human gene therapy*, 2003 **14**(5):425–33. ISSN 1043-0342.

M. J. Saxton and K. Jacobson. Single-particle tracking: applications to membrane dynamics. *Annual review of biophysics and biomolecular structure*, 1997 **26**:373–99. ISSN 1056-8700.

M. J. Saxton. Anomalous Diffusion Due to Binding : A Monte Carlo Study. *Biophysical Journal*, **70**(3):1250–1262, 1996. ISSN 0006-3495.

H. Scher and M. Lax. Stochastic Transport in a Disordered Solid. I. Theory. *Physical Review B*, 1973 **7**(10):4491–4502. ISSN 0556-2805.

D. W. Scott. On optimal and data-based histograms. *Biometrika*, 1979 **66**(3):605–610. ISSN 0006-3444.

D. W. Scott. *Multivariate Density Estimation: Theory, Practice, and Visualization*. John Wiley & Sons, 2009. ISBN 047031768X.

H. Shimazaki and S. Shinomoto. A method for selecting the bin size of a time histogram. *Neural computation*, 2007 **19**(6):1503–27. ISSN 0899-7667.

T. Shors. *Understanding Viruses*. Jones & Bartlett Learning, 2011. ISBN 978-1449648923.

A. Sihvola. Mixing rules with complex dielectric coefficients. *Subsurface Sensing Technologies and Applications*, **1**(4):393–415, 2000.

A. Sihvola. Homogenization principles and effect of mixing on dielectric behavior. 2013 *Photonics and Nanostructures - Fundamentals and Applications*. ISSN 15694410.

E. Smith, J. Breznik, and B. D. Lichty. Strategies to enhance viral penetration of solid tumors. *Human gene therapy*, 2011 **22**(9):1053–60. ISSN 1557-7422.

G. D. Smith. *Numerical Solution of Partial Differential Equations: Finite Difference Methods*. Oxford University Press, 1985. ISBN 0198596413.

T. Stylianopoulos, B. Diop-Frimpong, L. L. Munn, and R. K. Jain. Diffusion anisotropy in collagen gels and tumors: the effect of fiber network orientation. *Biophysical journal*, 2010 **99**(10):3119–28. ISSN 1542-0086.

E. Swabb, J. Wei, and P. Gullino. Diffusion and convection in normal and neoplastic tissues. *Cancer research*, **34**(October):2814–2822, 1974.

E. Syková and C. Nicholson. Diffusion in brain extracellular space. *Physiological reviews*, **6**:1277–1340, 2008.

Y. Tao and Q. Guo. The competitive dynamics between tumor cells, a replication-competent virus and an immune response. *Journal of mathematical biology*, **74**:37–74, 2005.

S. Tatarkova, W. Sibbett, and K. Dholakia. Brownian Particle in an Optical Potential of the Washboard Type. *Physical Review Letters*, 2003 **91**(3):038101. ISSN 0031-9007.

O. Trédan, C. M. Galmarini, K. Patel, and I. F. Tannock. Drug resistance and the solid tumor microenvironment. *Journal of the National Cancer Institute*, 2007 **99** (19):1441–54. ISSN 1460-2105.

J. Tunaley. Theory of ac conductivity based on random walks. *Physical Review Letters*, **3**(5220):1037–1039, 1974.

C. Uebing, V. Pereyra, and G. Zgrablich. Diffusion of interacting lattice gases on heterogeneous surfaces with simple topographies. *Surface science*, **366**:14–16, 1996.

J. van Brakel and P. Heertjes. Analysis of diffusion in macroporous media in terms of a porosity, a tortuosity and a constrictivity factor. *International Journal of Heat and Mass Transfer*, 1974 **17**(9):1093–1103. ISSN 00179310.

L. van Hove. The approach to equilibrium in quantum statistics. *Physica*, 1957 **23**(1-5): 441–480. ISSN 00318914.

M. Vicente-Manzanares, D. J. Webb, and a. R. Horwitz. Cell migration at a glance. *Journal of cell science*, 2005 **118**(Pt 21):4917–9. ISSN 0021-9533.

S. Wang, S. Wang, and X. Song. Hopf bifurcation analysis in a delayed oncolytic virus dynamics with continuous control. *Nonlinear Dynamics*, 2011 **67**(1):629–640. ISSN 0924-090X.

Y. Wang, J. K. Hu, A. Krol, Y.-P. Li, C.-Y. Li, and F. Yuan. Systemic dissemination of viral vectors during intratumoral injection. *Molecular cancer therapeutics*, 2003 **2**(11):1233–42. ISSN 1535-7163.

Y. Wang, J. P. Tian, and J. Wei. Lytic cycle: A defining process in oncolytic virotherapy. *Applied Mathematical Modelling*, 2013 **37**(8):5962–5978. ISSN 0307904X.

L. M. Wein, J. T. Wu, and D. H. Kirn. Validation and analysis of a mathematical model of a replication-competent oncolytic virus for cancer treatment: implications for virus design and delivery. *Cancer research*, 2003 **63**(6):1317–24. ISSN 0008-5472.

B. a. Westrin and A. Axelsson. Diffusion in gels containing immobilized cells: a critical review. *Biotechnology and bioengineering*, 1991 **38**(5):439–46. ISSN 0006-3592.

E. F. Wheelock, K. J. Weinhold, and J. Levich. The tumor dormant state. *Advances in cancer research*, 1981 **34**:107–40. ISSN 0065-230X.

D. Wodarz. Viruses as antitumor weapons: defining conditions for tumor remission. *Cancer research*, 2001 **61**(8):3501–7. ISSN 0008-5472.

D. Wodarz. Gene therapy for killing p53-negative cancer cells: use of replicating versus nonreplicating agents. *Human gene therapy*, **159**:153–159, 2003.

D. Wodarz. *Killer cell dynamics: mathematical and computational approaches to immunology*. Springer, New York, NY, 2007. ISBN 9780387687339.

D. Wodarz. Computational modeling approaches to studying the dynamics of oncolytic viruses. *Mathematical Biosciences and Engineering*, 2013 **10**(3):939–957. ISSN 1551-0018.

D. Wodarz, A. Hofacre, J. W. Lau, Z. Sun, H. Fan, and N. L. Komarova. Complex spatial dynamics of oncolytic viruses in vitro: mathematical and experimental approaches. *PLoS computational biology*, 2012 **8**(6):e1002547. ISSN 1553-7358.

J. T. Wu, H. M. Byrne, D. H. Kirn, and L. M. Wein. Modeling and analysis of a virus that replicates selectively in tumor cells. *Bulletin of mathematical biology*, 2001 **63**(4):731–68. ISSN 0092-8240.

M. Zeyaullah, M. Patro, I. Ahmad, K. Ibraheem, P. Sultan, M. Nehal, and A. Ali. Oncolytic viruses in the treatment of cancer: a review of current strategies. *Pathology oncology research : POR*, 2012 **18**(4):771–81. ISSN 1532-2807.

W. Zhu and L. R. Petzold. Asymptotic stability of linear delay differential-algebraic equations and numerical methods. *Applied Numerical Mathematics*, 1997 **24**(2-3):247–264. ISSN 01689274.

W. Zwerger and K. Kehr. On the frequency dependence of the conductivity in random walk models with internal states. *Zeitschrift für Physik B Condensed Matter*, **166**:157–166, 1980.